An experimental study of porosity collapse and deformation band formation in high-porosity sandstones

Thesis submitted in accordance with the requirements of the University of Liverpool for the degree of Doctor of Philosophy by

Elliot Rice-Birchall

October 2022

Abstract

Compaction bands are millimetre to several centimetre thick sub-seismic bands of localised deformation in sandstones, which form approximately perpendicular to the maximum principal stress. They are associated with intense grain crushing and pore collapse, which generally results in an intra-band reduction in porosity and permeability. Consequently, these structures can exert a significant control on fluid flow, with potential implications for industrial processes such as fluid extraction during petroleum or groundwater production, or fluid injection during geothermal or CO_2 sequestration projects. However, due to the heterogeneous nature of sandstones, determining the role that specific microstructural properties have on band formation is extremely challenging and consequently, much is still unknown regarding compaction band formation. The aim of this study is to attempt to better understand the microstructural properties and external factors which promote and govern the formation of compaction bands in sandstones.

A new methodology has been developed which enables the production of high-porosity sandstone samples for laboratory testing which have reproducible petrophysical properties that can be systematically controlled. The technique uses the chemical reaction between sodium silicate and hydrochloric acid to precipitate cementing amorphous quartz between initially incohesive sand grains. This enables the production of sandstone samples for laboratory testing which have reproducible petrophysical properties that can be systematically controlled. Microstructural and mechanical analysis of the synthetic sandstones shows them to have realistic and reproducible uniaxial compressive, tensile and hydrostatic yield strengths, and to also exhibit yield curves with comparable geometries to natural sandstones of similar porosity and grain size. They also display elastic moduli within the expected range for natural sandstones.

The effect of porosity and grain size on compaction localisation is investigated using synthetic sandstones produced using the new methodology developed. Twelve sandstones are produced with 3 different starting porosities (27, 32, 37%) and 4 different mean grain sizes (314, 411, 747 and 987 μm). The samples are each shortened by 5% axial strain at an effective stress equivalent to 85% of their grain crushing pressure (P^*). Discrete compaction bands (≤3 grain diameters in width) oriented normal to the axial loading direction are only observed in the sample with the lowest starting porosity (27%) and smallest grain size (314 μm), while diffuse bands (>3 grain diameters in width) are observed for the same porosity at a larger grain size of 411 μm. No compaction bands develop for any grain size in either the 32% or 37% starting porosity samples. Porosity analysis indicates grain size reduction does not necessarily

correspond to porosity reduction indicating that compaction by grain rearrangement is as effective as localisation through comminution for these high-porosity synthetic sandstones.

The role of cement in compaction band formation is examined using three sandstones, Bentheim, Castlegate and a synthetic sandstone that each possess similar porosities (~26-29%) and grain sizes (~230-300 μm), but which are cemented differently, with syntaxial quartz overgrowths, clay, and amorphous quartz cement respectively. Each sample forms discrete compaction bands when taken to 5% axial strain at a starting effective stress equivalent to 85% of its hydrostatic yield (P^*) value. The compaction bands are only located at the sample ends in Bentheim Sandstone, whereas, in Castlegate Sandstone they are distributed throughout the whole sample and in the synthetic sample, the bands are only located within the sample centre. The results suggest that cement type plays a significant role in the mechanics of deformation within each of the samples, which in turn, determines where the compaction bands nucleate and develop. Since all the compaction bands identified are discrete, cement is not the primary control regarding the preference for the formation of diffuse or discrete compaction bands.

The nature of strain localisation with increasing effective confining pressure is examined in Castlegate Sandstone. At low effective pressures, deformation localises into sets of dilational conjugate shear bands orientated ~30° to the maximum compressive stress (σ_1). With increasing effective pressure, the localisation structures transition into sets of conjugate compactional shear bands and compaction bands, and finally, into sets of sub-parallel compaction bands, orientated perpendicular to σ_1, as the effective mean stress approaches the hydrostatic yield pressure (P^*). The deformation bands are associated with intense cataclasis, and primarily, localised porosity decrease, and their densities and intensities increase with both increasing effective mean stress and increasing axial strain. Two additional samples taken only to 2.5% axial strain at 190 and 210 MPa exhibit density and intensity values approximately half that of those taken to 5% axial strain. All the compaction bands observed in this study are discrete and develop pervasively throughout the samples even at 2.5% axial strain, indicating that some lithological, as opposed to stress control, is influencing their shape and distribution.

This research has implications for sandstone reservoirs. The ability to combine microstructural data with information relating to the stress history and current stress conditions of the reservoir may aid predictions regarding the formation of compaction localisation structures, as well as contributing towards details about their abundance and distribution within the reservoir unit. Future studies should build upon these results and examine how the interplay between these key microstructural properties (porosity, grain size and cement type) may influence the deformation processes during compaction localisation across a range of different pressure conditions.

Table of Contents

List of Figures and Tables

Preface

i) Thesis structure

Chapter 1 outlines the motivation, background, and aims of this thesis. *Chapter 2* will describe the experimental setup and methodologies implemented to collect and analyse data throughout the course of this project. The original research conducted in this thesis are presented in *Chapters 3, 4, 5* and *6*, which have each been prepared as standalone manuscripts. Consequently, some of the key concepts and methodologies implemented are repeated, particularly in the chapter introductions and methodology sections. Changes to the versions prepared for journal submission have been made to ensure continuity throughout the thesis. These are that the figures and subheadings have been renumbered and the reference sections compiled into a single list at the end of the thesis. *Chapters 3, 4, 5* and *6* each have their own abstract and any supplementary material compiled for submission of the manuscript has been included at the end of each chapter, the contents of which, are as follows:

- **Chapter 3** presents the results of a new methodology for the production of synthetic sandstone cores for mechanical testing. The microstructure and mechanical properties are rigorously tested and compared to those of natural sandstones.
- **Chapter 4** presents an investigation examining the compaction behaviour of 12 synthetic sandstones with different stating porosities and grain sizes. The focus is on how the nature of compaction localisation varies, due to changes in these 2 microstructural properties.
- **Chapter 5** presents an investigation into the compaction behaviour of 3 sandstones with similar microstructural properties but different cements. This is to examine whether cement plays a role in the development and nature of compaction localisation in high-porosity sandstones.

- **Chapter 6** presents a systematic study examining how localised deformation varies in Castlegate Sandstone, as a function of increasing starting pressure at the onset of axial loading. This is to comprehensively examine how localised deformation changes around the whole of the yield curve for sandstones.

Chapter 7 provides a summary of the thesis and its main conclusions. Supplementary materials are abbreviated as SM in the text, while all references are consolidated into one list which can be found at the end of the thesis.

ii) Status of manuscripts and co-author contribution

The status of the manuscripts (at the time of submission) and a description of the contribution of each co-author to *Chapters 3, 4, 5* and *6* in this thesis is outlined below.

Chapter 3: Rice-Birchall, E., Faulkner, D. R., & Bedford, J. D. (2021). The manufacture, mechanical properties, and microstructural analysis of synthetic quartz-cemented sandstones. *International Journal of Rock Mechanics and Mining Sciences*, *146*, 104869.

Submitted: 19th December 2020
Accepted: 12th August 2021
Published: 19th August 2021

Co-author contribution:
Elliot Rice-Birchall- Principal investigator, primary author, data collection, data analysis
Daniel Faulkner- Manuscript review, discussion
John Bedford- Manuscript review, discussion

Chapter 4: Rice-Birchall, E., Faulkner, D. R., & Bedford, J. D. (2022). The effect of grain size and porosity on the nature of compaction localisation in high-porosity sandstone. *Journal of Structural Geology*, 164, 104740.

Submitted: 16th May 2022

Accepted: 3rd October 2022
Published: 1st November 2022

Co-author contribution:
Elliot Rice-Birchall- Principal investigator, primary author, data collection, data analysis
Daniel Faulkner- Manuscript review, discussion
John Bedford- Manuscript review, discussion

Chapter 5: Rice-Birchall, E., Faulkner, D. R., & Bedford, J. D. (2022). The effect of cement type on the occurrence and nature of compaction localisation in three high-porosity sandstones. *Geophysical Research Letters.*

Submitted: In preparation

Co-author contribution:
Elliot Rice-Birchall- Principal investigator, primary author, data collection, data analysis
Daniel Faulkner- Manuscript review, discussion
John Bedford- Manuscript review, discussion

Chapter 6: Rice-Birchall, E., Faulkner, D. R., & Bedford, J. D. (2022). Strain localisation in Castlegate Sandstone under triaxial compression. Journal *of Geophysical Research- Solid Earth.*

Submitted: In preparation

Co-author contribution:
Elliot Rice-Birchall- Principal investigator, primary author, data collection, data analysis
Daniel Faulkner- Manuscript review, discussion
John Bedford- Manuscript review, discussion

ii) Funding information

This work is supported by Natural Environment Research Council grant NE/L002469/1 as part of an EAO Doctoral Training Studentship

Acknowledgements

Firstly, I would like to say a huge thank you to my supervisor, Dan Faulkner for his guidance, ideas, and support over the last four years. I am extremely grateful to have been given the opportunity to work in the Rock Deformation lab and I have learned an enormous amount from him both in the lab and the field.

Two other people who have played an enormous part in helping me throughout my PhD are Mike Allen and John Bedford. Mike has always been around the lab to provide assistance and advice (as well as questionable topics of conversation) and has been there to stop me doing something a bit stupid on more than one occasion. John's insights and ideas have formed a pivotal role in many of the chapters within this thesis, to which I am extremely appreciative.

It has been a great experience working in the lab and I would particularly like to thank Izzy and Louisa for the many laughs they have provided over the past few years, as well as helping me work out what it is I'm supposed to be doing most of the time. I will be forever grateful for you guys looking after me when I got stranded with Covid in the US. Thanks as well to Mahesh, Gary, Betty, Joe, Pier and Karl, and to everyone else who I have shared my time in the lab with.

Thanks to my friends, Tom, Iain, and James who made my undergraduate and masters such a great experience here and which was a big part of what made me want to continue on to do a PhD. Thanks as well to my non-geology mates, Josh, Scott, Will and others who made all the Covid lockdowns more bearable.

My parents have provided enormous support and advice throughout my entire education for which I am extremely grateful. I would also like to thank the rest of my family and close friends for their encouragement, even though most of them probably have no idea what it is I've been studying for the past four years.

Finally, I would like to say a huge thank you to Bethany for your amazing support and understanding throughout the whole of my PhD, especially through the more stressful times.

1 Introduction

1.1 Project motivation

Porous rocks such as sandstones are crucial lithological formations, due to their ability to form hydrocarbon reservoirs and aquifers, whilst also being potential repositories for waste products such as carbon dioxide (Bachu, 2008; Tsang et al., 2015; Warren, 2006). Understanding the deformation behaviour of these units has been a key area of research across a range of geoscience disciplines, including geotechnical engineering, hydrogeology, and reservoir geomechanics, owing to the influence that certain deformation processes exert on the mechanical and petrophysical properties of the rock (Allen et al., 2020; Hecht et al., 2005; Liu et al., 2019). During burial of a porous sandstone, porosity loss is primarily accommodated via two mechanisms, mechanical compaction, and chemical cementation (Pittman, 1979). Although porosity loss during the deeper stages of reservoir burial is typically associated with chemical processes such as cementation and pressure solution, the initial stages of burial are dominated by mechanical processes, such as pore collapse, grain rearrangement, grain crushing and strain localisation, which have important implications for geotechnical and reservoir projects (Bjørlykke, 1999). Consequences related to effective pressure increases within a reservoir as a result of fluid extraction and pore pressure reduction are the most common issues faced. Within the reservoir unit this can manifest as inelastic compaction, potentially destroying reservoir quality and making the extraction of hydrocarbons more challenging and costly (Heap et al., 2015). Inelastic compaction of the reservoir may also result in surface subsidence, which has the potential to result in severe economic and social costs for the affected area (Zoback, 2010). For instance, surface subsidence of up to around 30 cm has been associated with production from the Groningen gas field (Netherlands), which is now 70% depleted. Furthermore, small magnitude earthquakes have been recorded since the 1990s, which have increased in strength, causing non-structural building damage and heightening public concern (Dost et al., 2017; Pijnenburg et al., 2018).

During drilling and production of the reservoir unit, if the stress concentrations around the wellbore exceed the lithostatic strength of the rock, this can lead to failure of the well (Zoback, 2010). These near wellbore stress concentrations have also been known to form strain localisation structures, such as compaction bands and shear bands, which may decrease the near wellbore porosity and permeability (Haimson, 2001; Han & Dusseault, 2003; Katsman et al., 2009). Lower permeability around the wellbore may also restrict pressure drawdown to the near wellbore, potentially promoting fault displacement due to perturbation of the local stress field (Fredrick et al., 1998). Continued fluid extraction could also promote the formation of strain localisation structures, such as shear bands and compaction bands throughout the rest of the reservoir unit, possibly resulting in compartmentalisation (Olsson et al., 2002). This will drastically reduce permeability and reservoir quality, which also has implications for fluid injection, for instance, during CO_2 sequestration, where compartmentalisation may result in overpressured sections of the reservoir, increasing the probability of fault reactivation (Allen et al., 2020). This could also have consequences regarding the effectiveness of the reservoir as a long-term storage unit, particularly if larger faults are able to propagate through the overlying seal formation (Allen et al., 2020; Orlic, 2016). In reservoir and geotechnical engineering studies, integrating information regarding the microstructural properties of the reservoir unit with its stress path history, is crucial to determining the occurrence, type, and amount of accumulated inelastic deformation, such as strain localisation (Ballas et al., 2015; Soliva et al., 2013). This ultimately necessitates an understanding of the microphysical and micromechanical processes of porous rocks, such as sandstones, during their deformation.

1.2 Porous rock deformation

When subjected to a stress state beyond its elastic yield strength, porous rocks, such as sandstones will exhibit an in instantaneous mechanical response (i.e., dilation or compaction), the type of which, is strongly influenced by the effective pressure the rock is subjected to. The rock may experience further deformation if left at inelastic conditions for a prolonged period, by way of time-dependent deformation mechanisms, such as pressure solution and sub-critical

crack growth (Atkinson & Meredith, 1981; Heap et al., 2009; Heap et al., 2015; Rutter, 1976; Wong et al., 1997; Zhang et al., 1990). However, throughout this study, the focus will be on the time-independent behaviour of sandstones in response to an applied stress, since in sandstone reservoirs the deformability of the rock can be altered due to sudden stress changes as a result of fluid injection/extraction. The strength evolution of the sandstone will be dictated by dilational and/or compactional processes, which may inhibit or promote instabilities, potentially resulting in the development of strain localisation structures such as faults and deformation bands (Fossen et al., 2018; Rudnicki & Rice, 1975; Wong & Baud, 1999).

The deformation of porous rocks has commonly been described using the principles of critical state soil mechanics (Roscoe et al., 1958; Roscoe & Burland, 1968; Schofield & Wroth, 1968; Wood, 1990). Here, a yield envelope is plotted in *P*-*Q* space (Figure 1.1a), where *P* is the effective mean stress ($P = \left(\frac{\sigma_1+\sigma_2+\sigma_3}{3}\right) - P_f$), P_f is the pore-fluid pressure and *Q* is the differential stress ($Q = \sigma_1 - \sigma_3$) (Wong et al., 1997; Zhang et al., 1990). The yield curve separates the field of elastic or limited inelastic behaviour from that of larger-scale inelastic behaviour. The first models based on critical state soil mechanics for describing the behaviour of soft soils such as clay, were the Cam-Clay (CC) and Modified Cam-Clay (MCC). In *P*-*Q* space, the yield surface of the CC is logarithmic, whereas in the MCC the yield surface plots as an elliptical curve. The elliptical curve of the MCC is also commonly termed the yield function. The nature of the inelastic deformation experienced by a porous rock will vary depending on the region of the curve that its stress state intersects. This can be broadly characterised into two regimes; dilatancy at low pressures, which is typically associated with faulting and localised deformation, and compaction at high pressures, which is often associated with distributed cataclasis or strain localisation structures such as shear-enhanced compaction bands and pure compaction bands (Figure 1.1b) (Baud et al., 2004; Issen & Rudnicki, 2000; Menéndez et al., 1996; Wong et al., 1997). Porous rocks can be compacted under purely hydrostatic stress (no differential stress), which is represented by a point on the high-pressure side of the P-axis,

known as *P**. The results of numerous empirical studies for sandstones (Baud et al., 2004, 2006; Bedford et al., 2019; Cuss et al., 2003; Rutter & Glover, 2012; Vajdova et al., 2004; Wong et al., 1997; Wong & Baud, 1999) have shown their yield curves to be broadly elliptical, as has been observed for soil mechanics.

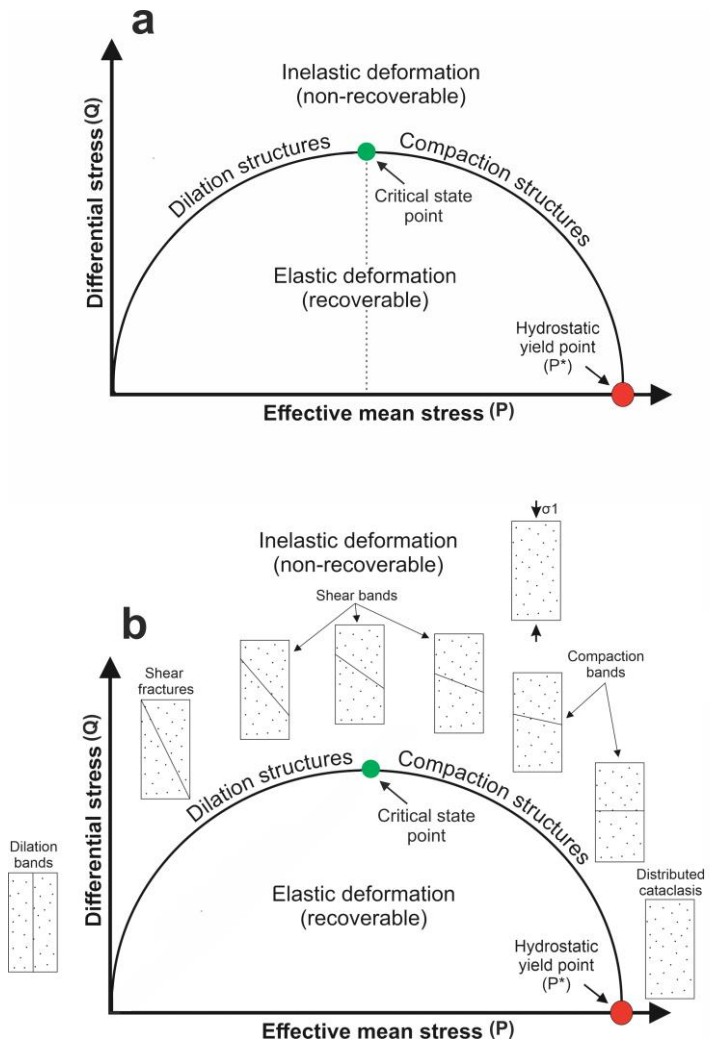

Figure 1.1. *a). A conceptual representation of an elliptical yield curve for a porous sandstone. Deformation is elastic (recoverable) within the curve, whereas outside of it the deformation will be inelastic (non-recoverable). The low-pressure side of the curve is associated with dilational deformation and the high-pressure side with compactional deformation. b) A graphical illustration of where the different types of localised deformation in a porous sandstone would be expected to occur, with respect to the stress state.*

P*, and consequently the size of the yield curve, has been shown to vary as a function of grain radius and porosity according to the Hertzian contact model of Zhang et al. (1990), which is derived from Hertzian theory (Hertz, 1881):

$$P^* \propto (R\phi)^{-3/2} \tag{1.1}$$

where R is grain radius (mm) and ϕ is fractional porosity. Sandstones with large grains and high porosity exhibit smaller yield curves compared to those with fine-grains and low porosity (Figure 1.2). The size of the yield curve for porous rocks, including sandstones, has also been shown to vary due to accumulation of inelastic strain and is termed the work hardening rule (Prager, 1956), which either increases or decreases the porosity depending on whether the rock is dilating or contracting. The new porosity will therefore define a new yield curve (Allen et al., 2020; Bedford et al., 2018, 2019; Pijnenburg et al., 2018, 2019a). An increase in porosity and/or grain size will cause the yield curve to shrink, while a decrease in porosity and/or grain size will cause it to expand. It is therefore possible to construct a family of yield curves for each subsequent yield state, with the compaction and dilation regimes separated at the crest by the critical state line (CSL) (Figure 1.2a). In 3D, this can be visualised with a third axis representing porosity × grain radius. Here, the respective P^* values for each yield curve form the normal consolidation line (NCL), with each ellipse spacing out along the porosity × grain radius axis (Figure 1.2b). However, the concept of a family with unique curve shape has been shown in experimental studies to not adequately describe porous rock deformation and that the accumulation of inelastic strain is associated with significant yield curve evolution (Baud et al., 2006; Bedford et al., 2018, 2019; Pijnenburg et al., 2018, 2019a). Alternative models to critical state soil mechanics have been suggested that permit the yield curve to evolve as the porosity decreases or increases with the buildup of inelastic volumetric strain (e.g., DiMaggio and Sandler, 1971; Carroll, 1991).

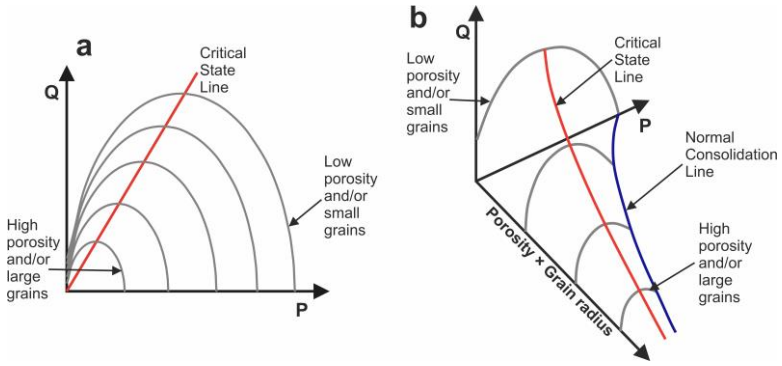

Figure 1.2. *a) The effect of grain size and porosity on the yield cap of porous sandstones, modified from Bedford et al. (2018). Larger grain size, higher porosity sandstones are inherently weaker than finer-grained, less porous sandstones, resulting in smaller yield caps. The critical state line (CSL) denotes the boundary between dilation and compaction. The diagram shown in a) can be represented in 3D (b) with the addition of a z-axis- porosity × grain size.*

1.3 Strain localisation in porous sandstones

This study is primarily concerned with addressing the questions surrounding the nature and development of compaction bands in high-porosity sandstones. Compaction bands are a type of deformation band which form approximately perpendicular to the maximum principal stress within the compaction regime on the high-pressure side of the sandstone yield curve (Baud et al., 2004; Eichhubl et al., 2010; Fossen et al., 2018). They are generally associated with intense cataclasis and permeability reduction relative to the surrounding rock (David et al., 1994; Main et al., 2003). However, to understand compaction bands, it is necessary to first understand the kinematics and deformation processes surrounding deformation bands as a whole. Deformation bands are strain localisation structures which develop in porous rocks, such as sandstones. Deformation bands have been observed to form in every tectonic regime, from pure extension to strike-slip, to contraction (Carbillet et al., 2021; Soliva et al., 2016) in

sandstones with porosities >13% (Fossen et al. 2018). Deformation bands can be classified kinematically into three main types: dilation bands, shear bands and compaction bands, with shear bands being the most common (Mollema & Antonellini, 1996; Olsson & Holcomb, 2000; Wong et al., 2001). As deformation bands have become more widely recognised in different tectonic settings across the world, it has become clear that on the kinematic spectrum (Figure 1.3), most bands develop somewhere between compaction bands and shear bands, with most bands possessing a more dominant shear component (Fossen et al., 2018). Various microscale deformation processes are associated with the formation of these different band types, including rotation and frictional grain sliding, grain crushing, dissolution (pressure solution) and cementation. The latter two mechanisms are slow processes which can occur during or after deformation band formation (Ngwenya et al., 2000; Philit et al., 2015). More recently, deformation bands have been found to organise into kinematic subgroups on the shear-compaction spectrum (Fossen et al., 2018) (Figure 1.3).

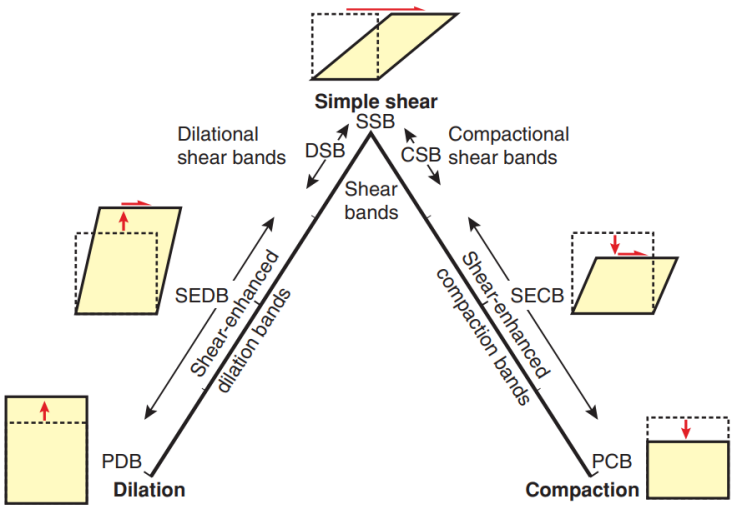

Figure 1.3. *a) Diagram taken from Fossen et al. (2018) showing the end members of dilation, shear, and compaction on the kinematic spectrum. PDB: pure dilation band; SEDB: shear-enhanced dilation band; DSB: dilational shear band; SSB: simple shear band (or just shear band); CSB: compactional shear band; SECB: shear-enhanced compaction band; PCB: pure compaction band.*

Simple shear bands are a kinematic subgroup of shear bands whereby the grains deform by translation and rigid rotation with negligible cataclasis (Figure 1.3 and Figure 1.4). For well packed grains to move past one another without fracturing, intermittent periods of compaction and dilation are required; however, these processes are of small importance since they usually cancel each other out over time (Fossen et al., 2018). No significant change in porosity with relation to the host-rock occurs in simple shear bands and only if phyllosilicate minerals are realigned along the band will the porosity decrease. However, if force chains oblique to the band walls form, the structure of the grain framework may change (Ballas et al., 2013; Bésuelle, 2001; Eichhubl et al., 2010; Soliva et al., 2013).

By contrast, some compaction element is always present in cataclastic shear bands (Figure 1.3) and so these diverge from simple shear to form compactional shear bands (CSBs) (Aydin et al., 2006; Fossen et al., 2007; Soliva et al., 2013). The shear displacement in these bands is often much greater than the compaction displacement (Figure 1.4), as observed by Aydin (1978) for classical cataclastic deformation bands. CSBs typically display thicknesses of ~1 mm and displacements of a few centimetres, with the porosity decreasing from around 25% to 10-15% within the band. Thus, for a 1 mm thick band, compaction displacement is 0.13–0.2 mm (13–20%) and the shear displacement is approximately two orders of magnitude greater. CSBs are found in both the contractional and extensional regimes in well-sorted quartz sandstones deformed at depths at or greater than 1.5 km (Fossen et al., 2018).

Shear-enhanced compaction bands (SECBs) (Figure 1.3) usually exist as conjugate sets within high porosity sandstone formations (Eichhubl et al., 2010). Using the scheme of band-perpendicular shortening (compaction, C) plotted against shear displacement (S) (Figure 1.4, Fossen et al., 2018), SECBs generally display smaller degrees of shear offset ($S/C<2$), less cataclasis and are thicker (several centimetres) compared to CSBs (Figure 1.5) (Charalampidou et al., 2014; Eichhubl et al., 2010). Since their shear offsets are often very small (mm scale), they can be difficult to discern from pure compaction bands (PCBs) in the field, although their appearance as conjugate sets generally implies some component of shear (Sternlof et al., 2005).

In Figure 1.4 they plot close to the S/C=1 line, exhibiting similar degrees of shear and compaction displacement. SECBs have so far only been identified from contractional tectonic regimes, including sandstones deformed during the Laramide Orogeny in southern Utah (Fossen et al., 2011; Schultz, 2009; Schultz et al., 2010), the Sevier Orogeny in Nevada (Eichhubl et al., 2010; Fossen et al., 2015) and the Pyrenean Orogeny, separating France and Spain (Ballas et al., 2013; Robert et al., 2018).

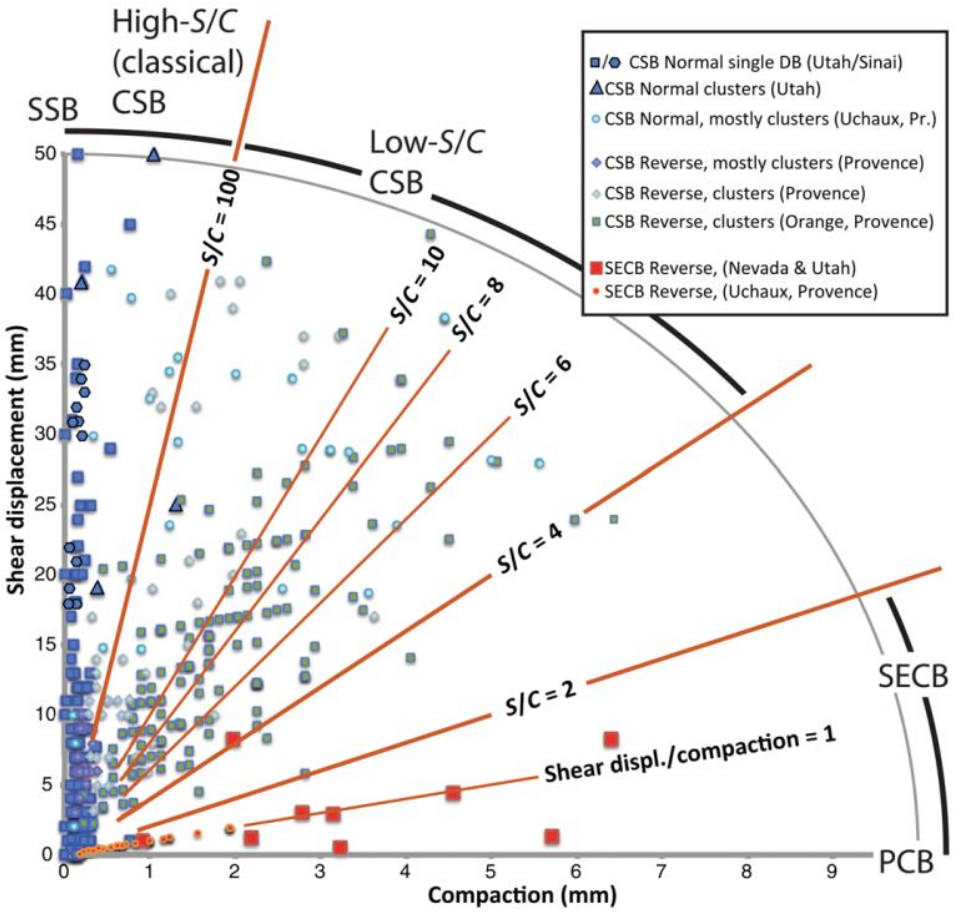

Figure 1.4. *Figure taken from Fossen et al. (2018) displaying a plot of compaction (band-perpendicular shortening) versus shear displacement. In the lower portion of the figure, near the S/C=1 line, where the contributions from shear and compaction are comparable in size, shear-enhanced compaction bands (SECBs) are generally observed. Classic compactional shear bands (CSBs) plot in the upper section of the diagram, while clusters of CSBs from Provence (extensional and contractional) plot in a greater area of the upper figure.*

Pure compaction bands (PCBs) have likewise only been documented in regions of contractional deformation, in sandstones with very high porosities (Eichhubl et al., 2010; Fossen et al., 2011, 2015; Mollema & Antonellini, 1996; Schultz, 2009; Schultz et al., 2010). PCBs exhibit negligible shear offset (Figure 1.4) and can be divided into 2 types in the field. These are a sinuous type with small-scale, sinusoidal undulations which share kinematic and geometrical similarities with stylolites, and a zigzag, chevron-style type, whereby each limb of the chevrons can be considered a SECB (Figure 1.5). The smaller, sinusoidal type are a few millimetres thick with a 0.5 mm wavelength, whereas the chevron-style PCBs are approximately 1-3 cm thick with a wavelength of around 5–10 cm (Fossen et al., 2018). PCBs can become almost planar in some cases and always form perpendicular to the principal shortening direction, bisecting the obtuse angle between contemporaneous CSBs or SECBs (Liu et al., 2015). For the small strains these structures represent, in most cases the principal shortening direction strongly correlates with the local maximum principal stress direction (σ_1). Two types of compaction bands have also been identified from laboratory studies, based on the classification scheme of Baud et al. (2004). Compaction bands with a thickness ≤3 grains are described as discrete, whilst those with a thickness >3 grains are described as diffuse.

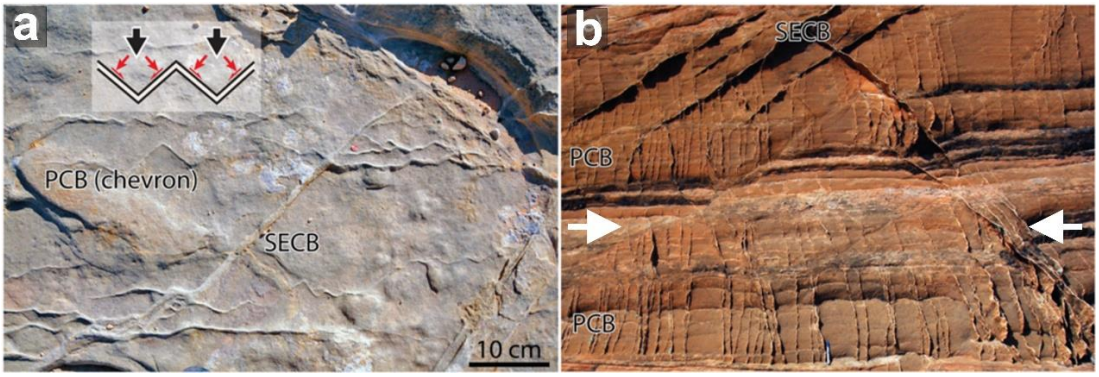

Figure 1.5. *Field examples of compaction bands from the Buckskin Gulch, Utah, modified after Fossen et al. (2018). a) Chevron-type PCBs and SECBs. b) SECBs and PCBs (vertical). The PCBs form in the highly porous (25–30%) sandstone units, while the SECBs form in slightly lower porosity beds. The white arrows in b) represent the compression direction.*

1.4 Field studies of pure compaction bands (PCBs)

Although PCBs were the first type of compaction band to be formally identified (Mollema & Antonellini, 1996), natural examples of PCBs are relatively rare. This is largely due to them forming coincident to bedding in extensional tectonic regimes and so are hard to identify in many basinal settings. However, two field sites exist where PCBs have been well documented. These are the Buckskin Gulch in southern Utah (USA) and the Valley of Fire State Park in southeastern Nevada (USA), both of which are located in Jurassic aeolian sandstones.

1.4.1 Navajo Sandstone Formation (Utah)

Mollema & Antonellini (1996) described localisation structures in the aeolian Jurassic Navajo Sandstone Formation, Utah as lying perpendicular to the inferred direction of maximum compression, and consequently, named them compaction bands. They identified two band morphologies: 'crooked' compaction bands approximately 0.1-0.5 cm thick, up to 2 m in length and with wavelengths and amplitudes of 1-5 cm, and 'thick' compaction bands, which were straight over lengths of around 10 m and around 0.5-1.5 cm thick, but which thinned towards the terminations. They also noted that at their terminations the thick compactions bands often transformed into crooked compaction bands. The bands usually occurred within shear band fault compressional quadrants, trending normal to the direction of the maximum principal stress. Shear offset was found to be negligible across the bands, with grain crushing and comminution also being limited, despite considerable grain fracturing. However, micrographic analysis found that significant pore volume reduction did occur within these localisation structures. The authors concluded that the PCBs typically resided in large grain size (0.3-0.8 mm) and high porosity layers (20-25%).

Schultz (2009) also studied the subparallel compaction bands from the Buckskin Gulch site. The band lengths were found to range from 0.57-15.3 m, with thicknesses ranging from 5.1-25.4 mm. The authors obtained a displacement-length scaling with a power law exponent

of ~0.5 and compaction energies of G_c = 55-120 kJ/m^2. From the field measurements, they inferred a band-normal compressional value of 24-30 MPa, with the bands forming at a depth of 0.92–1.3 km. The authors also remarked that favourable host-rock properties likely also played a significant role in PCB formation.

A second study in the area by Schultz et al. (2010) found that PCBs formed in sedimentary layers which have the highest porosities (28%), largest average grain sizes (0.42 – 0.45 mm) and the lowest critical pressure values (~22 MPa). From this, they inferred the compaction bands to have developed after burial, at a depth of ~1.5 km, slightly greater than those predicted in their previous study.

Fossen et al. (2011) examined the wavy (0.5–2cm thick) compaction bands in the Navajo Sandstone in the Buckskin Gulch site. They concluded that PCBs only formed when the grain size was >0.4 mm, porosity was higher than 29% and permeability was >10^7 darcies (9.87×10^{-6} m^2), with these conditions being met in the lower parts of the grain flow units within the dunes where the grains were most coarse.

1.4.2 Aztec Sandstone Formation (Nevada)

Sternlof et al. (2004, 2005) identified PCBs in the Aztec Sandstone which is exposed across the Valley of Fire State Park/Muddy Mountains area in southeastern Nevada and is the stratigraphical equivalent of the Navajo Sandstone. The PCB structures observed in the poorly lithified outcrops were tabular, bounded and penny-shaped, with fins produced due to the weathering out of the bands in positive relief, forming a high-angle to depositional bedding. In the central sections, the PCBs were 1–2 cm thick, with lengths considerably greater than those in the Navajo Sandstone at tens to over 100 m. The band spacing varied from centimetres to over a metre. Within the compaction bands, the reduction in porosity from approximately 25 to 15% was found to be a result of primary compaction, with intense intra-granular fracturing accommodating the deformation of quartz grains. This porosity reduction was present in zones ranging from a few grain diameters in width (~0.5 mm) to a few centimetres.

Aydin & Ahmadov (2009) characterised bed-parallel compaction bands in the Jurassic Aztec sandstone. These cut through the depositional bedding and were mostly sub-horizontal, with an echelon geometry and positive relief. Microstructural observations found the bands to be half as porous as the host rock, with an order of magnitude lower permeability. The authors suggested that the abundance of the bed-parallel bands in the area would provide significant heterogeneity and anisotropy in relation to seismic and hydraulic rock properties.

Eichhubl et al. (2010) also identified PCBs in the Valley of Fire, describing them as lacking any component of shear and forming perpendicular to the loading direction. They were usually wavy in shape, rarely planar and often seen to transition into chevron patterns of alternating right and left-lateral SECBs along strike. From their observations, they concluded that the PCBs and SECBs observed would have required a high initial porosity, close to the loose packing value, along with good sorting and a high maximum principal effective stress of about 20 MPa.

Fossen et al. (2015) examined several deformation band types in the Aztec Sandstone in the Muddy Mountain Thrust footwall in the Buffington Tectonic Window. PCBs were observed but were relatively rare. The PCBs exhibited non-planar, sinuous, or chevron-shaped geometries, similar to those identified by Eichhubl et al. (2010), as well as a lack of any shear offset, characteristic of PCBs. They were also only observed in the most porous and permeable sections of the layers, with values of 20–25% and 2–15 darcy permeability, as has been observed previously in both the Navajo and Aztec sandstones. The PCBs only exhibited small degrees of cataclasis, similar to those observed by Eichhubl et al. (2010) but less than those in the Navajo Sandstone.

1.5 Field studies of shear-enhanced compaction bands (SECBs)

Like PCBs, SECBs have only been observed in contractional tectonic regimes, such as in the Najavo and Aztec sandstones in Utah and Nevada. They were previously called compaction bands, until Eichhubl et al. (2010) distinguished that they are related differently to

the principal stress and strain directions and thus, kinematically different. As mentioned previously, unlike PCBs they form oblique to the maximum principal stress direction and consequently, have an element of shear strain.

1.5.1 Navajo Sandstone Formation (Utah)

SECBs were observed by Fossen et al. (2011) in the quartz-rich aeolian Navajo Sandstone in the Buckskin Gulch area. These were dipping structures and thicker than the PCBs at ~2 mm to several centimetres. As well as the significant compaction within the SECBs, there was evidence of reverse shear offset (~2 mm) where the bands cross-cut one another. The SECBs commonly manifested as conjugate sets, with the dihedral angle being 73°, close to the 75° reported by Eichhubl et al. (2010). Microstructural investigation found the SECBs to exhibit more intense grain crushing than PCBs, supporting the previous findings that shear results in more grain crushing within deformation bands (Baud et al., 2006). They were also concentrated in the lower sections of the sand dune beds, where porosity and permeability were highest.

SECBs were also recorded in the Navajo Sandstone located in the East Kaibab monocline by Schultz et al. (2010). These were steeply dipping structures exhibiting small shear strains, evident by the offsetting of pre-existing markers such as aeolian cross beds, as observed by Eichhubl et al. (2010). They found a contemporaneous relationship between the formation of the PCBs and SECBs, with some of the PCBs transitioning to SECBs in certain layers. The SECBs were found to form in the most porous layers of the sequence (24–28% porosity), with the largest grain sizes (0.27–0.45 mm).

1.5.2 Aztec Sandstone Formation (Nevada)

Prior to their formal characterisation and kinematic identification by Eichhubl et al. (2010), Aydin & Ahmadov (2009) noted the possible presence of SECBs in the Aztec Sandstone in the Valley of Fire. They observed compaction bands parallel to bedding with sub-horizontal to moderately inclined (>20°) dip angles. The greater the band inclination, the greater

the percentage of fractured grains and the more fractures that were seen in each grain. The more inclined bands also exhibited some microscopically detectable shear offset, with these characteristics being suggested by the authors to represent shear-enhanced compaction.

Eichhubl et al. (2010) described SECBs in the Aztec Sandstone as being bands of oblique shortening which accommodated similar degrees of band-parallel shear displacement and band-perpendicular shortening. The bands were orientated at 38-53° to the maximum compressive principal stress. Like PCBs, the SECBs exhibited grain breakage at the grain contacts, however, force chains were also observed due to grains aligning in contact, orientated at 45° to the band. These force chains were considerably longer, with stronger modal attitudes compared to those in PCBs. However, the porosity reduction compared to the host-rock was the same as for PCBs at 5-7%, with similar degrees of cementation. Eichhubl et al. (2010) suggested that while large porosities, good sorting and 20 MPa pressures are required for PCB and SECB formation, SECBs may be able to develop between σ_2 and σ_3 under greater differential stress.

Fossen et al. (2015) also identified SECBs which were thick (several cm) structures, with a relatively planar geometry. Similarly, to the aforementioned studies, the SECBs exhibited mm scale (or less) reverse offsets, with the bands exhibiting intense cataclasis through the presence of fractured grains, although intact grains were also observed. Evidence was also seen for pressure solution at grain contacts, where some quartz grains intruded into others. However, there was little evidence for quartz cementation. Permeability reductions in the SECBs were on the scale of 0 to 2.8 orders of magnitude, with the bands that exhibited the most dissolution and fracturing showing the largest decreases. The authors also noted that the SECBs preferentially formed in the most porous, permeable, and coarse-grained of the aeolian dune layers, similarly to the results obtained by Fossen et al. (2011) for the Navajo Sandstone.

1.6 Laboratory studies of compaction bands

The following section will present an overview of some of the key laboratory studies on compaction bands, which have examined both external controls and intrinsic microstructural properties which influence compaction band formation and development.

1.6.1 Effective stress

Numerous laboratory studies have shown effective stress (pressure) to influence the failure mode and ultimately, the type of localisation structures which form in porous rocks such as sandstones. At relatively low effective pressures, the dominant failure mode is shear fracturing (dilational shear) (Bésuelle et al., 2000; Charalampidou et al., 2011, 2014, 2017; El Bied et al., 2002; Fortin et al., 2005, 2009; Menéndez et al., 1996; Rizzo et al., 2018), whereas compaction bands or homogeneous cataclastic flow dominates at higher effective pressures (Baud et al., 2004; Charalampidou et al., 2014; DiGiovanni et al., 2000; Fortin et al., 2005, 2006, 2009; Menéndez et al., 1996; Mollema & Antonellini, 1996; Olsson & Holcomb, 2000; Sternlof et al., 2005; Vajdova et al., 2003; Wong et al., 1997). Hybrid deformation can occur at mid to high effective pressures (i.e., near the centre of the yield curve), whereby shear-enhanced compaction, is present alongside other hybrid failure mechanisms, including conjugate compactional shear bands and possibly pure compaction bands (Baud et al., 2004, 2021; Bésuelle, 2001; Fortin et al., 2005, 2006; Klein et al., 2001; Louis et al., 2006, 2007; Mair et al., 2000, 2002; Sari et al., 2022; Wong et al., 2001).

1.6.2 Axial strain

As the amount of axial strain increases (post-failure), laboratory studies have shown that the damage within compaction bands also increases (Klein et al., 2001; Louis et al., 2006; Mair et al., 2000; Vajdova & Wong, 2003; Wu et al., 2000). However, the damage observed at the same axial strain varies depending on the regime. For instance, Wu et al. (2000) found that in Darley Dale Sandstone (~13% porosity and 0.22 mm grain size), at the same strain value, within the dilational regime (low pressures) the crack density was twice that recorded for the

compactional regime (high pressures). The number of compaction bands has also been observed to increase with higher amounts of axial strain. For instance, Heap et al. (2015) performed triaxial compression experiments on the Bleurswiller Sandstone at an effective pressure of 80 MPa. Samples were loaded to 1.5, 3% and 13% axial strain and the number of bands were observed to increase with increasing axial strain. At 13% axial strain, the samples contained so many bands that it was difficult to distinguish individual ones. Other studies have reported similar observations (Baud et al., 2004, 2015; Charalampidou et al. 2014; Fortin et al., 2005, 2006; Tembe et al., 2008), as have studies examining other porous rocks (Abdallah et al., 2021; Chen et al., 2020; Huang et al., 2019; Wu et al., 2020).

1.6.3 Pore fluid

The effect of pore fluid chemistry and pressure on the mechanical stability and elastic properties of different reservoir rocks has been examined in previous studies (Aldrich Jr, 1969; Asahina et al., 2019; Dropek et al., 1978; Falcon-Suarez et al., 2017; Jones et al., 1998; Lesmes & Frye, 2001; Mann & Fatt, 1960; Sayers & Han, 2002; Wang et al., 2016; Wu et al., 2018). For instance, David et al. (2015) found that creep, due to subcritical crack growth (Atkinson, 1984; Atkinson & Meredith, 1981) in weakly consolidated Sherwood Sandstone occurred at a much slower strain rate for oil injection compared to water injection. Water was also found to trigger mechanical instability in under 30 minutes, via the process of water weakening, whereas oil injection did not, even after several hours. Yang et al. (2014) found that the creep contribution to rock deformation in red sandstone increased with increasing pore pressure, with the specimens exhibiting significant time-dependent effects at higher deviatoric stresses. The mineralogy of the reservoir rock has also been shown to be important, with various studies finding water weakening to be particularly strong in calcite-cemented sandstones and carbonate rocks (Carles & Lapointe, 2004; Heggheim et al., 2005; Madland et al., 2006; Risnes et al., 2005).

Some studies have also examined the effect of pore fluid on the formation of compaction bands. Baud et al. (2000) conducted triaxial compression experiments on samples

of Berea, Boise, Darley Dale, and Gosford sandstone. The authors found that at comparable pressures, the wet samples started to develop SECBs at lower pressures than the dry samples, which they attributed to water-weakening due to water reducing the specific surface energy. A study by Tembe et al. (2008) found that whilst there was a water weakening effect for samples of Diemeldstadt and Bleurswiller Sandstone, Bentheim Sandstone seemed to be insensitive to the presence of water. However, in samples of wet Bentheim Sandstone, at the slowest displacement rate, Stanchits et al. (2009) found that the stress needed to nucleate compaction band propagation was 20% lower than for dry samples. Furthermore, they observed that compaction nucleation was strain rate sensitive and increased as strain rate increased, similar to the findings of Baud & Meredith (1997) on Darley Dale Sandstone. A possible explanation for this behaviour was attributed to stress corrosion processes being more prevalent at slower strain rates (Atkinson & Meredith, 1981), which was confirmed by the lack of strain rate dependence for the stress in dry Bentheim Sandstone samples. A later study on Bleurswiller Sandstone by Baud et al. (2015) also found that in wet samples shear-enhanced compaction developed at significantly lower stresses, which was attributed to be a result of water weakening, similar to that observed by Baud et al. (2000).

1.6.4 Porosity

The results of numerous laboratory experiments have found that compaction bands form in natural sandstones with porosities ranging from approximately 13-30% (Baud et al., 2004, 2015; Carbillet et al., 2021; Charalampidou et al., 2011; DiGiovanni et al., 2000; Haimson, 2001; Haimson & Lee, 2004; Olsson et al., 2002; Stanchits et al., 2009; Tembe et al., 2008; Wong et al., 2001). Compaction band nucleation sites may also be controlled by any local heterogeneities, including large pores, as seen in Rothbach Sandstone, where high porosity areas (along with pre-existing microcracks) promoted compaction band formation (Louis et al., 2007). During axial compression of Bleurswiller Sandstone, stress concentrations were associated with the high porosity regions and compaction bands nucleated from these sites. These local high porosity regions were suggested to act similarly to notches by Fortin et al.

(2009), which promote compaction band propagation via the induction of a stress concentration at their tip (Stanchits et al., 2009). However, in notched Bentheim Sandstone samples only 1 compaction band propagated from the tip, whereas local heterogeneities in Bleurswiller Sandstone nucleated several bands which subsequently merged (Fortin et al., 2009).

1.6.5 Grain size, sorting and morphology

Alongside porosity, numerous experimental studies have shown grain size to be a principal microstructural control on the mechanical and hydraulic properties of sandstones (Carbillet et al., 2021; Paterson & Wong, 2005; Rutter & Glover, 2012; Zhang et al., 1990). However, there have been very few laboratory studies which have examined the effect of grain size on compaction band development. UCS values for sandstones have been observed to increase non-linearly with an increasing gradient against logarithmic strain rate for fine-grained sandstone (105 μm), while a linear increase was observed for medium-grained (228 μm) sandstone and unsystematic for coarse grained (321 μm) sandstone (Wasantha et al., 2015). Some experimental studies have shown larger grains to contain more flaws than smaller grains (Balsamo & Storti, 2011; Griffith, 1921) and thus, be more prone to fracturing under lower axial stress, possibly facilitating the development of compaction bands (Ballas et al., 2013; Skurtveit et al., 2014). However as discussed in section 1.5, field observations of compaction bands have recorded them across a wide range of grain sizes (~0.3–0.8 mm) (Carbillet et al., 2021; Fossen et al., 2018).

Grain sorting has been shown to have a significant effect on compaction localisation. Cheung et al. (2012) compared well-sorted Bleurswiller Sandstone with poorly-sorted Boise Sandstone and found that discrete compaction bands formed over a wide effective pressure range in Bleurswiller Sandstone, whereas no bands developed in the Boise Sandstone. They observed that the larger quartz and feldspar grains remained relatively undamaged and suggested that this was analogous to the ‘constrained comminution’ model of Sammis et al. (1987), whereby the contact force in a granular assembly is distributed such that larger particles are cushioned and shielded from the stress concentration by the smaller grains.

Grain shape will likely have a significant effect on compaction band formation, since more rounded grains will exhibit smaller contact surfaces, creating higher stress concentrations at these points, promoting grain fracturing and the initiation of cataclasis (Cheung et al., 2012; Fossen et al., 2018). However, there have been very few experimental studies examining this microstructural property of sandstones, especially in relation to compaction band formation, largely due to the difficulty in obtaining natural sandstones with controlled grain shapes for testing. Experiments using 2D analogue materials have found the shape and orientation of particles to either facilitate or prohibit shear localisation (Charalampidou et al., 2009), while the presence of elongated grains, such as micas and clays has been shown in some laboratory studies to accommodate the majority of deformation, although this is also likely due to their high-deformability (DiGiovanni et al., 2000; Fortin et al., 2005, 2009).

1.6.6 Mineralogy

Mineralogy has been shown by numerous experimental studies to significantly influence the mechanical and elastic properties of reservoir rocks, such as sandstones and limestones (Arizzi et al., 2015; Cuesta-Cano et al., 2021; Carmichael, 2017; Dobereiner, 1984; Dyke & Dobereiner, 1991; He et al., 2019; Pan et al., 2016; Wolcott et al., 1989). Wong et al. (1997) examined the transition from brittle faulting to cataclastic flow by assessing the mechanical deformation of Berea, Boise, Darley Dale, Kayenta, and Rothbach, sandstones with varying grain sizes, mineralogical compositions, and porosities (14.5–35%). Mineralogy was suggested to be of considerable importance since discrepancies in the yield envelopes were observed between Berea and Keyenta sandstone which have similar grain sizes and the same porosity but different mineral compositions. However, whether or not mineralogy has a strong influence on compaction band formation is still debated. Wu et al. (2000) and Zhu & Wong (1997) observed significant intra-granular cracking and grain crushing in Darley Dale Sandstone, which has a high feldspar content (14%). Consequently, they suggested that sites of crack nucleation during compaction were likely to develop along pre-existing cracks in the

cleavage planes of feldspars, with Zhu & Wong (1997) suggesting that the Hertzian fractures which developed preferentially in feldspars, acted as sites for grain crushing initiation.

Klein et al. (2001) suggested that the homogeneous mineralogical composition in Bentheim Sandstone (~95% quartz, 3% kaolinite, 2% orthoclase) may favour discrete compaction band formation. However, laboratory studies on the mineralogically immature Bleurswiller Sandstone by Fortin et al. (2005), which contained 50% quartz, 30% feldspar, and 20% oxide-micas, found it to also form discrete compaction bands, leading them to conclude that mineralogical composition is unlikely to be a critical factor for discrete compaction band development.

1.6.7 Cementation

The type, quantity and mineralogy of cement has been shown to affect the mechanical properties of sandstones (Acar & El-Tahir, 1986; He et al., 2019; Huang & Airey, 1998; Prosser et al., 1993; Wong & Wu, 1995). The quantity of brittle silica-glass cement consolidating Fontainebleau sand grains was found by David et al. (1998) to increase the strengths, critical pressures and elastic moduli of the samples and shift the brittle-to-ductile transition towards higher pressures, when increased from 3-5% volume. In Rotliegendes Sandstone, differences in static/dynamic moduli between samples found quartz cement to be much more effective in suturing grains together, compared to clay. However, similar to mineralogy, the role of cement on compaction band formation is still poorly understood and there have been very few experimental studies examining its control on the formation of compaction bands. The dolomite cement at the grain contacts in Berea Sandstone was proposed by Menéndez et al. (1996) to prohibit micro-crack nucleation and propagation. The authors found that under deviatoric and isotropic compression, both the feldspar and quartz grains developed Hertzian fractures, whilst regions which remained undeformed were highly dolomite cemented. Consequently, Menéndez et al. (1996) proposed that the weakly cemented regions were more prone to grain crushing and pore collapse, which may nucleate compaction bands. Compaction bands in the laboratory were argued by Sternlof et al. (2004) to develop at high confining pressures in moderate to well

cemented sandstones (Berea, Bentheim, Castlegate), whilst in the field, they formed at middle mean compressive stresses in very poorly cemented sandstones. Since cemented sandstones are stronger than those with little or no cement, this was suggested to account for the differences in required confining pressure for compaction band formation.

1.6.8 Bedding heterogeneity

Studies have highlighted how bedding and other heterogeneities can increase rock mass anisotropy in sandstones and limestones (Baud et al., 2005; Chen et al., 2020; Shahin et al., 2020; Tembe et al., 2008). Louis et al. (2007, 2009) found that samples of Rothbach Sandstone cored parallel to the bedding direction exhibited lower axial yield stresses compared to those cored perpendicular to it. Since the compactive failure and strain localisation developed away from the bedding heterogeneity, the authors proposed that the bedding inhibited strain localisation. The deformation bands that were observed, formed sub-parallel to the bedding, with the failure mode also being controlled by the bedding heterogeneity, since parallel cored samples developed homogeneous compaction (no localised features), specimens cored at 45° formed compactant shear bands, and samples cored perpendicular to bedding developed diffuse compaction bands. Similar observations were also made by Bésuelle et al. (2003) in an earlier study also on the same sandstone. It was suggested by Aydin & Ahmadov (2009) that the propagation paths of compaction bands and their resulting geometry is controlled to some extent by bed interfaces, with this based on the geometrical characteristics observed for bed-parallel compaction bands. The effects of rock heterogeneity in the formation of compaction bands in porous carbonates has been examined in some studies. Cilona et al. (2014) performed experiments at 25 MPa confining pressure on two samples cored at different orientations with respect to bedding. They found that different types of microstructures formed (compactive shear bands and diffuse deformation) due to varying the angles between bedding and the maximum compressive stress.

1.6.9 Specimen geometry

Several studies have implemented a notch in laboratory sandstone specimens in order to promote compaction localisation in the centre of the sample. Vajdova & Wong (2003) introduced the V-shaped notch, with this also being used by Tembe et al. (2006) and Charalampidou et al. (2011, 2014). A circumferential U-shaped notch was implemented by Stanchits et al. (2009). The presence of a notch provides stress heterogeneity and forces compaction bands to nucleate from its tip. However, non-symmetric initiation and propagation of compaction bands may result from imperfections in the notch, meaning that its presence exerts a significant control on compaction band morphology (Tembe et al., 2006; Vajdova & Wong, 2003). The impact of compaction bands on fluid flow was examined by Pons et al. (2011) on three cylindrical, notched (0.8 mm wide and 5 mm deep) specimens of Bentheim Sandstone. AE data showed the compaction bands to propagate from the notch, with the X-ray imaging results of the capillary rise in the deformed samples showing that the compaction bands disturbed the water flow and slowed imbibition.

1.6.10 Mechanisms of compaction band formation

The micromechanics of compaction bands have been investigated in numerous studies. Triaxial deformation experiments on natural sandstones such as Bleurswiller, Castlegate, Diemelstadt, Rothbach, Berea, Bentheim and Darley Dale have found compaction localisation in these samples to generally be characterised by pore collapse (resulting in a porosity and permeability reduction) and grain crushing (initiating at the stress concentrations at the grain contacts). Pore collapse can also be associated with grain rearrangement since grain-cement or grain-grain bonds must be broken in order for a pore to collapse. It should also be noted that in nearly all laboratory studies, the region outside the compaction band is relatively undamaged (Baud & Meredith, 1997; Baud et al., 2004, 2015; Charalampidou et al., 2011, 2017; Louis et al., 2007; Menéndez et al., 1996; Stanchits et al., 2009; Wu et al., 2000).

Different types of localisation have also been found to exhibit distinct acoustic emissions (AE) signatures. Continuous accumulation of AE usually characterises the formation of high-angle shear bands, whereas episodic AE surges punctuated by episodic stress drops with an overall strain hardening trend, are characteristic of discrete bands (Baud et al., 2004). The number of discrete bands correlates with the number of AE surges and stress drops. In Castlegate Sandstone DiGiovanni et al. (2000) suggested that there was an initial stage of porosity reduction due to grain rotation and bond-breakage, before a secondary phase of more intense grain breakage and comminution which resulted in a larger porosity decrease. In Berea Sandstone, compaction was suggested by Menéndez et al. (1996) to be associated with the initiation of brittle micro-cracking at the grain contacts, via the formation of Hertzian fractures, which also facilitated pore collapse and grain crushing. However, due to the poor cementation, grain movement was limited at high stresses. Porosity reduction was facilitated via the comminuted grains filling the pore space. Studies on notched Bentheim Sandstone specimens also observed moderate grain crushing and significant cracking near the peak stress, with the bands propagating from the notch tip to the sample centre (Stanchits et al., 2009; Tembe et al., 2006; Vajdova & Wong, 2003).

1.6.11 Compaction band morphology

A classification system for deformation bands formed in the brittle – ductile transitional regime was developed by Baud et al. (2004), based on the orientation and width of the localised structures. Using the classification system, discrete bands are defined as tabular features 1-3 grains in width whereas diffuse bands have a thickness of more than 3 grains. Castlegate Sandstone was identified from AE data to form diffuse compaction bands and exhibited strain hardening behaviour (DiGiovanni et al., 2000; Olsson et al., 2002; Olsson & Holcomb, 2000; Olsson, 2001). By contrast, Bentheim Sandstone formed discrete compaction bands with the overall strain hardening behaviour punctuated by stress drops. These variations in mechanical behaviour between Bentheim and Castlegate Sandstone were suggested by Olsson et al. (2002) to shed light on the factors which govern compaction band formation, and who went on to

speculate that the variation may be a result of the core orientation in relation to bedding. In unnotched specimens of Bentheim Sandstone, tortuous, discrete compaction bands were observed (Baud et al., 2004), whilst parallel compaction bands initiated from the notch tips in notched specimens (Vajdova & Wong, 2003). In Diemelstadt Sandstone tortuous discrete compaction bands were recorded by Louis et al. (2006), whilst in Bleurswiller Sandstone Fortin et al. (2006) observed discrete, non-planar compaction bands.

1.6.12 Permeability and localisation

Several experimental studies have examined permeability evolution within sandstones during compaction (David et al., 2001; Fortin et al., 2005; Yu et al., 2019; Zhu & Wong, 1997). However, there have been fewer laboratory investigations which have examined permeability specifically across compaction bands. Main et al. (2000) developed a model for fault-sealing rates due to the sequential formation of deformation bands, based on laboratory and field observations, which predicts a post-failure nonlinear dependence of permeability on sample strain. A permeability reduction of 1-2 orders of magnitude was recorded by Holcomb & Olsson (2003) across compaction bands in Castlegate Sandstone. A similar permeability decrease was also recorded in Bentheim Sandstone by Vajdova et al. (2004), with both studies suggesting that compaction bands may act as barriers for fluid flow in porous rocks. Baud et al. (2012) examined permeability evolution during triaxial compression of Diemeldstadt sandstone. The authors observed permeability reductions to be around 1 order of magnitude greater in samples cored perpendicular to the bedding direction, compared with those cored parallel to it. The permeability measurements across the compaction bands also found them to have permeabilities 2-3 orders of magnitude less than the host rock, thus supporting the findings of Holcomb & Olsson (2003) and Vajdova et al. (2004). A later study by Baud et al. (2015) examined strain localisation and compaction in Bleurswiller Sandstone. They observed a significant permeability decrease at an axial strain of 0.42%, which they interpreted as the onset of shear-enhanced compaction. They found the permeability evolution to be similar to that observed by Fortin et al. (2005) in Bleurswiller samples but with two notable differences. The

first was that the permeability of Bleurswiller samples decreased by a factor of ~2-5 which is less than that seen by Fortin et al. (2005). Secondly, the samples had significantly lower permeability values of 10^{-14} m^2. They attributed these findings to be a result of mineralogical differences, with their Bleurswiller containing more clay, which is likely to have decreased the permeability. The permeability results of Baud et al. (2015) are also significantly lower than the permeability reductions observed in the Bentheim and Diemelstadt sandstones by Vajdova et al. (2004) and Baud et al. (2012) respectively. Deng et al. (2015) examined permeability variations using core-flooding experiments in samples of Aztec Sandstone which contained compaction bands. Their results showed that the permeability within the compaction bands was generally 0.5 to 3 orders of magnitude lower than that of the host rock.

1.7 Nature of the problem

Since the identification of compaction bands by Mollema & Antonellini (1996), numerous laboratory and field studies have been undertaken in order to better understand both the intrinsic microstructural properties of sandstones and the external influences which control their nature and development. While significant progress has been made regarding how these structures propagate, largely due to the development of new imaging techniques and experimental apparatus (Charalampidou et al., 2014; Louis et al., 2007; Stanchits et al., 2009), much is still unknown with respect to the microstructural properties of sandstones which favour the growth of compaction bands. Properties such as porosity, grain size and cement have been suggested by previous authors to be key controls on the development of compaction localisation, however, the heterogeneous nature of sandstones has meant that determining exactly what influence properties such as these have on band development is extremely challenging. Furthermore, there are disparities which exist between observations of natural compaction bands and those produced within natural sandstones in laboratory studies; for instance, laboratory compaction bands formed in natural sandstones generally require much greater effective stresses to form compared to natural equivalents and are usually associated with larger amounts of cataclasis.

1.8 Research aims

The overall aim of this study is to develop a better understanding of compaction bands in high porosity sandstones, with particular focus on the microstructural properties which promote and control their formation. However, as mentioned previously, the heterogeneous nature of sandstones means that it is difficult to identify the control that specific properties have on compaction band formation. To tackle the problem of sandstone heterogeneity, a new methodology for the production of synthetic sandstones has been developed, whereby microstructural properties can be systematically controlled, and the effects of certain microstructural heterogeneities can be minimised. Combining the use of these synthetic sandstones with natural equivalents has enabled several systematic laboratory studies to be performed throughout this project, whereby the role of specific microstructural properties on compaction localisation is examined. By combining these experimental methodologies with newly developed image analysis techniques, this study will attempt to address the following questions:

1. What microstructural properties of sandstones promote or inhibit the growth of compaction bands?
2. How do variations in microstructural properties and other external physical factors affect the nature and distribution of compaction localisation in sandstones?

2 Methods

The following chapter will outline in detail the experimental and analytical methods used to obtain and analyse the data presented in *Chapters 3, 4, 5* and *6* of this thesis. It has been divided into two sections. The first section gives a detailed overview of the high pressure, high temperature triaxial deformation apparatus in the Rock Deformation Laboratory, Department of Earth, Ocean and Ecological Sciences, University of Liverpool, which was used to conduct most of the experiments throughout this project. The second section outlines the various image analysis techniques which were developed in order to extract quantitative information, associated with strain localisation, from the experimental samples.

2.1 Experimental apparatus

2.1.1 Triaxial rig overview

The apparatus used to conduct the triaxial deformation tests during this research was Triaxial Rig 1 (TR1), a high pressure, high temperature triaxial deformation rig, comprising servo-controlled pore pressure, confining pressure, and axial load systems (Figure 2.1). The rig, first described by Mitchell & Faulkner. (2008), can be divided into three main sections: (1) the pressure vessel which houses the sample assembly, (2) the force gauge block which contains the force gauge, (3) the axial loading system, which comprises the gear trains, drive motor and ball screw. The axial load is applied from the bottom of the axial loading column, not the top, as is the case for other deformation apparatus. Triaxial deformation experiments can be performed using this rig at temperatures of up to 250º C and pressures of up to 250 MPa, (equivalent to conditions found at 10 km in the Earth's crust). In this research most of the experiments are performed under axisymmetric compression whereby the greatest principal stress (σ_1) is increased axially whilst the other principal stresses (σ_2 and σ_3) are held equal:

$$\sigma_1 \geq \sigma_2 = \sigma_3$$

An overview of the temperature apparatus of the rig has not been included, as this condition was not altered in any of the experiments throughout this project. During deformation

experiments, the servo-controlled pore fluid system can measure ultra-low sample volume and permeability changes of ~0.1 mm^3 and 10^{-22} m^2 respectively. Samples with approximate dimensions of 50×20 mm can be accommodated, with a maximum loading capacity of 30 tonnes being provided by a servo-controlled ball-screw driven actuator. High performance materials (maraging steel C300 with a yield strength of ~2 GPa) are incorporated into the design of the internal force gauge to maximise the sensitivity of the load measurement. The full 30 tonne loading capacity can be applied directly to the sample, due to the balanced piston design; however, this was bypassed throughout this PhD for simplicity, as such high loads were not required. Fluid pressure at the upstream end of the sample is controlled by a servo-controlled pore fluid system, with this also serving as a high precision volumometer (Figure 2.2). A low volume reservoir is connected to the downstream end of the sample, which can utilise the pulse transient method of Brace et al. (1968) and pore pressure oscillation technique of Fischer (1992) in order to measure permeability and volume change.

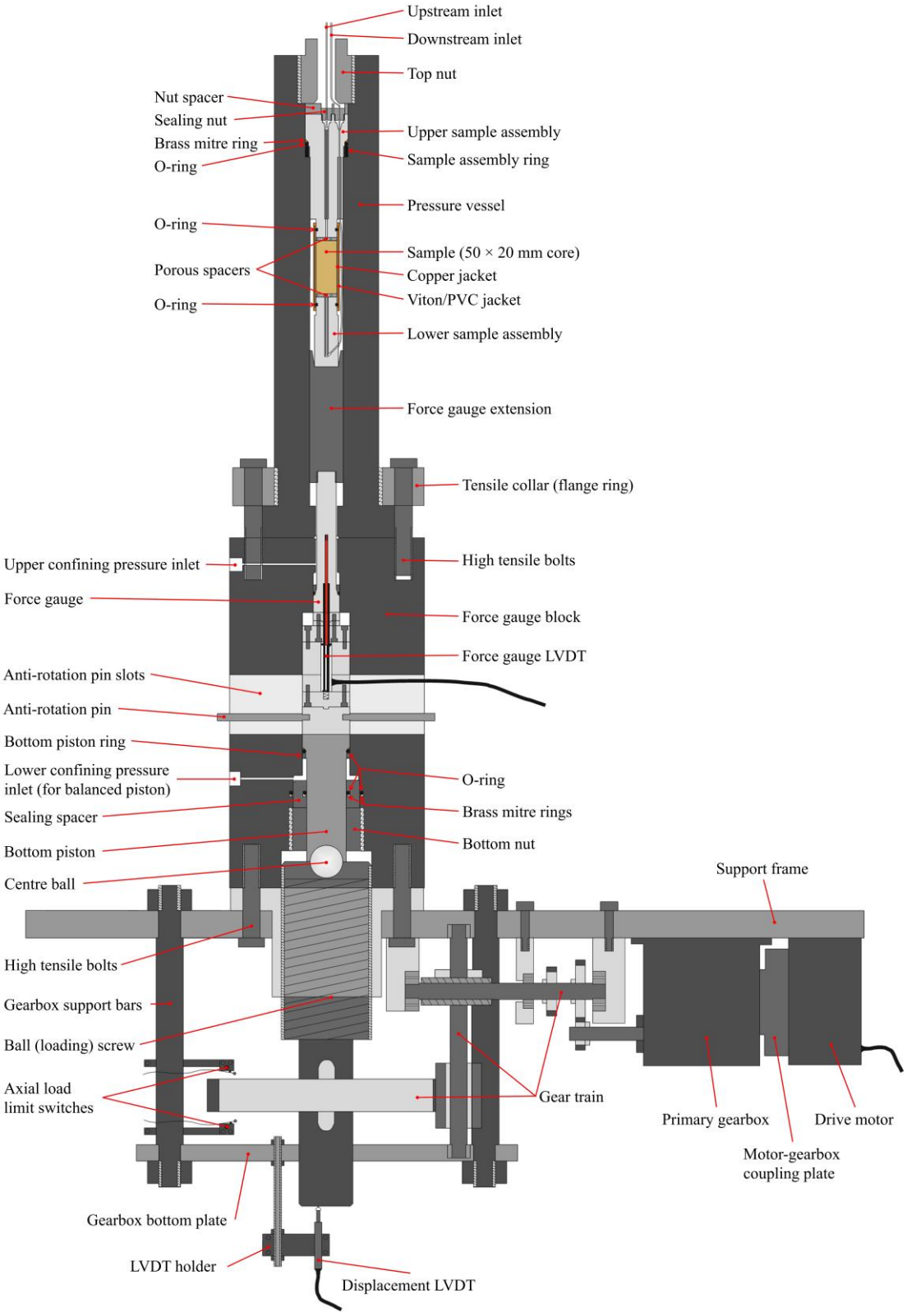

Figure 2.1. *The triaxial deformation apparatus used for the majority of the mechanical experiments in this study. Modified after Mitchell & Faulkner (2008).*

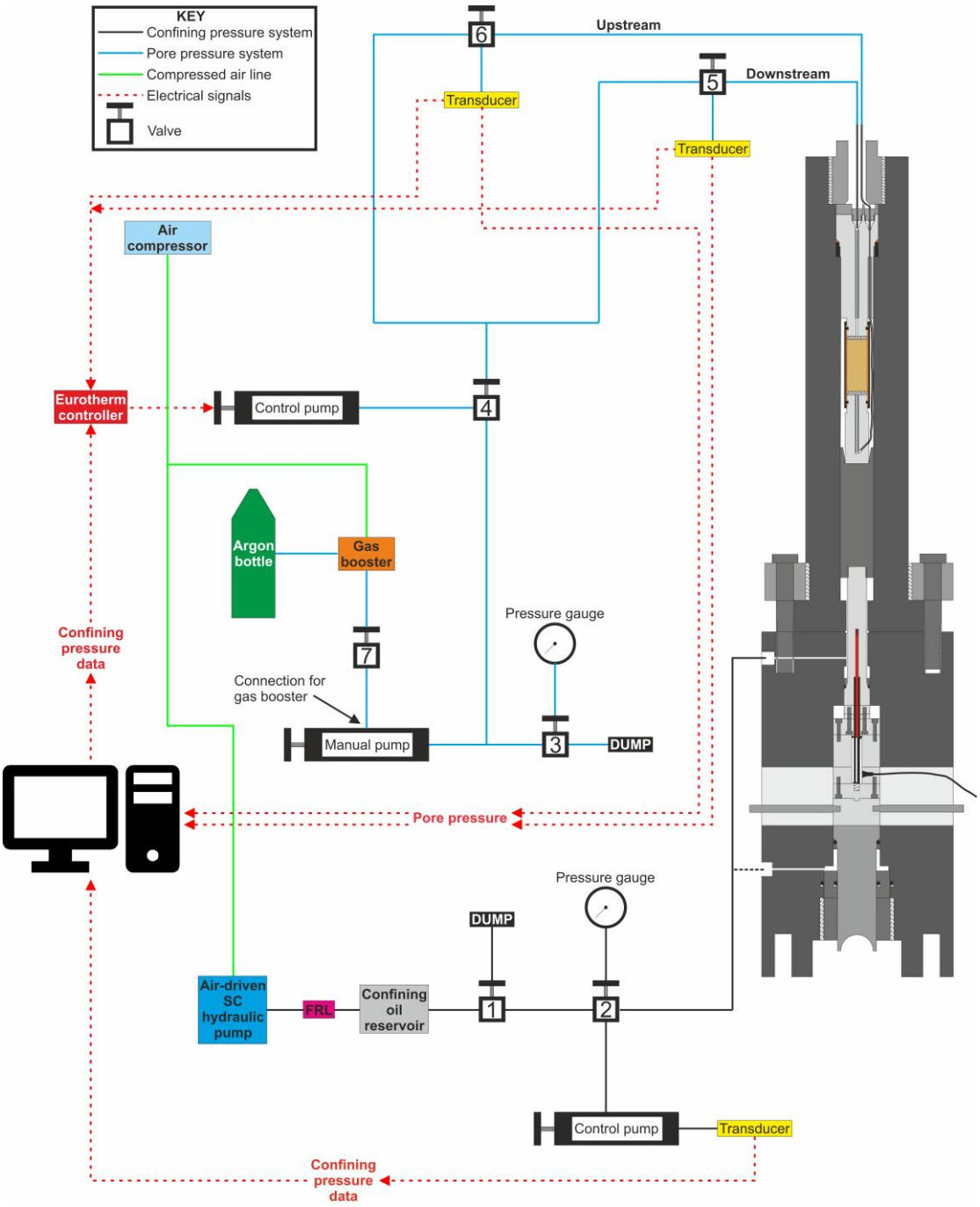

Figure 2.2. *Schematic diagram of the plumbing of the triaxial deformation apparatus.*

2.1.2 Pressure vessel and sample assembly

The pressure vessel for the rig was made from Jessop Saville H. 50 (AISI H. 13) hot worked tool steel, with silicon oil pressurised by a compressed air-driven hydraulic pump used

as the confining medium (Figure 2.3a). The preferential use of silicon oil over water is to prevent rust in certain parts of the system, thus enhancing the lifespan of the vessel. The sample assembly is inserted into an opening in the top of the pressure vessel, which is positioned at the top of the apparatus (Figure 2.3b). A threaded top nut secures the sample assembly in the pressure vessel, with a brass mitre ring and O-ring configuration sealing the gap between the inside of the pressure vessel and the upper sample assembly (Figure 2.3c). A pressure transducer and analogue gauge enable confining pressure to be maintained during experiments. The vessel has been tested at confining pressures of up to 375 MPa but is designed for long periods of use at up to 250 MPa. The sample assembly is composed of 3 main parts; the top and bottom sample assemblies and the space in the middle, which is occupied by the sample (Figure 2.4). Samples 50 mm in length and 20 mm in diameter are designed to be accommodated. The sample is jacketed before being placed into the sample assembly to keep it separate from the confining medium, with a double jacket arrangement preferred for most of the tests in this study. Each sample was first inserted into an annealed copper jacket, to better preserve the deformation microstructures from damage during de-pressurisation and post-experiment handling. This arrangement was then inserted into a Viton/PVC jacket to prevent any leaks of the confining fluid into the sample, should the wall of the thin copper jacket perforate (Figure 2.5). A seal is achieved where the copper jacket touches the O-rings in the upper and lower sample assemblies, due to the confining pressure being greater than the pore pressure. Distilled water or argon gas can be used as the pore fluid, with argon being the fluid predominantly used throughout this PhD project. A high-pressure thin bore (0.5 mm) pipe, which is attached to the upstream connector at the top of the upper sample assembly, delivers pore fluid pressure to the sample assembly. After flowing through the upper sample assembly, pore fluid pressure is introduced to the sample and passes through it, before exiting through the lower sampler assembly. A thin bore pipe silver soldered into the bottom of the lower sample assembly enables pore fluid to exit on the downstream side, with this pipe wrapped around the jacketed sample and threaded through into the upper sample assembly where it is secured with a connector (Figure 2.4). To

ensure pore pressure is evenly distributed across the faces of the sample, porous alumina spacers are inserted onto both its downstream and upstream ends.

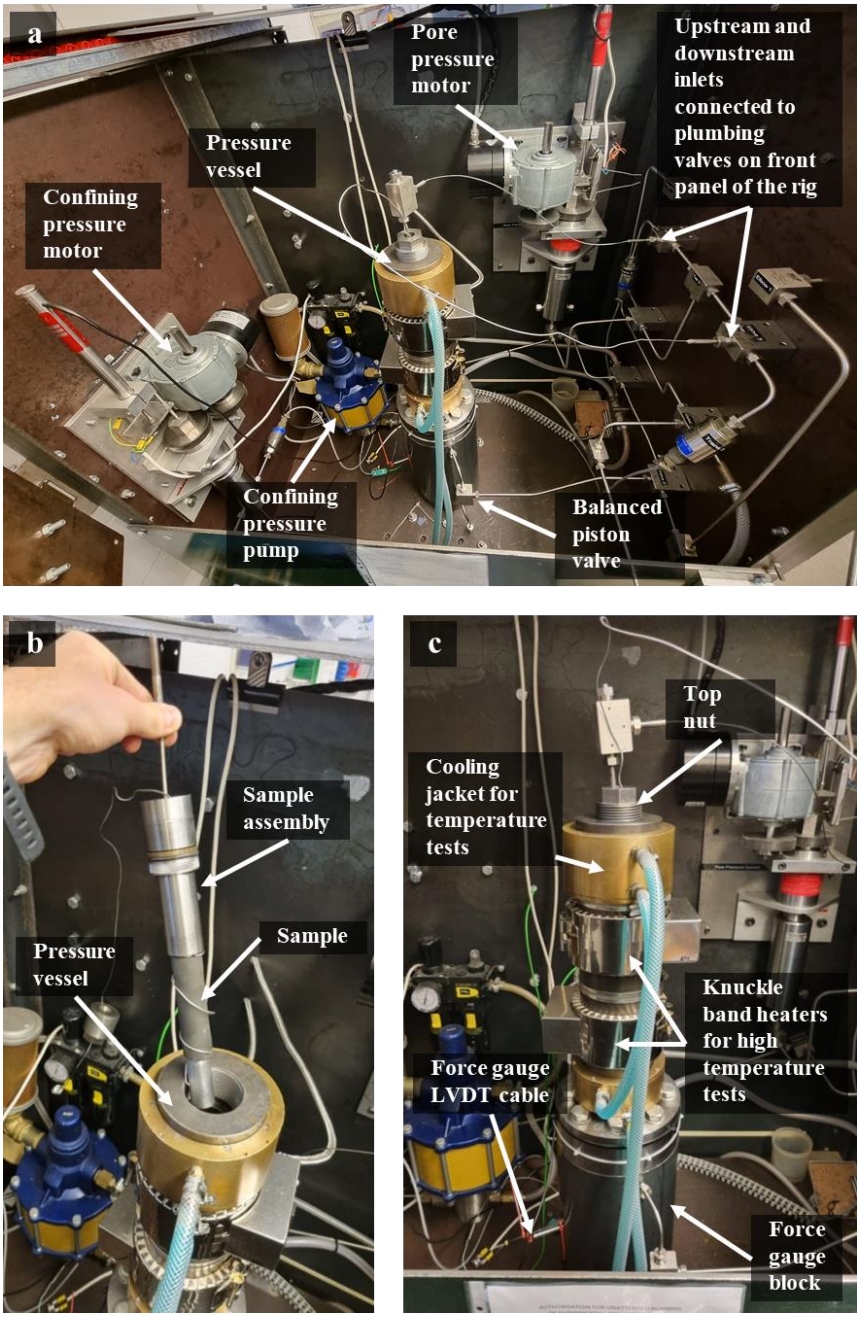

Figure 2.3. *a) External view of the upper deformation apparatus, showing the confining and pore pressure systems and the pressure vessel and force gauge block. b) Insertion of the sample assembly into the pressure vessel. c) Sample assembly secured within the pressure vessel and sealed with the top nut, ready for pressurisation.*

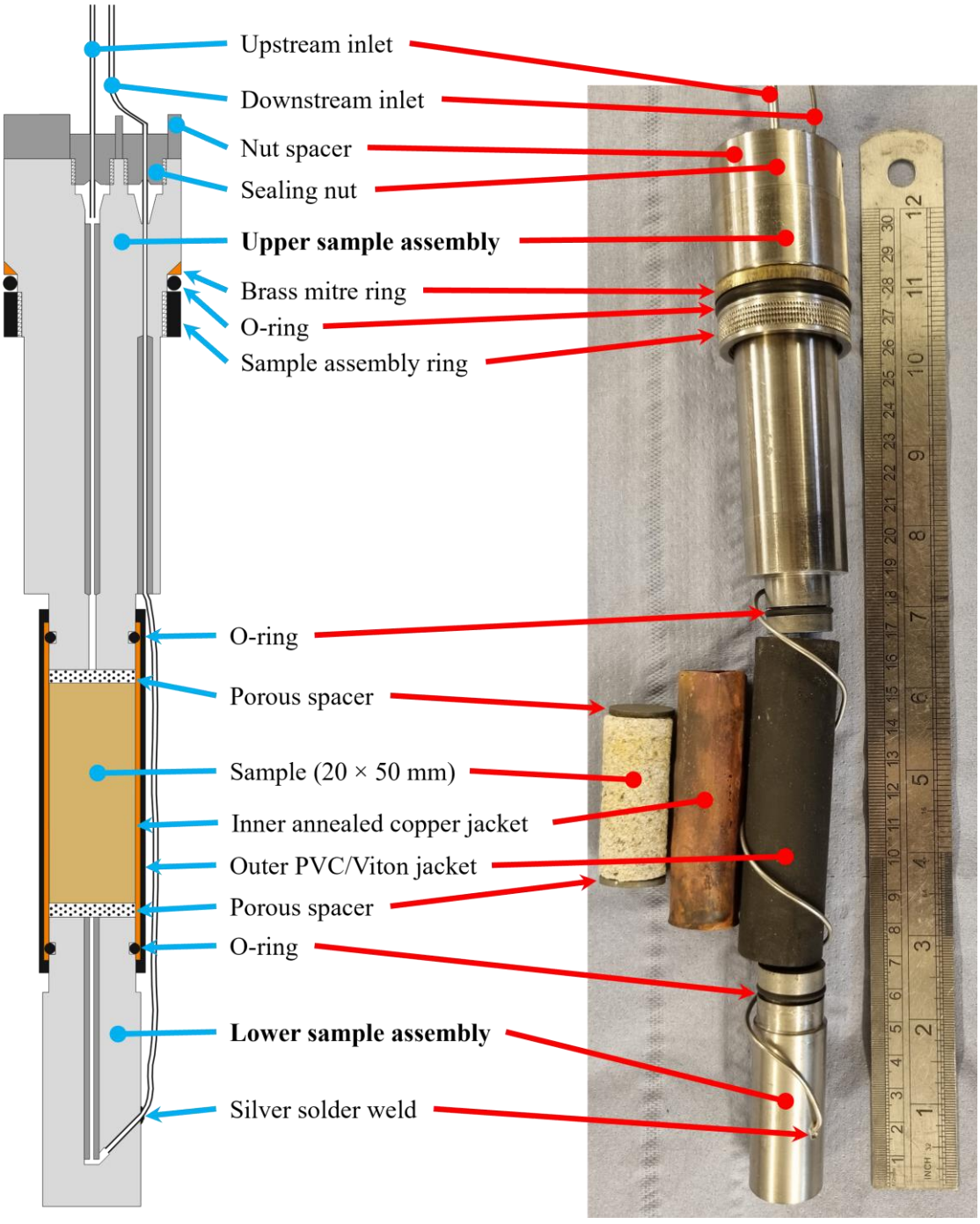

Figure 2.4. *The sample assembly, showing the size of the samples used (20×50 mm cores) and the double jacket arrangement which prevents leaks.*

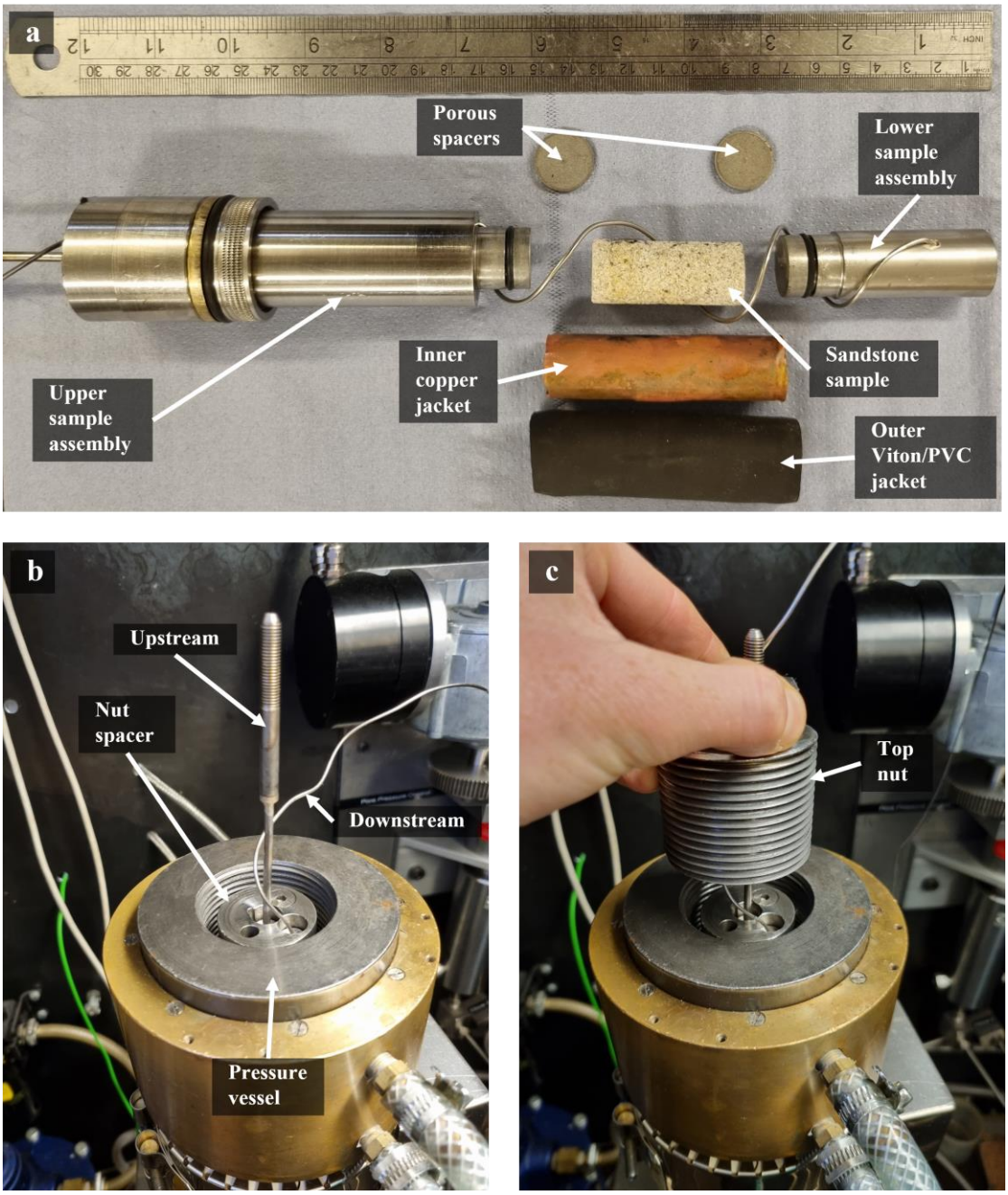

Figure 2.5. *Sample assembly arrangement. a) Sample assembly, sandstone sample, inner copper jacket, outer Viton/PVC jacket and porous disks. b) Sample assembly inside the pressure vessel showing the nut-spacer and upstream and downstream thin-bore piping. c) Top nut.*

2.1.3 Confining pressure system

An air-driven SC hydraulic pump generates the confining pressure in the system using low-viscosity 10 cSt (~0.01 Pa·s) silicon oil (Figure 2.6). Once the confining pressure target has been achieved, the pump can be isolated from the confining pressure system (Figure 2.2). A manual gauge and an RDP Z-type DC transducer is used to measure the confining pressure, which has a resolution of 0.007 MPa (Figure 2.7). Pressure during the experiment can be controlled using the Nova Swiss 10cc pump (Figure 2.7), which is connected to the confining pressure system and has been adapted so that it is driven by a servo-controlled gearbox and motor. The pump is limited to 6500 mm^3 of oil and on a full stroke, is typically able to change the pressure in the vessel by approximately 40-50 MPa. However, this depends on initial pressure, as well as the amount of volume in the vessel taken up by the axial piston, since the pump can change pressure more efficiently if there is a small volume of vessel space occupied by oil. The confining pressure can be held at a constant value by the servo-controlled pump, which can respond to any change sensed by the transducer and adjust it accordingly. The key role of the pump is to counteract the pressure changes triggered by the movement of the axial piston inside the pressure vessel. Variations in volumetric strain of the sample as a result of compaction or dilation can also be tracked by the pump, which acts as a volumometer (resolution = 0.1 mm^3). The pump position is monitored by a linear variable displacement transducer (LVDT) connected directly to the piston.

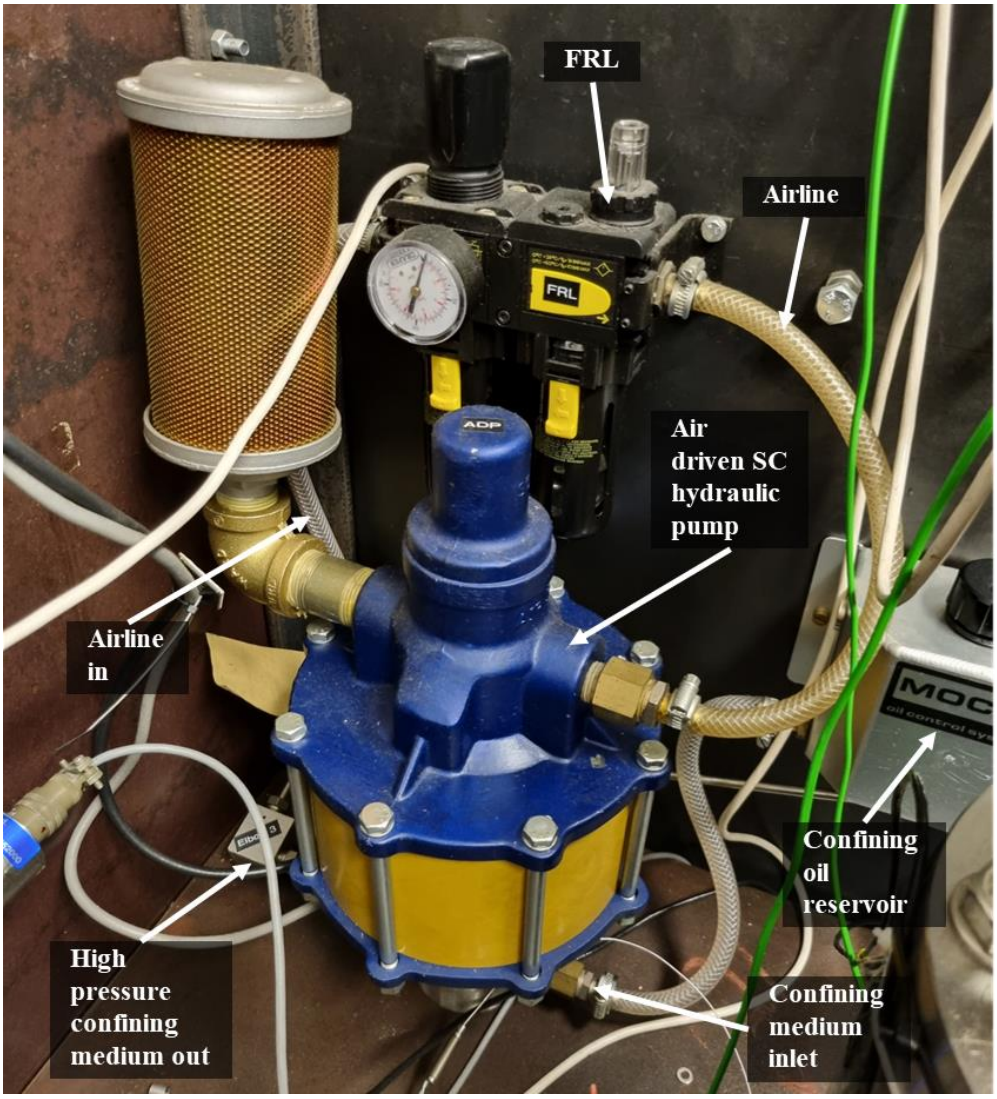

Figure 2.6. *Air-driven confining pressure pump. The air flow into the pump is controlled by a manual valve on the front of the rig, and air passes through a filter regulator lubricator (FRL) that is designed to remove compressor lubricants, water and dirt from the air stream. Confining oil is transferred to the pump from the storage reservoir to be pressurised and sent to the vessel.*

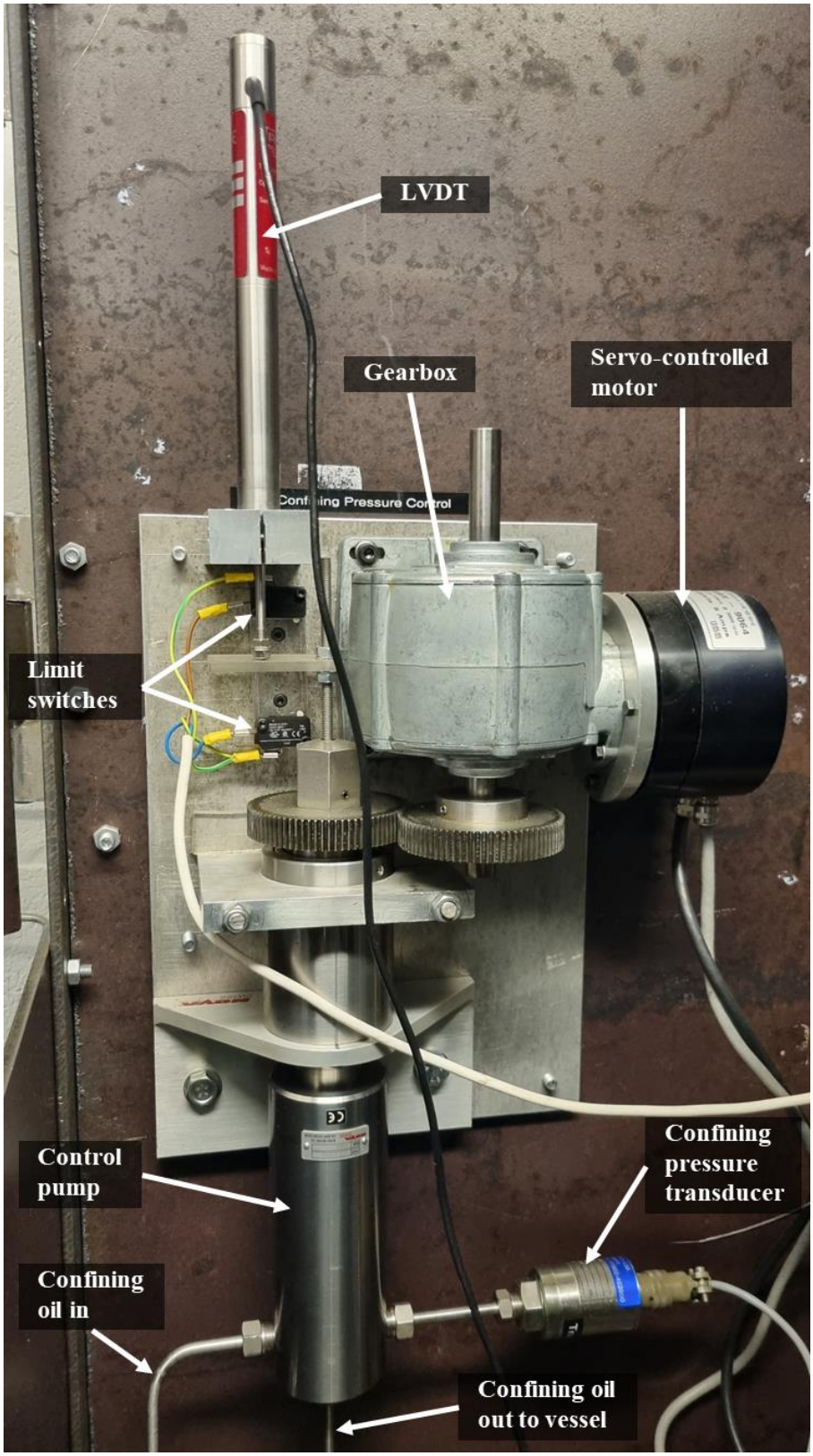

Figure 2.7. *The NovaSwiss confining pressure control pump connected to a servomotor and gearbox. The displacement of the pump piston is monitored by an LVDT.*

2.1.4 Pore fluid system

The rig is capable of using a variety of different pore fluids, although only de-ionised water and argon were used in this work. When de-ionised water is the pore fluid, a NovaSwiss hand pump is used to increase the pore fluid pressure in the system (Figure 2.8a). However, due to the high compressibility of gas, a Haskel AGT-32/152H gas booster is instead connected to the rig to initially pressurise the system for argon pore fluid (Figure 2.8b and Figure 2.9). Other gaseous phases such as CO_2 can be pressurised using the gas booster up to a maximum of 120 MPa. Once the desired pressure has been achieved, both the gas booster and NovaSwiss hand pump can be isolated from the rest of the system (Figure 2.2). Pore fluid pressure is measured by two RDP transducers (resolution = 0.007 MPa), which are connected to the upstream and downstream reservoirs (Figure 2.8c). The pressure can subsequently be controlled with the upstream pore fluid controller (Figure 2.10). The pore fluid controller is composed of a servo-controlled NovaSwiss 5cc pump, connected directly to the upstream reservoir plumbing. The NovaSwiss pump piston displacement is measured using an LVDT, which subsequently calculates the pore volume change with the movement of the piston pump. When the pressure is held constant, the pump will respond to pore volume changes as the sample deforms. Therefore, the relative pore volume evolution of a sample can be tracked during an experiment by monitoring the piston position (0.1 mm^3 resolution).

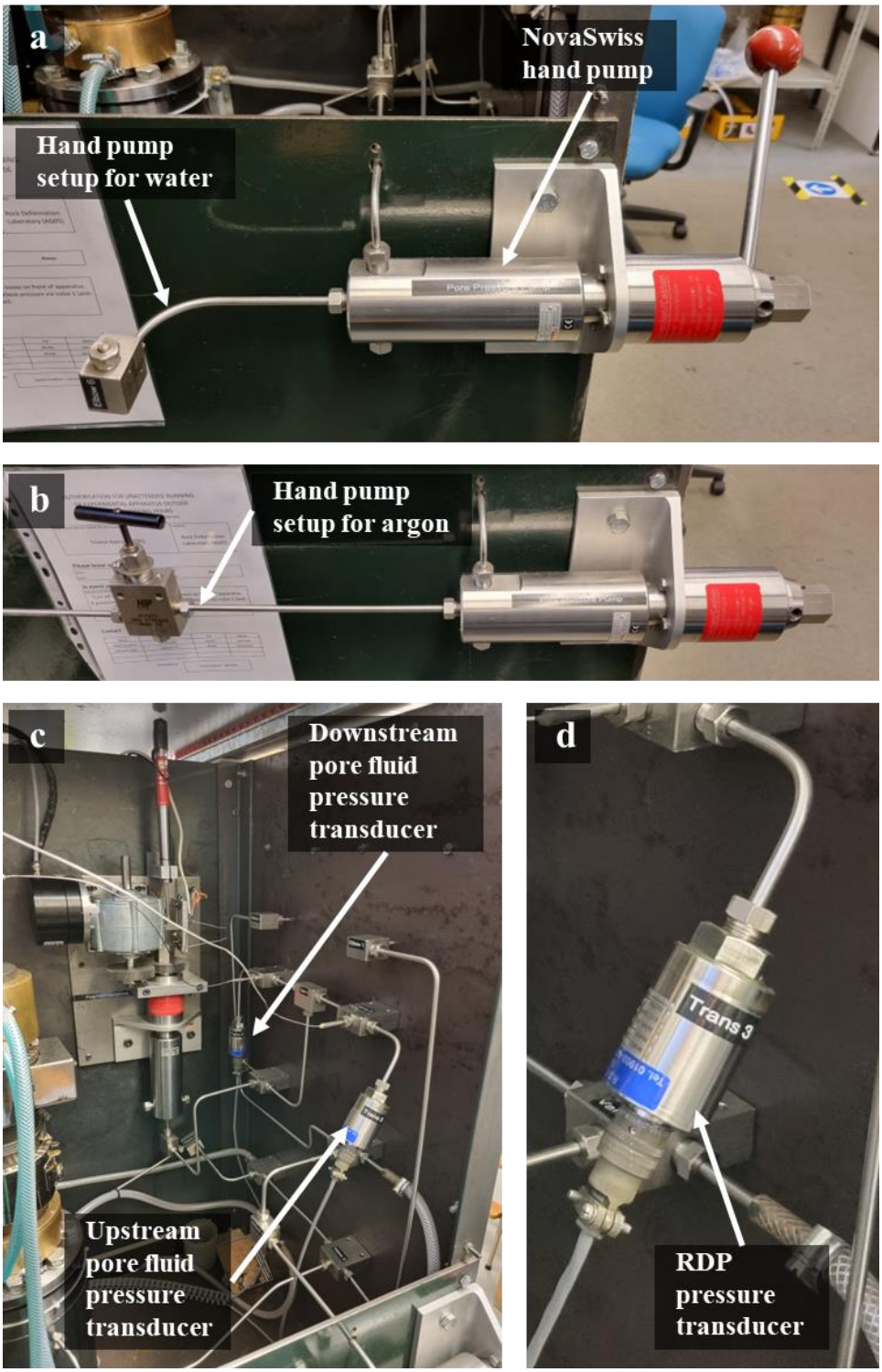

Figure 2.8. *a) The NovaSwiss hand pump setup for water. b) The setup for argon. c) Pore fluid pressure transducers are connected to the upstream, downstream and confining pressure systems. d) Closeup image of an RDP pressure transducer.*

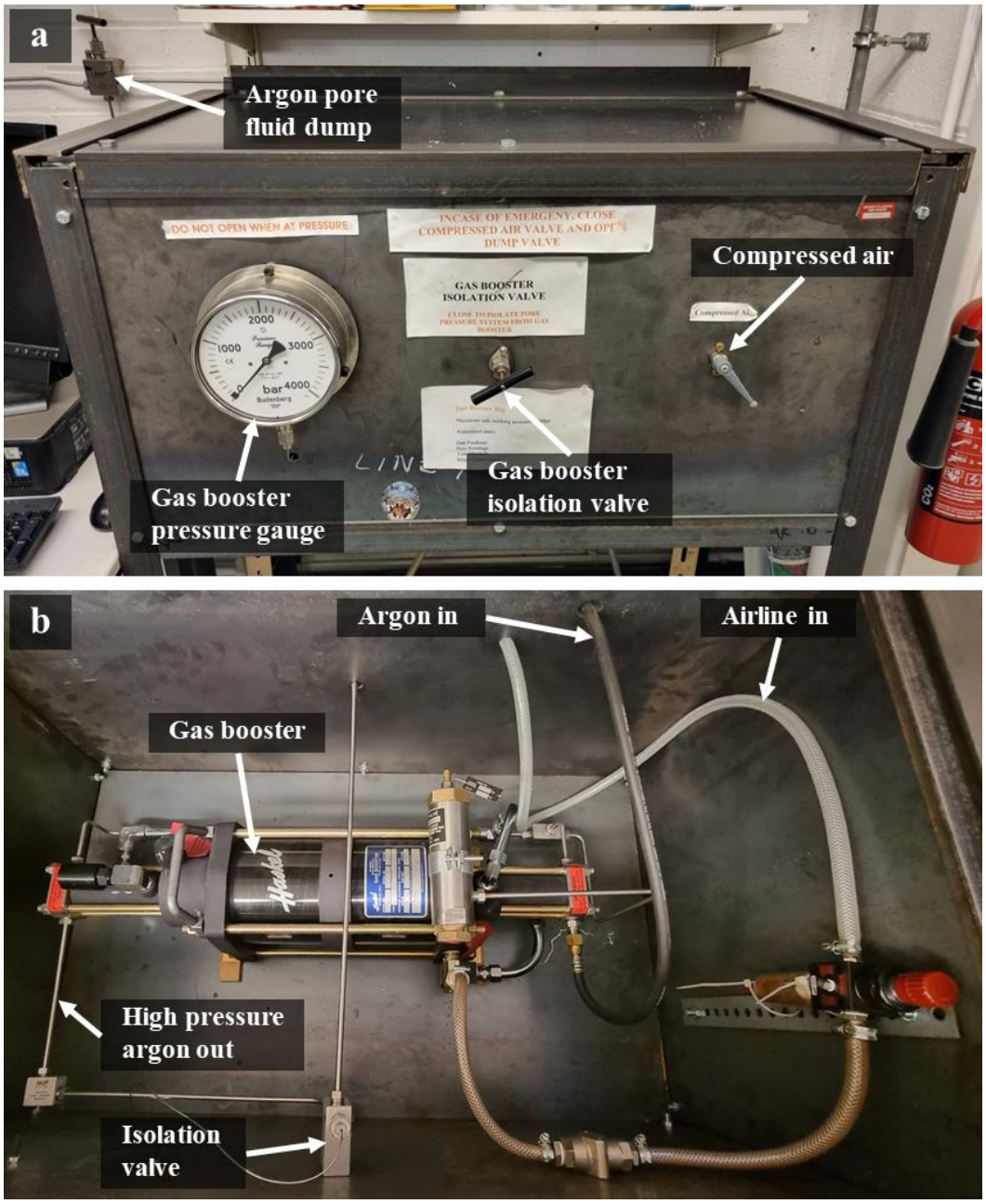

Figure 2.9. *a) External housing and b) internal configuration of the gas booster used to pressurise argon and other gaseous pore fluids.*

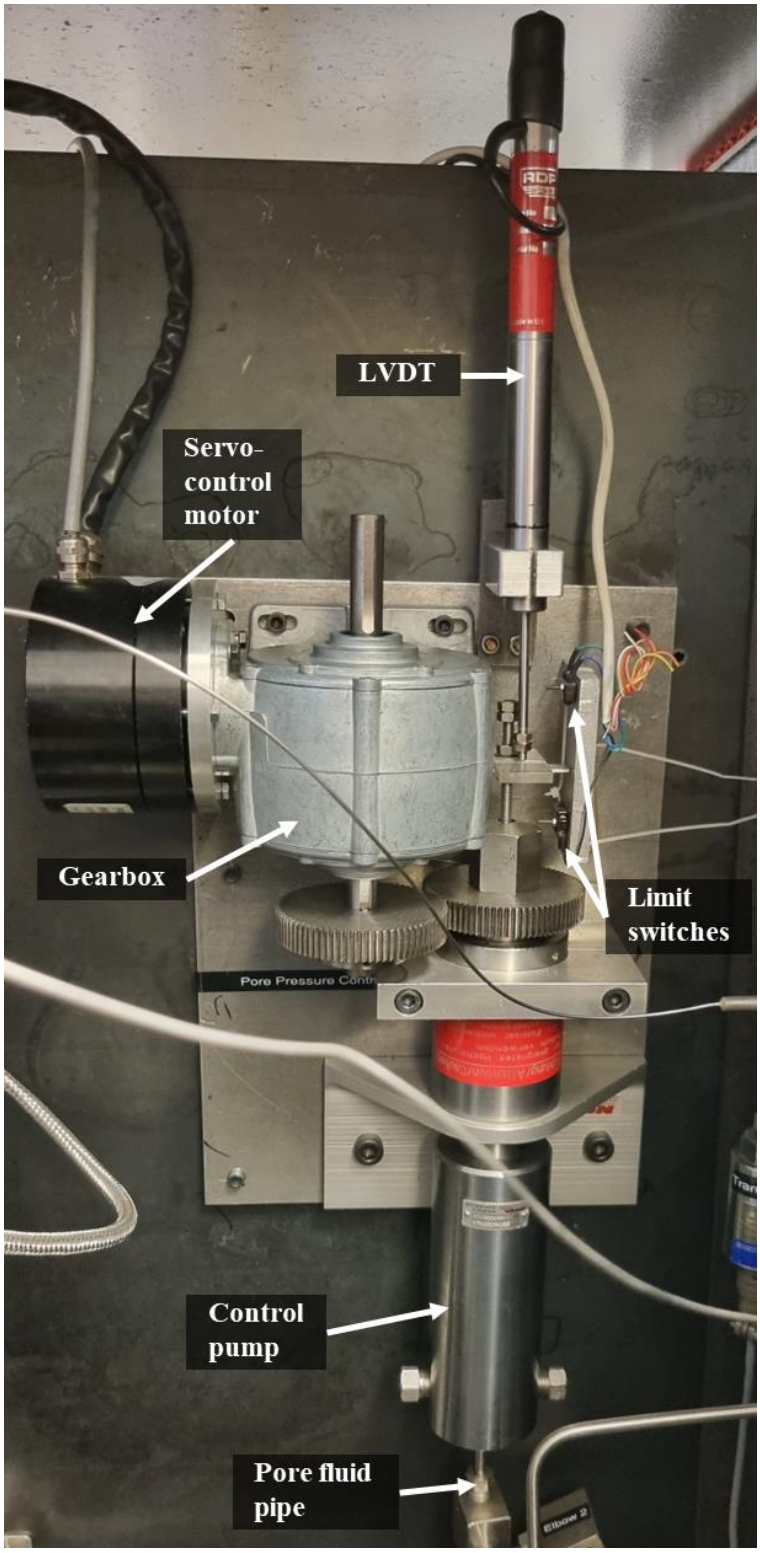

Figure 2.10. *The NovaSwiss pore pressure control pump. The LVDT and limit switches monitor the pump piston displacement to ensure the pump is not driven beyond its full stroke by the motor.*

2.1.5 Force gauge block and force gauge

The force gauge column is housed inside the force gauge block (Figure 2.11). The drive motor and gearbox drive the ball screw which supplies the axial load to the sample assembly from below. The top part of the force gauge column protrudes out of the top of the force gauge block into the bottom of the pressure vessel, where a force gauge extension connects it to the lower sample assembly (Figure 2.1). Eight high-tensile bolts connect the pressure vessel to the to the force gauge block, with these passing through the flange ring (tensile collar) which is screwed into eight threaded holes in the top of the force gauge block (Figure 2.11). The seal at the connection with the pressure vessel is a delta ring, which is placed between the faces at the top of the force gauge block and base of the pressure vessel, in angled seats, and elastically deforms against the seat walls by the force exerted by the eight bolts.

The entire loading column supports the axial load that is exerted onto the sample. To calculate the load applied to the sample, an LVDT in the form of an internal load cell is used, which measures the distortion in the force gauge column. The LVDT is forced against a T-section tube base, which itself is forced against a shoulder positioned above the level of the moving piston seal and mid-way up the inside of the force gauge column (Figure 2.11 and Figure 2.12). During axial loading, a spring accommodates any distortion of the piston beneath the top of the T-section tube and any displacement the LVDT measures is entirely a result of the shortening of the column between the top of the un-stressed rod and the top of the T-section tube. Consequently, no correction for force measurement or seal friction is necessary as the actively deforming section of the force gauge lies entirely between the pressure seals. A load cell is used to calibrate the LVDT.

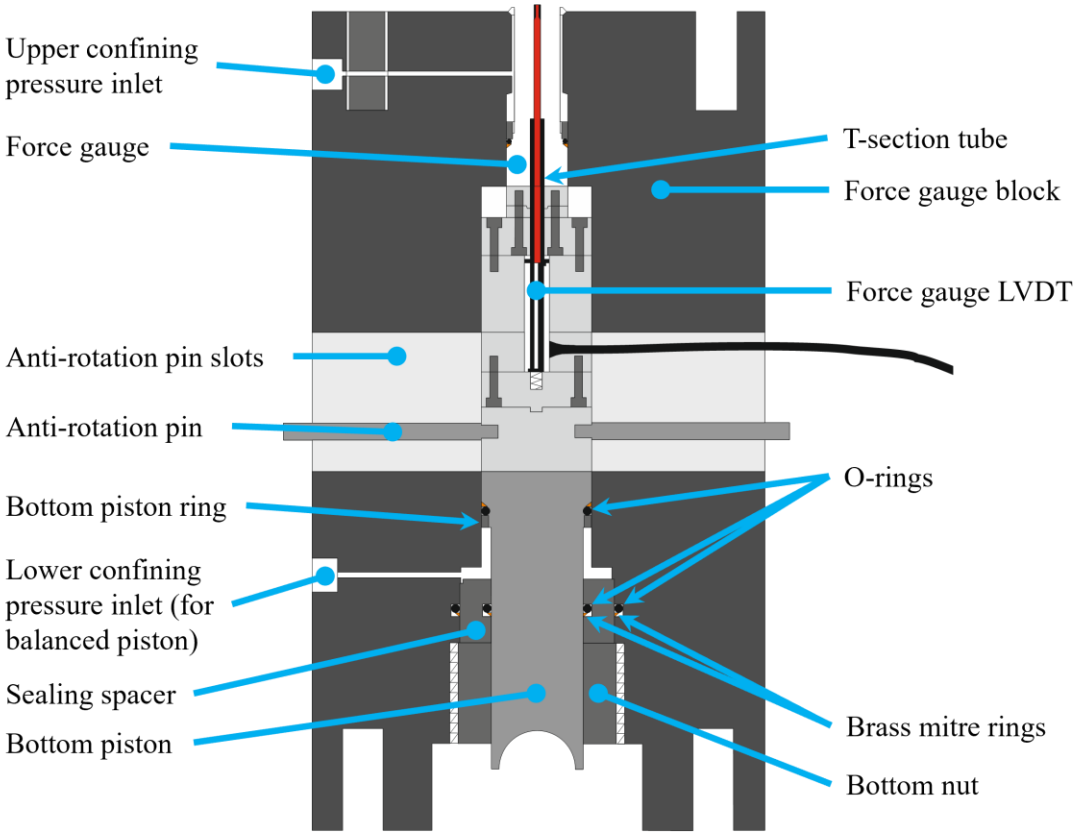

Figure 2.11. *Arrangement of the force gauge block and force gauge column.*

The force gauge column (Figure 2.12) as opposed to the rest of the force gauge assembly, is made of maraging steel. This steel is an iron-nickel alloy known for its toughness (without the loss of malleability) and ultra-high yield strength of up to ~2GPa GPa. Therefore, although at its smallest width the force gauge column is 19 mm, with a 3 mm internal hole for the T-tube and LVDT, it has high durability.

Three pressure seals are located on the force gauge assembly, with a non-pressurised zone located between the seal at the top of the force gauge column and the seal on the bottom piston. The non-pressurised zone enables the LVDT wire to exit the force gauge block via a hole in the side of the force gauge LVDT housing, via the anti-rotation pin slots. The anti-rotation pins are screwed into the bottom piston and pass out through the anti-rotation pin slots. The pins are used to prevent the force gauge column from rotating above the bottom piston

when the load is applied from the ball screw, which rotates as it screws upwards, applying the load. Without the pins, the rotation would be passed upwards into the experimental sample, as well as shearing the LVDT cable. Two isolated volumes are supplied by two confining pressure inlets (Figure 2.11). The upper pressurised volume consists of the pressure vessel and the top of the force gauge block, sealed respectively by the upper sample assembly seals and the seal of the force gauge column against the force gauge block. The lower confining pressure inlet supplies confining pressure to this area. The top nut holds down the sample assembly in the pressure vessel, with the sealing spacer containing the lower-most seal, secured by the bottom nut. The ball screw and bottom piston base both possess identical hemispherical seats, allowing the two to be connected, with these contacting via a hardened steel ball, positioned within the seats. This arrangement ensures that the loading column remains central as the concentricity of the loading column is applied.

The sealing arrangement of the confining pressure system can be understood with reference to Figure 2.1. Within the force gauge block, the seals consist of a brass mitre ring or anti-extrusion ring and an O-ring of the necessary diameter. The increase in confining pressure deforms the O-ring elastically outwards, i.e., against the force gauge block's inner surface, and inwards against the piston/force gauge assembly, sealing the vertical flow of silicon oil. The finely polished surfaces ensure a good seal. At high pressures (> 100 MPa) conventional hydraulic seals cannot be used and the roll of the brass mitre ring is to stop the O-ring being extruded through the small gap. Deformation of the seal during an experiment enacts a large frictional force on the piston and only when the axial load is large enough to overcome this force can piston movement commence.

The force gauge block has two confining pressure inlets (Figure 2.11) due to its balanced piston arrangement, although, as mentioned previously, this system was bypassed throughout this project. Between these inlets a valve is present which can control the confining pressure supply so that it reaches both inlets or is isolated to just the top one. Full ball screw capacity (30 tonnes) can be applied axially to the sample when the confining pressure is allowed

through both inlets, rather than it having to support the load applied to the piston by the confining pressure. Using the internal configuration described in this section, sample shortening up to 20 mm can be accommodated by the rig.

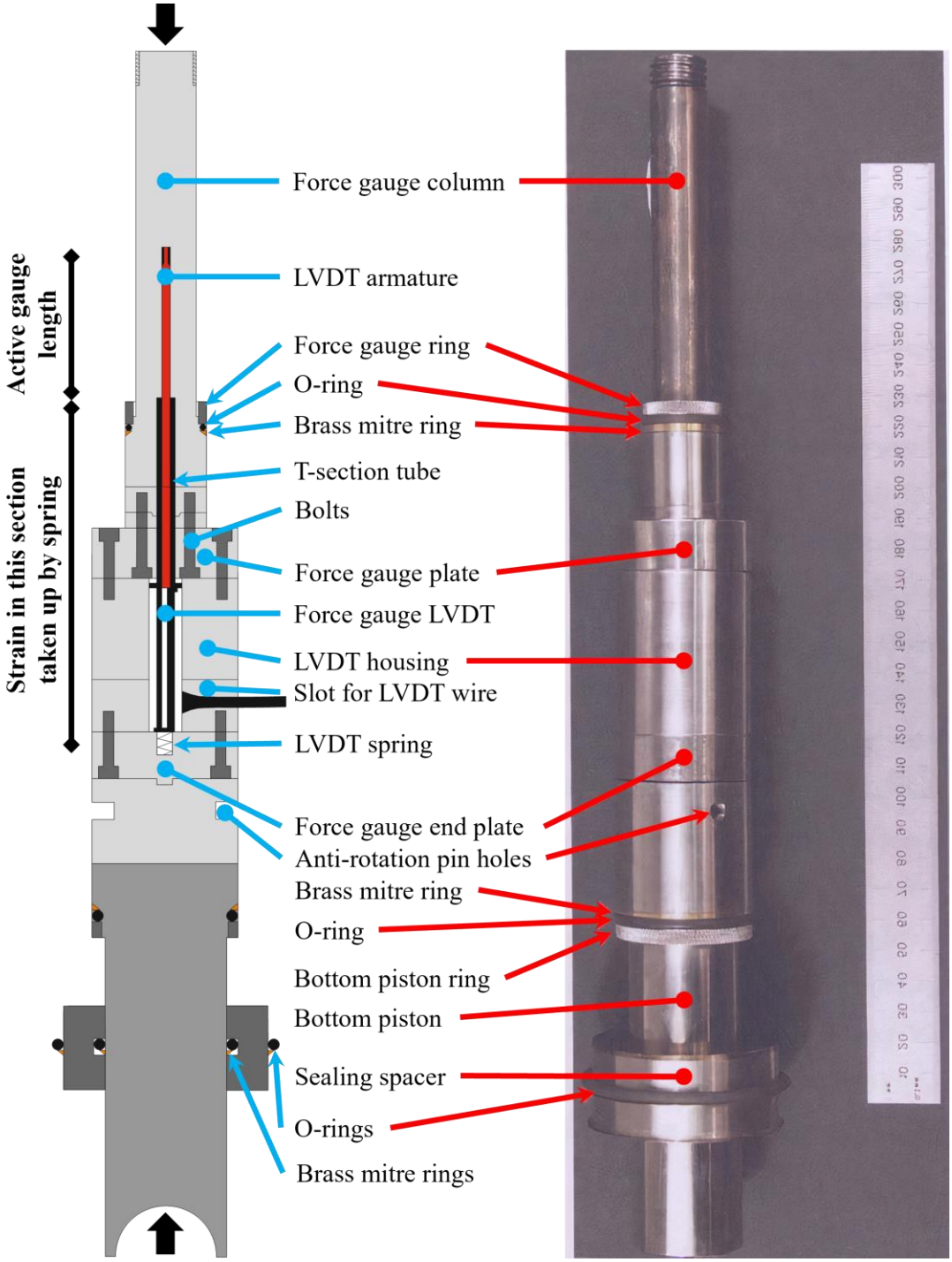

Figure 2.12. *Photo and labelled diagram of the force gauge assembly.*

2.1.6 Axial loading system

A servo-controlled axial displacement system applies the load to the sample and comprises a gear train and drive motor which drive a ball screw (Figure 2.13a). Preloaded, high precision ball-bearings sitting on a helical raceway provide an almost frictionless operation for the ball screw. The ball bearings carry the load between the screw and nut and provide the only contact between them. The gear train and gearbox were designed and custom built in house. Four primary gear couples make up the gear train, the largest of which is secured by a key and keyway to the base of the ball screw and connects to a smaller gear, giving a gear ratio of 5:1. On the same spindle, a gear ratio of 40:1 is provided by a worm connected to a wheel (Figure 2.13b). A gear, coupled with a smaller gear (connected to the primary gearbox) sits on the same spindle as the worm and gives a gear ratio of 2:1.

A gear ratio reduction of 120:1 is produced by the primary gearbox, which connects to the drive motor via a custom-built coupling plate. From the ball screw to the drive motor the total gear ratio is 48000:1. A max torque of 131 Ncm is produced by the drive motor, with the gearbox increasing this to 6,288,000 Ncm, not counting the torque loss and friction within the gear train. The gearbox frame comprises a 15 mm-thick bottom plate, which is attached to the main loading frame by 4 separator bars. Between these plates sit the vertical shafts, the ends of which sit in either deep-groove ball bearings or iolite fittings. Specially designed steel holding blocks bolted onto the main loading frame plate hold the horizontal axels in place. A feather key, and keyway combination, lock each gear onto its spindle. A displacement LVDT is used to measure axial displacement by measuring the amount of displacement at the ball screw base (Figure 2.13b). The hard limits of the limit switches are wired into the axial load controller (Figure 2.13b).

To determine the true sample displacement, the measured axial displacement measurement must be corrected for the elastic distortion of the loading column (Figure 2.12) The stiffness of the loading column (119 kN/mm) is used for the correction. At especially low loads (<1kN) the correction is somewhat non-linear, likely owing to the closure of the various

interfaces throughout the loading column. The effect of increasing confining pressure on the force value measured by the force gauge must also be corrected for, which is calibrated by determining the change in force with increasing confining pressure under zero axial load. When working at various confining pressures this linear calibration can be subtracted from the force value.

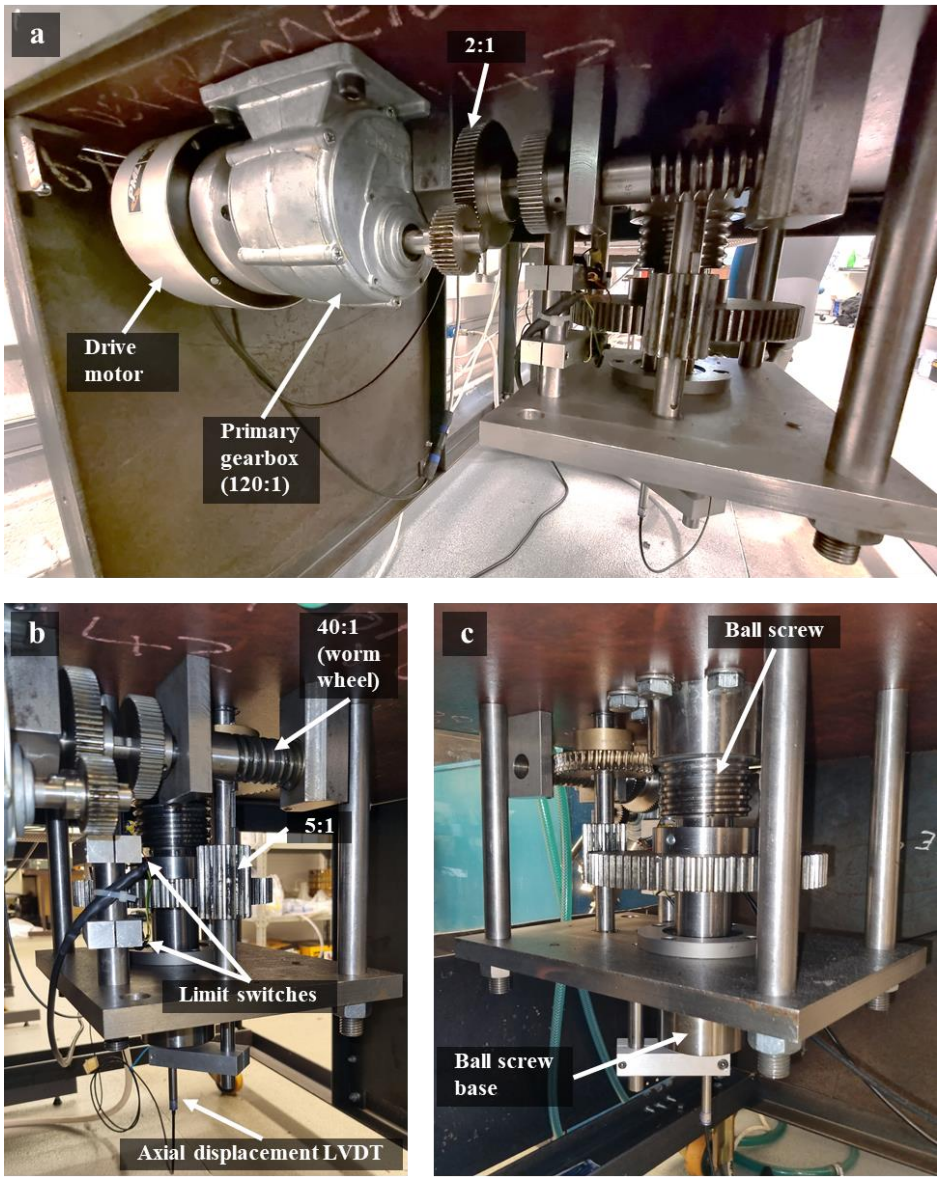

Figure 2.13. *Axial loading system. a) Drive motor, drive train and primary gear box. b) Worm wheel, limit switches and axial displacement LVDT. c) Side on view of the drive motor, gear train and ball screw.*

2.1.7 Data logging and servo-control system

All experimental data output produced by the displacement and pressure transducers are logged by LabVIEW software on the PC (Figure 2.14a) and a National Instruments compactRIO 9022 (NI-cRIO-9022) (Figure 2.14b). The millivolt signals from the transducers pass through an amplifier (Figure 2.14b) before the data is logged, to increase them to the ±10V range of the NI-cRIO-9022. The 4-channel, 16-Bit analogue input modules (NI 9215) inserted into the NI-cRIO-9022 then receive the amplified signals (Figure 2.14c). In the LabVIEW PC software, the working set points (WSPs) of the confining pressure, pore fluid pressure, and axial load systems are inputted (Figure 2.15). A servo loop then compares WSPs sent from the PC to the NI-cRIO-9022, to the input module and should the signals not match, the NI-cRIO-9022 4-channel, 16-bit analogue voltage output module (NI 9263) sends a signal to the rig's control boxes which drive the actuators (e.g., ballscrew or pumps) for the confining pressure, pore fluid pressure and axial load systems (Figure 2.15). The PID parameters (Proportional gain, Integral gain, and Derivative gain) control the magnitude of this signal. A servo amplifier (Figure 2.14d) then amplifies the signal that the control boxes receive, to obtain the higher voltage and current necessary to operate the actuators.

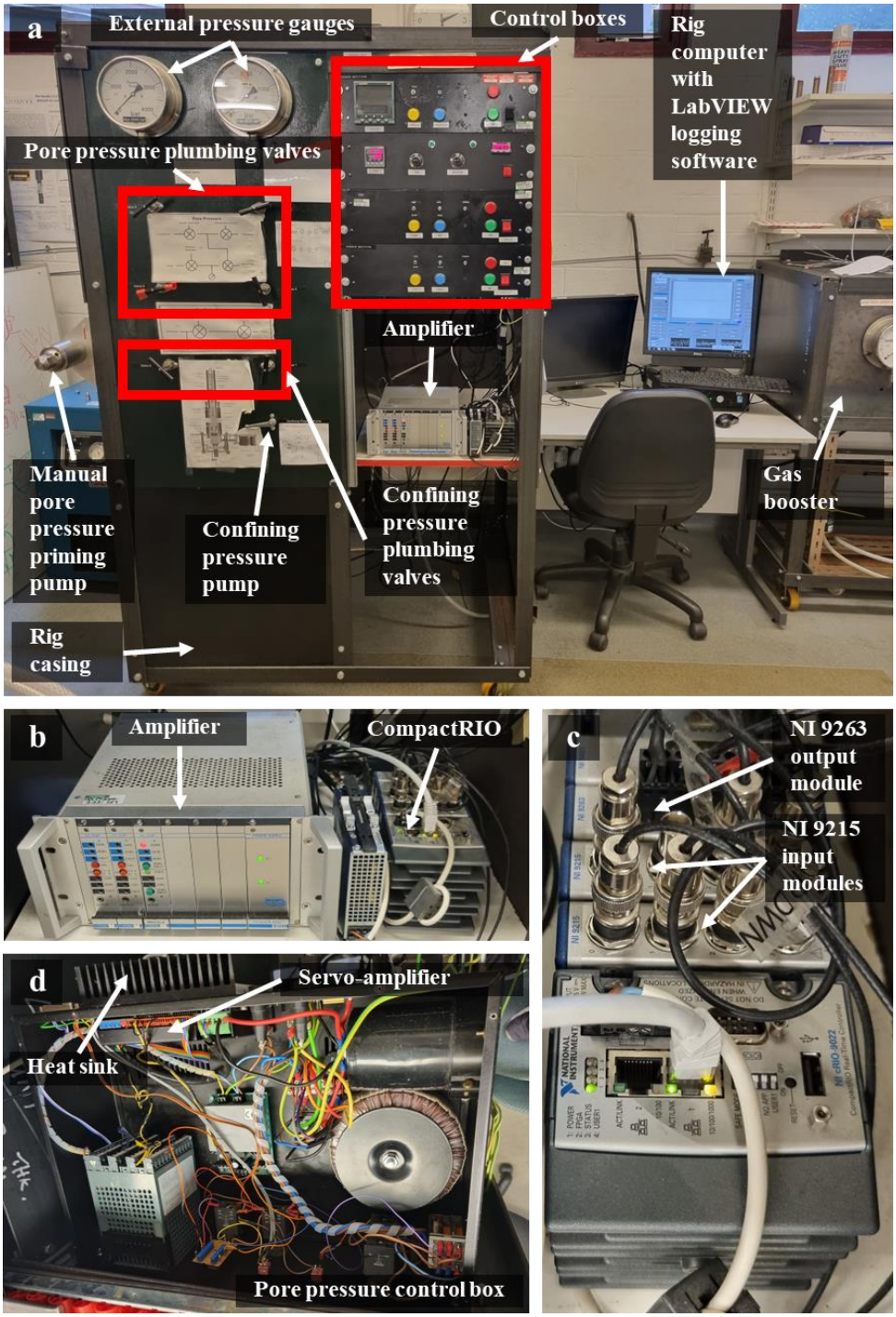

Figure 2.14. *a) The front of the rig displaying the external pressure gauges, confining and pore pressure system valves and servo-control boxes. b) The amplifier and NI-compactRIO. c) The NI 9263 output and 9215 input modules are inserted into the NI cRIO-9022. d) Servo-amplifier inside the control boxes, which sends a high voltage, high current signal to the actuators.*

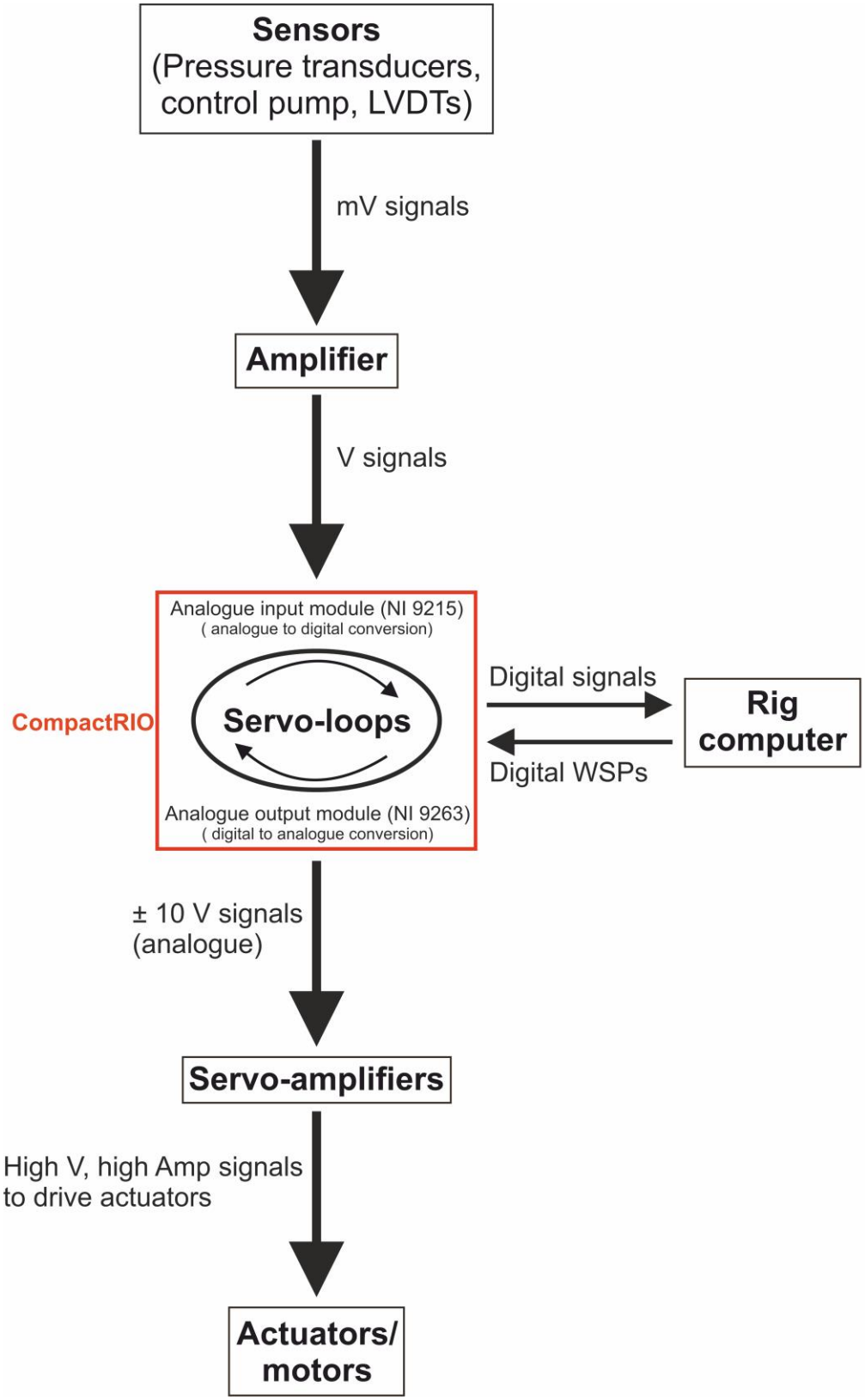

Figure 2.15. *A schematic diagram of the servo-control system.*

2.1.8 Potential sources of error and calibration

Calibration of the force gauge distortion measured by the internal LVDT (Figure 2.12), and voltages recorded by the pressure transducers (Figure 2.8c), requires calibration against a load cell and external pressure gauge respectively (Figure 2.16). Control pump displacement in the pore pressure and confining pressure systems are measured by LVDTs, which also require calibrations (Figure 2.7 and Figure 2.10). This will ultimately lead to calibration errors in any measurement. However, repeat calibrations and careful procedures can help to minimise their significance. Low magnitude errors, for example in pressure readings, can also be produced due to electrical noise. However, these are very small (<0.01 MPa) and so have minimal effect.

Fluctuations in laboratory temperatures are another source of error, as these can lead to thermal expansion/contraction and consequently, cause a drift on the force and pressure signals. Experiments carried out over many hours or days are particularly susceptible to these fluctuations. In this research, all tests on a single sample were carried out within a day, with each sample subjected to several different experimental procedures performed over multiple pressure and loading increments. Fluctuations in temperature during these increments will therefore be small. Long term drift is accounted for during post-processing of the data, whereby the force value corresponding to the hit-point of each loading increment (the point where the loading piston contacts with the sample assembly base) is zeroed. For the experiments in this study long-term drift was small and generally on the order of ~0-2 N.

As previously described, the force is measured by calculating the amount of elastic distortion of the force gauge (Figure 2.12). A linear loading versus displacement curve should therefore be produced. However, given that several interfaces are present along the loading column, loading curves may be produced which are not perfectly linear, particularly during the initial stages of loading when the different sections are pushed together. This artefact can be seen when analysing the loading curves from the test samples. Consequently, great care must be taken to discriminate between machine and sample responses.

Lastly, sample preparation can result in errors. In this study, all triaxial samples were cores with dimensions of 50×20 mm and the sample ends ground to a tolerance of <0.01 mm using a surface grinder. However, inaccuracy during the preparation and measurement stage can affect the sample material response during deformation, by leading to a heterogeneous stress distribution during testing. Careful sample preparation procedures are the best way to reduce these errors.

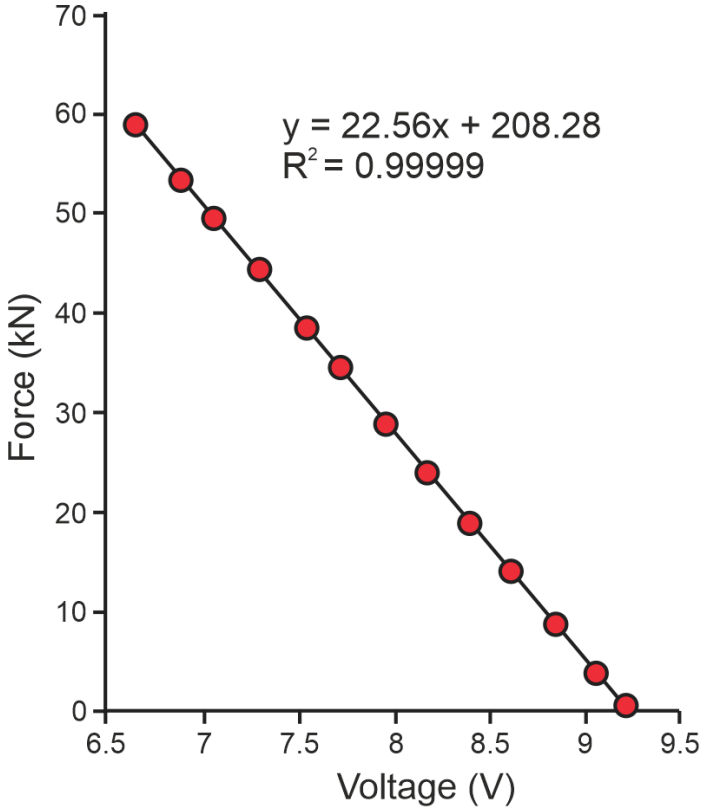

Figure 2.16. *Force gauge LVDT calibration.*

2.2 Image analysis

In the context of this study, image analysis can be defined as a technique for extracting quantitative information from images for the purpose of constructing diagrams which illustrate the distribution of certain microstructural rock properties, including porosity and grain size. Variations in the distributions of these properties can often be markers of deformation localisation, and thus, may help to identify deformation bands in deformed core samples. However, due to the lack of available software packages capable of performing such analyses, new quantitative image analysis techniques were developed in this work. The input images on which these new analyses in this study were performed were exclusively backscatter electron (BSE) images in TIF format. The following section will outline the sample preparation, image processing and image analysis techniques developed and applied to quantitatively analyse variations in microstructural rock properties.

2.2.1 Sample preparation and image acquisition

Most of the experiments throughout this study were conducted on relatively large sandstone cores (50×20 mm) and consequently, specific techniques were required to prepare these specimens for microstructural analysis. Upon removal from the triaxial deformation apparatus (Figure 2.1), the cores were extracted from the outer PVC/Viton jacket but kept enclosed within the copper jacket to better preserve the deformation microstructures from damage during post-experiment handling. The cores were each were oven dried for 24 hours before being vacuum impregnated, while still within their copper jackets, with low-viscosity (0.55 Pa-s) EpoFix (epoxy) resin from Agar Scientific. Occasionally, some of the lower porosity samples required two rounds of epoxy resin vacuum impregnation. Once epoxied, the cores were cut in half down their long axes and this surface was then polished and carbon coated ready for imaging using a Hitachi TM3000 scanning electron microscope (SEM). In order to construct BSE images of the whole core, individual BSE images were obtained across the whole sample at either ×40 or ×50 magnification. Depending on the size of the core, this usually

amounted to around 60 to 80 BSE images per sample (Figure 2.17a). These images were then stitched together using GigaPan Stitch software (© 2013 GigaPan Systems) to produce a whole core image (Figure 2.17b).

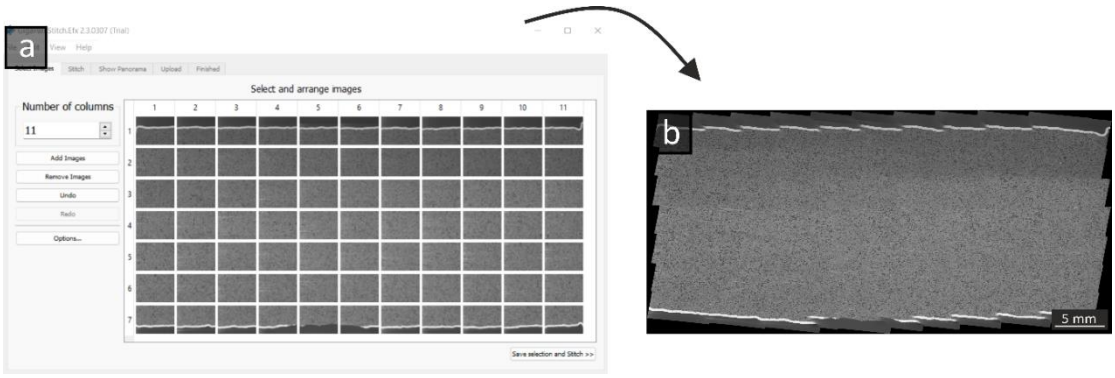

Figure 2.17. *a) Gigapan stitch software containing 77 individual BSE images ready for stitching. b) Stitched whole core sample BSE image.*

2.2.2 Image analysis software

Image processing software is required in order to perform detailed image analysis. The popular open-source software 'Fiji' was used throughout this project, which is an enhanced version of the image analysis tool 'ImageJ' (Schindelin et al., 2012). Fiji is able to store numerous powerful software libraries whilst also combining them with a large range of scripting languages, to facilitate the use of image processing algorithms (plugins). Unlike ImageJ, these plugins are stored in the software, with users able to share their scripts through the integrated update system. Fiji has been a particularly popular tool in the field of biological science, where it is commonly used for cell and particle analysis, due to its ability to identify and isolate shapes and then perform analysis of multiple properties, including their geometry, colour, size and density. In the field of earth sciences, Fiji has been primarily applied to the analysis of grains and crystals (Heilbronner & Barrett, 2013).

For image analysis to be successful, consistent processing methods are required, whereby certain regions of interest and structures are separated from the rest of the image. For sandstones, this predominantly involves the discrimination of pore space from grains, as well as the isolation of individual grains and pores for size analysis. The next section describes these image processing and analysis workflows in detail.

2.2.3 Scaling of the raw image

When the stitched SEM images are opened, they have no scale other than their pixel dimensions (Figure 2.17b). For accurate image analysis, the image must be scaled to its true size, which requires that either there is a scale on the image, or that the true magnification of a given objective with respect to the pixel density is known (Heilbronner & Barrett, 2013). In this study, the SEM images were each scaled after being uploaded into Fiji. This was done using the scale bars on the individual SEM images or by using the known sample dimensions. The latter method was preferred and is generally more accurate, since automated image stitching can sometimes produce a slightly distorted image (Figure 2.17b). To provide a clear and detailed description of the image processing workflow, a small section of a sandstone sample, rather than a full stitched core will be used (Figure 2.18a). This is so that the figures clearly show each of the steps, making certain processes clearer. To set the scale, the line tool can be used to draw a line to a known length on the image i.e., a scale bar or the sample length. The ‘Set Scale’ command in the ‘Analyse’ tab can then be used and will display a dialog box which contains ‘Measured Distance’ in pixels. The correct units can then be selected from the pop-up menu and the ‘Known Distance’ can be input. The conversion will then be shown, for example 1 mm = 400 pixels.

2.2.4 Pre-processing

At this point, the scaled SEM image is still in its raw data format (Figure 2.17b and Figure 2.18a) meaning that some significant flaws, such as uneven lighting and noise may be present in the image. Pre-processing aims to try to correct some of these defects to reduce

erroneous measurements in later image processing and analysis stages. Since almost all the images in this study were obtained from the same Hitachi TM3000 SEM, which did not produce significant noise or lighting discrepancies, only two pre-processing steps were performed. Each image was converted to 8-bit greyscale prior to pre-processing, as this results in faster processing times and smaller file sizes (Figure 2.18a).

2.2.4.1 Background correction

Raw images will often have uneven backgrounds, for example, dark smudges or shading from one side of the image to the other (Figure 2.18a). Uneven backgrounds may be created in SEMs, for instance, when there is a slight tilt of a specimen with respect to the detector (Heilbronner & Barrett, 2013). Some samples examined in this study displayed a more uneven background than others; however, the background was corrected in every sample to ensure that the shading was even across each image (Figure 2.18b). The correction method used was the 'Subtract Background' function in the 'Process' menu, which is based upon the rolling ball algorithm of Sternberg (1983). This algorithm works by determining a local greyscale background value for every pixel by averaging the greyscale pixel intensity over a large circular radius around each one. Any spatial variations in the background intensities can subsequently be removed by subtracting the local background value from the original image. The radius of the circle should be set to at least the size of the largest non-background object. A value of 50 pixels was generally used throughout this project.

Once the background subtraction was implemented, a median filter was applied (Figure 2.18c) with a resolution of 1 pixel to remove noise (particularly speckling) from the image. Median filtering is one of the most common methods for noise reduction and hence, it is commonly known as 'Noise Reduction' or 'De-speckle'. Median filtering will be discussed in more detail in the following sub-sections. Finally, the contrast of the images was enhanced using the 'Auto-brightness' function (Figure 2.18d).

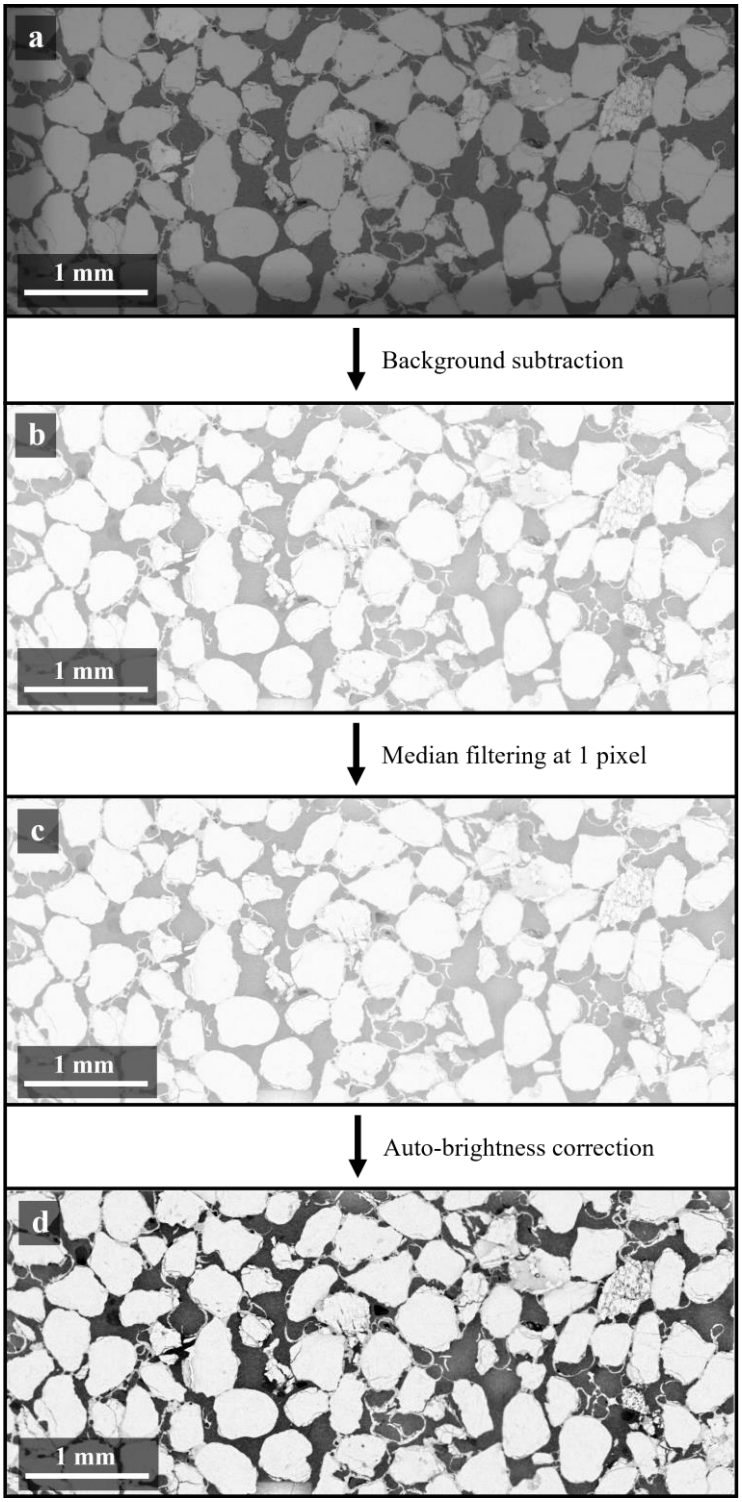

Figure 2.18. *a) Original SEM image of a sandstone exhibiting localised shading in the left and bottom sections of the image. b) Image after background subtraction showing the removal of the uneven shading. c) SEM image with a median filter applied to remove background noise such as speckling. d) Auto-brightness correction of the image to enhance the contrast.*

2.2.4.2 Grey-level histogram and image segmentation

Segmentation is the process of assigning a grey level or energy threshold to a digitised image, thus converting it to a binary signal which has the effect of partitioning the image into non-overlapping regions (Castleman, 1996; Heilbronner & Barrett, 2013; Loebl, 1985). Therefore, thresholding is the process whereby all the pixels in the initial 8-bit greyscale image are mapped in terms of their grey value and assigned a binary output of either 0 or 1, depending upon whether they have energy levels up to and including a certain threshold (0) or above a certain threshold (1). In the context of deriving the distribution of certain rock properties, including porosity and grain size, in a sandstone sample, a threshold is required which enables the discretisation of the pore space from the solid grains, as is representative of the original SEM micrograph (Heilbronner & Barrett, 2013). Determining the segmentation threshold is a vital part of the image analysis process and must be approached carefully, because the result will influence the measurements, and consequently, any data obtained from the binary image. When determining the segmentation threshold, the histogram window accessible in the software provides a good visual aid. In this project, since the BSE images inputted into Fiji were 8-bit greyscale, the variations in grey values between the pixels were represented by up to 256 shades of grey. Consequently, each pixel is assigned a greyscale brightness value ranging between 0 (black) and 255 (white). For a given greyscale image, the histogram provides a visual summary of the grey-level content of the image, by computing the number of pixels that correspond to a certain grey-value. A typical histogram for a non-processed sandstone SEM micrograph from this study is shown (Figure 2.19a). Four peaks are present, 2 representing the pore space and 2 the solid grains. The extra two peaks are due to the darker shaded regions creating a different grey value for the pore space and for the grains. It is these extra peaks which are corrected for in pre-processing. Two grey-value peaks are often typical of carbonate rocks and mineralogically mature quartz sandstones, whereas multimineral sandstones will typically exhibit 3. This can be attributed to the fact that different mineral phases will display different grey values (Lock, 2001).

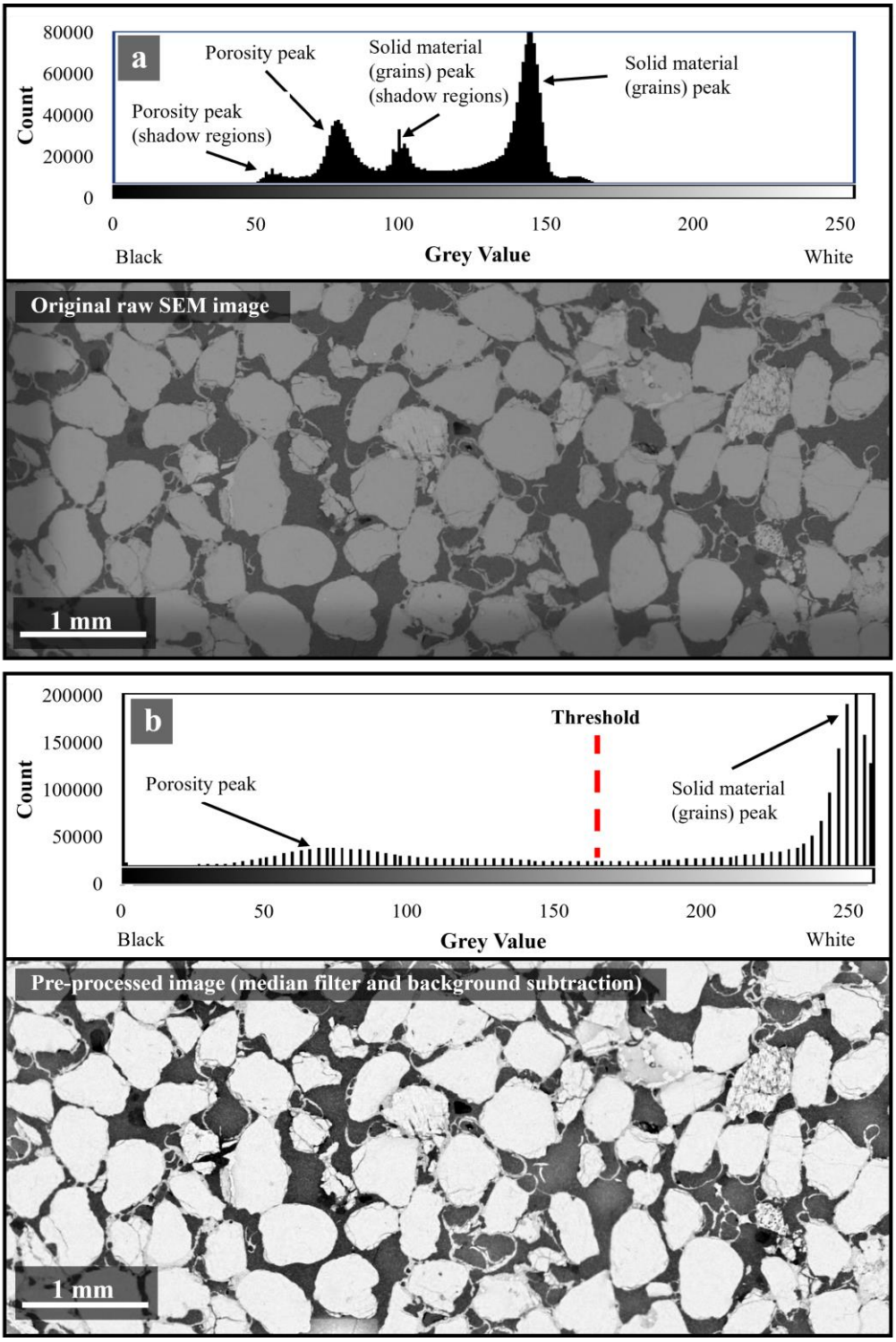

Figure 2.19. *a) Original SEM image and corresponding histogram of a sandstone exhibiting localised shading in the left and bottom sections of the image. b) Image and associated histogram after background subtraction, showing the removal of the uneven shading. The excess peaks, as a result of the shading, can be removed during pre-processing.*

For a given set of mineral phases, a grey-level histogram is ideally composed of a series of delta-type functions, the heights of which are proportional to the relative proportions of a mineral phase present in the field view of the image (Lock, 2001). However, this is not usually the case with SEM images of rocks for several reasons. The first is that since the pixel size is finite, more than one mineral (and pores) may be present in the pixel, which will ultimately result in the signals being broadened to Gaussian-type functions. Furthermore, there may be issues relating to the reflection and dispersion of the energy, since a grain positioned on the sample surface may not be at an exact 90º angle to the electron beam, and the surface of the sample may also not be flat. Consequently, obtaining the correct segmentation threshold is difficult and although the peaks can be separated using certain convolution algorithms, these are not considered to be ideal (Lu et al., 1994).

One technique for selecting the threshold in a multi-modal histogram is suggested by Weszka & Rosenfeld (1978), whereby a reasonable threshold value can be selected by locating the lowest point between two non-overlapping peaks (Figure 2.19b). The reasoning behind this method is that in the dip, the relatively small values are taken on by the histogram which implies that the area function changes slowly with grey-value. The effect of the grey-value on the boundary is therefore minimised if it is placed at the dip, due to the relatively small number of pixels associated with these features. Generally, a threshold can be assigned which is applicable to the whole image if the background grey-value is relatively constant and has a consistent range of grey-values. This is known as the global thresholding segmentation method and was applied to the samples in this study (Figure 2.20).

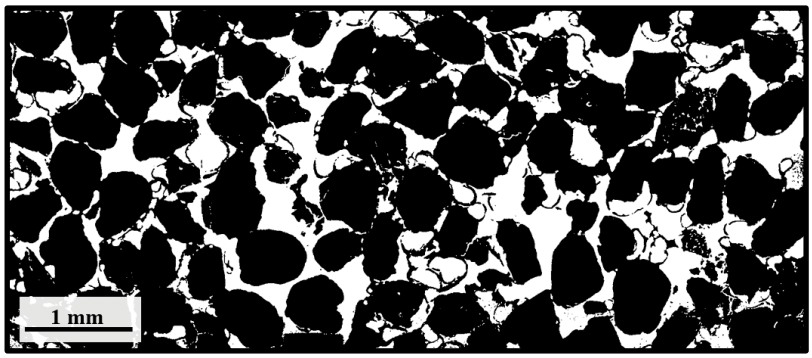

Figure 2.20. *Thresholded binary image obtained using the global thresholding technique of Weszka & Rosenfeld (1978).*

2.2.5 Post-processing

The previous stage of the image analysis workflow has been concerned with pre-processing and thresholding of the image and detailed how to separate pore space from solid grains. However, perfect spatial segmentation of individual particles, i.e., grains, is a more complicated process that cannot be achieved in one single step. The images created in the first step require additional processing, which most commonly involves noise cleaning and structural filtering.

2.2.5.1 Filtering

Noise reduction is the first post-processing step carried out on the thresholded binary image (Figure 2.20) and is achieved by using the median filter. This is a ranking filter and works by ordering the grey values in the neighbourhood of a pixel (Figure 2.21) (Heilbronner & Barrett, 2013). Since this section deals with post-processed images, the images are binary, and therefore, only two grey values exist, 0 or 1. Consequently, the ranking is a count of the black and white pixels in the neighbourhood. Median filtering can be explained by means of a 3×3 neighbourhood comprised of a central white pixel, surrounded by 6 black and 2 white pixels (Figure 2.21a). Ranking of all 9 pixels will produce the sequence shown in Figure 2.21b, where 0 is white and 1 is black. A median filter will replace the central pixel with the median value

(Figure 2.21c). In this research, the median filter was used to remove noise at a size of 1 pixel (Figure 2.22a). Noise was only removed on the scale of 1 pixel, since structures larger than could be small grain fragments and thus, are important to analyse in terms of grain fragmentation in relation to compaction localisation (Figure 2.22b).

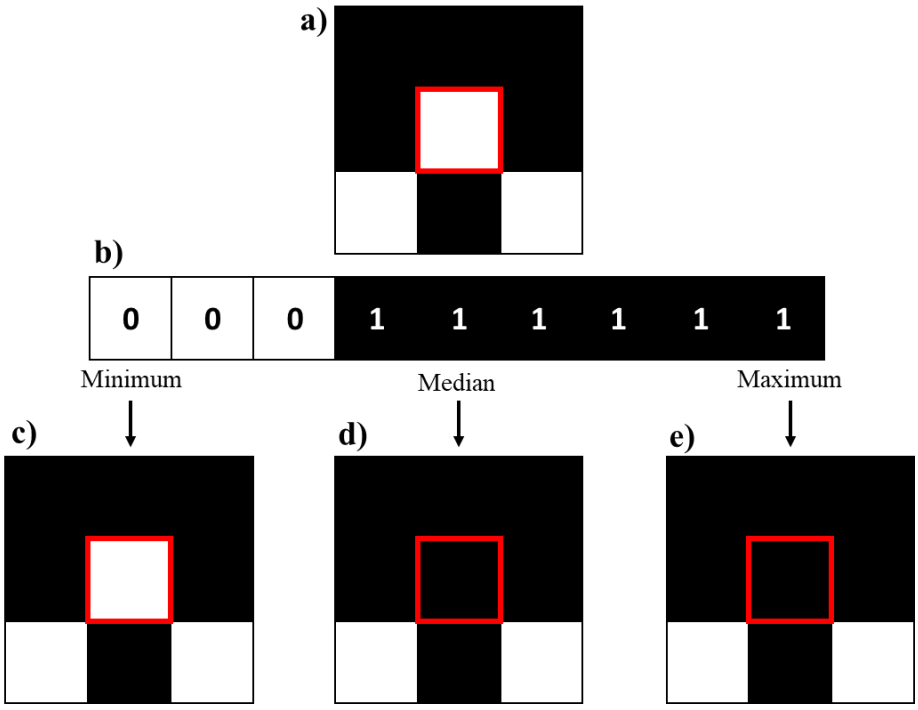

Figure 2.21. *Example of how ranking filters, such as the median filter used in this study, can be used to reduce noise in an image.*

Once median filtering has been completed, porosity analysis across the image can be performed on the sample. This will be discussed in detail in section 2.2.6. It is recommended that porosity analysis is performed at this stage because further processing of the image for particle analysis involves the segmentation of grains, which automatically introduces a white boundary with its own area, surrounding the sample. Since the 'Analyse Particles' function in Fiji will only work correctly when each grain is separated by a 2-pixel gap, this creates a bias, whereby the image porosity is increased. This can be easily corrected for when examining

particle size but is less easy to correct for in terms of porosity. The next stage of processing involves grain segmentation using the watershed algorithm.

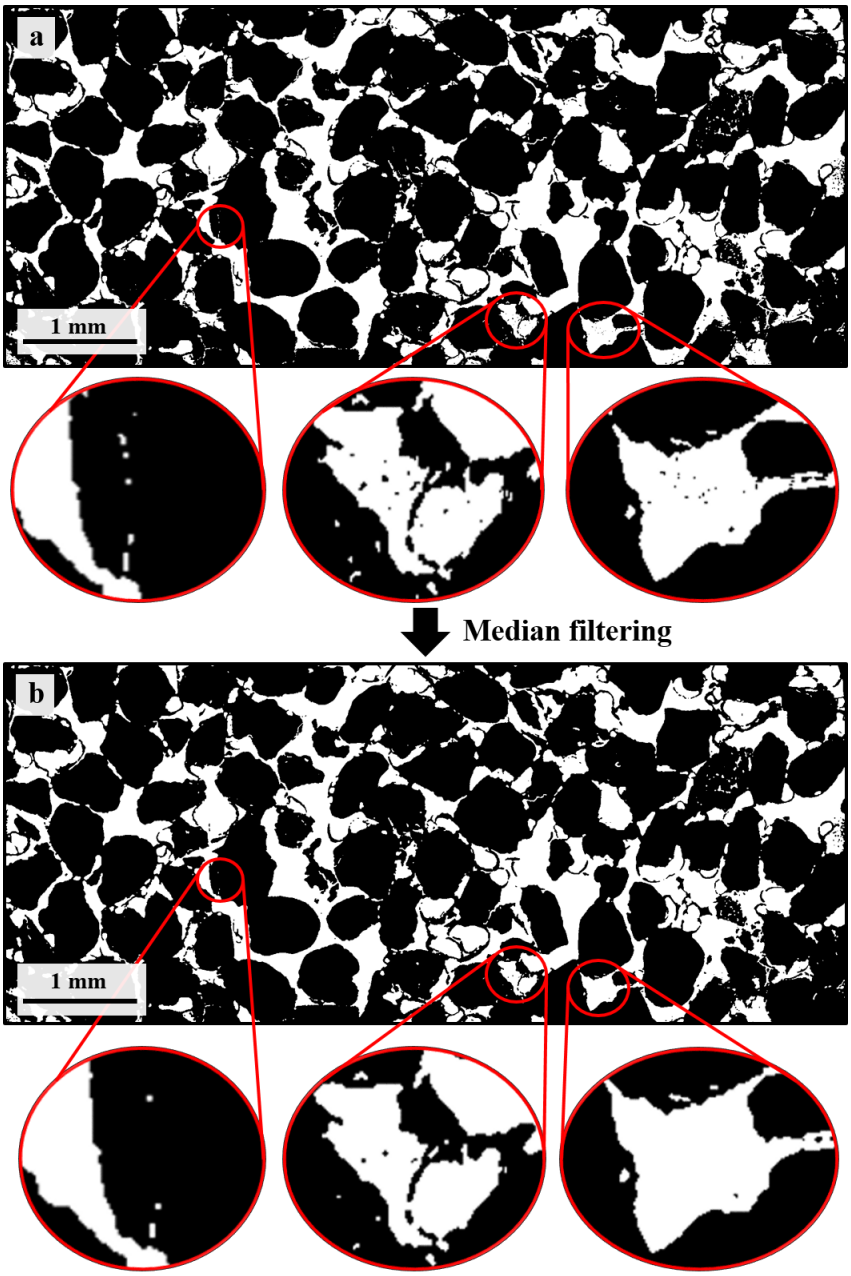

Figure 2.22. *a) A thresholded sandstone image before median filtering was applied. The black and white pixel-sized speckles represent noise and must be removed for the next segmentation stage to be effective. b) The same image, post median filtering, showing a reduction in the pixel-sized speckling, which was removed at a threshold value of 1 pixel.*

2.2.5.2 Grain segmentation

In order to perform particle analysis in Fiji, further processing steps are required. After median processing (Figure 2.22b) there is no distinction between separate grains, and therefore, if they were analysed, Fiji would only recognise large clusters of particles. To avoid this, the watershed algorithm is used (Figure 2.23).

This algorithm consists of a series of processes (Rabbani et al., 2016) the first of which is the identification of the ultimate eroded points (UEPs), which is achieved with the formation of a Euclidean distance map (EDM) (Figure 2.23b). To construct the EDM, the black pixels (grains) are replaced by grey pixels with an intensity proportional to their distance from the nearest white pixel. For example, black pixels close to the grain edges are dark grey and those in the centre are lighter grey. From this EDM, the UEPs can be calculated, which are centres of the objects or points that are equidistant from the edges and that will be separated during segmentation (Figure 2.23c). The UEPs are then each dilated as far as possible until either the edge of the particle is reached, or contact is made with the edge of another growing particle. The last pixel is then left white, creating a boundary between the two particles (Figure 2.23d).

Although this process has been shown to work well compared to manual segmentation, over-segmentation is common, whereby boundaries are added where none exist (Figure 2.24a). The eraser tool can be used to remove surplus segment boundaries from large grains. Finally, any excess segment branches left over from the clipping process are removed by using the 'Analyse Skeleton' plugin (Figure 2.24b). Finally, since the 'Analyse Particles' function in Fiji will only work correctly when each grain is separated by a 2-pixel-wide gap, the 'Erode' binary command is applied at 1 pixel, which removes a single pixel from the edges of the grains in the binary image (Figure 2.24c). This can be corrected for (see section 2.2.8).

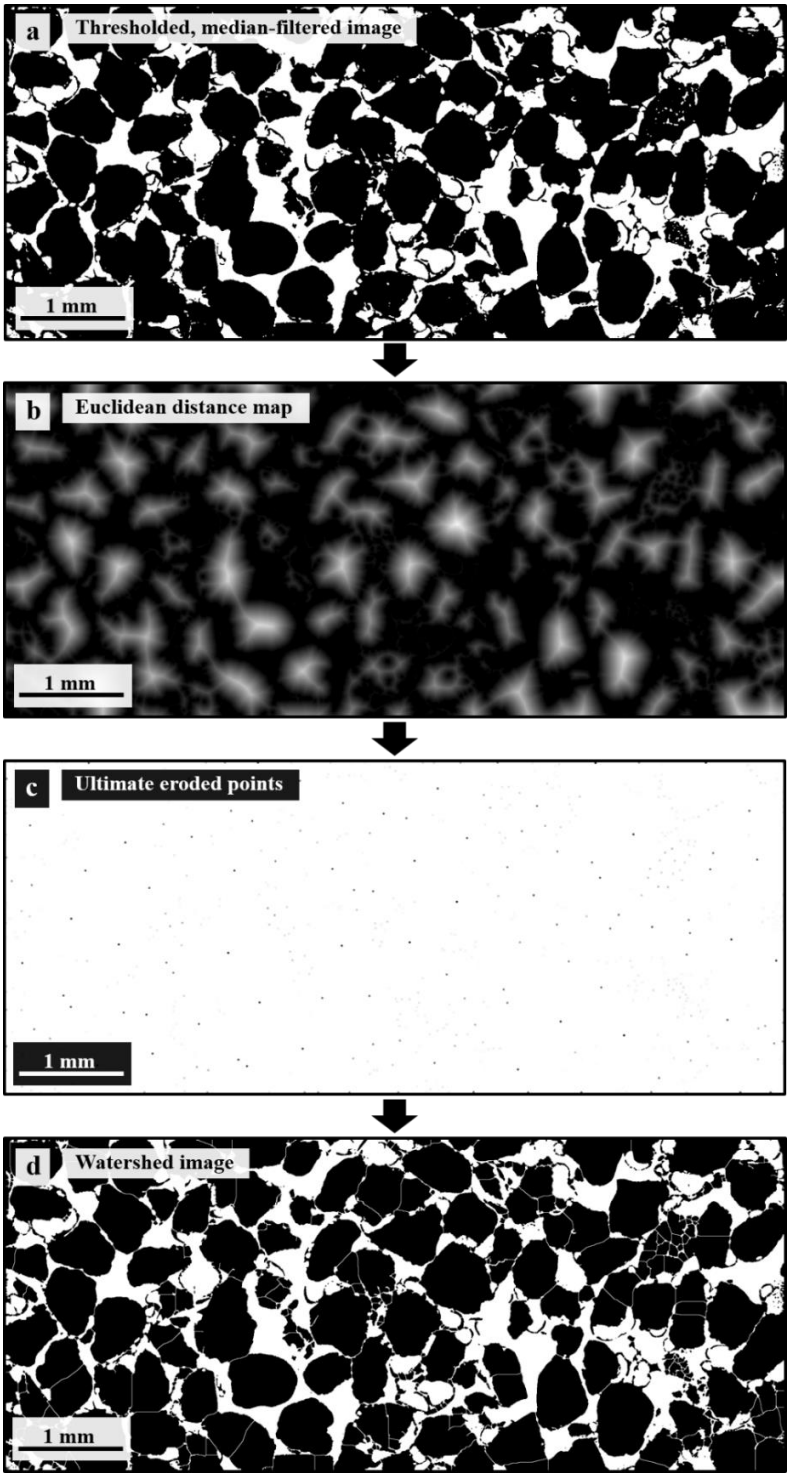

Figure 2.23. *a) Thresholded, filtered synthetic sandstone image. b) Euclidean distance map (EDM) used during the watershed process to calculate the ultimate eroded points (UEPs). c) UEPs representing the centre of each object. d) Image obtained post-watershed showing the white lines segmenting the individual objects.*

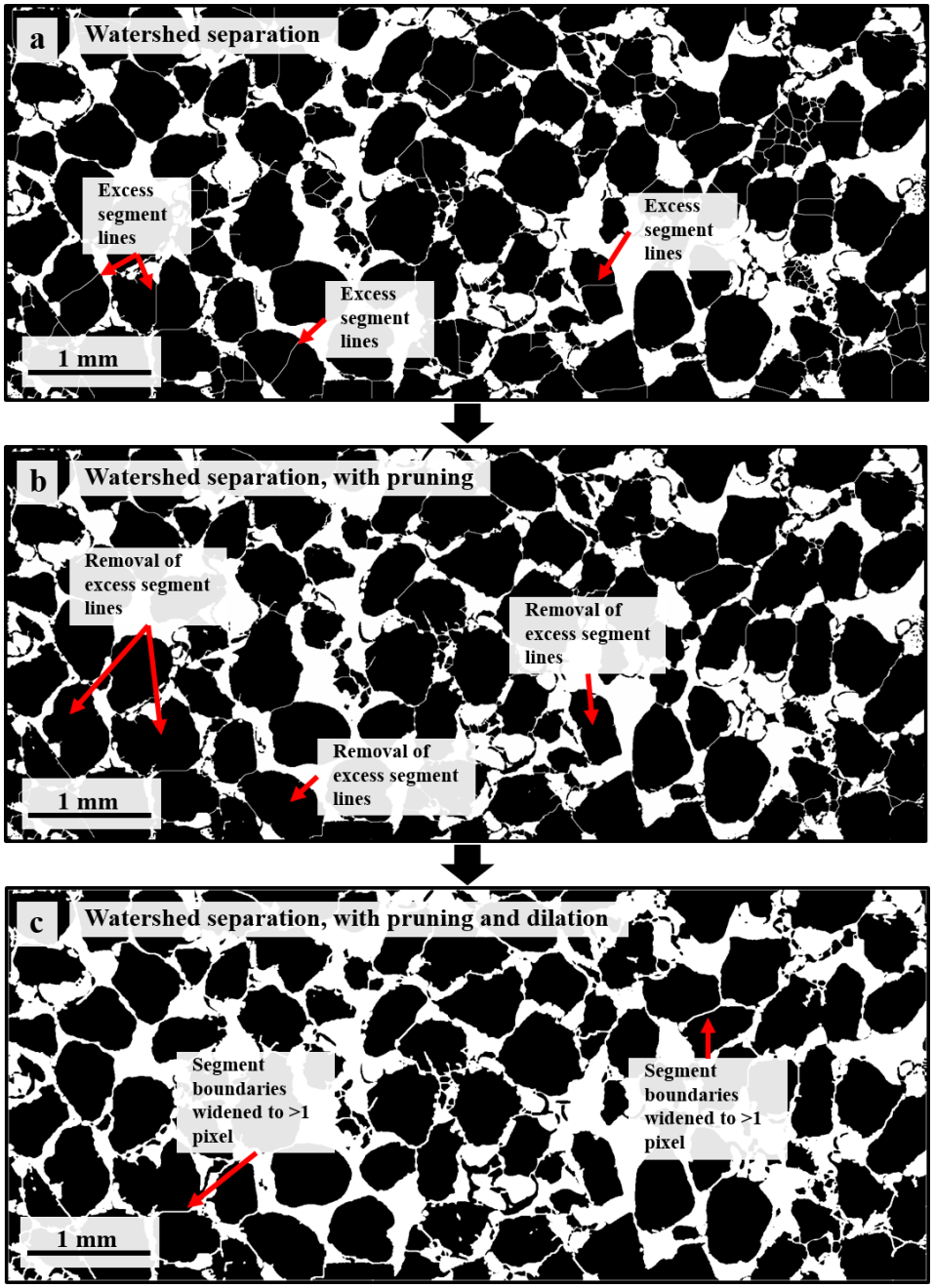

Figure 2.24. *a) Image produced after watershed segmentation showing some excess grain boundaries. b) Removal of the excess grain boundaries using the eraser tool and pruning algorithm. c) Dilation of the pruned image to produce a >1 pixel gap between individual grains so that analysis can be performed accurately.*

2.2.6 Creating porosity distribution colourmaps

Once the median filter has been applied to the image, the total porosity of the image can be calculated. Fiji does this by calculating the proportion of black pixels (solid grains) to white pixels (pore space) across the image. However, this project is primarily concerned with how porosity is distributed across the samples, and therefore, it is necessary to break the image down into series of smaller grids, where each grid has a value of porosity calculated by using the ratio of black to white pixels in that grid. Since strain localisation structures are often associated with localised porosity changes, one of the key elements of porosity distribution analysis is selecting the appropriate grid scale to use in order to see past uniform porosity distributions to examine these localised porosity variations post deformation. The following sections will outline the methodology used to construct these porosity colourmaps.

2.2.6.1 Grid size determination

The first issue when analysing porosity distributions is determining the appropriate grid size to use which is representative of the overall sample porosity, whilst also providing enough resolution to pick out small-scale details. For instance, for a schematic image consisting of closely spaced circles in a regular pattern with a central low porosity zone, an ideal grid size should produce a uniform porosity map for the regions of uniform circles but identify a region of low porosity in the centre of the image (see section 2.2.6.2). To determine the ideal grid size, an approach based on a continuum model is utilised, which assumes a concept known as the representative elementary volume (REV) (Bear, 1972). A schematic illustration in Figure 2.25 demonstrates the concept of the REV curve, whereby a property of a porous medium changes as the sample volume is altered. When the sample size is between V_{min} and V_{max} a constant value of porosity, for example, will be observed. Any value less than V_{min} will encompass only spatially varied, small portions of the property, i.e., porosity, and the individual influence of pores means that rapid fluctuations in said property are observed. Volumes greater than V_{max} may cause the property to drift to new values due to the inclusion of additional morphological structures, resulting in large field variability. When a sample volume between V_{min} and V_{max}

is selected, only minor fluctuations in the medium property are expected, due to numerous pores being factored into the average. The REV can be defined as the volume range where the averaged geometrical characteristics at a given time and point are single value functions of the location (Brown et al., 2000). The REV size of a selected hydrological property within a given domain can be expressed as:

$$V_p \ll V_{min} \leq V_0 \ll V_{max} \tag{2.1}$$

where V_p is the pore volume. It should be noted that the size of the REV may vary depending on the physical property. When considering a fluid mechanics-based view, the REV represents the transition from the deterministic microscopic processes of traditional fluid mechanics, towards the macroscopic processes of porous media flow (Bear, 1972). In this study, since 2D, as opposed to 3D images are examined, the concept of the representative elementary area (REA) will instead be applied. This is analogous to the REV, however, only considers two dimensions. Volume can be substituted for area, when talking about this concept.

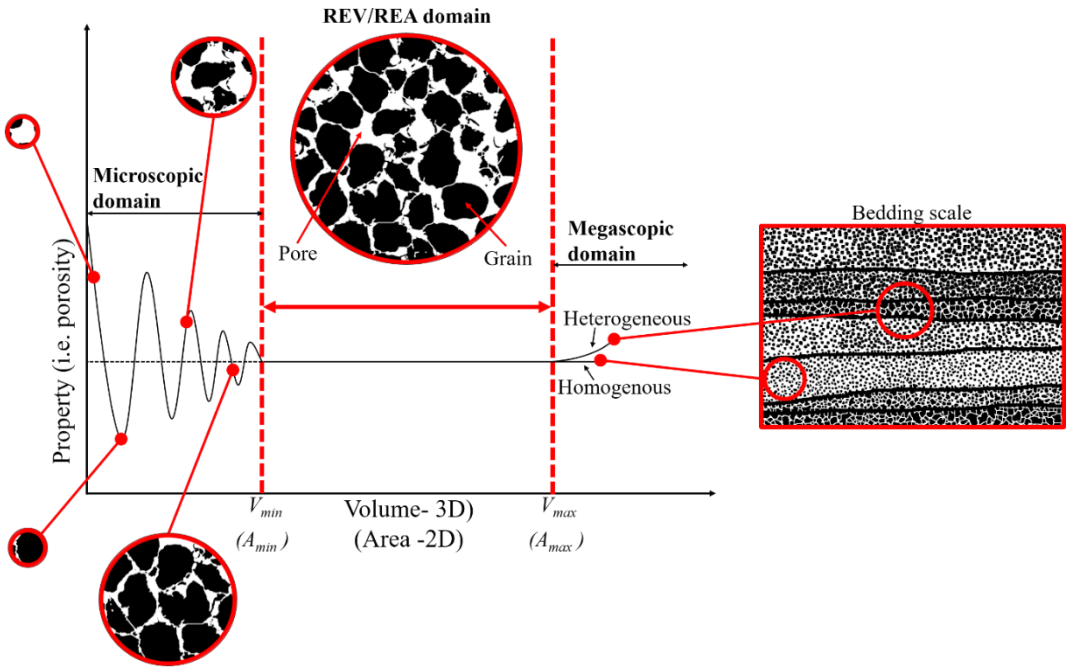

Figure 2.25. *Schematic diagram illustrating the concept of the REV/REA. Solid material is black and pore space is white.*

The porosity sampling procedure used to determine the REA is one adapted from Brown et al. (2000) for 3D REV analysis, whereby they expanded a cube incrementally from fixed points inside the sampling area to generate a number of volume scales across different parts of the sample. In this study, to ensure that any heterogeneities in the deformed samples were recorded in the porosity distribution maps, the REA was calculated using a non-deformed starting sample. To calculate the lower bound of the REA (A_{min}), and thus, the minimum square size that could be used for porosity analysis, the non-deformed starting sample was initially overlain by a 2D square grid. The initial square size must be relatively large to ensure that it is larger than the A_{min}; however, still be small enough so that the image has good coverage of squares. For the purposes of this section, the methodology will be outlined using two cores of natural Boise Sandstone, one of which is intact (Figure 2.26a) and one of which has been deformed (Figure 2.26b). Boise Sandstone is coarse-grained and exhibits clear grain size and porosity variations throughout and so is a good sample to demonstrate the methodology.

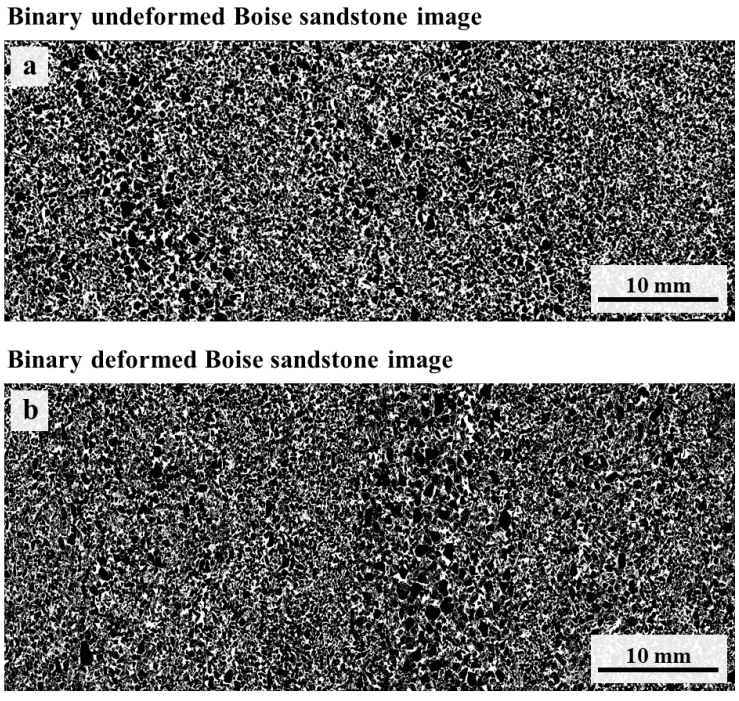

Figure 2.26. *Binary undeformed (a) and deformed (b) Boise Sandstone images used to highlight the porosity map methodology.*

To create the grid, a macro was constructed, which could be run in Fiji (Figure 2.27). A macro can be defined as a programmable pattern which translates a series of inputs into a pre-set sequence of outputs. The grid square size can be defined by inputting the side length of the desired grid square size in pixels (Figure 2.27).

```
run("Set Measurements...", "area perimeter area_fraction centroid fit redirect=None  decimal=2");

A=700;   //Grid square size

w = getWidth();
h = getHeight();
setForegroundColor(0, 0, 0);
for (j=1;j<=nSlices;j++){
        setSlice(j);
        for (ii=0;ii<h/A;ii++){
                for (i=0;i<w/A;i++){
                        run("Clear Results");
                        x=i*A;
                        y=ii*A;
                        makeRectangle(x, y, A, A);
                        roiManager ("add");
                        run("Analyze Particles...", "size=0-Infinity circularity=0.00-1.00  show=Nothing results include");

                }
        }
}
```

Figure 2.27. *Fiji macro used for constructing the initial grid overlay. The individual grid square edge length in pixels for the overlay grid can be set by inputting the value of 'A'.*

The macro creates the ROI (region of interest) grid and overlays it over the image (Figure 2.28a). For the Boise Sandstone an initial overlay grid size of 700 pixel edge lengths (PEL) was deemed reasonable. The porosity in each grid square was calculated by computing the percentage of black (grain) and white (porosity) pixels in each square. The square edge lengths were subsequently reduced by 10 pixels, with the centroid of each square remaining fixed and the porosity for each square again being obtained (Figure 2.28b). This process was repeated at increments of 10-pixel PEL until a final square edge length of 10 pixels was obtained (Figure 2.28c). This produces 70 REA curve realisations from 10–700 PEL for each of the 70 grid squares.

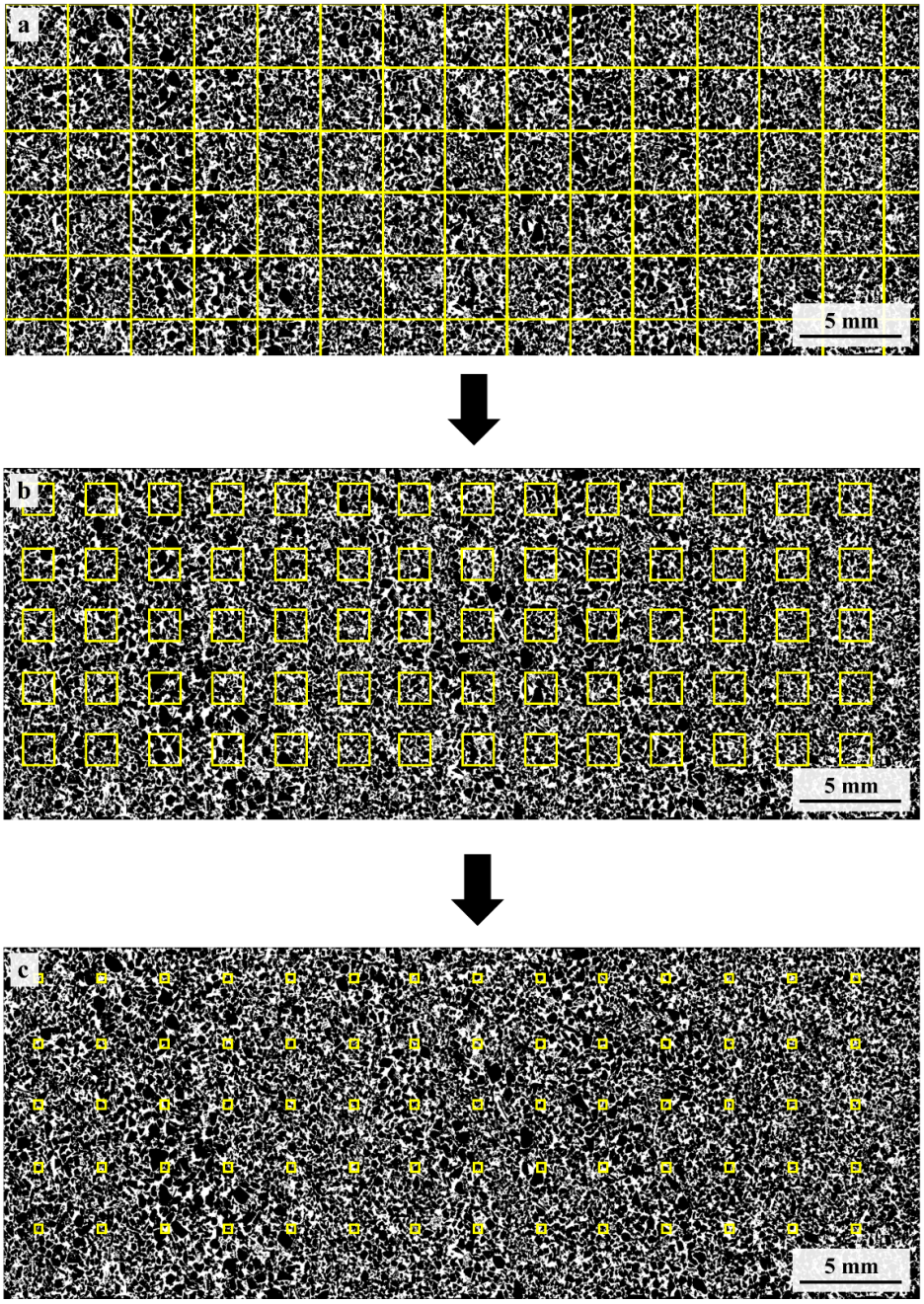

Figure 2.28. *Sampling technique used to find the minimum REA (A_{min}) grid square size in a core section of natural Boise Sandstone. a) The initial 700 PEL grid square overlay across the non-deformed Boise Sandstone sample. b) and c) Reductions in the lengths of the grid square edges by 10-pixel increments to a final value of 10 PEL. Partial squares are deleted and not used in the analysis.*

A statistical methodology similar to that of. Bruns et al. (2017), Koestel et al. (2020), Mu et al. (2016) and Zhang et al. (2000) was adopted in this study to calculate A_{min}, whereby it was observed as being the point at which the mean of a certain physical property (in this case porosity) became approximately constant and the Coefficient of Variation (CV), defined as the ratio between the standard deviation and the mean, was less than a certain value. Mean and standard deviation values were calculated for each of the different area sizes, with these values being used to calculate CV (Figure 2.29a). The REA for porosity was then estimated based on a threshold value of CV (Figure 2.29b). CV values of 0.1 and 0.2 have been used in previous studies and it often depends on whether smaller scale or larger scale porosity trends are desired and the resolution of the porosity variation that needs to be obtained.

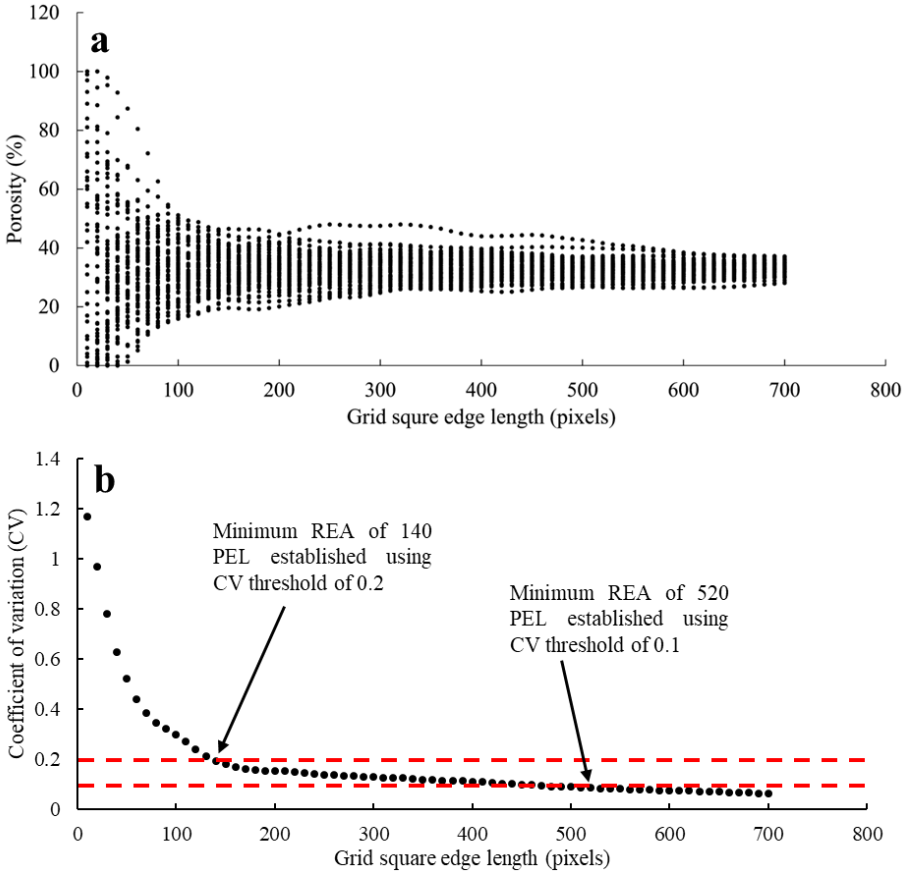

Figure 2.29. *a) Porosity values obtained from each of the grid squares over the 70 different area scales from 10–700 PEL for the non-deformed Boise Sandstone image. The curve exhibits the classic REA/REV trend, shown in Figure 2.25, of rapid fluctuations in the porosity towards smaller area scales. b) CV values plotted against their respective square sizes. The 0.1 and 0.2 CV thresholds are denoted by the dashed red line, with grid square sizes of 140 and 520 PEL representing* A_{min}.

Once the REA is obtained for the respective sample, a sliding window of that size can be applied across the deformed sample to analyse porosity variation. One method to produce a sliding window is by using a macro in Fiji, which initiates a sliding window from left to right and top to bottom across the binary image (Figure 2.31a). The amount of overlap can be altered within the macro. At each window position, the porosity value (*Z*), determined as the ratio of black (grain) to white (pore) pixels, and XY coordinates for the centre of the sliding window

are obtained. A second method is using the MATLAB block processing tool Blockproc, which divides the image up into *M*×*N* blocks (Figure 2.30) and feeds each one into a function, which in this case, calculates the mean of all the pixels in each block (Hugo et al., 2015). This value then becomes a single pixel in the new image.

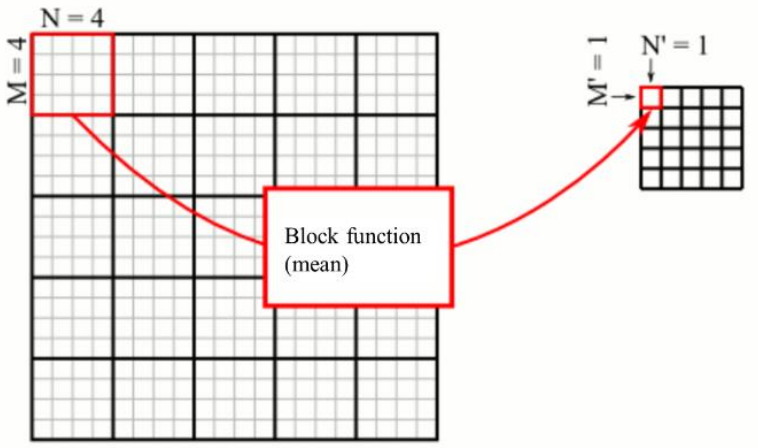

Figure 2.30. *Schematic image of 20×20 pixels to outline the MATLAB Blockproc function, with a setting of M=4 and N=4 and using 'mean' (which outputs M'=1 and N'=1). The final image is 5×5 pixels. In this example no overlap is shown between neighbouring block functions (M×N); however, these can be set so that overlap is present.*

The block functions can be set to overlap by using the BorderSize function which determines the size of the border around each specified block (Figure 2.31a). For a given centre of a block, BorderSize enables *2M+2N* more pixels beyond the dimensions of the originally sized block to be captured, where *M* and *N* are the horizontal and vertical border sizes.

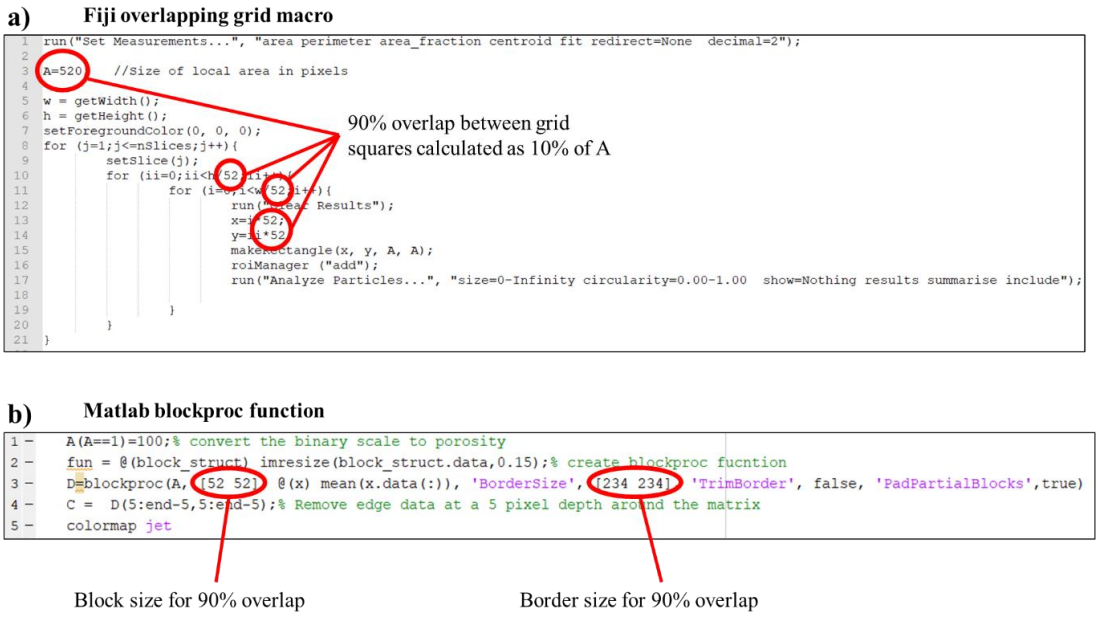

Figure 2.31. *Example of the Fiji overlapping grid macro (a) and MATLAB Blockproc function (b) both set to run the same grid edge length size of 520 pixels, with the same degree of grid overlap of 90%.*

Thus, for an example matrix of values *A*, as for a binary image (Figure 2.32a), if a square size of 8 was desired with an overlap between squares of 50%, then the BlockSize is set to [4 4] and the border size is set to [2 2]. Thus, each *4×4* pixel square is surrounded by 2 rows of pixels, producing an overall square size of *8×8* (Figure 2.32a). The next *8×8* square on the right would be centred around the *4×4* pixel squares on the right with the [2 2] border size providing the overlap (Figure 2.32b). The size of the squares and the overlap can be determined using the following equations:

$$BlockSize\ [X\ X] = square\ size - \left(\frac{square\ size * percentage\ overlap}{100}\right) \qquad (2.2)$$

$$BorderSize\ [X\ X] = \frac{square\ size - blocksize}{2} \qquad (2.3)$$

TrimBorder must also be set to ‘false’ so that those pixels that were originally captured upon expansion of the block can be kept. PadPartialBlocks should also be ‘true’ to ensure that the blocks at the edge of the matrix are the same size as those within.

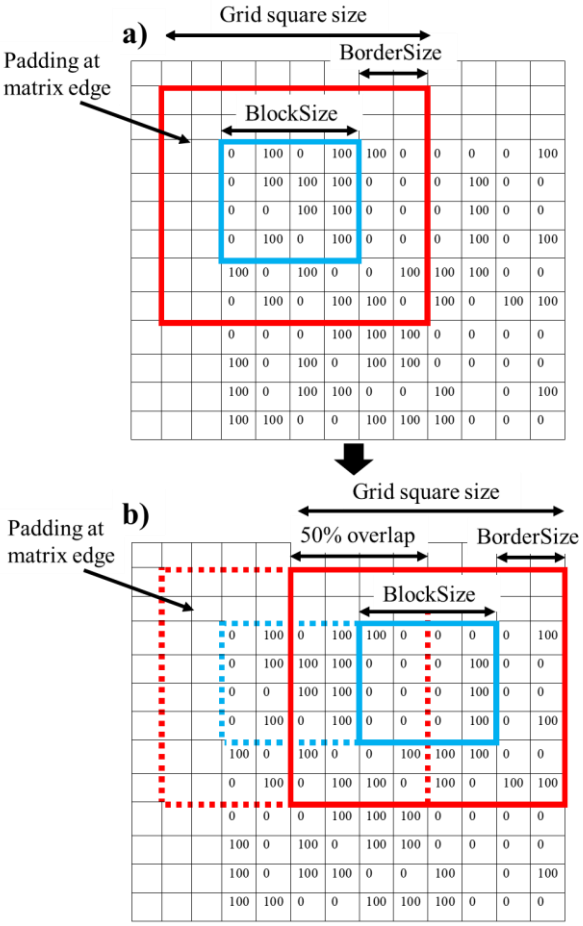

Figure 2.32. *Matrix of 100 porosity values (0 or 100%) each representing 1 pixel, converted from the binary image, where originally 0 (black)=grain and 1 (white)=pore. An 8×8 pixel grid square with a 50% overlap between each square is displayed in red. The BlockSize ([4 4]) is represented by the blue square and the BorderSize ([2 2]) represents the 2 pixels surrounding the BlockSize in the vertical and horizontal directions.*

In both the Fiji and MATLAB methodologies incomplete squares will be produced, unless in the unlikely event that the image is perfectly divisible by the number of whole squares. These should be deleted to avoid outliers in the subsequent porosity maps. The edge effects due to the padding in MATLAB can be removed using the TrimBorder function, whilst in Fiji, partial squares can be removed from the ROI manager prior to initiation of the macro. Both methods for producing the overlapping grids yield almost identical results in the subsequent colourmaps. However, Blockproc has a key advantage in that it is significantly faster, especially when a sliding window is required which has small grid squares and more frequent overlaps. This methodology is therefore favoured for most of the analyses within this study. A summary of the image analysis workflows used to process the original 8-bit greyscale SEM images and construct grain size and porosity distribution colourmaps is displayed in Figure 2.33.

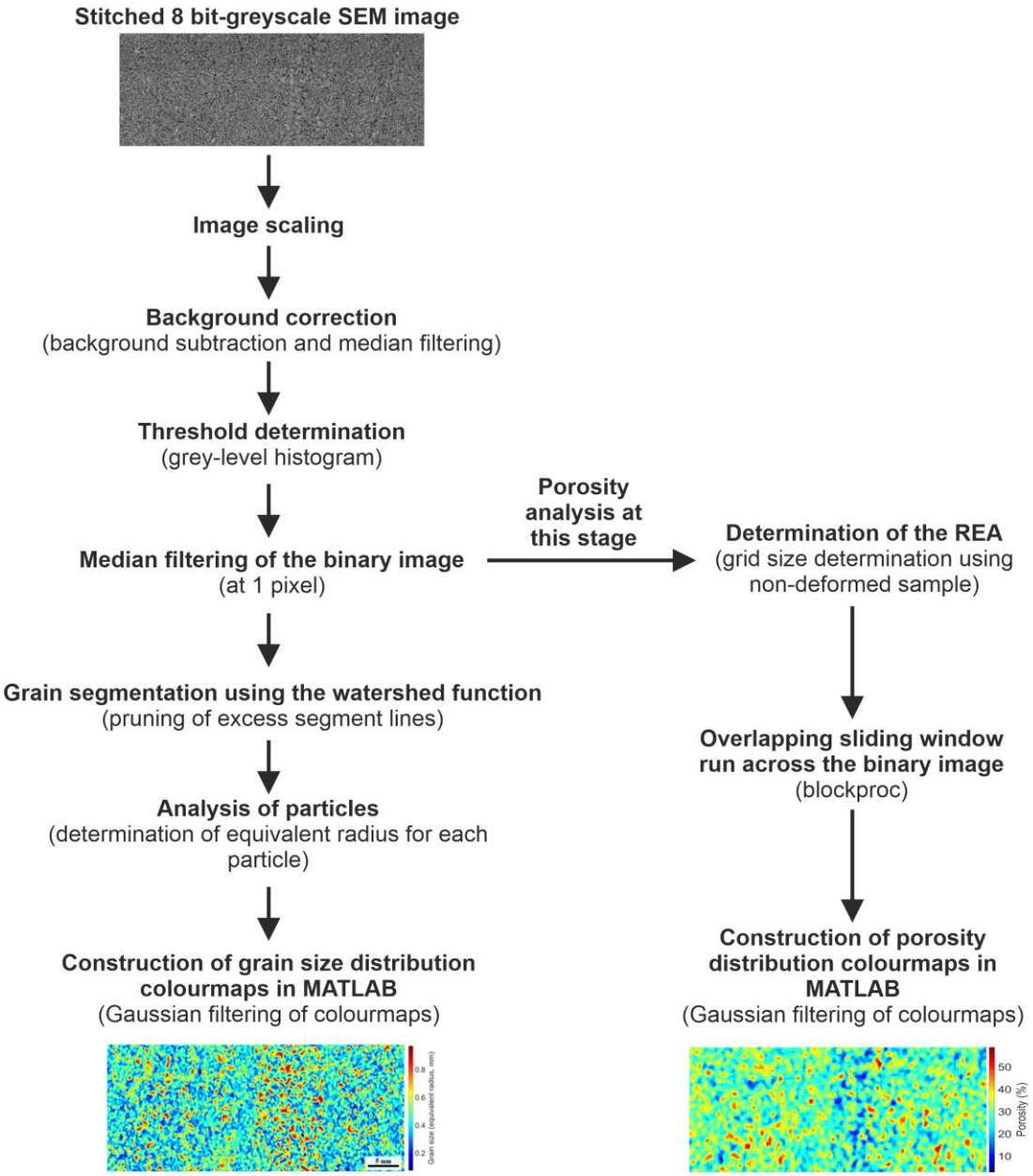

Figure 2.33. *Summary of the image processing and analysis workflows used to construct grain size and porosity distribution colourmaps from the original, stitched, 8-bit greyscale images.*

2.2.6.2 The effect of grid size and grid overlap

To examine the effect that different grid sizes and degrees of overlap can have on the resultant colourmaps, several porosity maps for the Boise Sandstone with variations in these parameters are shown below (Figure 2.34). The larger grid size of 0.1 CV produces a lower resolution image overall and does not clearly resolve grains or pores (Figure 2.34b, d, f, h, j). However, the porosity values and fluctuations are more representative of the overall sample porosity. The smaller grid size of 0.2 CV resolves more detail (Figure 2.34a, c, e, g, i); however, it produces much higher and lower departures from the average sample porosity. This indicates that the influence of individual pores and grains is starting to exert a greater effect, suggesting that the grid size is too small. With increasing grid overlap, the resolution increases in both the 0.1 and 0.2 CV grid sizes. However, in the 0.2 CV grid size the porosity values also deviate further from the average porosity (Figure 2.34a, c, e, g, i). In the 0.2 CV grid size, with increasing overlap, this deviation is considerably smaller (Figure 2.34b, d, f, h, j).

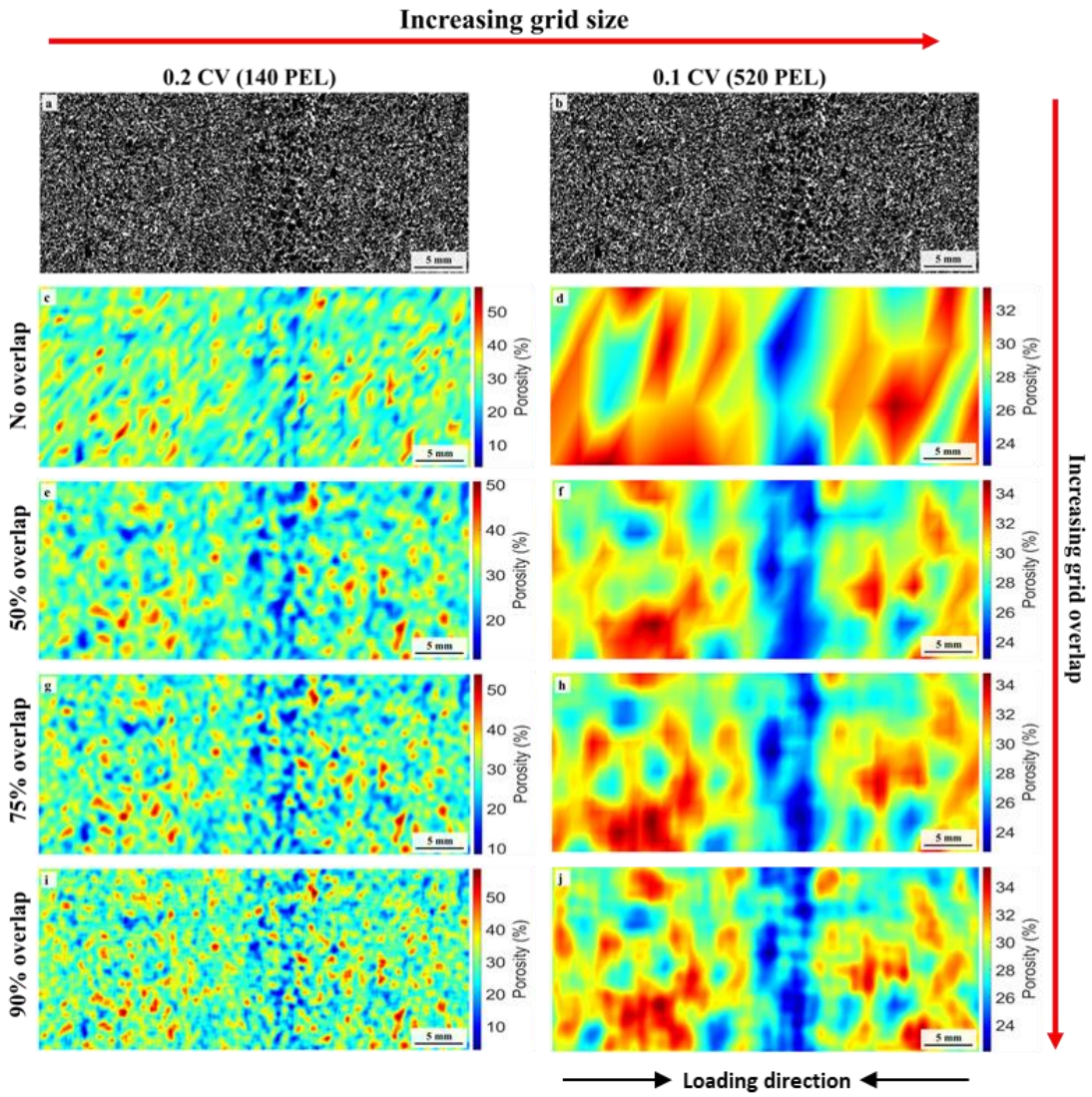

Figure 2.34. *Porosity maps produced for the deformed Boise Sandstone. The processed binary image is displayed in a) and b) for comparison with the porosity maps. Each image has been smoothed using a Gaussian filter to remove excess noise and produce a clearer image.*

To identify whether there is an optimal grid size and amount of overlap for porosity analysis, and also to ensure that these porosity maps can function as a viable method of displaying porosity variations, the methodology will be validated using sample images constructed with known porosities and porosity distributions. The models constructed each have low porosity regions representing deformation bands, with these being similar dimensions to those which have been identified in previous laboratory studies on natural sandstones. The first image is the most basic, with a vertical, low porosity 'band' across the centre of the image (Figure 2.35a). Secondly, two closely spaced bands across the sample centre are inserted, to observe whether the close spacing affects the sliding window's ability to properly resolve the porosity in between them (Figure 2.35b). In the third image, 'wiggly' compaction bands are inserted at either ends and in the centre of the image, to examine whether bands at orthogonal, more complex angles to the sliding widow can also be resolved (Figure 2.35c). Finally, an image with a central, low porosity region but more complex, heterogeneous pore structure is created (Figure 2.35d). The total porosities of the images are calculated using Fiji. Each of the images is constructed with black grains and white pores to minimise any issues regarding thresholding cut-offs during binarisation. The REA is calculated for both the homogeneous (Figure 2.35a) and heterogeneous (Figure 2.35b) pore network starting samples.

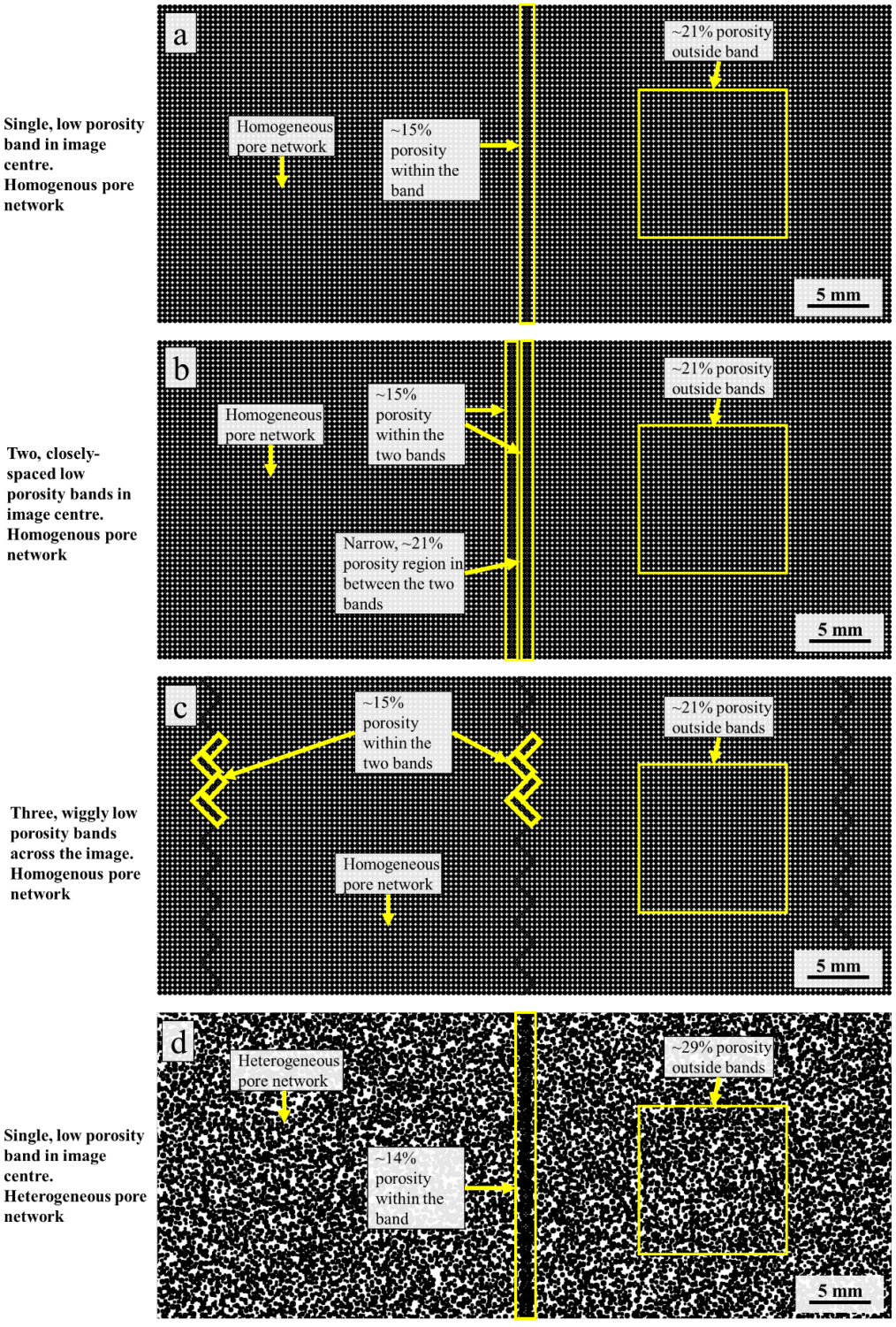

Figure 2.35. *a), b) and c) Schematic images depicting a homogeneous grain and pore network with three different band localisation types. d) heterogeneous grain and pore network with a low porosity central band.*

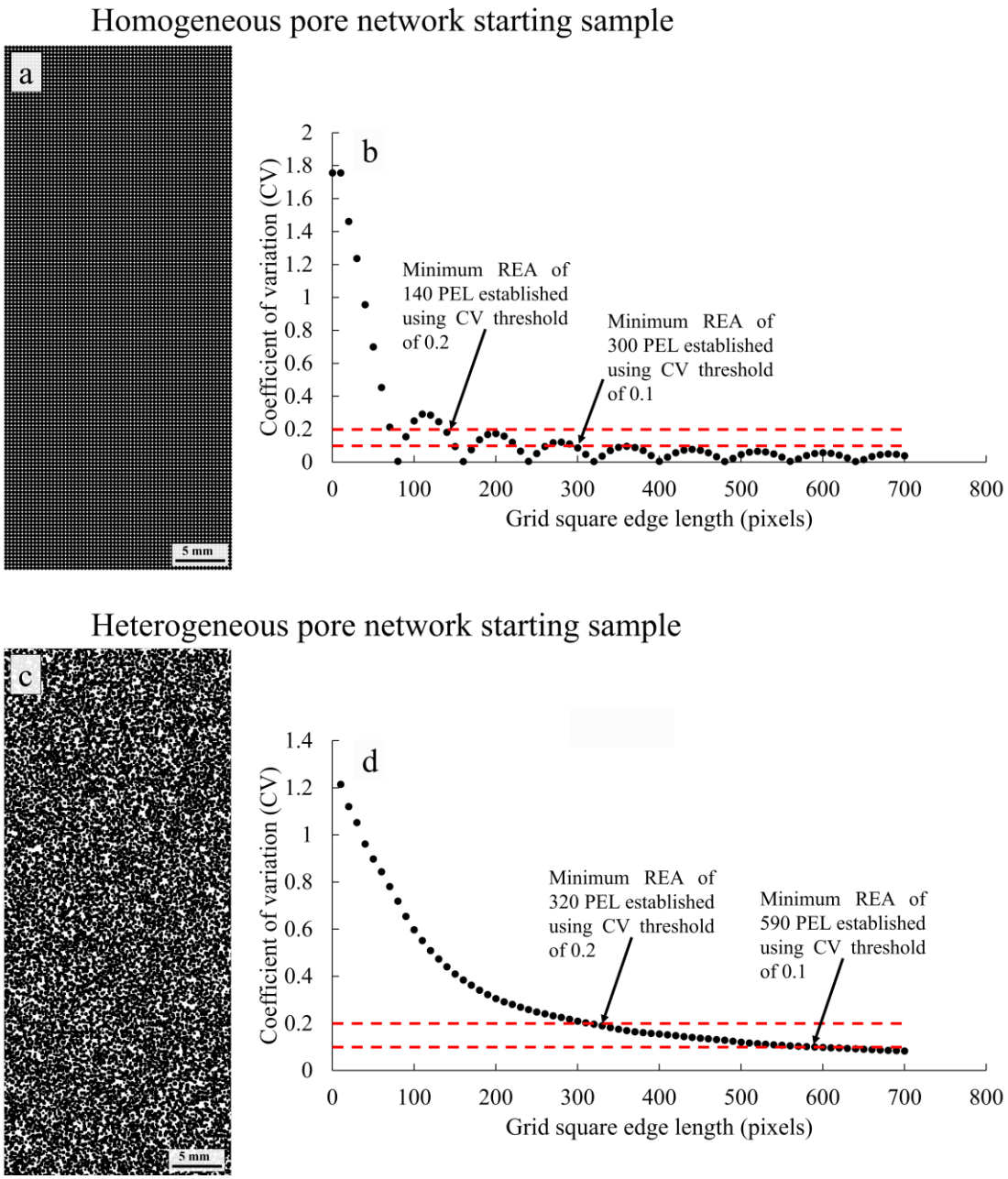

Figure 2.36. *Starting samples with no localised features for the homogeneous (a) and heterogeneous (c) images. These images were used to determine the REA for the images in Figure 2.35. The pattern in b) is likely a result of the homogeneous pore structure. A conventional REA pattern is observed for the heterogeneous pore structure image (d).*

From each image set it is evident that increasing the grid overlap results in a better-resolved porosity map. This is particularly clear in the images with the homogeneous pore structure (Figure 2.37, 2.38, 2.39), since in both the 0.1 and 0.2 CV samples, the grids do a poor job of resolving the porosity, even after Gaussian smoothing at 0%, 50% and 75% overlap. Whilst the homogeneous pore structure exacerbates the issues with the resolution, it suggests that overlap less than 10% will result in a poorly resolved image, even in more heterogeneous, natural samples, such as Boise Sandstone, which might not have otherwise been easily identified.

The grid size (0.1 or 0.2 CV) also controls the porosity map produced. The larger grid size of 0.1 CV can resolve most of the localised structures (Figure 2.37, 2.38, 2.39, 2.40), though, with less precision than the 0.2 CV image and the low porosity regions are usually wider in the colourmap compared to the original image. The porosity of these features is also higher than those calculated directly from the binary image, due to the structures being relatively small in relation to the 0.2 CV grid size. Furthermore, the two closely spaced bands could not be resolved at all by the larger grid size, with one wide, low porosity region instead being produced (Figure 2.38b, d, f, h, j). Therefore, the larger grid size cannot resolve as much detail and produces lower-resolution images.

However, although the smaller grid size does produce higher-resolution images and can capture more of the image details in the homogeneous pore-structure images, it does encounter problems when the pore space becomes heterogeneous (Figure 2.40). This is because the heterogeneous pore structure will contain porosity outliers, such as larger pores or clumps of grains which fall far outside the average of the REA. When the smaller grid size encounters these structures, it produces very high or low porosity values (Figure 2.40a, c, e, g, i). In reality, the true porosity of these structures is not being measured because the grid size is likely below their REA. This results in bright or dark porosity spots on the porosity map. For the larger grid size of 0.1 CV, there will be fewer regions which fall outside the REA, because large pores or clumps of grains are less likely to take up a whole grid square. As a result, the 0.1 CV porosity

maps reflect a more accurate representation of porosity distribution, with fewer extreme peaks, although it does mean that if the size of the localised structures such as compaction bands are very small, then their porosity may not be resolved, because the REA of the band may be much lower than the REA of the whole sample.

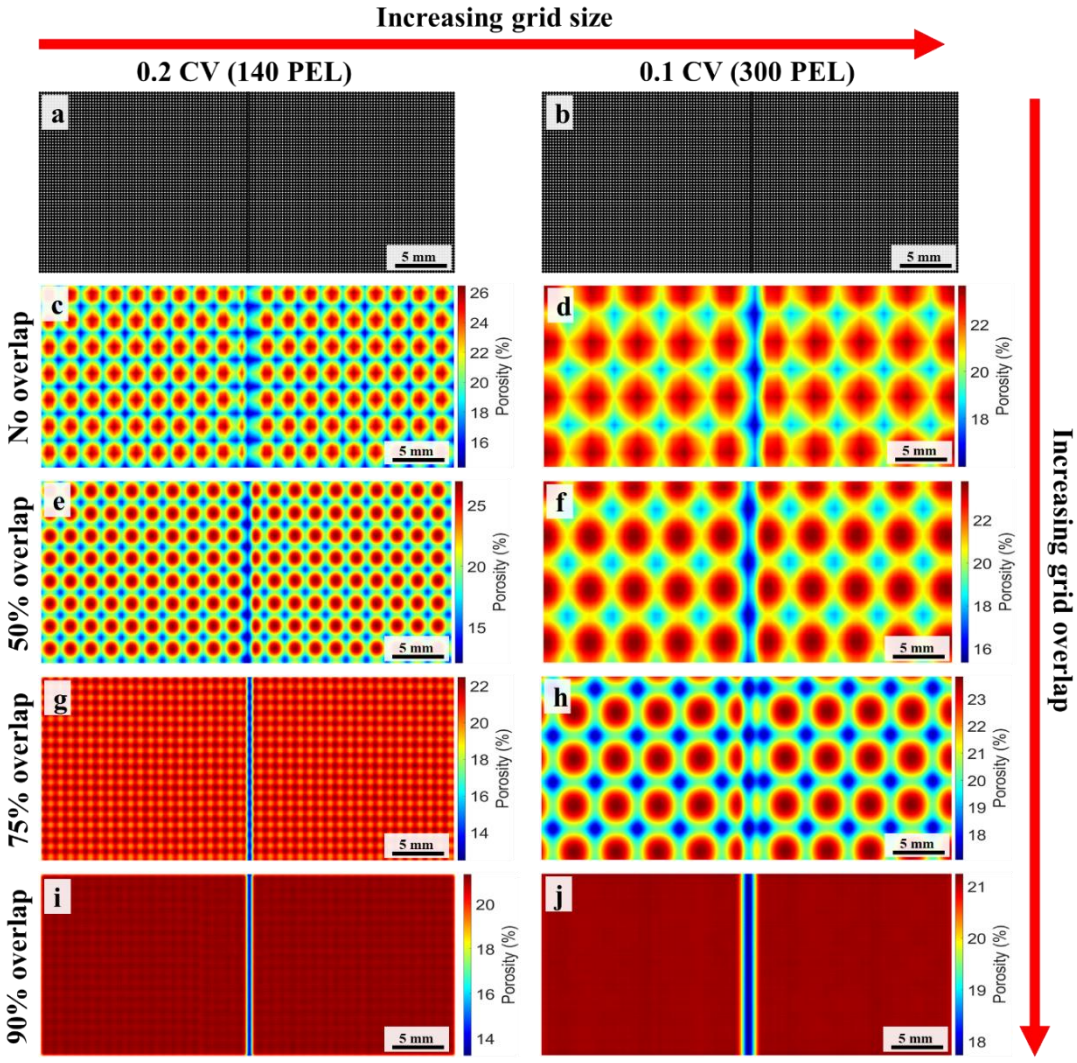

Figure 2.37. *Porosity maps for the schematic image depicting a homogeneous grain and pore network with a single, low porosity central band for two grid sizes (0.2 and 0.1 CV), with varying amounts of grid overlap (0%, 50%, 75% and 90%).*

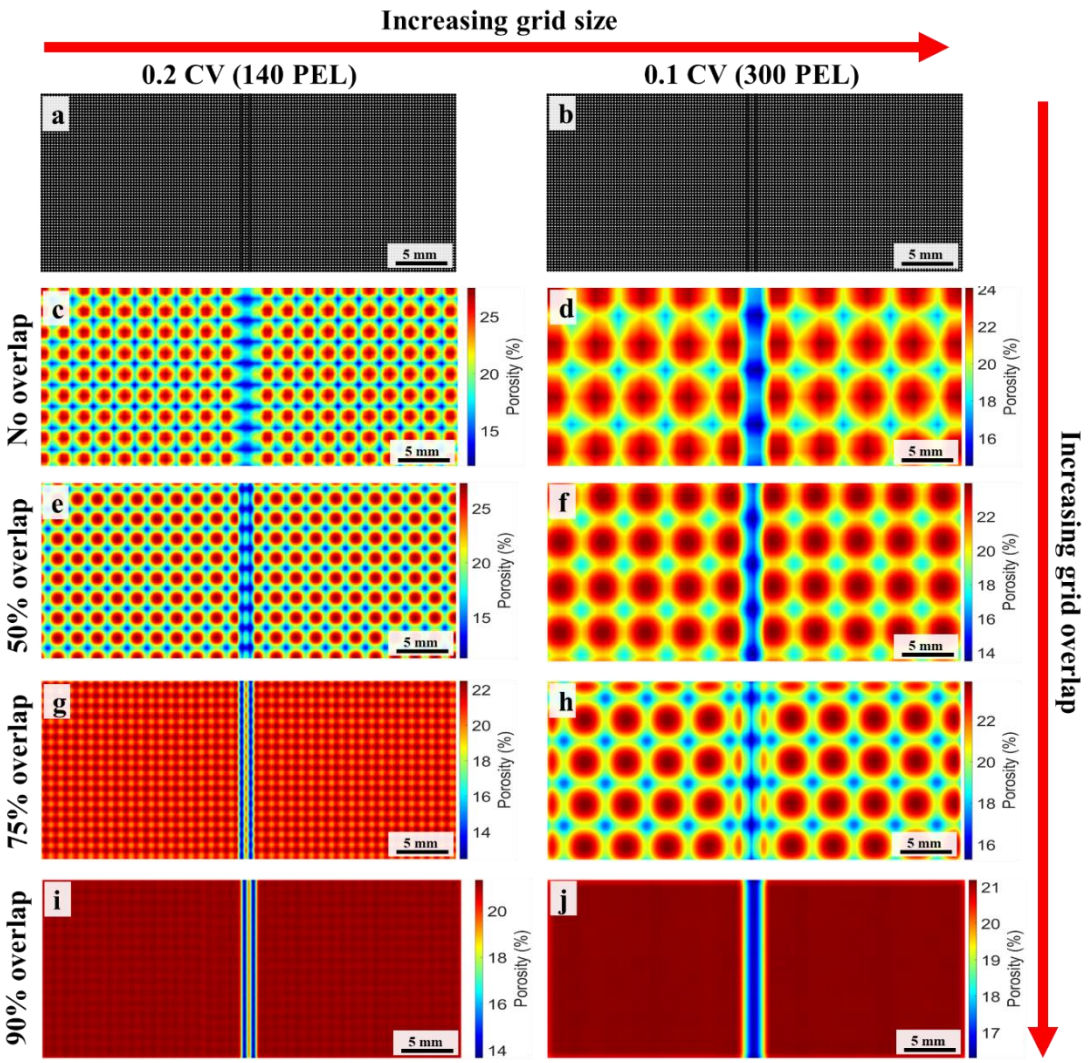

Figure 2.38. *Porosity maps for the schematic image depicting a homogeneous grain and pore network with two closely spaced, low porosity central bands for two grid sizes (0.2 and 0.1 CV), with varying amounts of grid overlap (0%, 50%, 75% and 90%).*

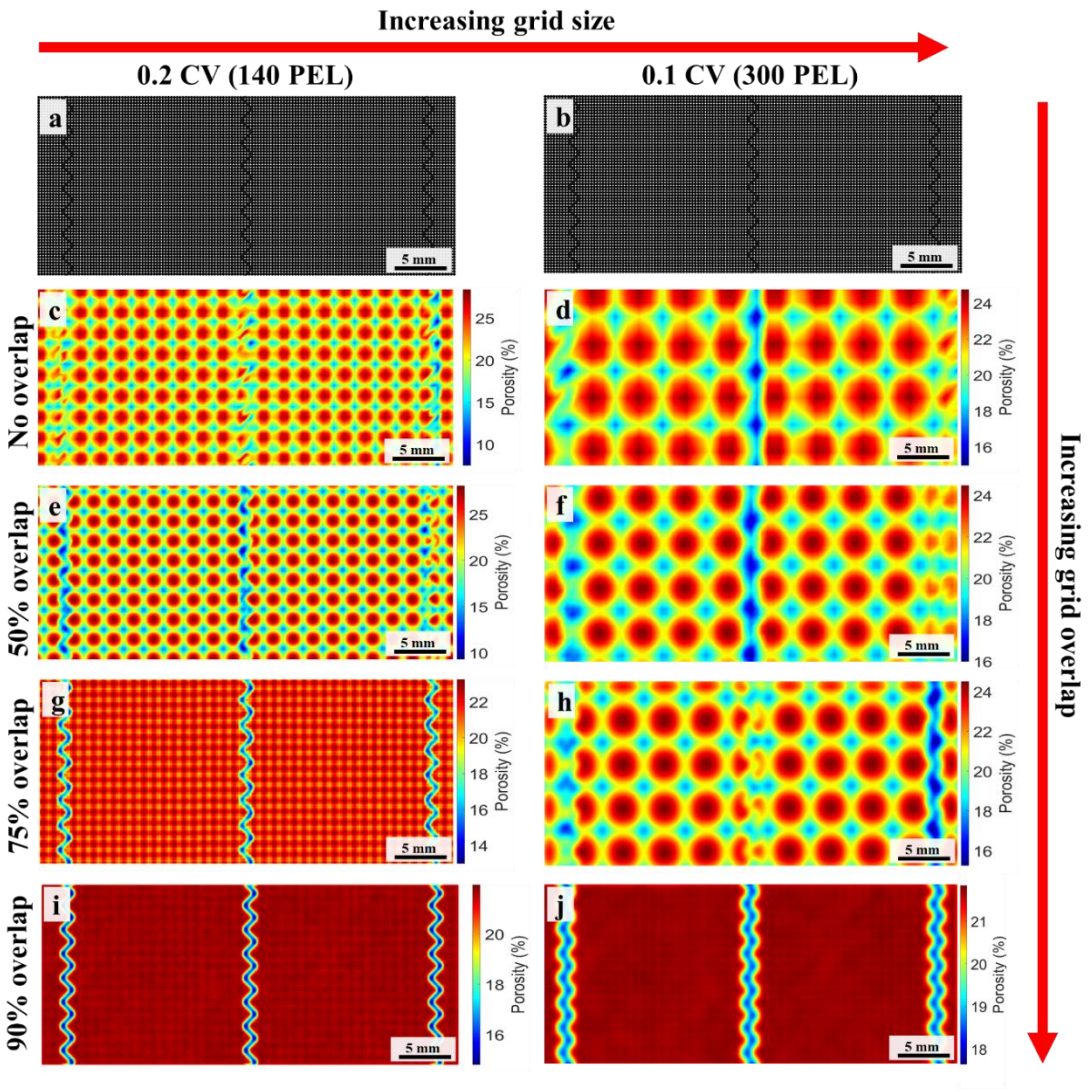

Figure 2.39. *Porosity maps for the schematic image depicting homogeneous grain and pore network with three wiggly low porosity bands across the sample for two grid sizes (0.2 and 0.1 CV), with varying amounts of grid overlap (0%, 50%, 75% and 90%).*

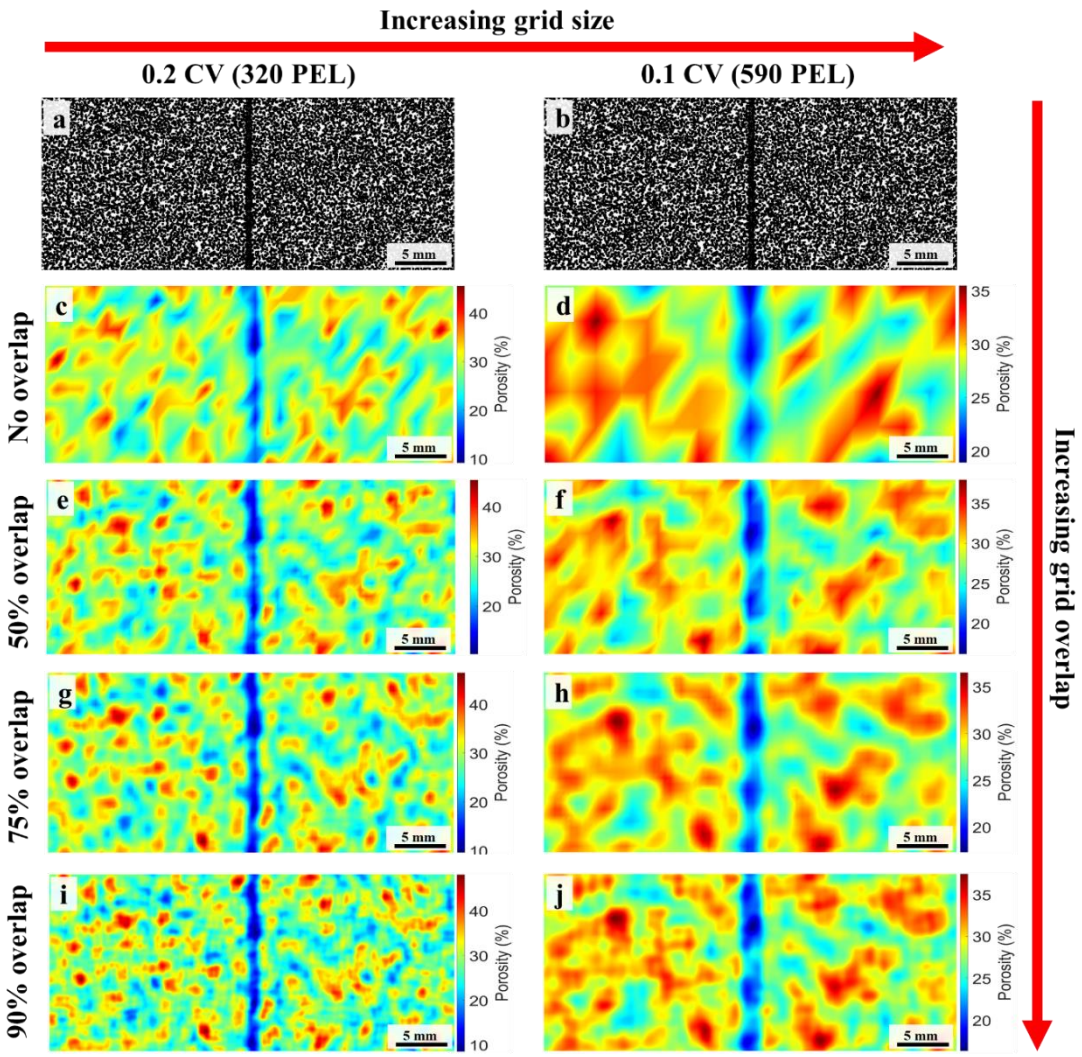

Figure 2.40. *Porosity maps for the schematic image depicting a heterogeneous grain and pore network with a single, low porosity central band for two grid sizes (0.2 and 0.1 CV), with varying amounts of grid overlap (0%, 50%, 75% and 90%).*

2.2.7 Combing BSE images with porosity maps

Porosity maps can be combined with their respective BSE images to better examine small-scale microstructural properties. In this research, this method was predominantly used to examine porosity and grain size relationships within deformation bands. The technique utilises the image calculator in Fiji, which performs arithmetic and logical operations between two images (Ferreira & Rasband, 2012). The two images input into the calculator are the source image (*img1*), which is the RGB porosity colourmap for the desired area (Figure 2.41a), and the destination image (*img2*), which is the 8-bit greyscale BSE image of the same area (Figure 2.41b). Both images must be the same scale. The 'minimum' operator is then performed on both images, which executes the function:

$$img1 = \min(img1, img2) \tag{2.4}$$

and replaces each pixel for the same given coordinates in each image with the lowest value pixel out of the two images. This operation gives the impression that the porosity map has been overlain over the BSE image, since the dark porosity regions in *image 2* will be the lowest pixel values (i.e., around 0) from the two images and so the contrast between the grains and the pore space is preserved (Figure 2.41c). However, the light colour of the white grains produces much higher pixel values (around 255) and so the white colour of the grains is replaced by the darker RBG colours of the porosity map.

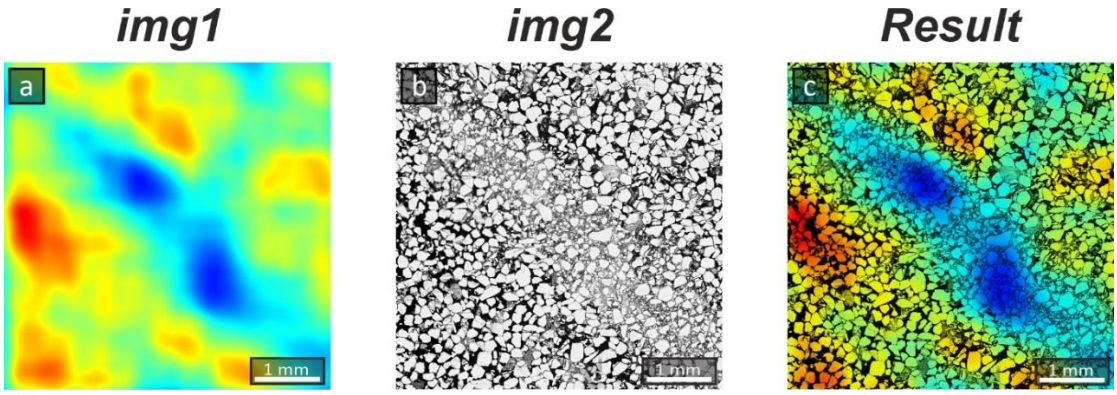

Figure 2.41. *Example of the 'minimum' function in the Fiji image calculator being used to produce a combined BSE-porosity map image (c) from a porosity map image (a) and initial BSE image (b) of a deformation band.*

2.2.8 Analysing particles

Grain size distribution maps can also be produced in a similar way to porosity maps. Once the individual grains have been separated using the segmentation techniques described in section 2.2.5.2, they can be analysed in terms of their characteristics using the features in the 'Analyse' tab in Fiji. The desired measurements can first be set by going to 'Set Measurements' within this tab and selecting the desired parameters (Figure 2.42a). For a grain size colourmap to be produced in MATLAB, the 'Area', 'Centroid' and 'Perimeter' options must be selected, with the centroid corresponding to the XY coordinates for the centre of each grain. The 'Analyse Particles' function can then be selected, ensuring that holes are included in the analysis (Figure 2.42b). Either the 'Display Results' or 'Add to Manager' options can be selected as both options will display the tabulated data (Figure 2.42c). However, adding the data to the ROI manager enables more flexibility if any further processing or measurements are required. Each grain is identified as a ROI during analysis, illustrated by the yellow outline and label and added to the ROI manager (Figure 2.42c). The data can then be saved as a CSV, TXT or Excel workbook file.

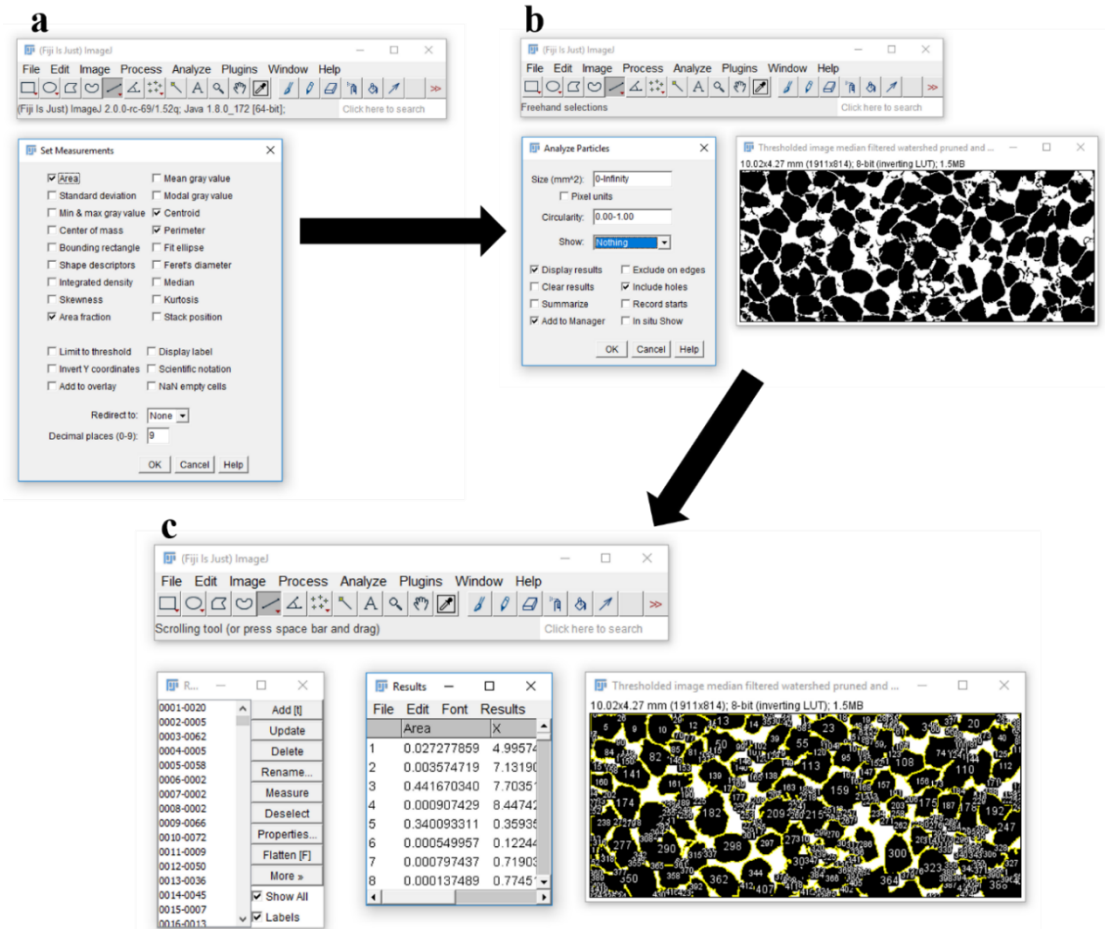

Figure 2.42. *Grain size analysis workflow using the Fiji software. a) Selection of the desired measurements. b) Implementation of the 'Analyse Particles' function to measure each grain. c) Resulting data.*

The area of each grain is the sum of the number of pixels in each segment. If the image is scaled, then the pixel area is scaled to the appropriate area measurements. In order to derive a linear size measurement of a grain, i.e., radius or diameter, the concept of the equivalent circle is used (Figure 2.43), which is the radius of a circle with the same area as that of the segment (grain):

$$r_{equ} = \sqrt{\frac{A}{\pi}} \qquad (2.5)$$

where A is the segment area (Heilbronner & Barrett, 2013). Since segments are required to be separated by a gap of at least two pixels, the segment size may underestimate the true cross-sectional area of a given grain. This can be corrected for if the image is unscaled, i.e., in pixel units, using the area A and perimeter P (Figure 2.43).

$$r_{equ} = \sqrt{\frac{A_{corr}}{\pi}} = \sqrt{\frac{A+P}{\pi}} \tag{2.6}$$

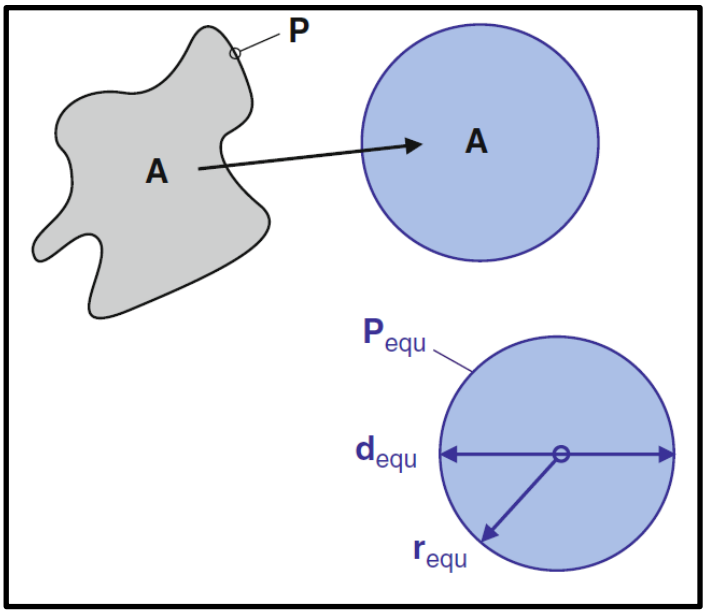

Figure 2.43. *Size and shape measures from segments, after Heilbronner & Barrett (2013). The original segment (grain) is shown in grey, and the equivalent circle in blue. P represents the perimeter of the original segment, whereas A is the area of both the original segment and the equivalent circle. The equivalent radius of the equivalent circle was used throughout this study to represent grain size.*

The equivalent radius, r_{equ}, derived from Equation 2.6, can subsequently be converted back into millimetres using the pixel scaling value. These values can then be uploaded into MATLAB to create a grain size colourmap. An example of a colourmap produced for the Boise Sandstone, which has a grain size of 0.5 ± 0.3 µm, is displayed in Figure 2.44. The sandstone

displays clear grain size variations throughout the binary image, the most notable being in the centre-right. These variations are clearly picked out in the grain size map which also accurately reflects the true grain size (0.5 ± 0.3 µm).

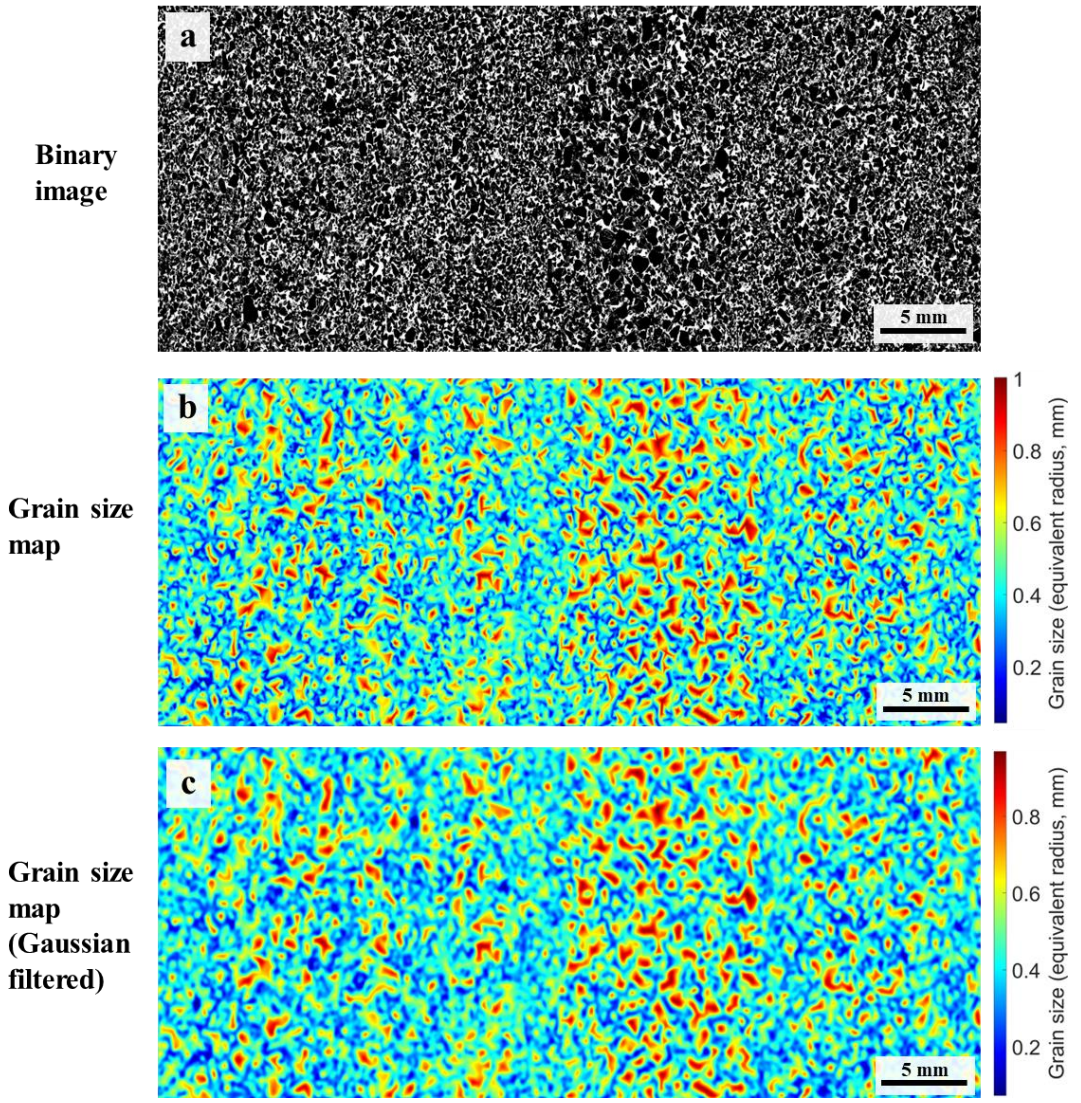

Figure 2.44. *Original (b) and Gaussian filtered (c) grain size maps produced from the Boise Sandstone binary image (a). The grain size maps accurately reflect the grain size variations seen in the binary image.*

Similarly, as for porosity maps, it is also important to ensure that the grain size maps can pick out any grain size variations as a result of localised compaction. Consequently, the schematic diagram showing the two closely spaced bands in Figure 2.35b was analysed for grain size using the techniques described above (Figure 2.45a). Since the two low porosity bands contain smaller grains between the larger ones, these should correspond with a grain size decrease on the grain size map. The large grains have a radius of 0.17 mm, whereas the smaller ones have a radius of 0.07 mm. Both the original (Figure 2.45b) and Gaussian-filtered (Figure 2.45c) grain size maps show a clear colour change in the compaction band region, with the vertical lines representing the smaller grains. The sizes produced by the colourmap also correspond well to the actual sizes of the grains in the schematic diagram. Therefore, the use of grain size colourmaps can accurately pick out small-scale grain size changes, thus helping to identify compaction bands.

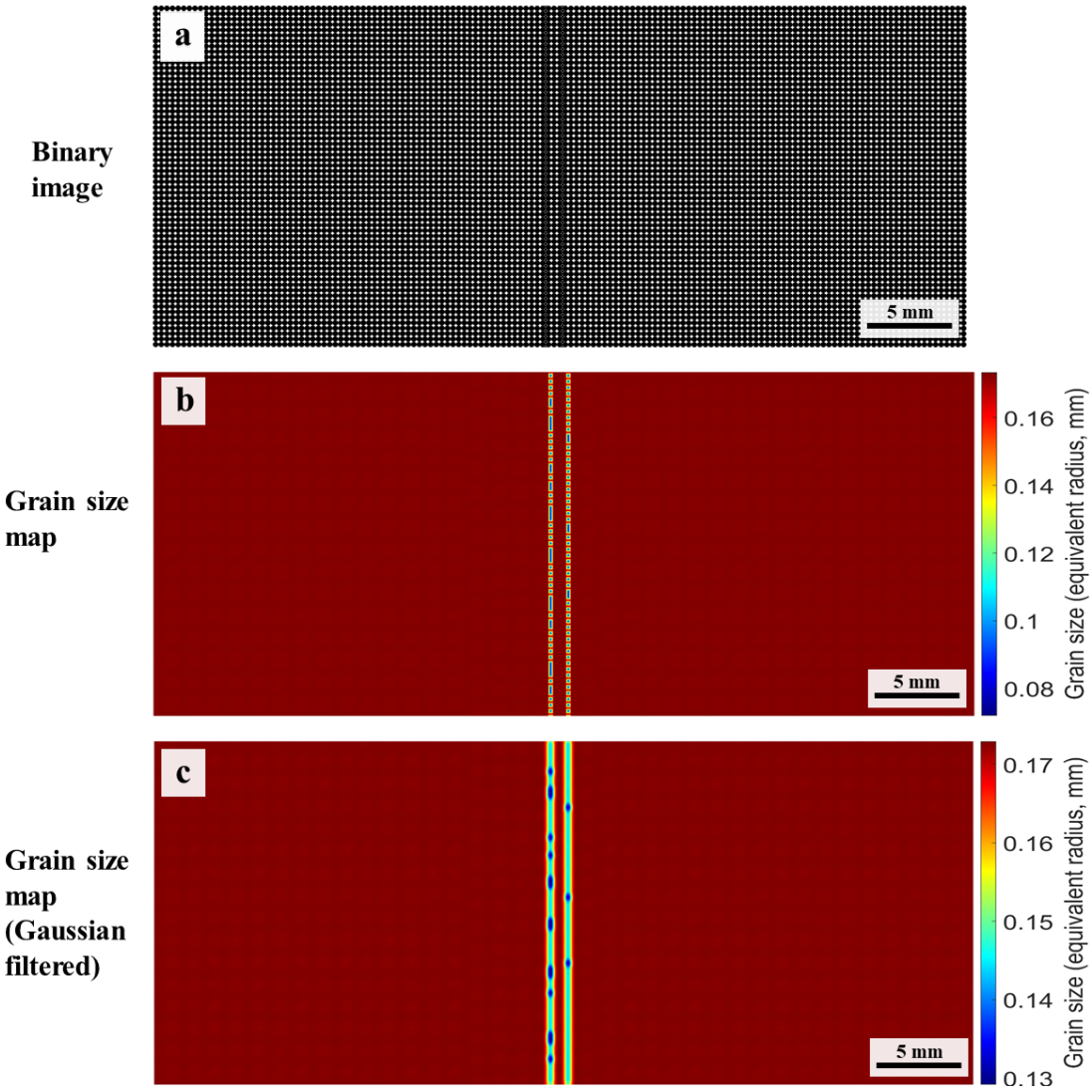

Figure 2.45. *Original (b) and Gaussian filtered (c) grain size maps produced from the schematic binary image with two closely spaced low porosity central bands (a). The grain size maps accurately reflect the grain size variations seen in the binary image.*

2.2.9 Quantitative analysis of strain localisation using FracPaQ

In this section, a brief outline of the use of the MATLAB toolbox FracPaQ for quantitative analysis of strain localisation traces will be presented. FracPaQ was initially developed for the purpose of fracture pattern analysis (Healy et al., 2017). However, in this study it has been adapted in order to analyse strain localisation structures, such as shear and

compaction bands, which involves the correct processing of the stitched whole core BSE images. The most robust and preferred input file type for FracPaQ are node files, since these provide XY coordinate pairs for each node along every fracture/localisation trace (Healy et al., 2017). To produce these node files from the stitched SEM images for analysis in FracPaQ, the localisations are first enhanced by applying the 'find edges' function in Fiji, which uses a Sobel edge detector to highlight sharp changes in intensity in the image (Figure 2.46b). This has the effect of drawing a line around the grain boundaries. A Gaussian filter is then applied at a radius of approximately 50 pixels to suppress small-scale contrast changes and better constrain the localisation (Figure 2.46c). The image is then binarised (Figure 2.46d) which allows the 'skeletonise' function to be applied. This repeatably removes pixels from the edges of objects in a binary image until they are reduced to single-pixel-wide structures (Figure 2.46e). Excess skeletons or noise, below 3 pixels in length, can be removed here using the skeleton pruning function in Fiji. The image is still in bitmap form at this stage and must be converted into an SVG node file for analysis in FracPaQ. The quickest method to do this is using the 'Trace Bitmap' function in CorelDRAW which is a powerful vectorisation tool (Figure 2.46f). The SVG image produced (Figure 2.46g) is composed of multiple curves, bounded by nodes (Figure 2.46h), which are not compatible with FracPaQ, since it will only accept straight lines bounded by nodes (Healy et al., 2017). To convert to the latter type, the 'convert to lines' function in CorelDRAW must be selected (Figure 2.46i). The nature of the FracPaQ analysis means that each individual node-bounded line is analysed. Consequently, it is important to remove excess nodes, using the automated node removal function in CorelDRAW, so as to reduce the number of data points for each trace The image can then be uploaded into FracPaQ and processed using an SVG to TXT conversion script within the FracPaQ toolbox (Figure 2.46j).

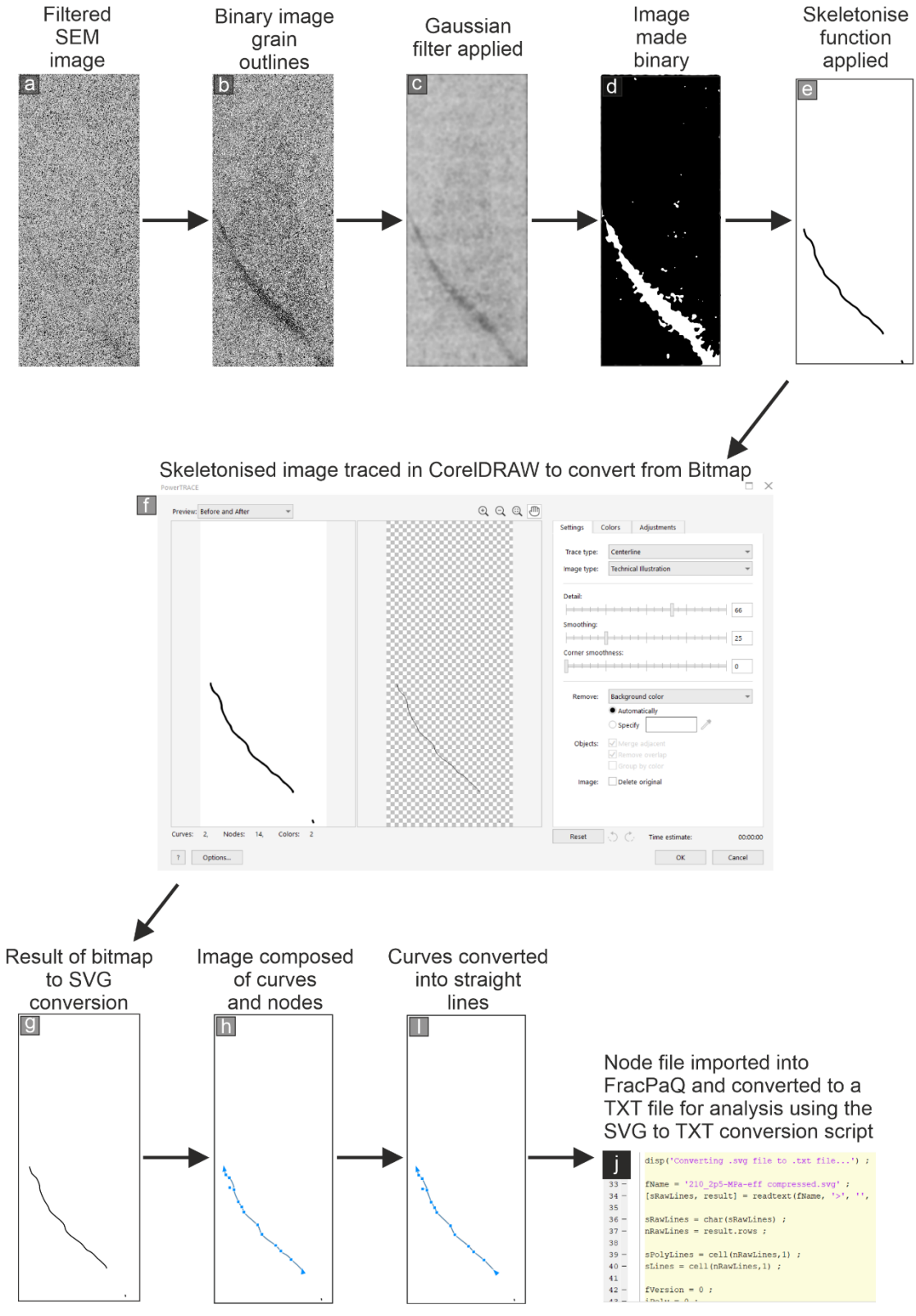

Figure 2.46. *Workflow used to prepare original BSE images for quantitative analysis in FracPaQ.*

The orientation of the strain localisation traces can be analysed in FracPaQ using a variety of techniques and plots. As displayed in the Graphical User Interface (GUI) (Figure 2.47a), maps, wavelets and graphs of the localisation traces can be produced and their lengths, angles and fluid flow properties can also be examined. In this study, FracPaQ was used primarily to construct orientation rose diagrams and density and intensity maps of the strain localisation traces. Length-weighted rose diagrams can be produced for the localisation traces (Figure 2.47b), whereby trace angles are defined as the angle of the trace segment measured clockwise from the *Y*-axis, for the default assumption, throughout this study, that the *Y*-axis (long-axis) is the loading direction (σ_1).

The characteristics and spatial distributions of the localisation traces can be quantitatively established by constructing maps of localisation density and intensity. The circular scan window method of Mauldon et al. (2001), applied to the coordinate geometry of the fracture trace network of the 2D trace images, is used to calculate these properties. Fracture density is defined as the number of fractures per unit area and is calculated as $m/2\pi r^2$, where m is the number of fractures terminating within the circle of radius r and fracture intensity is defined as the total length of cracks in a given area and calculated as $n/4r$, where n is the number of fractures intersecting the perimeter of the circle (Figure 2.47c). A 2D grid of commensurate, evenly spaced, circular scan windows which fits within the trace image area is generated by FracPaQ and the intersections (n) and terminations (m) of the fracture segments within these circles are calculated (Figure 2.47d). The centre of each circle is then assigned a computed value of intensity/density and this grid of values is contoured using the standard MATLAB triangulation function to produce the maps of estimated fracture density (Figure 2.47e) and estimated fracture intensity (Figure 2.47f).

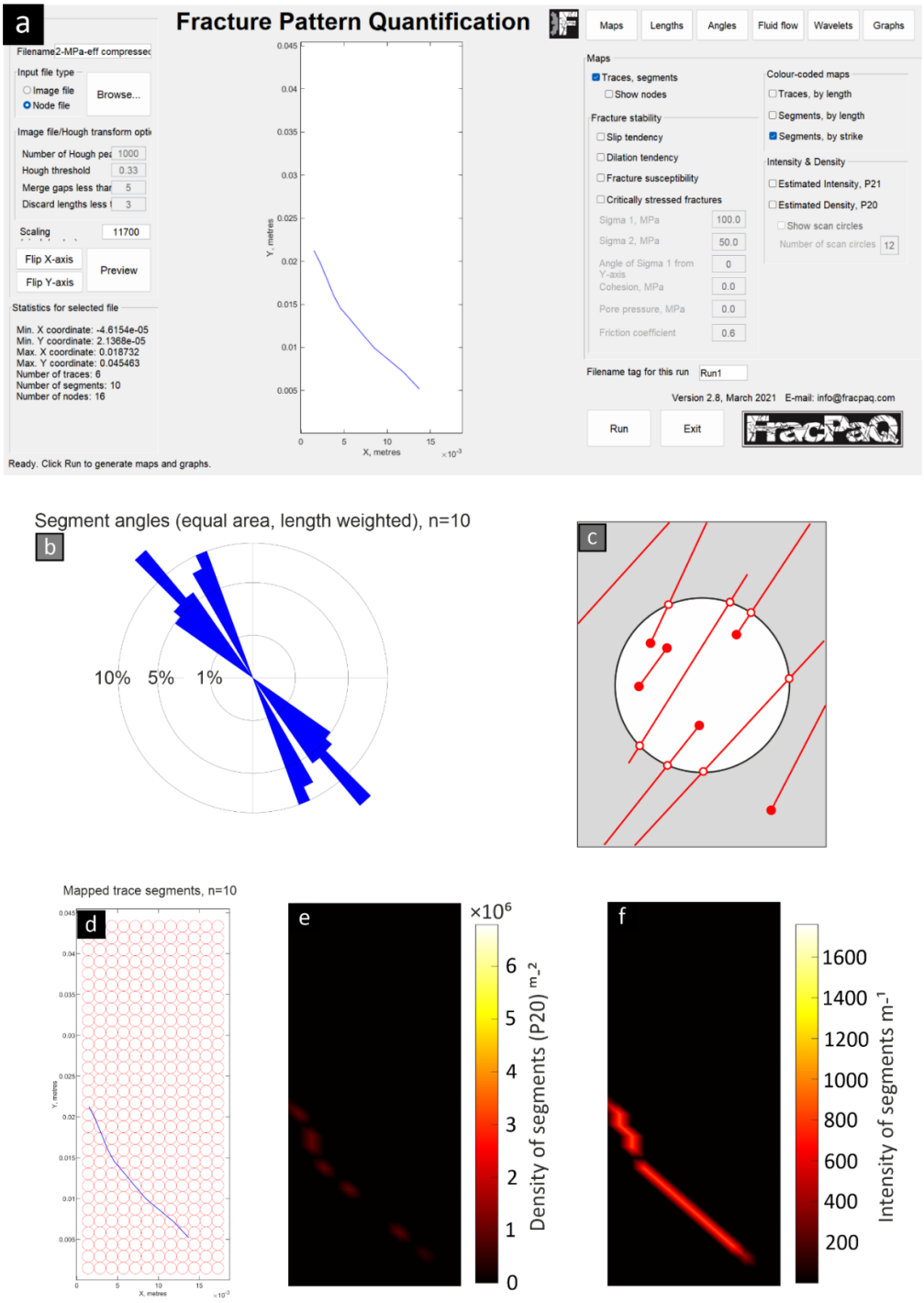

Figure 2.47. *a) FracPaQ GUI. b) Rose plots of strain localisation trace orientations. c) Circular scanline with n trace intersections (white dots, n=7) and circular window (white) with m trace endpoints (red dots, m=5), adapted from Mauldon et al. (2001). d) Visualisation of the circles used to fit within the fracture trace map. Colourmaps of localisation trace density (e), and localisation trace intensity (f).*

3 The manufacture, mechanical properties, and microstructural analysis of synthetic quartz-cemented sandstones

Abstract

A key issue in the field of porous rock geomechanics is finding suitable suites of samples in which petrophysical characteristics systematically vary, in order to determine the controlling factors on the mechanical behaviour. To resolve this problem a new methodology has been developed, whereby high-porosity synthetic sandstone samples are produced from initially incohesive sand, by using the chemical reaction between sodium silicate and hydrochloric acid to generate amorphous quartz cement and thus, provide cohesion. This enables the production of sandstone samples for laboratory testing which have reproducible petrophysical properties that can be systematically controlled, including porosity, grain size, cement content, grain shape and grain size distribution. Here, poorly-sorted, high-porosity (36–38%) sandstones are produced and subjected to a range of geomechanical tests, including uniaxial and triaxial experiments, to see if their microstructure and mechanical response is similar to equivalent natural samples. The 36-38% porosity synthetic sandstones have realistic and reproducible uniaxial compressive and tensile strengths of 5.18 (± 0.76) MPa and 0.167 (± 0.117) MPa respectively, as well as hydrostatic yield strengths (P^*) of 67–69 MPa. They also exhibit yield curves with a comparable geometry to natural sandstones of similar porosity and grain size and display elastic moduli within the expected range for natural sandstones. The methodology outlined in this contribution allows for the production of sandstones for laboratory testing with reproducible behaviour, that can be utilised in future studies to systematically investigate how different petrophysical properties control the mechanical response of sandstone to elastic and inelastic deformation.

3.1 Introduction

Sandstones are abundant and important lithological formations, as their porous structure allows them to form groundwater and hydrocarbon reservoirs, whilst also being potential repositories for waste products such as carbon dioxide. Consequently, their mechanical and physical properties must be carefully assessed prior to production of, or injection into, the reservoir unit (Allen et al., 2020; Hangx et al., 2013). However, a key issue in experimental rock physics and geomechanics is that for natural sandstones it is difficult to systematically analyse the effect of one lithological variable, such as grain size, porosity, or grain shape, on the mechanical and physical properties, whilst controlling all other variables. Consequently, an element of uncertainty is introduced in the data produced from natural sandstones, as it may be difficult to discern whether a response is solely a result of the lithological variable being investigated or a result of slight variations in the other rock properties. This ultimately has implications when validating experimental results against theoretical models and numerical simulations (Chen et al., 2018; Fjar et al., 2008; Kong et al., 2019; Li et al., 2016). The primary depositional and diagenetic processes during the formation of natural sandstones often produce significant variability, such as changes in porosity and grain size over relatively small spatial scales, which may not be initially obvious when extracting specimens from the field. This issue may be further compounded by the destructive nature of many experiments and the need to use multiple samples to characterise fully their mechanical properties (Osinga et al., 2015).

Over the past few decades, researchers have attempted to address the problems outlined above by using various methods to produce artificial rocks with similar mechanical, acoustic and petrophysical properties to natural sandstones (Kong et al., 2019). These include sintering of both natural sand grains and artificial beads (Carbillet et al., 2021; Costa et al., 2017; Herring et al., 2013; Wadsworth et al., 2016), the use of artificial cement (Acar & El-Tahir, 1986; Conde-Vázquez et al., 2019; David et al., 1998; Huang & Airey, 1998), and more recently, through 3D printing (Gomez et al., 2019; Ishutov et al., 2015; Kong et al., 2019; Osinga et al.,

2015). However, there are drawbacks with each of these methodologies. Sintering quartz sandstone between 400–600°C has been shown to result in an α-β-phase change, resulting in the microstructural deterioration of the rock (Glover et al., 1995; Lintao et al., 2017; Shen et al., 2018), while the artificial cements often used, such as resins, are not chemically similar to those precipitated in natural reservoirs (Ass' ad et al., 1992; Rathore et al., 1995). 3D printing of artificial rocks is a promising new technology. However, it is expensive and relatively few studies have yet applied the methodology to replicate successfully the petrophysical, geomechanical and geophysical properties of natural sandstones simultaneously (Gomez et al., 2019; Ishutov et al., 2015; Perras & Vogler, 2019).

In this study, we demonstrate a new, simple, low-cost methodology for producing synthetic quartz-cemented porous sandstones, by utilising the chemical reaction between sodium silicate and hydrochloric acid. Uniaxial compressive strength (UCS), splitting tensile (Brazilian) and hydrostatic and triaxial tests were performed in order to obtain the mechanical and elastic properties of the synthetic sandstones for comparison with natural equivalents, whilst scanning electron microscopy was undertaken to enable quantitative analysis of their microstructure. These sandstones have petrological, geomechanical and geophysical properties similar to natural, high-porosity reservoir sandstones, as outlined below. This technique allows for consistent production of sandstone cores with reproducible properties, minimising sample variability and enabling the production of sample sets where a particular property can be systematically investigated.

3.2 Materials and Methods

3.2.1 Reaction stoichiometry

In order to produce synthetic sandstone, initially unconsolidated grains of sand were cemented together by precipitating amorphous quartz via the neutralisation reaction between aqueous sodium silicate solution (water glass) and hydrochloric acid:

$$Na_2SiO_3 + 2HCl \rightarrow SiO_2 + 2NaCl + H_2O \quad (3.1)$$

The commercial sodium silicate solution used here had a chemical composition of 40% Na_2SiO_3 and 60% H_2O, with a density of 1.5 g/cm^3 and a pH of 11.2. The hydrochloric acid used was 37% concentration, with a density of 1.18 g/cm^3. The addition of the hydrochloric acid to the sodium silicate solution produced silicic acid, before subsequent polymerisation of the silanol groups to siloxane bonds and the settling of precipitated silica (Eneng & Rifki, 2018; Wilhelm & Kind, 2015). The formation of silica gel was avoided by vigorously mixing the solution and placing it at elevated temperature (200°C) (Wilhelm & Kind, 2015). The mass of quartz cement precipitated can be controlled by varying the quantity of reactants. In this study, 15 g (10 ml) of sodium silicate solution was reacted with 3.6 g (3.04 ml) of concentrated HCl in a balanced reaction, to produce a maximum theoretical yield of 2.95 g of SiO_2, along with 5.75 g NaCl and 0.89 g of water. Since the sodium silicate solution contained 60% water; the total mass of water released from the reaction was 9.89 g.

3.2.2 Synthetic sandstone methodology

The principal benefit of this methodology is that the petrophysical properties of the sandstone can be controlled, by varying parameters such as mineralogy, grain size, grain size distribution, grain shape, porosity and cement content. In this study, to test the applicability of this new methodology we used a natural, sub-angular, sand comprising 90% quartz, 5% plagioclase and 5% K-feldspar, measured using X-ray powder diffraction (XRD). Alternatively, glass beads could be used as opposed to quartz grains if pure silica or perfectly spherical grains are required. The grain size distribution was controlled by sieving the sand into different grain size fractions before mixing these size fractions together to obtain a known grain size distribution. These pre-lithified samples each had a mean grain size of 339 (± 145.4) µm, quantified using laser diffraction particle size analysis with a Beckman Coulter LS 13 320.

To produce a single sample for laboratory testing, 40 g of sand was placed in a plastic beaker before 15 g (10 ml) of sodium silicate solution was added at room temperature (Figure 3.1a, b). The mixture was stirred for one minute to ensure that all the sand grains were evenly coated. Then, 3.6 g (3.04 ml) of 37% hydrochloric acid was added (Figure 3.1c), with the

mixture immediately becoming more viscous due to the formation of silica gel (Figure 3.1d) as silica crystals started to precipitate (Wilhelm & Kind, 2015). The solution was vigorously mixed for one minute, in order to coat the grains evenly and prohibit the formation of gel by fragmenting the silica chains (Wilhelm & Kind, 2015).

In order to produce cylindrical samples (~50 mm length × 20 mm diameter) for mechanical testing, 40 g of the mixture was transferred into a mould (Figure 3.1e). This consisted of two copper tubes, with length and internal diameter dimensions of 91 × 20.2 mm and 91 × 19.9 mm respectively, both with a wall thickness of 0.3 mm. The tubes were both cut down their long axis to ensure the samples could be removed easily after they had been produced. This double tube arrangement was used in order to control the sample diameter, as well as for minimising any external contamination of the sample from the grease used in the outer steel jacket (see below for details). The copper tubes were then placed within a thick-walled steel tube 65.75 mm long, with an internal diameter of 20.5 mm, and a 3.05 mm wall thickness, to ensure the copper tubes did not bulge during consolidation (Figure 3.1f). The inside of the steel tube was lined with a small amount of grease to allow the copper tubes to be removed easily once the sample had been made. Once the mould was ready, an aluminium end piece 40 mm long and with the same diameter of the inner copper tube (19.9 mm), was inserted at one end before the mixture was added at the other. During filling of the mould, air pockets were removed by agitating the mixture with a glass stirring rod. The solution was then gently compacted with a thicker steel stirring rod as the mould was filled. Once the mould was filled with the sample, a second aluminium end piece was inserted and the two end pieces were then lightly pressed together by hand, slightly compacting the mixture, before placing the apparatus in an oven at 200°C for 10 minutes. This time allowed for the majority of the water from the reaction to evaporate away, resulting in a gel-like solution which could then be compressed around grains to form a cement, without significant loss of SiO_2 in the excess water. The mould was then removed from the oven and placed in a G-clamp, with this being carefully tightened by hand to ensure that the aluminium end pieces remained square within the copper tube (Figure

3.1g). Alternatively, a hydraulic press could be used. The degree to which the clamp is tightened depends upon the porosity to be obtained. For the majority of these tests, the clamp was tightened until the mould was ~141 mm long (i.e., the total length of the sample plus the two end pieces), equivalent to a compressional stress of 2.41 MPa, calculated using a load cell on a hydraulic press. This produced a nominal sample length of 61 mm, with a porosity of 36–38%. However, two lower porosity (33.5% and 29.4%) samples were also produced by compressing the clamp further to lengths of ~139 mm and ~136 mm respectively, equivalent to higher compressional stresses of 3.96 MPa and 6.37 MPa. The clamped mould was then placed in the oven at 200°C for a further hour, until the solution had dried completely and all the silica and sodium chloride had precipitated. Once the mould was taken out from the oven it was left to cool before the G-clamp was removed. The copper tubes were then pushed out from inside the steel jacket, before being carefully peeled open along their cut axis to extract the sample from inside.

Upon removal from the mould, the high-porosity cylindrical sandstone samples had a porosity of approximately 32%. This was due to the precipitation of NaCl salt during the reaction (Equation 3.1). To increase the porosity to 36–38%, the salt was dissolved by continuously flushing the sample with cold water for 15 hours. This duration was selected as no salt was observed via XRD in samples flushed beyond this length of time. The sample was inserted into a PVC jacket which was then sealed onto a tap (Figure 3.1h) and water was flowed through at a rate where it trickled out the bottom but was not fast enough to force the sample out of the jacket. The unidirectional flow ensured that water, saturated with NaCl, did not sit in the pore space and subsequently re-precipitate the NaCl. After the salt was dissolved completely the sample was removed from the PVC jacket and dried in an oven at 80°C (Figure 3.1i). The sample was then cut down to 50 mm length using a diamond saw and the ends were squared to a tolerance of ± 0.01 mm using emery paper (grit size 100) and a V-block (Figure 3.1j). The porosity of each core plug was then measured using a He-pycnometer. The measured porosities were all between 36-38% for the samples compressed to 141 mm, whilst lower porosities of

33.5% and 29.4% were recorded for the samples compressed to 139 mm and 136 mm respectively.

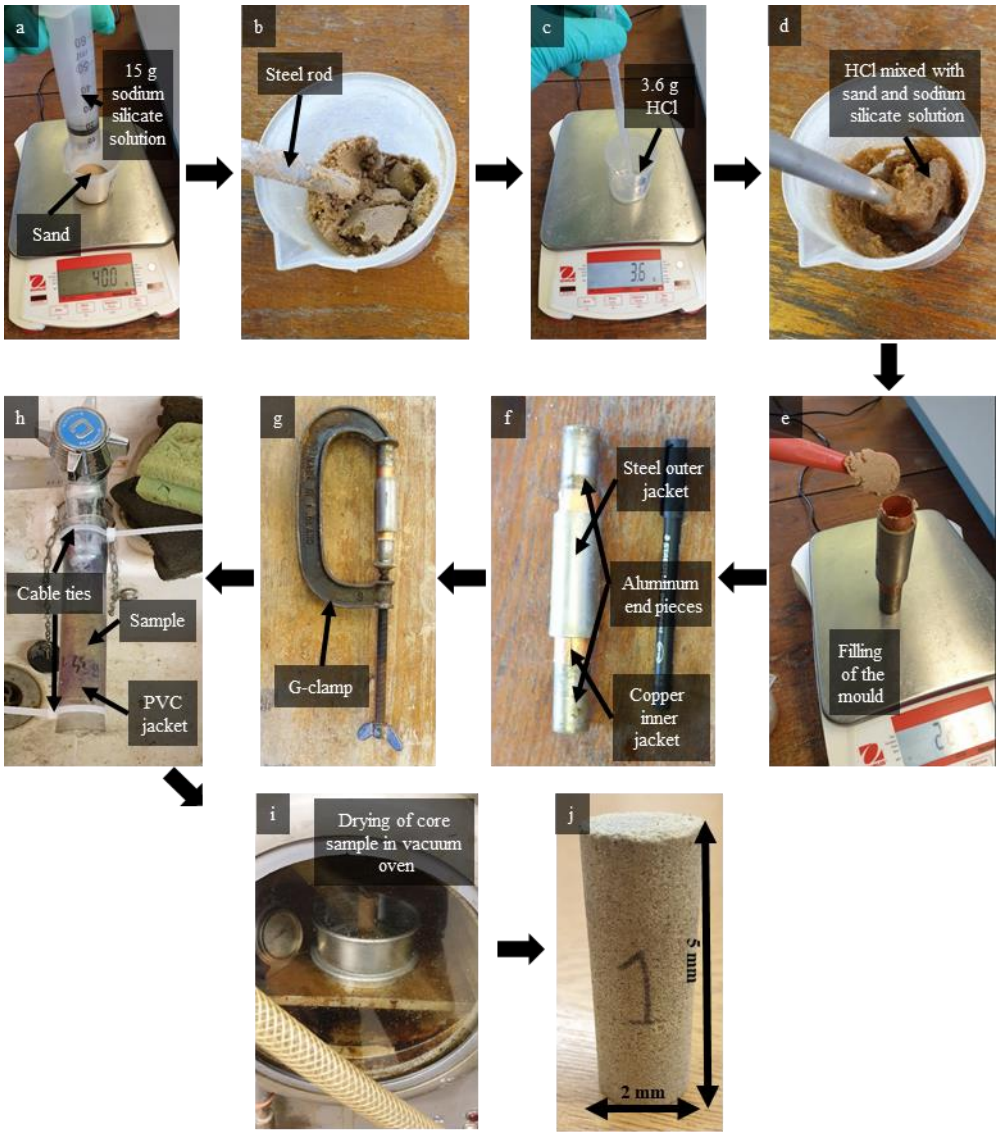

Figure 3.1. *Simplified workflow used to create the synthetic sandstone cores. See main text for description of the different steps in the production procedure.*

3.2.3 Microstructural analysis

In order to analyse any porosity, grain size or cement heterogeneity in the starting material, that may have resulted from the production process, one of the undeformed cores with ~37% porosity was impregnated with epoxy resin for microstructural analysis. The core was then cut in half, down its long axis and this surface was polished and carbon coated ready for imaging using the Hitachi TM3000 scanning electron microscope (SEM). Secondary electron microscopy was also performed on two undeformed cores, pre and post salt dissolution, to observe how the porosity increased and to identify the distribution and morphology of the amorphous quartz cement in relation to the pores and grains. These images were then compared to secondary electron images obtained for two similar-porosity natural sandstones, Boise and Idaho Gray.

3.2.3.1 Microstructural quantification and representative elementary area (REA) analysis

A total of 54 backscatter electron (BSE) images were collected using the SEM (9 columns, 6 rows) at 40× magnification, with these images stitched together using GigaPan Stitch software to produce a whole core image. This was uploaded into the image analysis program Fiji and binarised into white porosity and black grains so that detailed image analysis could be performed (Schindelin et al., 2012). To enable the program to differentiate between separate grains, the watershed algorithm was applied (Rabbani et al., 2016). A macro was then run which implemented a square sliding sampling window with a pixel area of 96100 and a 25% overlap across the image from left to right and top to bottom. At each window position, the porosity value (Z), and XY coordinates for the centre of the sliding window were obtained. The sampling window size was determined using the asymptotic approach of statistical REA (representative elementary area) analysis (Brown et al., 2000; Bruns et al., 2017; Dyskin & Pasternak, 2015; Koestel et al., 2020; Mu et al., 2016; Zhang et al., 2000), which is analogous to the 3D representative elementary volume (REV) defined by Bear (1972). Since the REA is defined as the minimum visual area over which microscale characteristics (i.e., porosity) remain constant (Kong et al., 2018; Saraji & Piri, 2015), the REA was calibrated using a computer-

generated ‘sandstone’ sample composed of randomly generated circles, with a similar porosity and grain size distribution to the synthetic sandstone, to ensure that any heterogeneities in the starting material of the synthetic sandstone were recorded. A constant value in a certain porous medium property, such as porosity, is encountered when the property area is between A_{min} and A_{max} (Figure 3.2). Below A_{min}, only small and spatially varied portions of the property are measured and the influence of individual pores means that the fluctuations are rapid. Areas above A_{max} may include other morphological structures, enabling the property to drift towards other values if the domain is heterogeneous. Sample areas sized between the region of A_{min} and A_{max} are expected to exhibit only minor fluctuations in the medium property, due to numerous pores being factored into the average (Bear, 1972; Brown et al., 2000).

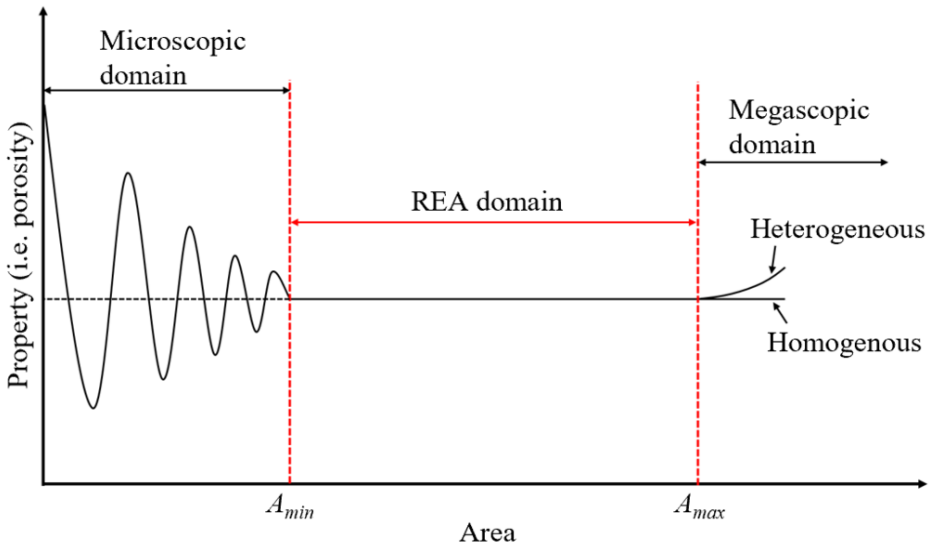

Figure 3.2. *Conceptualisation of the representative elementary area (REA), modified after Brown et al. (2000).*

In order to calculate the lower bound of the REA (A_{min}), and thus, the minimum square size that could be used for porosity analysis, the computer-generated image was initially overlain by a two-dimensional square grid, composed of 70 squares with edge lengths of 700 pixels (Figure 3.3a). The subsequent porosity sampling procedure used was one adapted from Brown et al. (2000) for 3D REV analysis, whereby they expanded a cube incrementally from fixed points inside the sampling area to generate a number of volume scales across different parts of the sample. In this study, the porosity in each grid square was calculated by analysing the percentage of black (grain) and white (porosity) pixels in each square. The square edge lengths were subsequently reduced by 10 pixels, with the centroid of each square remaining fixed and the porosity for each square again being obtained. This process was repeated at increments of 10 pixel edge lengths (PEL) until a final square edge length of 10 pixels was obtained (Figure 3.3b and 3.3c). This produced 70 REA curve realizations from 10-700 PEL for each of the 70 grid squares (Figure 3.3a).

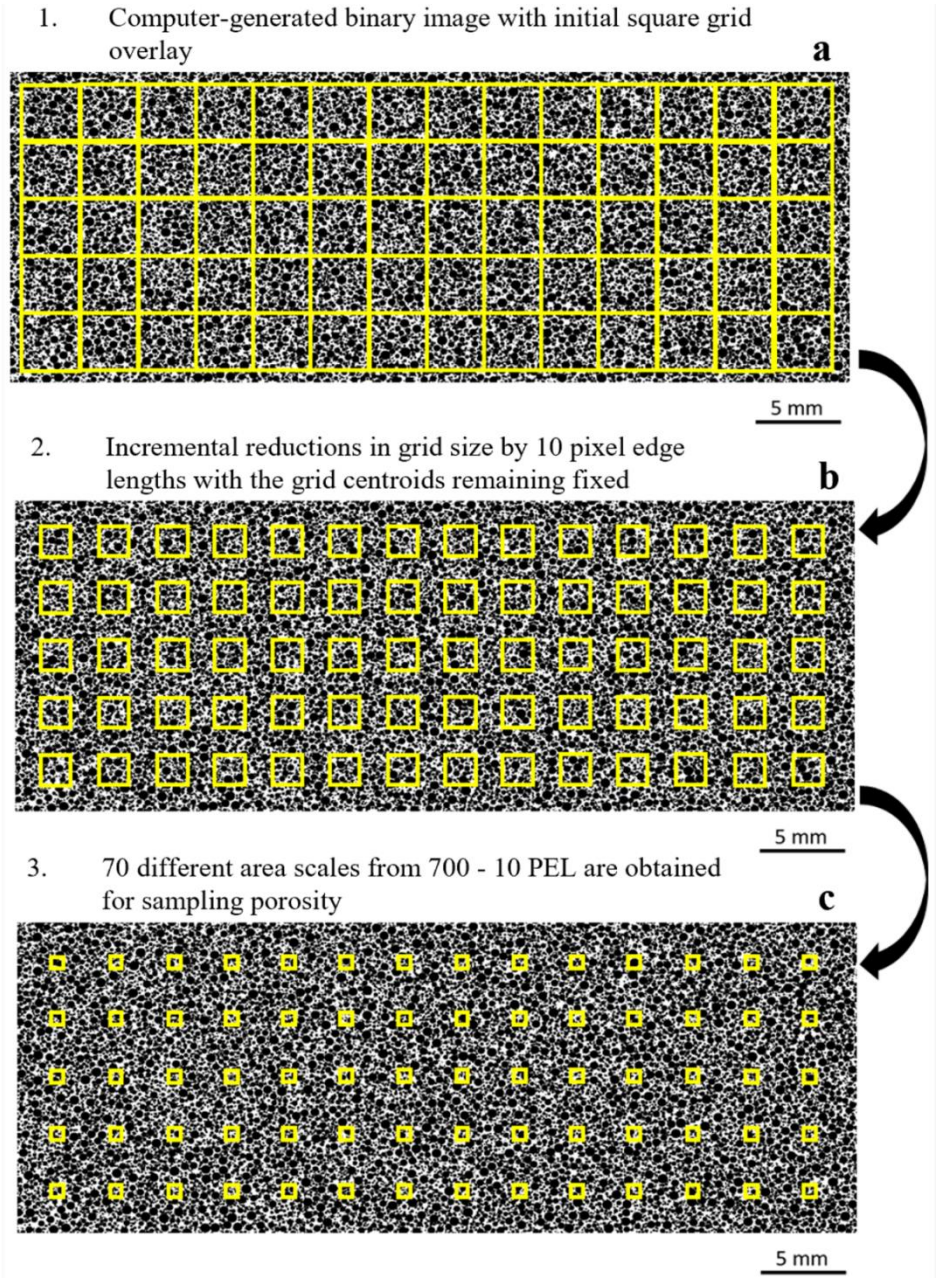

Figure 3.3. *Sampling technique used to find the minimum REA (A_{min}) square sampling size, calibrated using the computer-generated 'sandstone' image.*

A statistical methodology similar to that of Bruns et al. (2017), Koestel et al. (2020), Mu et al. (2016) and Zhang et al. (2000) was adopted to estimate A_{min}, whereby it was observed as being the point at which the mean of a certain physical property (in this case porosity) became approximately constant and the Coefficient of Variation (CV), defined as the ratio between the standard deviation and the mean, was less than a certain value. Mean and standard deviation values were calculated for each of the different area sizes with these values being used to calculate CV (Figure 3.4a). The REA for porosity was then estimated based on a threshold value of CV. In this study we adopted the CV threshold of 0.1 used by Mu et al. (2016) and Bruns et al. (2017). Mu et al. (2016) also suggested that a more relaxed CV threshold of 0.2 can be used, as has been done in other previous studies (Zhang et al., 2000). However, we settled on the lower threshold of 0.1, as we were more interested in observing any macro-scale porosity trends in the sample (Figure 3.4b). Based on the implemented CV threshold of 0.1, a square grid size of 310 PEL was identified as A_{min}, and thus, the smallest size that was representative of the local porosity, whilst also being small enough to provide suitable resolution of porosity variations (Figure 3.4b).

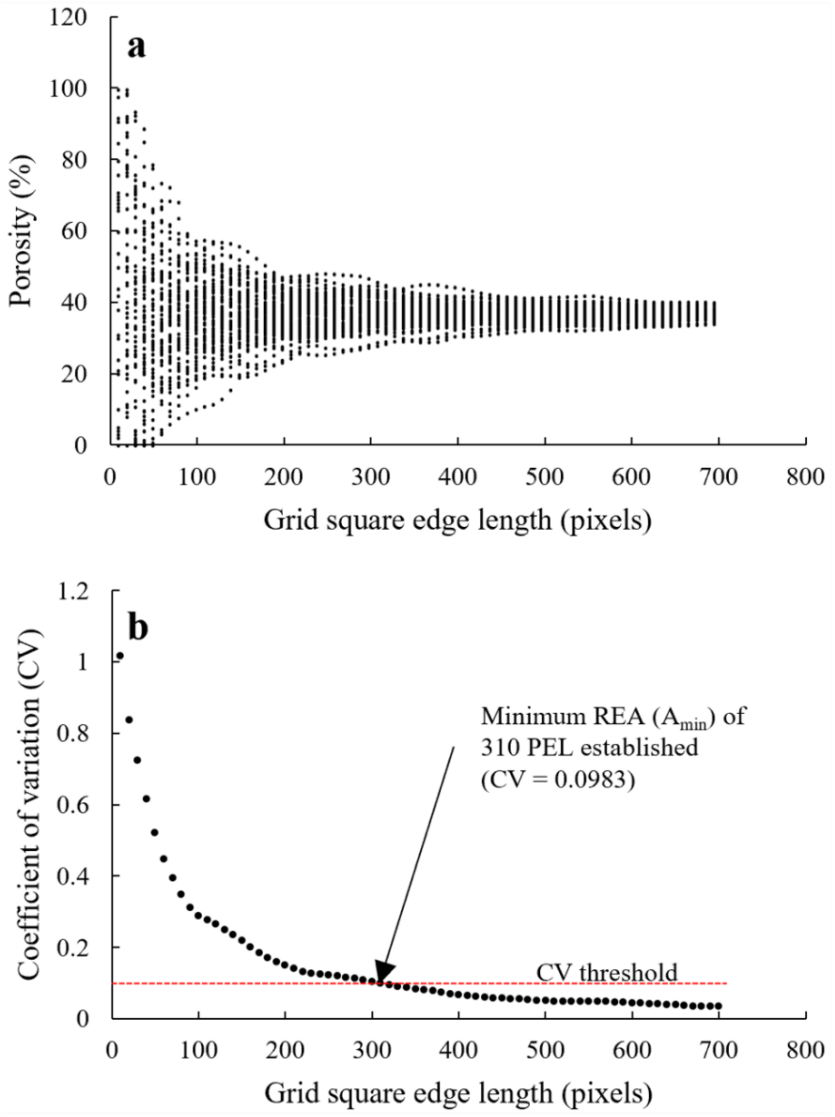

Figure 3.4. *a) Porosity values obtained from each of the 70 grid squares as a function of grid square length, from 10–700 PEL. b) CV values plotted against their respective grid square sizes. The CV threshold is denoted by the dashed red line, with a square size of 310 PEL being the cut-off value below the threshold and thus, the grid square size used to examine porosity variation across the sample.*

A moving sampling window rather than a static sampling grid was favoured due to the fact that the resolution is higher as each point is sampled multiple times (Brahme et al., 2012; Yang et al., 2016). Therefore, in the case of this study, small-scale porosity changes can be captured even when using a relatively large grid size, as specified by the REA analysis. The porosity values for each sliding window position were then uploaded into MATLAB as column vectors to produce a 3D scatterplot. A regular grid was defined using the meshgrid function, with the scattered data being interpolated over the grid to produce a porosity colourmap. The grain size variation across the sample was also analysed by defining each individual grain in the binary image as a region of interest (ROI). XY coordinates were then assigned to the centre of each grain, as was a value of *Z*, representing surface area in pixels of each ROI. Equivalent radius was used as the measure of grain size in this study, which is the radius of a circle with the same area as that of a measured binary grain (Heilbronner & Barrett, 2013). A colourmap showing the variation in grain size was then produced in the same way as for porosity.

3.2.3.2 Pore network coordination number

In order to determine the connectivity between the pores in these synthetic sandstones, the pore network coordination number (PNCN) was analysed. The PNCN represents the average number of pore bodies which are connected to a specific pore (Rabbani et al., 2016; Sahimi, 2011). This property was studied, as the precipitation characteristics of the amorphous quartz cement and any other potential heterogeneities resulting from the sample preparation methodology were not known, so it was important to ensure even pore connectivity throughout the sample. In order to observe the 2D PNCN variation, the binary synthetic sandstone image was divided into a grid of separate images, within the REA domain, of 5 rows and 14 columns, prior to the watershed algorithm being applied. Each image was then uploaded into MATLAB and run through a script developed by Rabbani et al. (2014a). Here the individual pores were segmented by the script, again using the watershed algorithm, however, in this case, boundaries between pores (pore throats) were identified, rather than the boundaries between grains. The number of individual pores connected to each specific pore could then be calculated. From the

2D PNCN, a prediction of the average 3D PNCN (μ_{3D}) was made using the empirical relationship devised by Rabbani et al. (2016) for sandstones

$$\mu_{3D} = 2.869\,\mu_{2D} + 0.279 \tag{3.2}$$

where μ_{2D} is the average of the 2D PNCN obtained from sample images.

3.2.4 UCS and splitting tensile tests

Six UCS and 10 splitting tensile tests were performed on the synthetic sandstone samples. For the UCS tests, four of these specimens were high-porosity sandstones (36-38%), while two lower porosity sandstones (33.5% and 29.4%) were also tested in order to investigate the evolution in mechanical and elastic properties with decreasing porosity. A natural sandstone (Idaho Gray) with a porosity of 34.1% was also tested to compare the synthetic sandstone mechanical and elastic properties against a natural equivalent. The specimens were loaded unconfined (σ_2=σ_3= 0) at a constant rate (strain rate ≈ 1.5×10^{-4} s^{-1}) between a fixed plate and hydraulic piston under ambient conditions. A Tedea-Huntleigh compression load cell (model 220, grade C4) measured the applied load, with the signal transmitted to the LabVIEW computer software via a National Instruments USB-6210 (analogue to digital convertor) device. The load cell has a maximum capacity of 294.3 kN and a resolution of ± 0.0075 kN. American Society for Testing and Materials (ASTM D3967-16 (ASTM, 2016)) standards were implemented for all tests. For the UCS tests, cylindrical cores, approximately 50 mm in length and 20 mm in diameter, were axially loaded at constant rate until failure, denoted by fracturing of the sample and a sudden force drop. To obtain data on the elastic properties of the synthetic sandstones, axial and radial strain gauges were attached to one of the high-porosity samples, as well as the two lower porosity samples and the natural Idaho Gray sample. Each strain gauge was wired in a 1/4 Wheatstone bridge configuration. The signals of the strain gauges are amplified using strain gauge transducer amplifiers (model RDP 628), with a 600 multi-channel signal conditioning system. The resolution of the strain gauges is ± 0.000001, with the amplified signals subsequently recorded by the computer.

For the splitting tensile tests, a Brazilian jig was used within the hydraulic press in accordance with ASTM D3967-16 (ASTM, 2016) standards. This consists of two mild steel blocks housing curved bearing platens (D2 steel, hardened to HRC 60), which reduce the contact stresses on the sample. A hemispherical seat houses a chrome ball in the top block, upon which sits a bearing block, with this configuration preventing asymmetric loading once the jig makes contact with the upper fixed plate of the uniaxial press. The specimens used in the Brazilian tests were discs with a diameter of 1.75 cm and length-to-diameter ratios of 0.5-0.6 in accordance with ASTM D3967-16 standards (ASTM, 2016). The following equation was used to calculate the splitting tensile strength of the synthetic sandstone samples:

$$\sigma_t = 1.272P/\pi LD \tag{3.3}$$

where σ_t is the splitting tensile strength (STS) in megapascals (MPa), P is the maximum force applied, indicated by the load cell in Newtons (N), L is the length of the specimen in millimetres (mm) and D is the diameter of the specimen in millimetres (mm).

3.2.5 Triaxial deformation experiments

3.2.5.1 Deformation apparatus

Triaxial tests were performed on the 36-38% porosity synthetic sandstone samples to determine their mechanical (yield curves) and elastic properties under confinement. The experimental apparatus used in these experiments was a high-pressure triaxial deformation rig designed and built at the University of Liverpool (Figure 3.5) (Mitchell & Faulkner, 2008). It is comprised of servo-controlled confining and pore pressure systems which can be measured to a resolution better than 0.01 MPa. The maximum working confining pressure of the rig is 250 MPa, with silicon oil used as the confining medium. Pore-fluid pressures of 200 MPa can be applied, with the servo-controlled pore-pressure pump also acting as a volumometer to monitor pore volume changes to a resolution better than 0.1 mm^3. Argon was used as the pore fluid in this study as it is chemically inert and so minimises the effects of any creep behaviour via sub-critical crack growth that may occur if using water as the pore fluid (Atkinson &

Meredith, 1981). The pore-fluid pressure was maintained at 20 MPa during all experiments in this study. Prior to insertion into the rig, each sample was inserted into an annealed copper jacket (20.2 mm internal diameter and 0.30 mm wall thickness) with two porous discs placed on either side of the sample. The sample and copper jacket were then inserted into a PVC jacket to prevent any leaks of the confining fluid into the sample, should the wall of the thin copper jacket perforate during deformation.

The axial load is generated by a servo-controlled electromechanical piston and is measured by an internal force gauge to a resolution better than 0.03 kN (Armitage et al., 2011). The axial displacement is measured by an LVDT attached to the base of the loading column. The axial strain that the sample experiences is calculated by subtracting the elastic deformation taken up by the loading column from the total axial displacement. The stiffness of the loading column is 119 kN/mm.

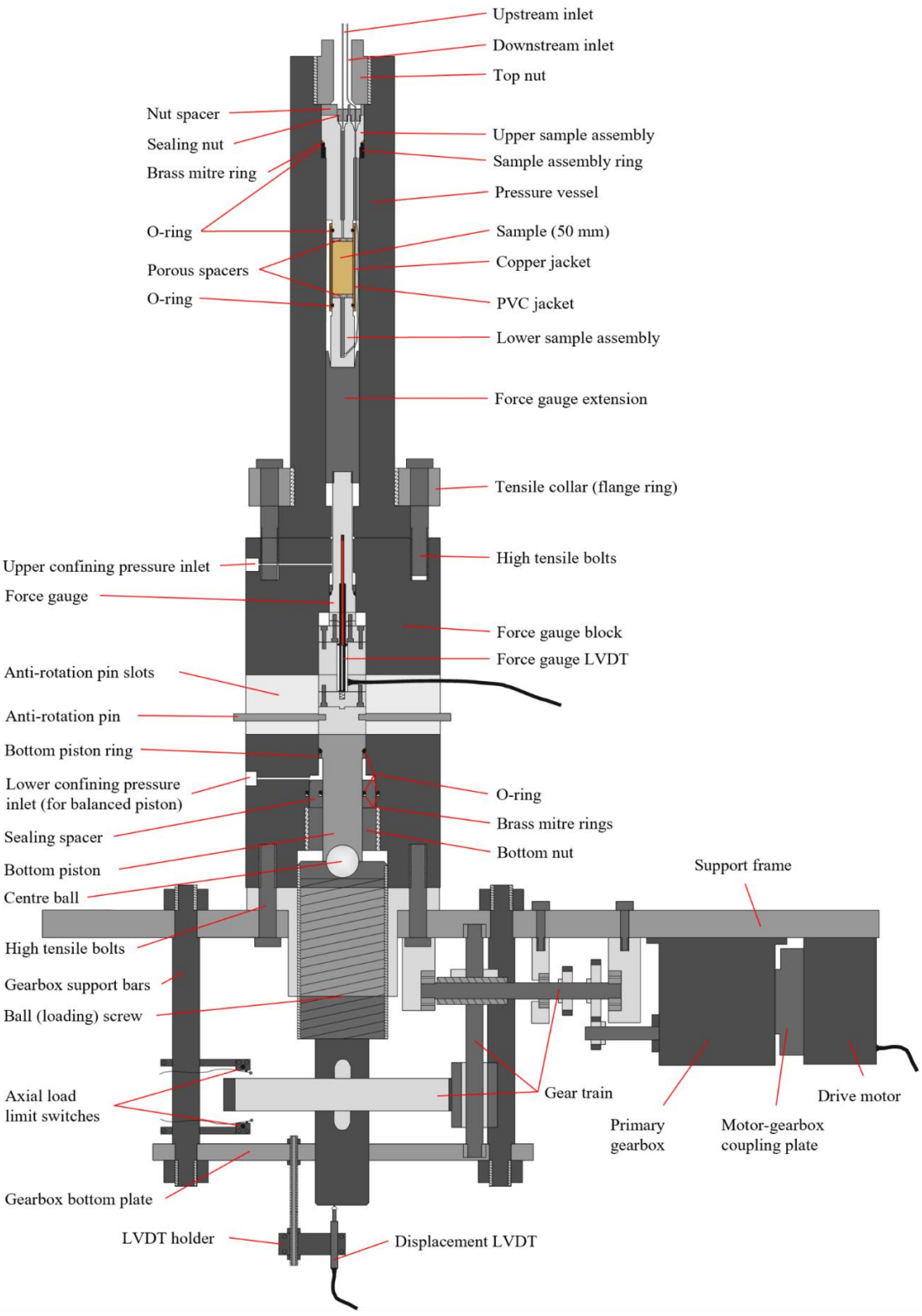

Figure 3.5. *Schematic drawing of the triaxial deformation apparatus used in this study. After Mitchell & Faulkner (2008).*

3.2.5.2 Triaxial experiments

Experiments were designed in order to determine the hydrostatic yield point (*P**) of the synthetic sandstones and also to map their yield curves in *P*-*Q* space, where *P* is the effective mean stress ($P = \left(\frac{\sigma_1+\sigma_2+\sigma_3}{3}\right) - P_f$), P_f is the pore-fluid pressure and *Q* is the differential stress ($Q = \sigma_1 - \sigma_3$). To determine *P** three samples were hydrostatically loaded by incrementally increasing the confining pressure while monitoring the change in pore volume as the pore-fluid pressure was held constant at 20 MPa. *P** is identified by a deviation from quasi-linear elastic pore volume reduction as the confining pressure is increased. The yield curve of the synthetic sandstone was mapped using two different techniques. Firstly, the yield curve was determined using the 'traditional' methodology whereby a suite of different samples are axially loaded under different effective mean stresses (e.g. Wong et al. (1997)). For this methodology seven samples were used to construct the yield curve, each loaded at a different effective mean stress between 10-65 MPa. Yield was identified by deviation from quasi-linear elastic loading, with each sample taken to 5% axial strain at a displacement rate of 1 μm/s. Secondly, yield curves were also constructed using the stress-probing methodology of Bedford et al. (2018), whereby a high-resolution curve is mapped using a single sample. This involves increasing the confining pressure until *P** is reached, before incrementally reducing the confining pressure (in 7 MPa increments) and axially loading the sample to probe the yield curve between each incremental reduction in pressure. For each probing increment the samples were axially loaded at a rate of 1 μm/s until yield occurred, with this again being identified by the deviation from quasi-linear elastic loading, before the axial load is immediately removed (at a rate of 5 μm/s) to ensure no permanent inelastic damage was imparted onto the sample. The confining pressure was then reduced further, and the stress-probing procedure repeated, to map the rest of the yield curve. This probing technique has been shown by Bedford et al. (2018, 2019) to cause minimal inelastic damage to the specimen, enabling the yield curve to be probed several times over a range of effective pressures.

3.3 Results

3.3.1 Microstructure of the starting materials

3.3.1.1 Porosity, grain size and pore network distribution

The porosity distribution of a ~37% porosity undeformed sample was examined to test whether the preparation of the specimen resulted in any migration of smaller grains to the centre of the specimen or whether compaction preferentially affects the ends or the edges of the samples. Figures 3.6a-c show no evidence for grain or porosity heterogeneity across the undeformed synthetic sandstone samples, post salt dissolution. It is also evident that compression of the samples during the preparation process did not result in the fracturing of any grains, suggesting that the compressive stress of 2.41 MPa applied to produce the 36-38% porosity samples was not enough to result in grain crushing. The mean 2D and 3D pore coordination values are 1.63 (± 0.1) and 4.96 respectively, with no significant change in pore connectivity across the sample, further supporting the even distribution of grains and cement across the synthetic sandstones.

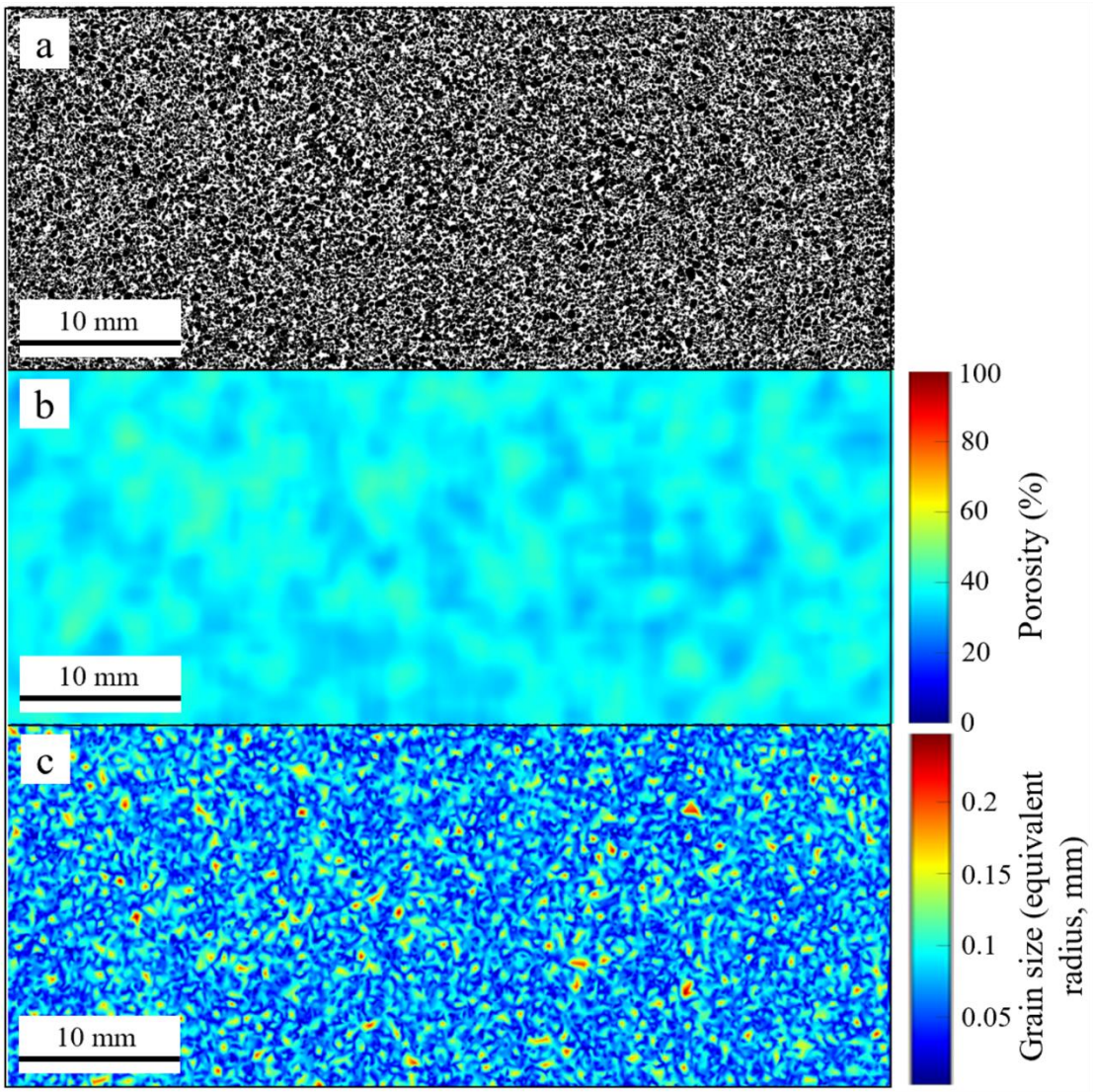

Figure 3.6. *a) Binary SEM image, b) porosity map and c) grain size map of a non-deformed synthetic sandstone sample. No obvious porosity or grain size heterogeneity is observed in the sample.*

3.3.1.2 Amorphous quartz cement

The secondary electron SEM micrographs show that prior to dissolution with water, the precipitated halite crystals fill much of the pore space in the synthetic samples (Figure 3.7a). After dissolution, no halite crystals are visible, significantly increasing the porosity (Figures 3.7b-d). The precipitated amorphous quartz is present coating the grains, as well as appearing between grains. It exhibits possible desiccation cracking in places, although it is not clear whether these cracks are superficial or cut through the cement. However, it still consolidates the grains in these areas (Figure 3.7d). Comparison of the synthetic sample with two natural microcrystalline quartz-cemented sandstones (Boise and Idaho Gray) highlights the difference between the two quartz-cement types (Figure 3.7e and f). Where the natural quartz cement exhibits euhedral, well-defined quartz crystals, the synthetic quartz cement has no identifiable structure and in places appears to coat whole grains.

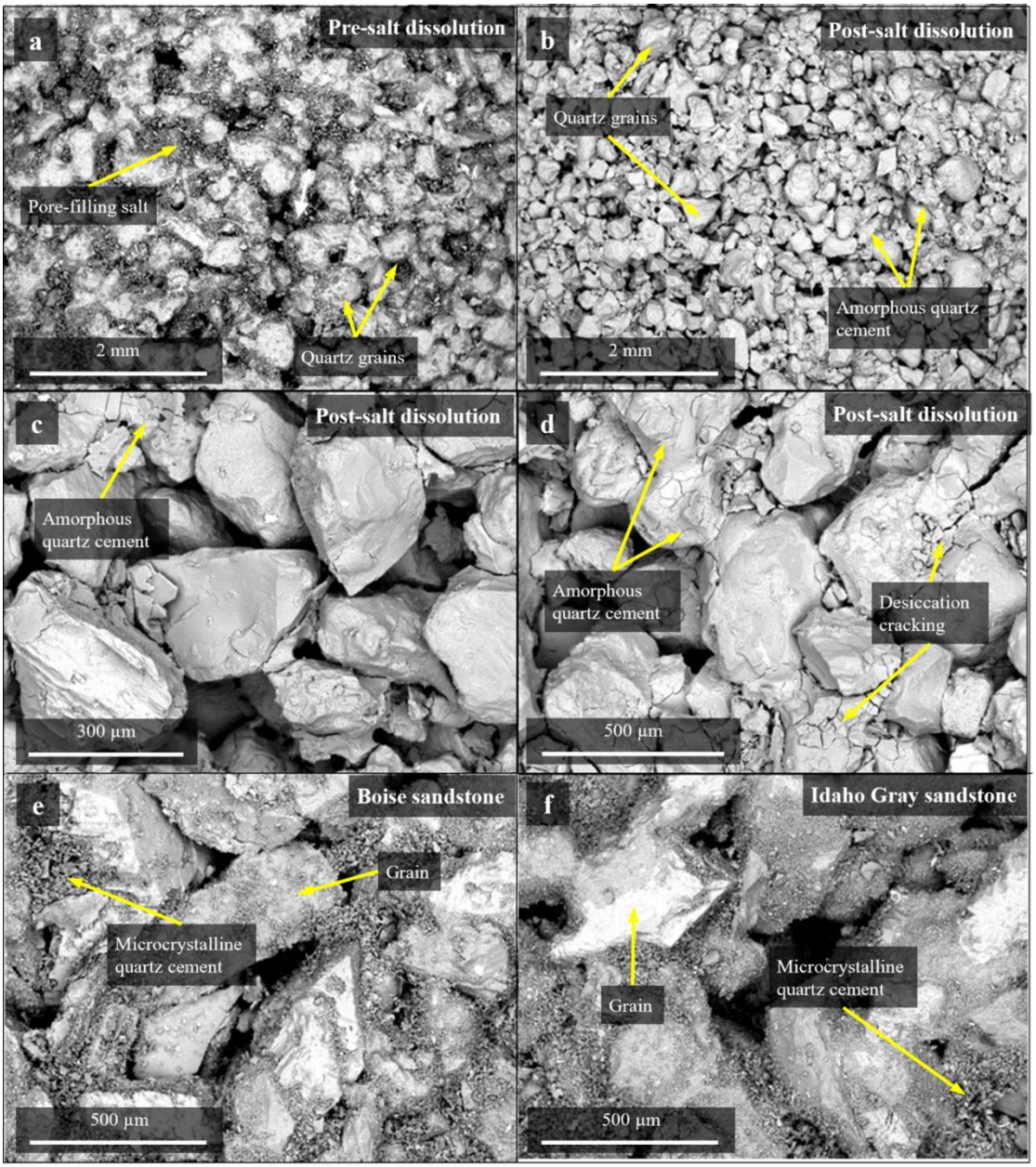

Figure 3.7. *Secondary electron images of synthetic and natural sandstones: a) A synthetic sample containing pore-filling halite crystals, prior to their dissolution with water. b) The same synthetic sample after halite dissolution, resulting in an increase in pore space. c) and d) Increased magnification images of the synthetic sample showing the amorphous quartz cement between the grains. e) and f) Samples of natural Boise and Idaho Gray sandstones respectively, which both exhibit microcrystalline quartz cement present in the pore space and coating the grains.*

3.3.2 Mechanical properties

3.3.2.1 UCS and tensile strength results

The results of the five UCS tests and 10 Brazilian tests are displayed in Table 3.1 where they are compared to data from previous studies on natural sandstones. The average UCS for the high-porosity (36-38%) synthetic sandstones is 5.18 (± 0.76) MPa, while the average tensile strength is 0.167 (± 0.117) MPa. The lower porosity (33.5% and 29.4%) synthetic sandstones recorded UCS values of 12.0 MPa and 24.7 MPa respectively. We also tested a natural Idaho Gray Sandstone sample (34.1% porosity) and found it has a UCS value of 13.1 MPa, comparable to that of the 33.5% porosity synthetic sandstone. UCS and tensile strengths of other high-porosity natural samples (Table 3.1) are similar to those obtained in this study suggesting that the synthetic sandstones show mechanically similar behaviour to natural sandstones when subjected to compressive and tensile stress. When plotted against porosity, the UCS data exhibit a non-linear trend of decreasing UCS with increasing porosity (Figure 3.8), which the synthetic sandstones with varying porosity also fit.

Table 3.1. *UCS_{dry} and tensile strength values for the synthetic sandstone samples tested in this study, as well as for a variety of natural sandstones.*

Sandstone	Location	Study	Porosity (%)	UCS_{dry} (MPa)	Splitting tensile strength (MPa)
36-38% porosity synthetic sandstone of this study	Laboratory	This study	36-38%	5.18 (± 0.76)	0.167 (± 0.117)
33.5% porosity synthetic sandstone of this study	Laboratory	This study	33.5	12.0	
29.4% porosity synthetic sandstone of this study	Laboratory	This study	29.4	24.7	
Greensand A	UK	Shi et al. (2016)	38.6	10.57	
Donetsk	Ukraine	Palchik (1999)	36.16	13.61	
Jurassic 3	UK	Nicholson et al. (1998)	35.5	6.1	
Shwezaye	Myanmar	Bandyopadhyay & Abdullah (2013)	35	10.5	0.9
Idaho Gray	USA	This study	34.1	13.1	
Captain	North Sea	Allen et al. (2020)	32.5		0.16
Nottingham Castle Sandstone Formation (sandstone)	UK	Sattler & Paraskevopoulou (2019)	30.7	1.023	0.095 (± 0.036)
Boise	USA	Baud et al. (2014)	28.1	30.1	
Castlegate	USA	Nicholson et al. (1998)	28	5.7	0.37 –0.86
Mansfield	UK	Katsman et al. (2009)	27	19.3	1.1
Lenton Formation (sandstone)	UK	Bell et al. (2009)	26.9	14.7	0.85 (± 0.32)
Salt Wash South	USA	Nicholson et al. (1998)	26.75	4.7	
Diemelstadt	Germany	Baud et al. (2014)	25.5	34.2	
Adamswiller	France	Baud et al. (2014)	24.5	49.4	
Bleurswiller	France	Baud et al. (2014)	24	41	
Bentheim	Germany	Baud et al. (2014)	23.4	60.6	0.61
Rothbach	France	Baud et al. (2014)	22.5	26.7	
Berea	USA	Baud et al. (2014)	21.3	47.1	1.7
Bunter	UK	Yates (1992)	17.5	11.6	0.35–0.75
Fontainbleau 3	France	Baud et al. (2014)	16.2	48	
Greensand B	UK	Shi et al. (2016)	15.75	74.34	
Darley Dale	UK	Baud et al. (2014)	13.3	60	
Wertheim	Germany	Baud et al. (2014)	13.1	93.4	
Penrith (B)	UK	Shi et al. (2016)	12.39	35.83	
Thornhill	UK	Shi et al. (2016)	12.24	90	
Fontainbleau 2	France	Baud et al. (2014)	12.2	75.1	
Millstone Grit (D)	UK	Shi et al. (2016)	9.32	127.26	
Pennant C	UK	Shi et al. (2016)	8.37	106.45	
Pennant A	UK	Shi et al. (2016)	7.57	114.81	
Hibernean Greensands Group (sandstone)	UK	Shi et al. (2016)	7.05	108.67	
Pennant B	UK	Shi et al. (2016)	7.05	106.01	
Lower Old Red Sandstone Group (sandstone	UK	Shi et al. (2016)	6.83	165.98	
Crab Orchard	USA	Baud et al. (2014)	6.5	161.4	9.8
Penrith (C)	UK	Shi et al. (2016)	5.51	91.85	
Penrith (D)	UK	Shi et al. (2016)	4.7	122.2	
Fontainbleau 1	France	Baud et al. (2014)	4.2	122.3	

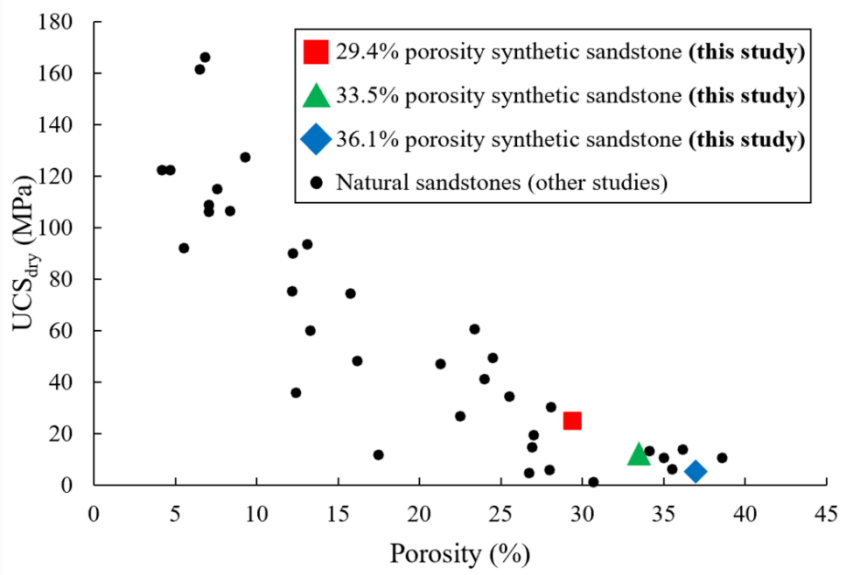

Figure 3.8. *Porosity plotted against UCS$_{dry}$ for the 29.4%, 33.5% and 36.1% porosity synthetic sandstones from this study, as well as for 35 natural sandstones from the studies listed in Table 3.1.*

3.3.2.2 Hydrostatic loading curves

The results of three hydrostatic loading tests on high-porosity (36-38%) synthetic sandstone samples are presented in Figure 3.9. The deflection in the curves from quasi-linear elastic loading marks the hydrostatic yield point (P^*) and the onset of inelastic deformation. The P^* values for the synthetic sandstones are realistic and compare well with values obtained from previous studies on natural sandstones (Table 3.2). Generally, for natural sandstones, P^* increases with decreasing porosity and grain size (Table 3.2). The smaller grain size of the synthetic sandstones is likely why they have slightly higher P^* values than similar porosity Boise and Idaho Gray sandstones. Samples S8 and S9 were not taken to higher effective mean stresses than P^* as they were used to map out the yield curve using the single sample methodology of Bedford et al. (2018) (see section 3.2.5.2), therefore we did not want to induce any inelastic deformation. Sample S10 was loaded beyond P^* to an effective mean stress of 130 MPa to map the inelastic part of the hydrostat, and the pore volume change was also

monitored during unloading of the sample. The unloading data confirm that the majority of deformation beyond *P** was inelastic as the porosity does not return to its initial value (approximately 6% porosity reduction). Similar hydrostatic loading/unloading curves were reported for Boise and Idaho Gray sandstones by Bedford et al. (2019).

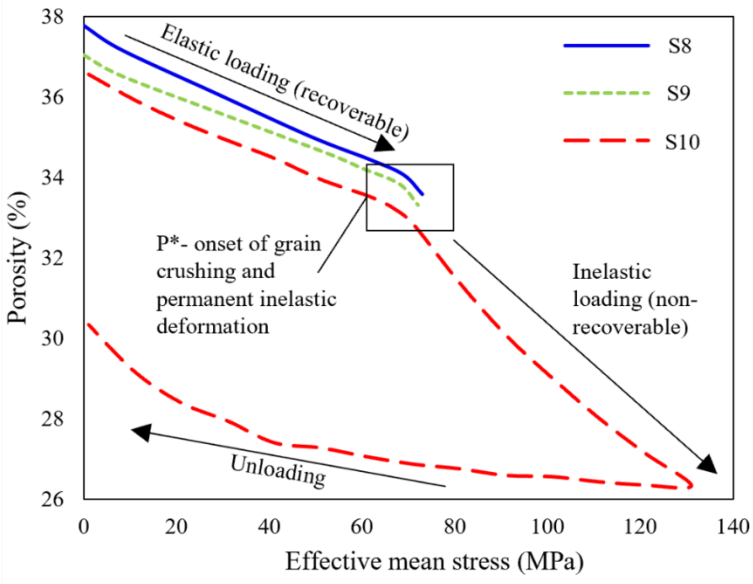

Figure 3.9. *Hydrostatic loading curves for three synthetic sandstone samples. The sharp deflection in the curve between 67 and 69 MPa marks the onset of inelastic deformation (P*), with each sample exhibiting a quasi-linear porosity decrease prior to the onset of P*. Samples S8 and S9 were not hydrostatically loaded beyond P*, however sample S10 was loaded to an effective mean stress of approximately 130 MPa to map out the hydrostat beyond P*.*

3.3.2.3 Elastic properties

Values for the Young's modulus (E), bulk modulus (K) and Poisson's ratio (ν) for the synthetic samples, as well as for some natural sandstones, are shown in Table 3.2. For samples (S8 and S9) used to construct yield curves via the stress-probing methodology (section 3.2.5.2), E was calculated from the axial loading data from a stress-probing increment at an effective mean stress equivalent to 85% of the sample's P^* value. Bulk moduli were obtained from the

linear elastic region of the hydrostatic loading curves (Figure 3.9). Values of *E* and *K* were also obtained from samples S11, S12, S13 and for Idaho Gray via the uniaxial strain gauge tests (Figure 3.10). For the high-porosity (36-38%) synthetic sandstones, the values of *E* obtained from the triaxial tests range from 3.58 to 5.63 GPa, while *K* ranges from 1.96 to 2.23 GPa. At low effective pressures, there is a trend of increasing *E* with increasing effective pressure, to 40 MPa, after which, no clear trend is evident. For comparison, the values of *E* for similar porosity natural Boise and Idaho Gray sandstones, obtained from triaxial testing, are 2.56-5.14 and 2.51-4.96 GPa respectively, with the same sandstones having respective *K* values of 1.74 and 2.42 GPa.

The *E* and *K* values obtained via the UCS strain gauge tests for the 36.1% porosity synthetic sandstone (sample S11) are 2.01 GPa and 1.26 GPa respectively, with a Poisson's ratio of 0.235. With decreasing porosity, the *E* and *K* values of the synthetic sandstones increase to 3.36 GPa and 1.93 GPa respectively, for a 33.5% porosity sample, and to 8.10 GPa and 4.36 GPa respectively, for a 29.4% porosity sample. The Poisson's ratios of the 33.5% and 29.4% porosity samples are 0.209 and 0.191 respectively. For comparison, a UCS strain gauge test was also performed on a natural sample of Idaho Gray Sandstone (34.1% porosity). The stress-strain curves are included in Figure 3.10 (grey curves) and show a close match to the stress-strain relationships for the similar 33.5% porosity synthetic sample. The elastic moduli of the Idaho Gray sample are also similar, with *E*, *K* and Poisson's ratio values of 3.28 GPa, 1.48 GPa and 0.130 respectively.

Table 3.2. *Petrological and petrophysical properties of triaxially deformed synthetic sandstones of this study. Also included for comparison are the properties of a range of natural sandstones with different porosities. Values for Young's modulus (E) Bulk modulus (K) and Poisson's ratio (v) are reported, as well as the effective pressures at which these were obtained.*

Sandstone sample	**Study**	**Mean grain diameter (mm)**	**Porosity (%)**	***P*** (Argon) (MPa)*	***P*** (H_2O) (MPa)*	***E*** **(GPa)**	**Effective pressure, *E* (MPa)**	***K*** **(GPa)**	**Effective pressure, *K* (MPa)**	***v***
S1	This study	0.339	37.6			3.58	10			
S2	This study	0.339	37.9			4.36	20			
S3	This study	0.339	37.7			4.73	30			
S4	This study	0.339	37.6			5.38	40			
S5	This study	0.339	38.3			5.28	50			
S6	This study	0.339	36.6			5.63	60			
S7	This study	0.339	37.9			5.03	65			
S8	This study	0.339	37.8	69		5.03	58.7	1.96	0-69	
S9	This study	0.339	37.0	68		5.11	57.8	2.23	0-68	
S10	This study	0.339	36.6	67				2.07	0-67	
S11	This study	0.339	36.1			2.01		1.26		0.235
S12	This study	0.339	33.5			3.36		1.92		0.209
S13	This study	0.339	29.4			8.10		4.36		0.191
Unconsolidated sand	Fjar et al. (2008)									~0.45
Hassi Messaoud Sandstone	Tiab & Donaldson (2015)									0.14-0.21
Boise	Bedford et al. (2019)	0.5 ± 0.3	37.6	37-48		2.56 5.14	5 40	1.74	5-40	
Idaho Gray	Bedford et al. (2019)	0.7 ± 0.2	36.2	54-59		2.51 4.96	5 40	2.42	5-40	
Idaho Gray	This study	0.7 ± 0.2	34.1			3.28		1.48		0.130
Boise	Jaeger et al. (2009)		26							0.15
Bentheim	Heap et al. (2010)	0.05-0.5	23.4 ± 1.2							~0.13
Adamswiller	Wong et al. (1997)	0.18	22.6		190	10.36 10.38 10.54	60 100 150	3.7	60-150	
Kayenta	Wong et al. (1997)	0.3	21.0		300	14.7 15.0	150 250	17.9	150-250	
Berea	Wong et al. (1997)	0.13	21		380	11.23 12.87	160 250	17.4	160-250	
Rothbach	Wong et al. (1997)	0.456	19.9		240	10.5 9.69 9.7 11.0	50 100 140 200	10.7	50-200	
Darley Dale	Wong et al. (1997)	0.334	14.5		360	8.84 13.45	100 200	24.5	100-200	
Darley Dale	Heap et al. (2010)	0.1-0.8	13.3 ± 0.8							~0.075
Weber	Jaeger et al. (2009)		6							0.15
Ruhr	Jaeger et al. (2009)		2							0.12

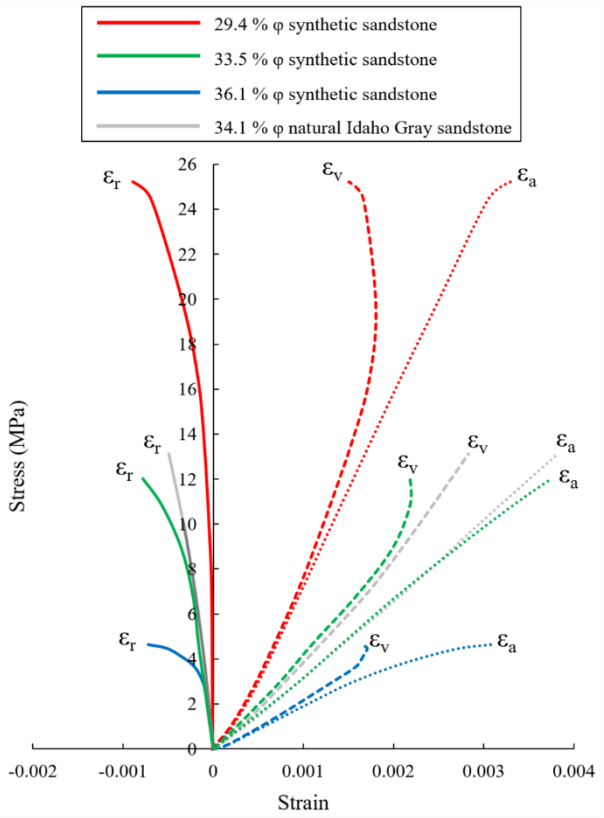

Figure 3.10. *Axial (ε_a), radial (ε_r) and volumetric (ε_v) stress-strain curves produced from the UCS strain gauge tests on the 29.4%, 33.5%, and 36.1% porosity synthetic sandstones as well as for the 34.1% porosity natural Idaho Gray Sandstone.*

3.3.2.4 Yield curves

The yield curve for the synthetic sandstone was constructed using two different methodologies. Firstly, the yield curve was mapped by axially loading multiple samples of synthetic sandstone from different starting effective mean stresses. The stress-strain curves for the seven synthetic sandstones used to construct the yield envelope via this methodology are shown in Figure 3.11a. The stress-strain curves all exhibit quasi-linear elastic loading before yield, which is identified by the inflection in the loading curve that occurs at axial strains of <1%. Once yield has been achieved all samples display strain-hardening behaviour.

The yield points are displayed in Figure 3.11b, alongside those mapped via the single-sample stress-probing methodology of Bedford et al. (2018). The yield curves constructed using the different methodologies are almost identical, with an approximately elliptical shape. On the compactive side of the yield curve, in the region close to P^*, the gradient becomes near-vertical, which was similarly reported by Bedford et al. (2018, 2019). To check the relative size of the yield curves relative to other sandstones, we compare those of the synthetic sandstones to the generalised parabolic envelope and elliptical cap for porous sandstone from Wong et al. (1997). To do this, the data are normalised by dividing each curve by its respective P^* value (Figure 3.11c). The majority of normalised data points for the synthetic sandstones sit between the bounds of the upper and lower elliptical caps proposed by Wong et al. (1997), although there are a few outliers in the region near P^*. The Q/P^* ratio at the peaks of the elliptical curves is between 0.53 and 0.55 for the synthetic sandstones.

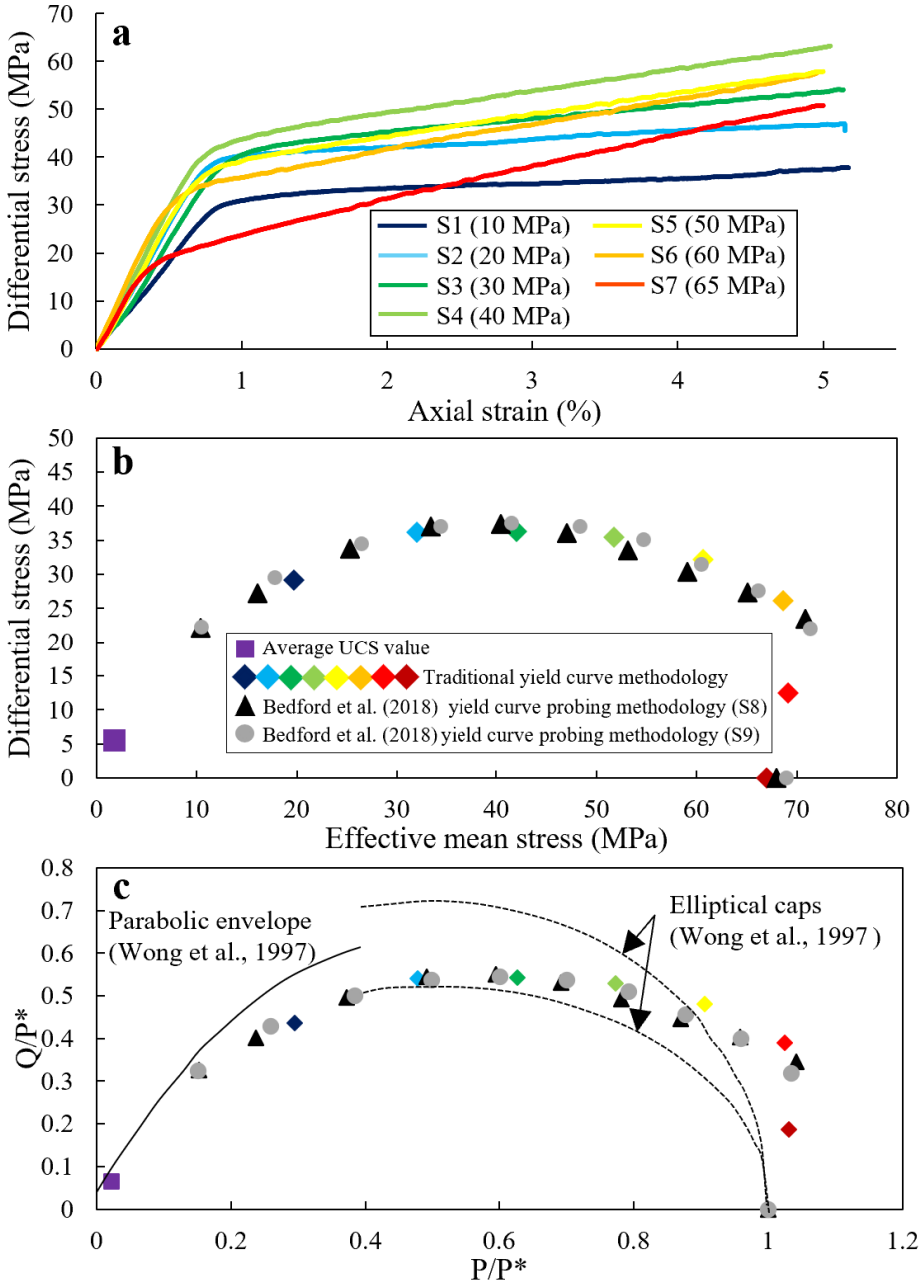

Figure 3.11. *a) Loading curves for the seven synthetic sandstone samples taken to 5% axial strain in order to construct the yield curve using the traditional methodology. The pressure values correspond to the effective pressure at which loading was initiated. b) Three yield curves for the synthetic sandstones, with one produced using the traditional methodology and two through the stress-probing methodology of Bedford et al. (2018). c) Normalised yield curves plotted alongside the parabolic envelope and elliptical yield caps of Wong et al. (1997).*

3.4 Discussion

3.4.1 The suitability of synthetic sandstone for geomechanical and petrophysical investigations

Since this work describes a new methodology of producing synthetic sandstones for geomechanical testing, it is first important to establish whether the physical properties are comparable to those of natural sandstones. Replicating all the properties of natural sandstones is complicated and previous methodologies for the production of synthetic samples have failed to satisfactorily achieve this, with samples often not possessing representative elastic or mechanical properties (Perras & Vogler, 2019; Primkulov et al., 2017). The porosity of most of the synthetic sandstones in this study is of a similar order to very high-porosity, poorly consolidated, reservoir sandstones found in nature (~36-38%). The porosity distribution of our samples appears to be fairly homogeneous (Figure 3.6b) with no significant stratification or heterogeneity in the distribution of the grain size or pore network caused by the production process (Figure 3.6c), suggesting that relatively homogenous samples are produced, making them suitable for mechanical testing. Two lower porosity (33.5% and 29.4%) samples were also produced successfully, showing that the production methodology we outlined in sections 3.2.1 and 3.2.2 can be used to replicate lower porosity sandstones. The average 2D and 3D pore coordination values recorded in this study are 1.63 and 4.96 respectively, similar to those obtained by Rabbani et al. (2016) (1.34 and 4.57 respectively) for natural sandstones with grains of similar shape and size. Furthermore, similar 3D pore coordination values were obtained by Gong et al. (2020), using X-ray computed tomography for samples of Bentheim (5.10), Berea (4.54), Boise (4.82) and Gildehauser (4.95) natural sandstones.

The cohesion of the synthetic sandstones is provided by an amorphous quartz cement which differs from natural cements that will be typically comprised of crystalline quartz or other mineral phases. The amorphous quartz cement produced in this study is similar to that produced by Tillotson et al. (2012) who used the reaction between sodium silicate and the acidic

compounds released from the breakdown of kaolinite at high temperatures. Although the methods are similar, pure amorphous quartz is only produced in the reaction of our study, with the salt and water both removed during the production process. More uncertainty regarding the sandstone composition is introduced when using the kaolinite thermal decomposition method, as excess aluminium-bearing compounds could be left over along with any excess kaolinite after production, potentially affecting the chemical and mechanical properties of the sandstone (Bergaya et al., 1996; Weldes & Lange, 1969). Our cement does display some surface cracking (Figure 3.7d) which is likely associated with desiccation as the samples are dried in the oven (Eneng & Rifki, 2018). The cracks are similar in shape to those observed in hardened cement paste, as well as natural cracks often seen in desiccated mud (Bisschop & Wittel, 2011; Groisman & Kaplan, 1994). However, it appears that these cracks are superficial and have minimal effect on the mechanical response of the sandstone. Evidence for this is in the strong linearity of the elastic part of hydrostatic loading curves (Figure 3.9). Typically, during hydrostatic loading of natural rocks, the initial part of the loading curve exhibits a non-linear porosity reduction relationship associated with the elastic closure of microcracks. For example, in the study of Bedford et al. (2019) both Boise and Idaho Gray sandstones, which are of a similar porosity (36–38%) to the synthetic sandstones used here, exhibit an initial non-linear porosity reduction of approximately 2%, as the hydrostatic pressure is increased from 0-10 MPa. By contrast, the porosity reduction for the synthetic sandstones over the same pressure range is only ~0.5% and displays a much weaker non-linearity (Figure 3.9). This suggests that the desiccation cracks in the amorphous cement do not have a strong influence on the mechanical behaviour of the synthetic sandstones and, in fact, natural sandstones probably possess more or larger natural microcracks and flaws, likely formed during diagenesis and exhumation, which result in the more significant non-linear porosity reduction observed at low pressures (e.g., Bedford et al. (2019)).

Despite there being differences in the initial mechanical response at low pressures (<10 MPa), the rest of the mechanical behaviour displayed by the synthetic sandstones is comparable

with natural equivalents. The UCS values of 5.18 (± 0.76) MPa, 12.0 MPa and 24.7 MPa, for the 36-38%, 33.5% and 29.5% porosity synthetic sandstones respectively, correlate well with values for natural sandstones with similar porosities (Figure 3.8). Furthermore, testing of natural Idaho Gray Sandstone with a similar porosity (34.1%) to the 33.5% porosity synthetic sample, yielded very similar UCS results of 13.1 MPa, indicating similar mechanical responses between the natural and synthetic samples. In contrast, Primkulov et al. (2017) recorded a UCS of 19.0 MPa (± 1.1) for 3D printed sandstone with ~41% porosity, which is significantly higher than would be expected for natural rocks with such porosity (Figure 3.8).

The hydrostatic yield point (P^*) of the synthetic sandstones is approximately 67-69 MPa (Figure 3.9), close to that of Idaho Gray (54-59 MPa), a similar porosity natural sandstone (Bedford et al., 2019). The slightly higher P^* values of the synthetic sandstone is likely caused by the lower mean grain size (Table 3.2), in agreement with Hertzian fracture mechanics (Zhang et al., 1990). In fact, using the Hertzian contact model of Zhang et al. (1990)

$$P^* \propto (R\phi)^{-3/2} \tag{3.4}$$

where R is grain radius (mm) and ϕ is fractional porosity, would predict that P^* should be about 62-65 MPa for the grain size and porosity of the synthetic sandstones produced in this study, in close agreement with our experimental measurements of P^*. The yield curves are also of a similar magnitude to natural sandstones, with the normalised curves (Figure 3.11b) falling between the upper the lower bounds of the elliptical yield cap model for sandstone proposed by Wong et al. (1997). Our results also add support to the use of the single-sample stress-probing methodology of Bedford et al. (2018) to construct yield curves, as the shape and magnitude of the curves produced using this technique are very similar to those obtained using the traditional methodology (e.g., Wong et al. (1997)) where multiple samples are used (Figure 3.11b).

The elastic moduli of the high-porosity (36-38%) synthetic sandstones are also representative of what would be expected for natural sandstones. The bulk moduli range from 1.26- 2.23 GPa, which are within the values expected for sandstones with high porosities, as

predicted from theoretical and experimental studies (Fjar et al., 2008; Gal et al., 1998; Lin et al., 2005). The bulk modulus values are also comparable to those obtained for the similar porosity Boise and Idaho Gray sandstones (Table 3.2). The Young's moduli values of the 36-38% porosity synthetic sandstones (2.01 to 5.63 GPa, Table 3.2) also fit into the range expected for high-porosity natural sandstones (Table 3.2). Consolidated sandstones can have a broad range of Young's modulus values from 0.1–30 MPa, whilst weakly-cemented North Sea reservoir sandstones with porosities of ~40%, similar to those in this study, exhibit values of around 0.4 GPa (Fjar et al., 2008; Zoback, 2010). The Young's moduli values are again similar to those of similar porosity Boise and Idaho Gray (2.56-5.14 and 2.51-4.96 GPa respectively). The synthetic sandstones also display an increase in Young's moduli with increasing effective pressure up to around 40 MPa (Table 3.2), This behaviour has been recorded in various materials, including natural sandstones such as Berea, Navajo and red sandstone (Yang et al., 2012; Yu et al., 2016; Zhang & Bentley, 1999) and is generally attributed to the closure of cracks and pores, with those of low-aspect ratio closing at low effective pressures, leading to a sharp increase in Young's modulus values. At higher effective pressures, the higher aspect ratio pores begin to close, however, the difficulty in closing these pores means that the increase in Young's modulus is less significant (Cheng & Toksöz, 1979; Toksoz et al., 1976; Walsh, 1965), as we see at effective pressures >40 MPa in our study. However, it should be considered that there are numerous parameters which can affect Young's modulus, including mineralogy, cement content and grain size (Zoback, 2010).

The elastic properties of the synthetic sandstone also remain comparable to natural sandstones as the porosity is decreased (Figure 3.8 and Table 3.2). For the 33.5% porosity sample, both the Young's and bulk moduli increase to 3.36 GPa and 1.92 GPa respectively, and they increase further for the 29.4% porosity sample to 8.10 GPa and 4.36 GPa respectively, following the trend of increasing elastic moduli with decreasing porosity (Figure 3.8 and Table 3.2). The calculated Poisson's ratio of 0.235 for the high-porosity (36-38%) synthetic sandstones is also representative of natural high-porosity, weak sandstones, which tend to

exhibit values of around 0.20 (Table 3.2), although sandstones can exhibit a wide range of values from 0-0.45 (Fjar et al., 2008). Lower values of Poisson's ratio of 0.209 and 0.191 were measured for the 33.5% and 29.4% porosity samples respectively, in agreement with the trend of decreasing Poisson's ratio with decreasing porosity, commonly seen for natural sandstones (Fjar et al., 2008; Yu et al., 2016; Zoback, 2010). The realistic elastic properties exhibited by the synthetic sandstones at the three different porosities can be visualised in the axial and radial stress-strain curves in Figure 3.10 which are similar in shape to natural sandstones (Hu et al., 2010), as shown by comparison with the stress-strain curves for 34.1% porosity Idaho Gray Sandstone also included in the figure.

Overall, the mechanical results from the synthetic rocks in this study fit well within the range reported for natural sandstones, and consequently, this methodology can provide a relatively inexpensive, rapid and simple procedure for forming sandstones with different porosities and controlled petrophysical properties. This has useful applications across a range of geoscience disciplines, including reservoir geomechanics and for geotechnical investigations.

3.5 Conclusions

A new, low-cost methodology has been successfully applied to produce synthetic, high-porosity quartz-cemented sandstones, which exhibit petrological and mechanical properties similar to those of natural sandstones. The production method, of using an amorphous quartz cement to consolidate loose sand, can reliably reproduce samples with homogeneous petrophysical properties, making them ideal for experimental studies. The synthetic sandstones show realistic mechanical properties with UCS and tensile strengths, hydrostatic yield strengths (P^*), yield curve geometries and elastic moduli all being comparable to naturally equivalent sandstones. The ability to manufacture reproducible sandstones with controlled properties provides opportunities to perform future studies where the petrophysical characteristics are systematically varied to analyse their effects on the mechanical behaviour of sandstone. For

example, future studies could be devised which examine a range of grain size distributions, porosities, grain sizes or grain shapes, whilst controlling all other parameters, to more accurately determine which factors control micromechanics in high-porosity sandstones.

4 The effect of grain size and porosity on the nature of compaction localisation in high-porosity sandstone

Abstract

Compaction bands are a type of deformation band with negligible shear in porous rocks such as sandstones and are important because they can impede subsurface fluid flow. However, the microstructural properties which favour their growth are not fully understood. We experimentally investigate the effect of porosity and grain size on compaction localisation using synthetic sandstones that permit control of the starting porosity (27%, 32%, 37%) and mean grain size (ranging from 314 to 987 μm). Each sample is subjected to the same triaxial test conditions and shortened by 5% axial strain at an effective confining pressure of 85% of their grain crushing pressure (P^*). Discrete compaction bands oriented normal to the axial loading direction are found only in the sample with the lowest starting porosity (27%) and smallest grain size (314 μm), while diffuse bands are observed for the same porosity at a larger grain size of 411 μm. No compaction bands are observed for any grain size in either the 32% or 37% starting porosity samples. Porosity analysis indicates grain size reduction does not necessarily correspond to porosity reduction indicating that compaction by grain rearrangement is as effective as localisation through comminution for these high-porosity synthetic sandstones.

4.1 Introduction

The Earth's upper crust contains numerous structural discontinuities such as faults, fractures and deformation bands. When present in porous rocks such as sandstones, these structures can exert a significant control on fluid flow (Sternlof et al., 2006; Zhu & Wong, 1997), with potential consequences for industrial processes such as fluid extraction during petroleum or groundwater production, or fluid injection during geothermal or CO_2 sequestration projects (Allen et al., 2020; Ballas et al., 2013; Hangx et al., 2013). Some of the most common

structures likely to inhibit fluid flow in sandstone reservoirs are deformation bands, which are sub-seismic, strain localisation structures often identified by increased grain cohesion (Fossen et al., 2018). Provided that the host sandstone has high enough porosity (>13%), deformation bands can form in every tectonic regime, including strike-slip, extensional and compressional (Fossen et al., 2018; Soliva et al., 2016). Deformation bands can be classified kinematically into three main types: dilation bands, shear bands and compaction bands (Mollema & Antonellini, 1996; Olsson & Holcomb, 2000; Wong et al., 2001). Compaction bands commonly have a small amount of shear and as such, can be further kinematically subdivided into shear-enhanced compaction bands (SECBs) and pure compaction bands (PCBs). Using the scheme of band-perpendicular shortening (compaction, C) plotted against shear displacement (S) (Fossen et al., 2018), SECBs are characterised by an S/C greater than zero but less than or equal to 2, while PCBs will have an S/C of 0. Shear bands which display a component of compaction and have a S/C of >2 are called compactional shear bands (CSBs) and are considered shear, rather than compaction bands (Charalampidou et al., 2011; Fortin et al., 2005; Fossen et al., 2018). Like shear bands, compaction bands are associated with reductions in grain size, porosity, and permeability (Baud et al., 2012; Charalampidou et al., 2011). They can therefore significantly reduce reservoir quality, and thus, it is important to understand the dominant controls that lead to their formation.

Since compaction bands were first identified in the field (Mollema & Antonellini, 1996), numerous laboratory studies have attempted to constrain the lithological properties and stress conditions that promote compaction localisation in porous sandstones. Baud et al. (2004) examined how the effective mean stress at the onset of inelastic compaction during differential loading affected the type of localisation observed in five natural sandstones (porosities ranging from 13-24%). They found compaction bands developed preferentially in more porous sandstones and formed at higher effective mean stress than shear bands; with compaction bands occurring as either discrete (≤3 grain diameters) or diffuse (>3 grain diameters) bands, although it is unclear what controls the development of the different types of compaction band. PCBs

and SECBs have been shown in laboratory experiments to form in sandstones with a broad range of porosities (DiGiovanni et al., 2000; Olsson et al., 2002; Olsson & Holcomb, 2000; Olsson, 2001; Wong et al., 2001). It has been suggested that the nucleation of compaction bands is favoured in sandstones containing local heterogeneities, such as large pores (Louis et al., 2007), high porosity regions or artificially cut notches (Fortin et al., 2005, 2009). Such heterogeneities produce stress concentrations which promote band propagation (Stanchits et al., 2009), although it should be noted that large pores can sometimes also act as barriers to compaction band propagation (Baud et al., 2015). Despite compaction band formation often being promoted by local heterogeneities, they have also been produced in sandstones that appear to be initially homogeneous at the sample scale, suggesting that other factors also influence their formation (Fortin et al., 2006; Klein et al., 2001).

Like porosity, grain size is an important parameter in controlling the compaction behaviour of porous sandstones (Wong et al., 1997), as the effective mean stress required to initiate mechanical grain crushing decreases with increasing grain size, according to Hertzian theory (Hertz, 1881; Zhang et al., 1990). However, the role of grain size in promoting compaction band formation is poorly constrained. Cheung et al. (2012) investigated the influence of grain-size distribution on compaction localisation and found that discrete compaction bands formed over a wide effective pressure range in well-sorted Bleurswiller sandstone, whereas no bands developed in the poorly-sorted Boise Sandstone that has similar porosity. They observed that Boise Sandstone compacted via distributed cataclastic flow, with larger grains acting as barriers to damage propagation and remaining largely intact. Cheung et al. (2012) proposed that these observations were analogous to the ‘constrained comminution’ model of Sammis et al. (1987). Since grain crushing is dependent on the size of neighbouring grains, sandstone grain size distribution (which evolves as the rock compacts) is likely an important parameter in controlling compaction band formation, as grain-to-grain fracturing is required for band propagation.

Field studies of PCBs and SECBs support the importance of porosity and grain size on controlling compaction band formation. One of the most widely studied sandstone formations is the aeolian Jurassic Navajo Sandstone Formation in southeastern Utah (USA), where previous investigations have found that PCB formation is favoured in layers with porosities ranging between 20-30% and grain sizes >0.3 mm (Fossen et al., 2011; Mollema & Antonellini, 1996; Schultz et al., 2010). PCBs were also found to occur in beds of similar porosity (20-25%) in the Aztec Sandstone Formation, Nevada (USA) (Fossen et al., 2015). SECBs also appear to be favoured by sandstones in this porosity and grain size range, as observed in the Navajo Sandstone located in the East Kaibab monocline (24-28% porosity, 0.27–0.45 mm grain size; Schultz et al., 2010), the Aztec Sandstone (25% porosity, 0.5 mm grain size; Fossen et al., 2015), and in the Uchaux Sands (26 ± 2% porosity, 0.6 ± 0.1 mm grain size) of the Orange area in the Provence region of France (Ballas et al., 2013). The textural control of sand on SECB formation in Boncavaï quarry, Provence, was examined by Skurtveit et al. (2014) who found more dense networks of SECBs in the coarse-grained (0.65 mm) and moderate porosity (27%) layers, whereas fewer bands developed in the high porosity (39%), fine grained (0.23 mm) units. The above field observations suggest that compaction bands are preferentially formed in medium to coarse-grained sandstones with porosities in the range of 20-30%.

In this study we aim to constrain experimentally the effects of porosity and grain size on the development of compaction localisation in high porosity sandstone, in an attempt to bridge the gap between field observations and laboratory studies. Unlike in previous experimental investigations of compaction localisation in natural sandstones, here we utilise a recently developed methodology to produce synthetic sandstones where the porosity and grain size can be precisely and systematically controlled (Rice-Birchall et al., 2021). This enables the production of samples for mechanical testing with a specific and controllable range of properties that would be very difficult to obtain using natural sandstones. We also describe image analysis techniques that we developed to identify deformation localisation features. Using these synthetic sandstones, plus detailed image analysis, enables the roles of porosity

and grain size on compaction band formation to be systematically investigated, elucidating the lithological controls that may promote compaction localisation in natural sandstone reservoirs.

4.2 Methods and materials

4.2.1 Synthetic sandstone production

To produce the synthetic sandstones, we follow the methodology outlined in detail by Rice-Birchall et al. (2021). We produced 12 synthetic sandstone cores, using sands obtained from Specialist Aggregates®, with three different starting porosities (27%, 32% and 37%) and four different mean grain sizes (314 ± 72 μm, 411 ± 119 μm, 747 ±130 μm and 987 ±163 μm), quantified using laser diffraction particle size analysis with a Beckman Coulter LS 13 320. Further analysis using the grain size quantification program GRADISTAT (Blott & Pye, 2001), determined the grain size distributions of all 12 synthetic sandstones to be representative of unimodal, very well-sorted sand, according to the classification scheme of Folk (1954).

To produce the synthetic sandstone samples, initially unconsolidated sand was sieved, compacted, and cemented together by precipitating amorphous quartz via the neutralisation reaction between aqueous sodium silicate solution (water glass) and hydrochloric acid (for full details of the methodology and cement characteristics see Rice-Birchall et al., 2021):

$$Na_2SiO_3 + 2HCl \rightarrow SiO_2 + 2NaCl + H_2O \quad (4.1)$$

The mass of amorphous quartz cement precipitated can be controlled by varying the quantity of reactants. In this study, 22.5 g (15 ml) of sodium silicate solution was reacted with 5.4 g (4.6 ml) of concentrated HCl in a balanced reaction, to produce a maximum theoretical yield of 4.43 g of SiO_2, along with 8.62 g NaCl and 1.33 g of water.

This solution was then mixed with 35 g of sand which had been sieved into the four grain size fractions stated above. We used a sub-angular sand comprised of 90% quartz, 5% plagioclase and 5% K-feldspar, measured using X-ray powder diffraction (XRD). In order to produce core plugs for mechanical testing (~50 mm length × 20 mm diameter), 45 g of the mixture (i.e., sand + solution) was placed into a cylindrical mould. Two end pieces were

inserted at either end of the mould and the mixture was then slightly compacted by hand before being placed in an oven at 350°C for 7 minutes. This time allowed for the majority of the water from the reaction to evaporate away, resulting in a gel-like solution which could then be compressed around grains to form an amorphous cement, without significant loss of SiO_2 in the excess water. Once removed from the oven, the mould was placed in a G-clamp, which was carefully tightened to ensure that the end pieces remained square within the mould. To produce samples with different starting porosities, the samples were compacted by tightening the G-clamp to compress the samples by different amounts, monitored by measuring the length between the end-pieces of the mould assembly. To produce the lowest porosity (27%) samples, the sands were further compressed using a hydraulic press to a maximum compressional stress of 9.37 MPa. This initial compaction stage resulted in only grain rearrangement and not grain fracturing, as shown by Rice-Birchall et al. (2021). The clamped mould was then placed back in the oven for a further hour until the solution had dried completely and all the silica and sodium chloride had precipitated. Upon removal from the mould, each sample was flushed with water for 24 hours to completely dissolve the salt produced by the reaction. The samples were then cut down to ~50 mm length using a diamond saw and the ends were squared to a tolerance of ± 0.01 mm using a surface grinder.

4.2.2 Triaxial deformation experiments

4.2.2.1 Deformation apparatus

Triaxial tests were performed to determine the mechanical and elastic properties of the different synthetic sandstones, and also inelastically deform the samples to investigate their localisation behaviour. The experimental apparatus used was a high-pressure triaxial deformation apparatus (Figure 4.1) designed and built at the University of Liverpool (Mitchell & Faulkner., 2008). It is comprised of servo-controlled confining and pore pressure systems which can monitor pressure to a resolution better than 0.01 MPa. The maximum working

confining pressure is 250 MPa, with silicon oil (10 cS viscosity) used as the confining medium. Pore-fluid pressures of 200 MPa can be achieved, with the servo-controlled pore-pressure pump also acting as a volumometer to monitor pore volume changes during compaction, to a resolution better than 0.1 mm^3. Argon was used as the pore fluid in this study as it is chemically inert and so minimises the effects of any creep behaviour via sub-critical crack growth (Atkinson & Meredith, 1981; Heap et al., 2009). The pore-fluid pressure was maintained at 20 MPa during all experiments in this study. Prior to insertion into the deformation apparatus, each sample was inserted into an annealed copper jacket (20.2 mm internal diameter and 0.3 mm wall thickness) with two porous discs with permeabilities of 1.2×10^{-13} m^2 placed on either side of the sample. The sample and copper jacket were then inserted into a Viton™ jacket to prevent any leaks of the confining fluid into the sample, should the wall of the thin copper jacket perforate during pressurisation or axial loading.

The axial load is generated by a servo-controlled electromechanical piston and is measured by an internal force gauge to a resolution better than 0.03 kN. Axial displacement is measured by an LVDT attached to the base of the loading column. The axial strain that the sample experiences is calculated by subtracting the elastic deformation taken up by the loading column from the total axial displacement. The stiffness of the loading column is 119 kN/mm.

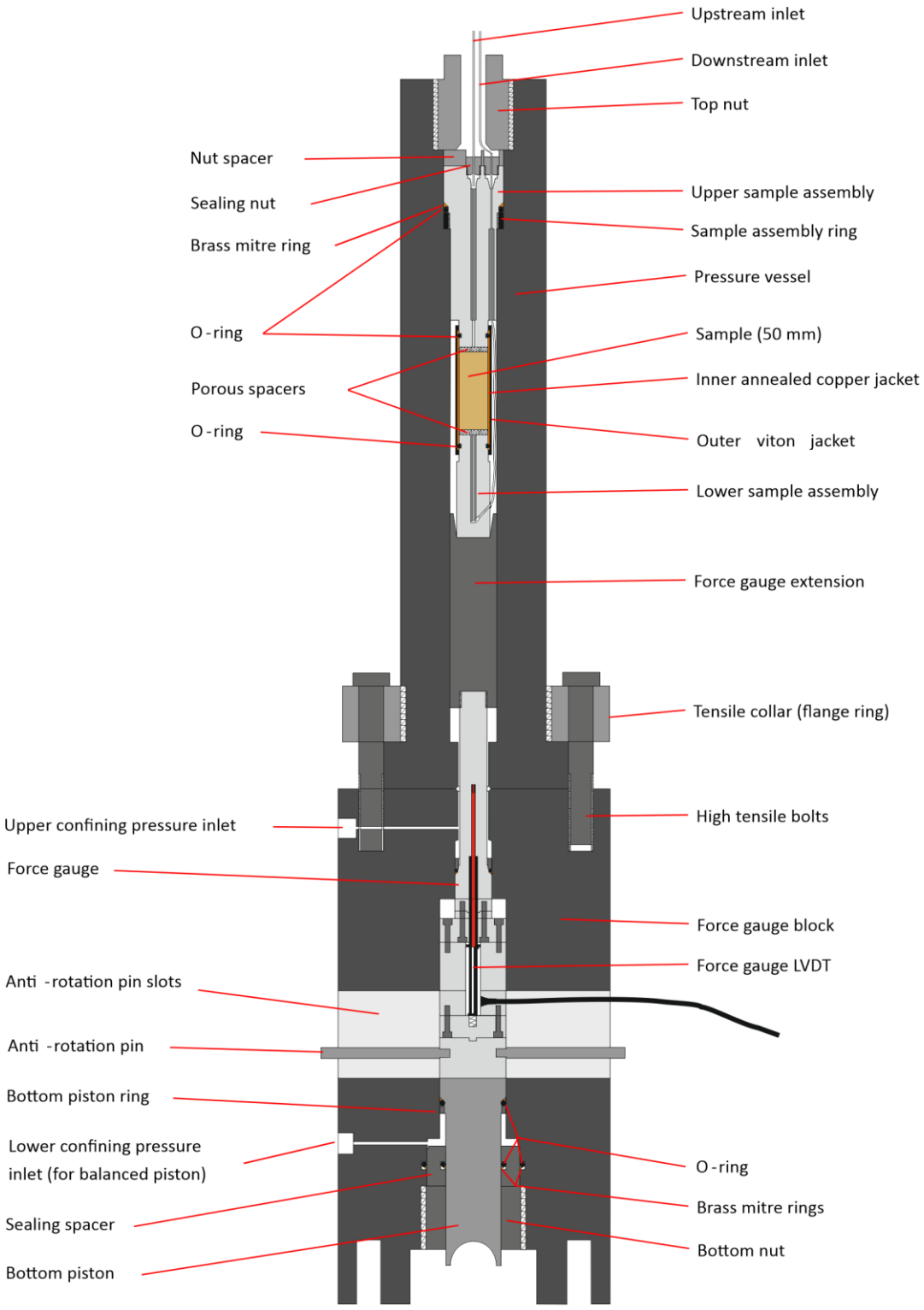

Figure 4.1. *Schematic drawing of the triaxial deformation apparatus used in this study. Modified from Mitchell & Faulkner. (2008).*

4.2.2.2 Experimental procedure

Since compaction band formation is dependent on effective mean stress (Baud et al., 2004), and the compactive yield strength of sandstone varies with porosity and grain size (Zhang et al., 1990), we first determined the inelastic grain crushing pressure (P^*) of the different synthetic sandstones. We did this so that when we inelastically deform the sandstones to investigate their localisation behaviour, we could axially load the different samples at the same equivalent effective mean stress relative to their respective P^* values, thus minimising any stress effects on the nature of localisation. To determine P^*, each sample was hydrostatically loaded by incrementally increasing the confining pressure while monitoring the change in pore volume as the pore-fluid pressure was held constant at 20 MPa. The change in pore volume was monitored for each increment until it equilibrated and showed no further reduction (equilibration was typically achieved after ~10 mins), at which point the confining pressure was increased again. P^* was identified by the deflection from quasi-linear hydrostatic loading (Figure 4.2), marking the onset of inelastic deformation (Zhang et al., 1990). In order to characterise further the mechanical properties of the sandstones, we then mapped out their respective yield curves in P-Q space, where P is the effective mean stress ($P = \left(\frac{\sigma_1+\sigma_2+\sigma_3}{3}\right) - P_f$), P_f is the pore-fluid pressure and Q is the differential stress ($Q = \sigma_1 - \sigma_3$). This was done by following the stress-probing methodology of Bedford et al. (2018), whereby the yield curve is mapped in high-resolution using a single sample. To map the yield curve the confining pressure is incrementally reduced from P^* and the yield curve is probed by axially loading the sample between each incremental reduction in pressure. For each probing increment the samples were axially loaded at a rate of 1 μm/s until yield was identified by the deviation from quasi-linear loading and an associated increase in the rate of pore volume reduction, whereupon the axial load was immediately removed (at a rate of 5 μm/s) to ensure minimal inelastic damage was imparted onto the sample. The confining pressure was then reduced further, and the stress-probing procedure repeated to map the rest of the yield curve. This probing technique has been

shown by Bedford et al. (2018, 2019) and Rice-Birchall et al. (2021) to produce comparative yield curves to those determined using multiple samples (e.g., Wong et al., 1997), without causing any significant inelastic damage to the specimen, enabling the yield curve to be probed several times over a range of effective pressures. We calculated the average amount of accumulated inelastic strain per probing increment to be <0.1%.

Once P^* was determined and the yield curves mapped for each sample, we inelastically compacted the samples to investigate their localisation behaviour. All samples were axially loaded at a rate of 1 μm/s (strain rate ≈ 2×10^{-5} s^{-1}) until 5% total axial strain was achieved, starting from an effective mean stress equivalent to 85% of their respective P^* values, so to deform the samples at conditions where compaction localisation structures would typically be expected to form (Baud et al., 2004). Pore volume data during axial loading was recorded and used to produce plots of porosity evolution versus effective mean stress, which can be compared to the porosity evolution during hydrostatic loading (Figure 4.2 and Figure SM 4.5). As well as the 12 samples taken to 5% axial strain, five additional experiments were also performed where the total strain was varied. Four of these were on the two endmember sandstones: 27% starting porosity and 314 μm grain size (lowest porosity and smallest grain size), and 37% starting porosity and 987 μm grain size (highest porosity and largest grain size). For each of these two endmembers, one sample was deformed to 2.5% axial strain and the other to 10% axial strain, so that the effect of total strain on compaction behaviour could be investigated. The final additional experiment was performed on a 27% starting porosity and 987 μm grain size sample, which, as will be outlined late in the paper, was taken to 2.5% axial strain to establish whether compaction progressed homogeneously as strain was accumulated. At the start of each of these additional five experiments, the samples were taken immediately to their starting conditions without probing P^* or the rest of the yield curve prior to loading.

4.2.3 Microstructural analysis

After each experiment, the samples were vacuum impregnated with a low-viscosity epoxy resin so that they could be prepared for microstructural analysis. Cores of the intact starting materials were also prepared in the same way to compare with the deformed samples. Once impregnated, the cores were cut in half down their long axes and this surface was polished and carbon coated ready for imaging using a Hitachi TM3000 scanning electron microscope (SEM). Backscatter electron (BSE) images were collected at 40× magnification with these images being stitched together using GigaPan Stitch software to produce a whole core image. Since each stitched image was approximately 10,000 pixels in length, the smallest grain size that could be identified was ~4.5 μm (equivalent to 1 pixel).

The stitched images were uploaded into the image analysis program Fiji (Schindelin et al., 2012) and binarised into porosity (white) and grains (black) so that detailed image analysis could be performed. To enable the program to differentiate between separate grains, the watershed algorithm was applied (Rabbani et al., 2016). Each binary image was then divided into grid squares with a 90% overlap with each neighbouring square, using the MATLAB-based distinct block processing function 'Blockproc' (Hugo et al., 2015). For each overlapping square the percentage of black (grain) and white (porosity) pixels were calculated to obtain a porosity value. The data were then smoothed using a Gaussian filter to remove any artifacts of the overlap and displayed as a porosity change colourmap. The goal of the image analysis was to have a resolution coarse enough that the initial features of the sandstones were smoothed out but fine enough that any resulting localisation could be recognised.

The sampling window size inputted into Blockproc for each individual specimen was determined according to the asymptotic approach of statistical Representative Elementary Area (REA) analysis, (Brown et al., 2000; Bruns et al., 2017; Dyskin & Pasternak, 2015; Koestel et al., 2020; Mu et al., 2016; Zhang et al., 2000) and was calibrated for each of the 12 samples using non-deformed counterparts (Figure SM 4.1 and SM 4.2) with homogeneous porosity distributions (Figure SM 4.3). Rice-Birchall et al. (2021) outlined in detail the considerations

for choosing an appropriate size sampling window to resolve key structures in the porosity maps, which must be of sufficient size to be representative of local porosity while also being small enough to identify variations caused by any localised porosity reduction features (e.g., compaction bands).

Equivalent radius was used as the measure of grain size in this study, which is the radius of a circle with the same area as a that of a measured binary grain (Heilbronner & Barrett, 2013). Colourmaps were produced show the percentage reduction in grain size from the starting mean grain size across each sample, using the formula:

$$Grain\ size\ reduction\ (\%) = \frac{R_m - R}{R_m} \times 100 \qquad (4.2)$$

where R_m is the mean equivalent grain radius of the non-deformed sample and R is the equivalent grain radius calculated for each individual grain in the deformed sample. The methodology of Rabbani et al. (2014) was deployed to calculate specific surface area of the solid/grain space for each of the deformed samples (Figure SM 4.8) as outlined in previous studies (Baud et al., 2004). For a given 2D image, this can be defined as the perimeter of the grains divided by their area. Since we wanted to examine the distribution of specific surface area, the grid size determined by the REA analysis was used to examine this property across the sample. The 2D grain coordination number was also obtained for the endmember undeformed samples and represents the average number of grains in contact with a specific grain (Salami et al., 2019) (Figure 4.5). To achieve this, both images were binarised and run through a script developed by Rabbani et al. (2016), where the individual grains were segmented and the boundaries between grains were identified.

4.3 Results

4.3.1 Mechanical results

4.3.1.1 Porosity reduction

Figure 4.2a-c displays graphs of porosity reduction versus effective mean stress for the hydrostatic and axial loading experiments performed on the 12 synthetic sandstone samples.

For each sample, the hydrostatic yield point (P^*), marking the onset of inelastic deformation, is identified from the deflection in the hydrostatic loading curves, as shown in previous studies (Brace, 1978; Wong et al., 1997; Zhang et al., 1990). The effective mean stress at which P^* occurs, increases as both porosity and grain size decrease, in agreement with Hertzian fracture mechanics (Hertz, 1881; Zhang et al., 1990). Apparent bulk moduli were obtained for each sample (Figure 4.2d) from the gradients of the hydrostatic loading curves at effective mean stresses below P^*, where the samples exhibit quasi-linear elastic behaviour. The apparent bulk modulus increases as both porosity and grain size decrease.

Porosity reduction versus effective mean stress during axial loading (at P = 85% of P^*) is also plotted on Figure 4.2a-c. For some of the lower porosity samples it is sometimes observed that the compactive yield points during axial loading (C^*) occur at a higher effective mean stress than P^*, which is not typically expected if assuming a parabolic yield envelope (e.g., Wong et al., 1997). This effect is reduced with increasing starting porosity, however, in most of the samples, C^* occurs in close proximity to P^*, as has been observed in some previous studies (e.g., Hangx and Brantut, 2019; Tembe et al., 2007). Higher-magnification plots to show how C^* was determined from the pore volume reduction (porosity) data can be found in Figure SM 4.4. Porosity loading curves and the determination of C^* for the additional experiments where the samples were taken to different amounts of axial strain are also presented in the supplementary material (Figure SM 4.5-4.7).

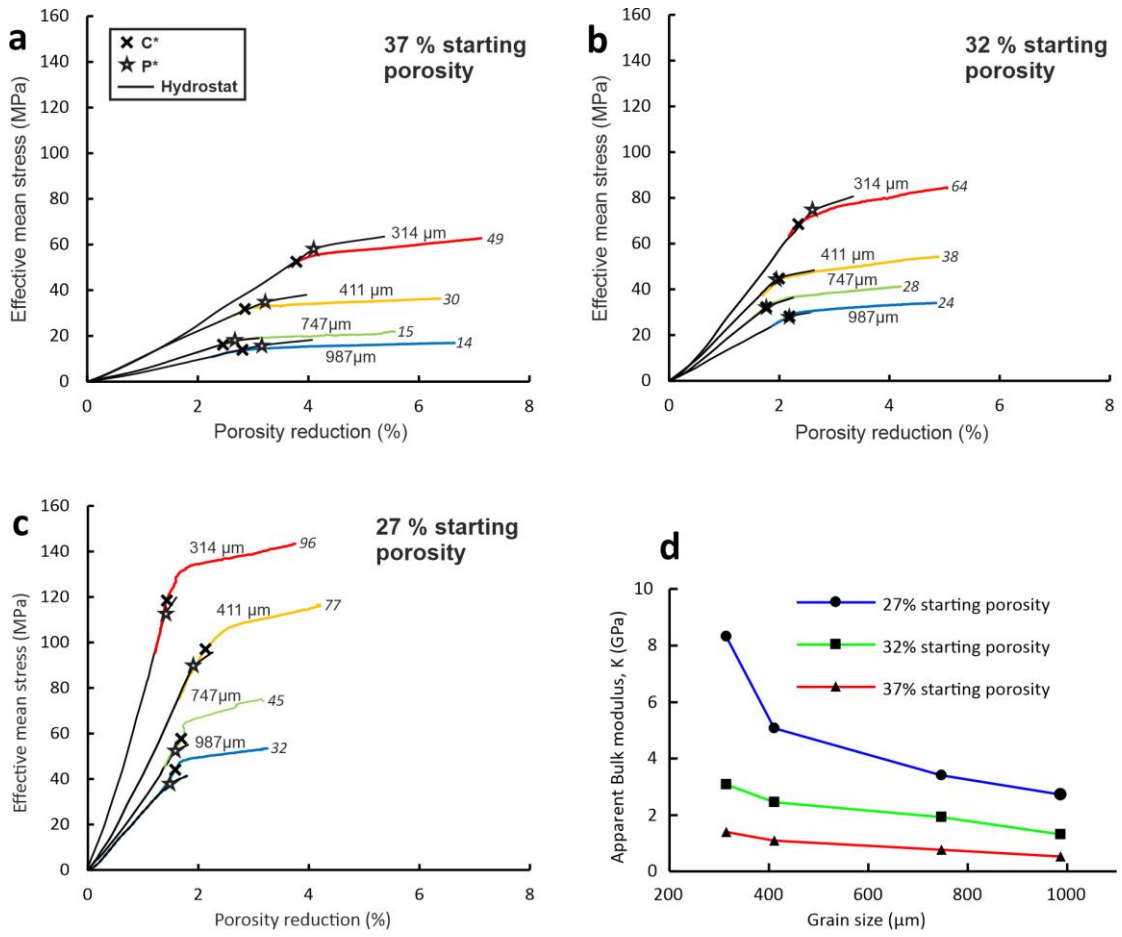

Figure 4.2. *Graphs of porosity reduction versus effective mean stress for the 12 synthetic sandstones for a) 26%, b) 32% and c) 37% starting porosity taken to 5% axial strain. The black lines and coloured lines represent porosity reduction during hydrostatic and deviatoric loading respectively. The values next to the curves correspond to the effective mean stress at the initiation of axial loading. d) The calculated apparent bulk modulus values for the different sandstones plotted against grain size.*

4.3.1.2 Yield curves

Figure 4.3 displays the yield curves for all 12 synthetic sandstones, constructed using the stress-probing methodology of Bedford et al. (2018). With decreasing porosity, the size of the yield curves increases; while for a given porosity, the size of the yield curves decreases with increasing grain size, consistent with the hydrostatic loading data in Figure 4.2. The yield curves

for the 37% porosity samples are all broadly elliptical, as is commonly reported for porous sandstones (e.g., Baud et al., 2006; Wong et al., 1997), while those for the 32% and 27% starting porosity samples sometimes exhibit near-vertical limbs, or limbs that slightly overhang P^* on the high-pressure side of the yield curve, as has been reported in some previous studies (Allen et al., 2020; Bedford et al., 2019; Hangx and Brantut, 2019; Klein et al., 2001; Pijnenburg et al., 2019a; Tembe et al., 2007). C^* values determined for the additional sandstone samples taken to varying amounts of axial strain are also plotted. During these additional tests the yield curve was not probed prior to loading and the samples were taken directly to their starting effective mean stress. The additional samples show very similar C^* values (Figure 4.3) to the main sample suite which were taken to 5% axial strain and had their yield curve probed prior to axial loading. The apparent similarity between the different sample sets indicates that the yield curve probing methodology does not impart a significant amount of inelastic strain onto the samples.

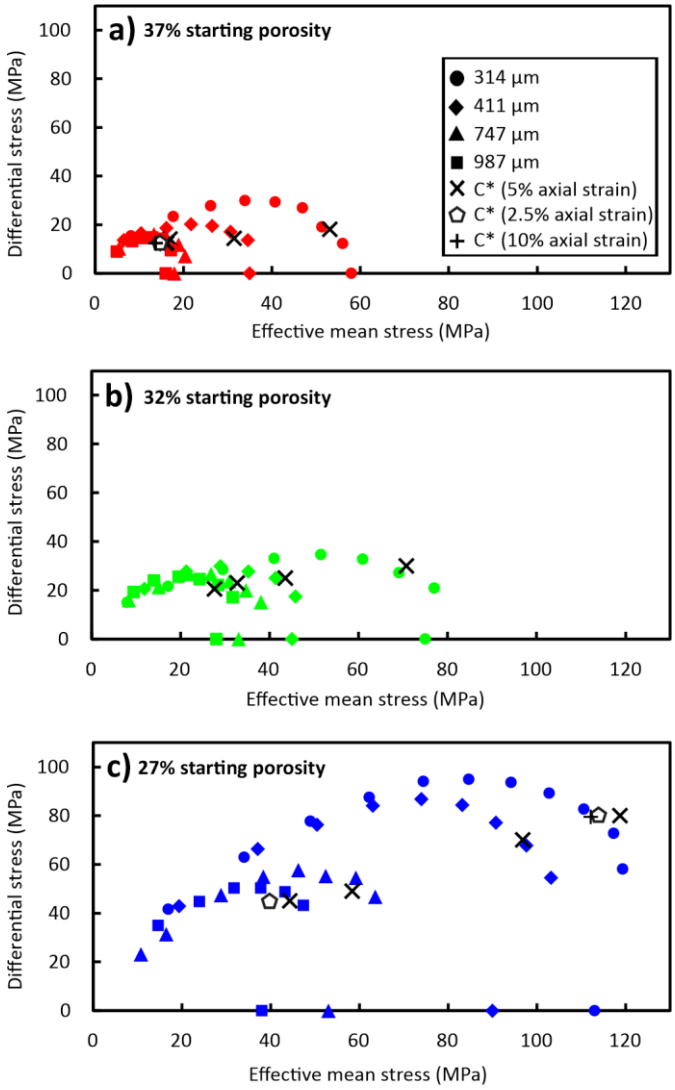

Figure 4.3. *Yield curves for the different grain size sandstones with starting porosities of a) 37%, b) 32% and c) 27%. With decreasing porosity and grain size, the size of the yield curve increases. The black crosses mark the onset of compaction and inelastic deformation (C*) for each sample taken to 5% axial strain during axial loading at an effective stress of 85% of their P* values. C* values for the additional experiments where the samples were either taken to 2.5% (pentagons) or 10% (plus signs) axial strain, and which were taken immediately to 85% of P* without probing the rest of the yield curve, are also included.*

4.3.1.3 Mechanical data during inelastic compaction

The axial loading curves (differential stress versus axial strain) for each of the synthetic sandstones, loaded at an effective mean stress equal to 85% of their respective *P** values, are displayed in Figure 4.4. All samples yield after ~1% axial strain, marked by the deflection in the loading curves, with the yield stress increasing with decreasing grain size and porosity, consistent with the yield curve data in Figure 4.3. Post-yield strain hardening is exhibited by all of the sandstones, which is synonymous with compactive deformation (Wong et al., 1997). Apparent Young's modulus values have been calculated from the elastic part of the axial loading curve for each of the samples (Figure 4.4d). Similar to the apparent bulk modulus (Figure 4.2d), there is an overall trend of increasing apparent Young's modulus with decreasing porosity and grain size.

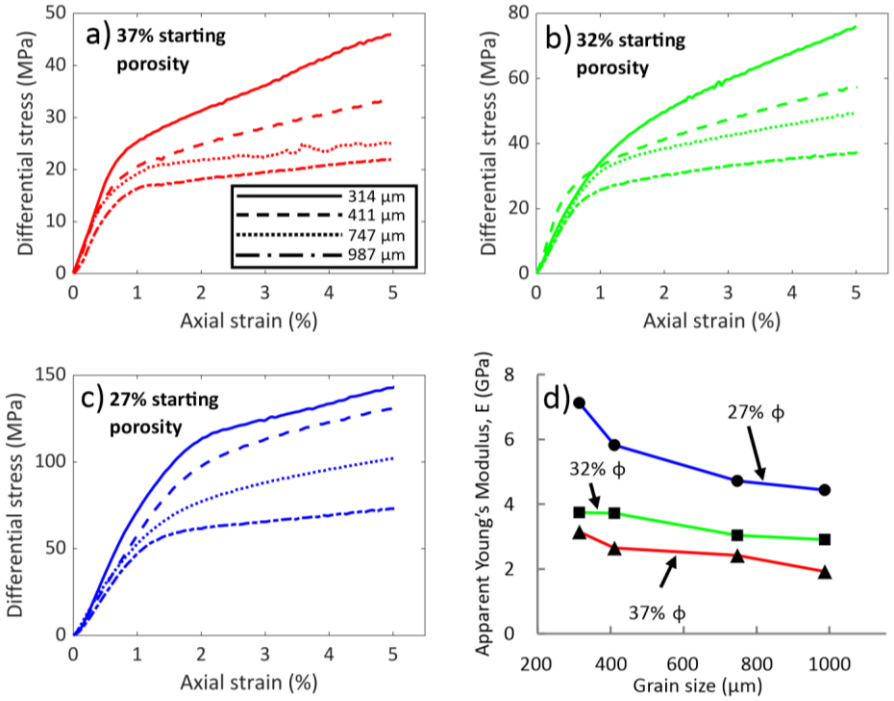

Figure 4.4. *Axial loading curves for the different grain size sandstones with starting porosities of a) 37%, b) 32% and c) 27%. Each sandstone was loaded to 5% axial strain, starting from an effective stress equivalent to 85% of P*. d) Apparent Young's Modulus values for the different sandstones plotted against grain size.*

4.3.2 Microstructural results

4.3.2.1 Starting materials (undeformed samples)

Figure 4.5 displays the microstructural characteristics of undeformed samples of the 27% porosity synthetic sandstone with end-member grain sizes of 314 μm and 987 μm. BSE images of the starting materials of all 12 sandstones produced in this study can be found in the supplementary material (Figure SM 4.2). Image analysis illustrating the porosity and grain size of the starting materials is also shown in Figure SM 4.1. From the BSE images of the end member grain size sandstones no obvious grain fracturing can be seen, suggesting that the consolidation stresses applied to the samples during production did not cause any significant damage or grain crushing. Both samples also display relatively homogeneous grain size and porosity distributions throughout the cores (Figure 4.5). The 2D coordination numbers for the smaller grain size (Figure 4.5a) and larger grain size (Figure 4.5b) samples are 3.12 and 2.83 respectively. Our microstructural observations of the undeformed samples are consistent with those of Rice-Birchall et al. (2021), where they performed detailed analysis of the synthetic sandstones manufactured using the same methodology and found that it produced consistent homogeneous sandstones with comparable microstructural and mechanical properties to natural sandstones.

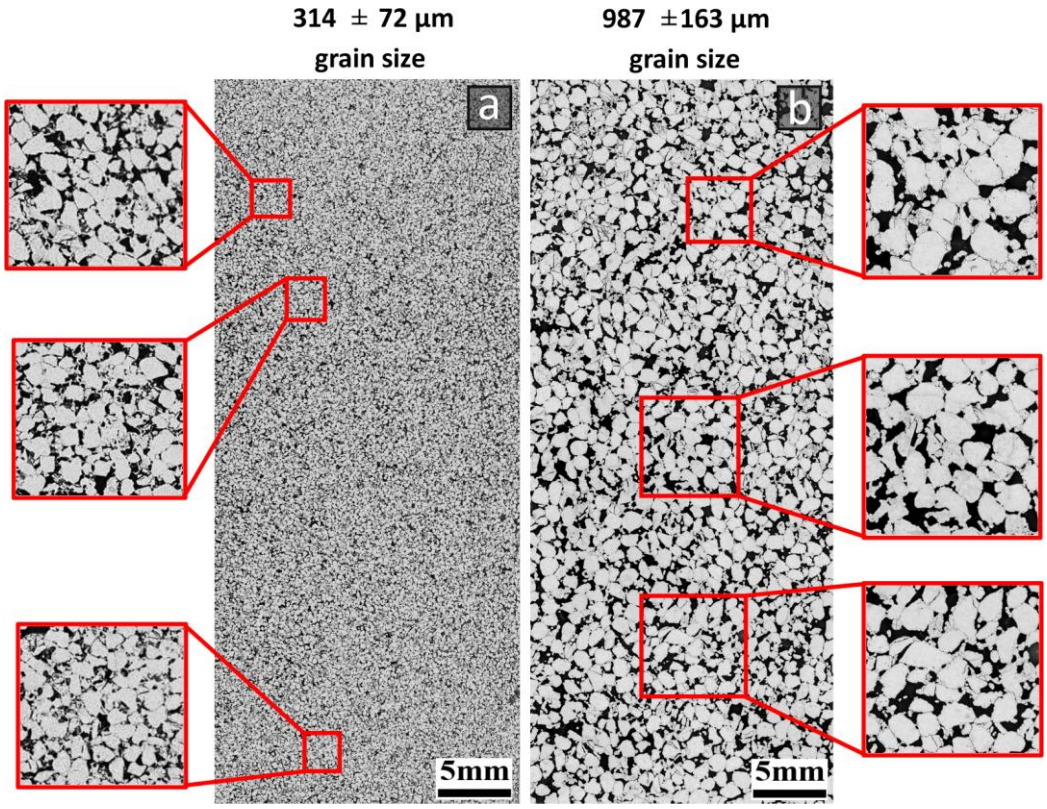

Figure 4.5. *Whole core BSE micrographs of the 27% starting porosity synthetic sandstones with grain sizes of (a) 314 µm and (b) 987 µm. Zoomed images are shown in the red boxes to highlight the homogeneous nature of the sandstones and show that no obvious damage was imparted on the individual grains during the production process.*

4.3.2.2 Grain size reduction and localisation during inelastic deformation

Figure 4.6 displays a series of 12 BSE micrographs of the deformed synthetic sandstone samples loaded to 5% axial strain from an effective mean stress equal to 85% of their respective *P** values. Figure 4.7 shows the associated grain size reduction maps produced from the micrographs in Figure 4.6. As the undeformed starting samples have a homogeneous distribution of undamaged grains (Figure 4.5), any variations in grain size in the deformed samples are assumed to be a result of the deformation to which they were subjected. Clear differences are observed with varying initial porosity and grain size. The greatest relative grain size reduction is observed in the 27% starting porosity samples (~70-99% reduction in the

deformed regions). For a given porosity, the amount of relative grain size reduction is highest in the initially coarse-grained samples (Figure 4.7).

The grain size reduction maps also reveal spatial differences in the compaction behaviour of the different sandstones. The lowest starting porosity (27%) and smallest grain size (314 μm) sandstone contains a well-defined region of grain size reduction (~70-90%) in the sample centre (Figure 4.7a). Closer inspection of this region shows heavily fractured grains contained within localised anastomosing bands of intense deformation, approximately 2-3 grain diameters in width, orientated sub-perpendicular to the greatest principal stress (Figure 4.8b). Using the definition of Baud et al. (2004) these can be classified as discrete compaction bands (≤3 grain diameters in width). Outside the central region, the grain size reduction is less significant (~20-40%) with most grains remaining intact (Figure 4.8a). At the same starting porosity but slightly larger grain size of 411 μm, a central region of more intense grain size reduction (~80-99%) is also present (Figure 4.7b); however, unlike the 314 μm sample, no clear discrete bands are observed within this region and the grain crushing spans multiple grains (Figure 4.8d), similar to the diffuse compaction bands (>3 grain diameters in width) of Baud et al. (2004). Further increasing the starting grain size of the 27% porosity sandstone (Figure 4.7c and d) leads to much more distributed deformation and relatively homogeneous grain size reduction (~70-99%) across the sample (Figure 4.8e and f), with no identifiable compaction localisation.

In the 32% starting porosity sandstones predominantly distributed deformation is observed, with average grain size reductions of ~40-60% (Figure 4.7e-h). There is perhaps some evidence of a central region of more intense deformation for the smaller grain size samples (Figure 4.7e and f); however, this is a broader and less well-defined region than observed in the 27% porosity samples of the same grain size (Figure 4.7a and b). For the 37% starting porosity samples, deformation appears to be homogeneously distributed in each of the tested grain sizes, with no evidence of localisation (Figure 4.7i-l). Higher magnification images of the 37% porosity sample with the largest grain size (987 μm) shows predominantly intact

grains (~20-40% average grain size reduction) with only minor fracturing (Figure 4.8g and h), suggesting that most of the compaction was accommodated by breaking of the cement bonds and grain boundary sliding/rearrangement.

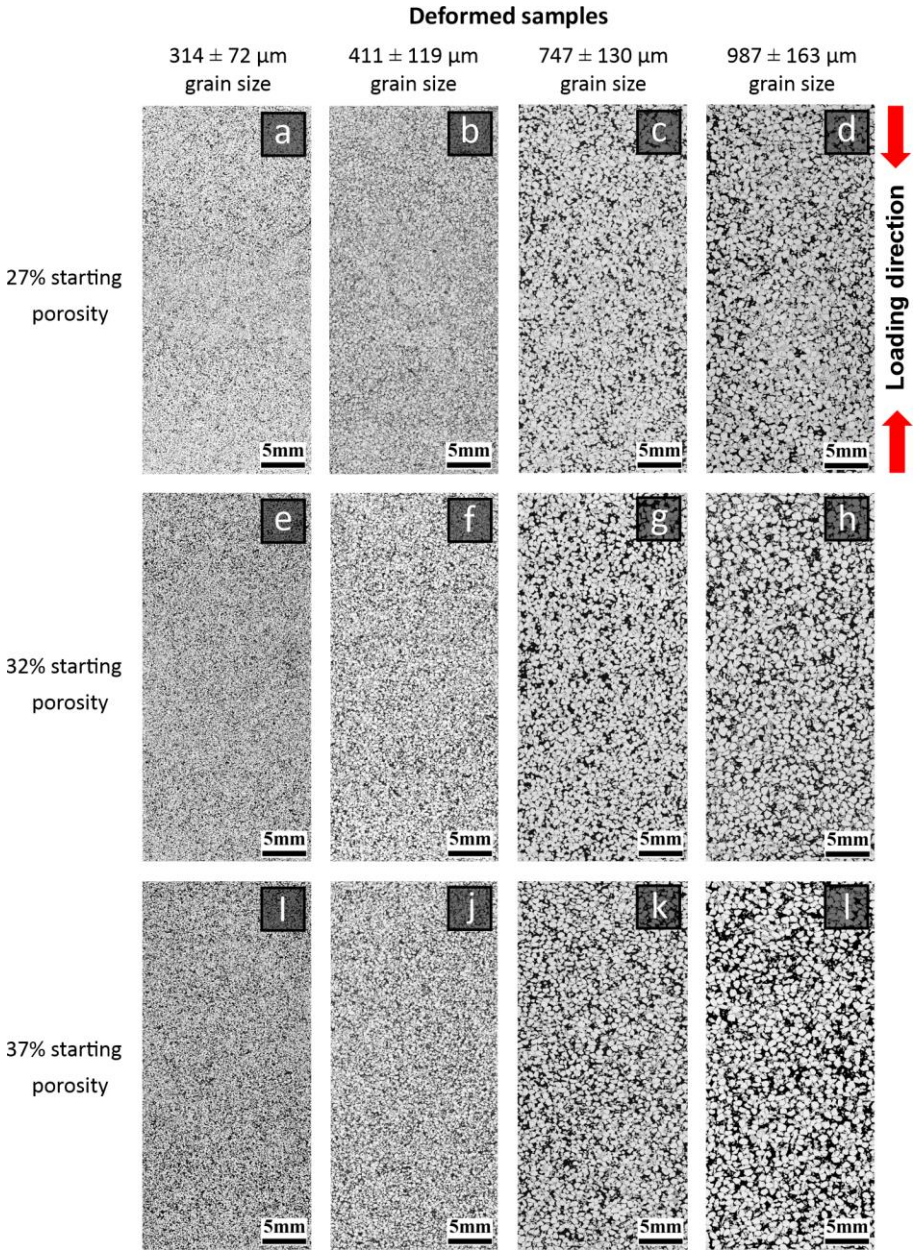

Figure 4.6. *Whole core length BSE images obtained for the 12 deformed synthetic samples with different initial grain sizes and starting porosities. The direction of maximum principal stress is parallel to the long axis of the core samples. Each sample was loaded to 5% axial strain starting from an effective mean stress equal to 85% of their respective P* values.*

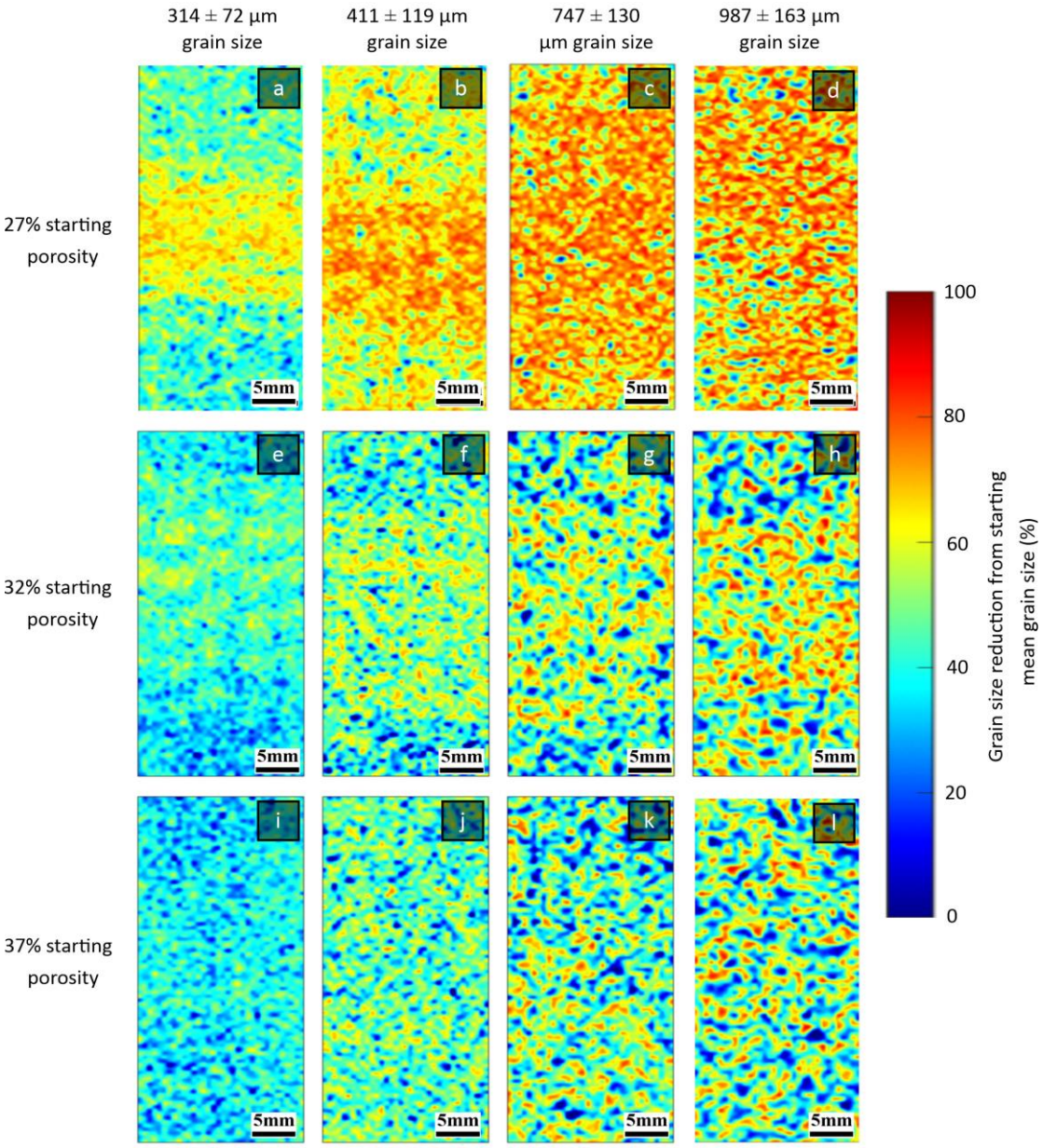

Figure 4.7. *Grain size reduction maps, produced from the micrographs in Figure 4.6, for the 12 deformed synthetic sandstones. The grain size reduction is shown as a percentage reduction relative to the starting mean grain size for each sample. For a given porosity, samples with the largest starting mean grain size show the greatest relative grain size reduction.*

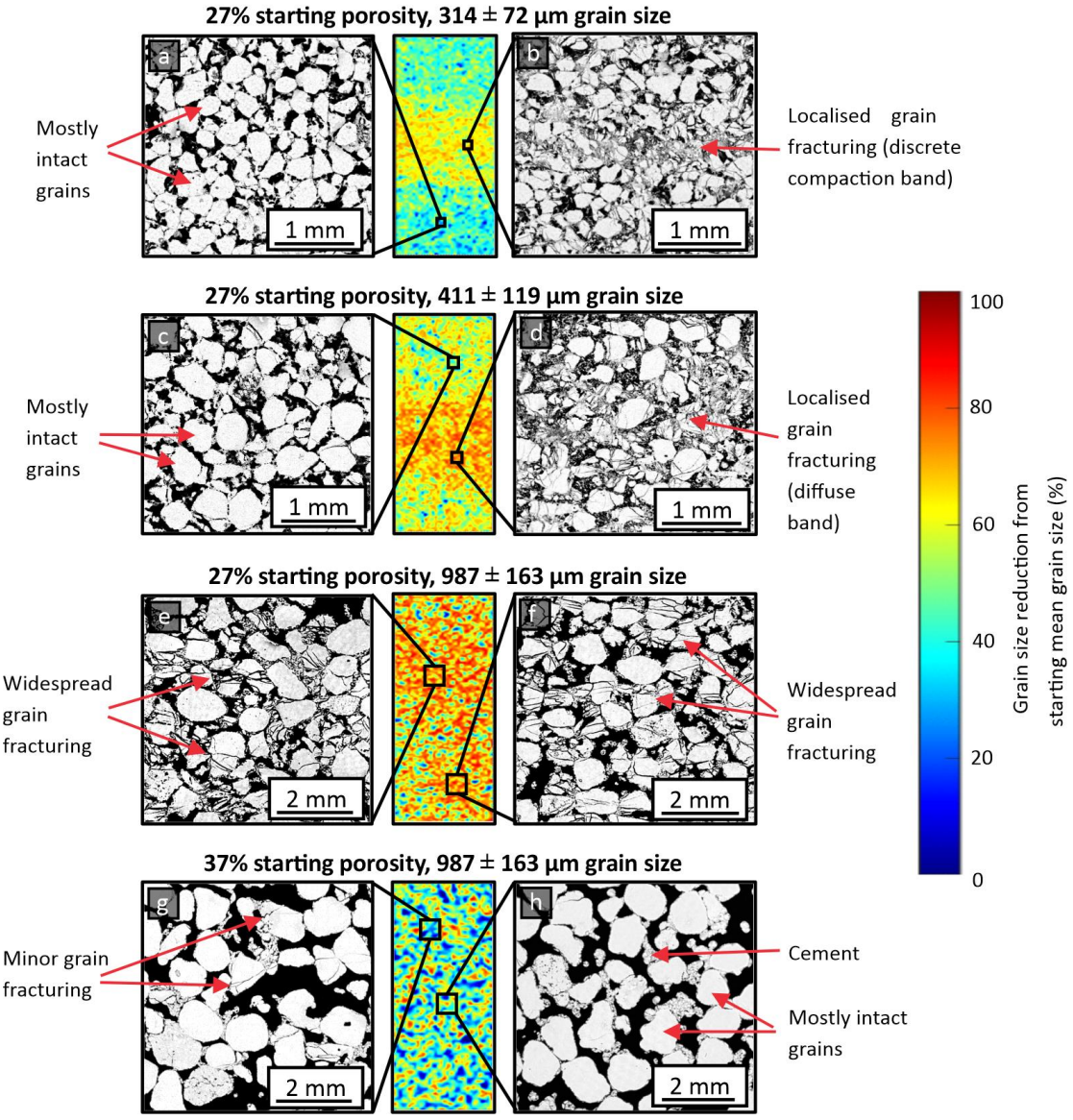

Figure 4.8. *Zoomed high-contrast BSE micrographs of the synthetic sandstone samples shown in Figure 4.7a, b, d and l. For the 27% porosity sandstone with grain sizes of 314 µm (a, b) and 411µm (c, d) the most intense grain fracturing is localised in the centre of the samples, whereas for the largest grain size of 987 µm (e, f) grain fracturing is distributed homogeneously through the entire sample. At a starting porosity of 37% (g, h) most of the grains remain intact with only minor grain fracturing observed.*

To investigate how the compaction behaviour evolves as a function of accumulated strain, we performed five additional experiments. Two additional experiments were performed on each of the endmember sandstones: (i) the lowest porosity and smallest grain size sandstone (27% and 314 μm respectively), and (ii) the highest porosity and coarsest grain size sandstone (37% and 987 μm respectively), whereby a different sample of each endmember sandstone was deformed to 2.5 and 10% axial strain. Another experiment to 2.5% axial strain was also performed on an additional 27% porosity, 987 μm grain size sample. Figures 4.9a, c, d and f show micrographs and grain size reduction colourmaps for the two endmember sandstones deformed to different amounts of axial strain. For the lowest starting porosity, smallest grain size sample, after 2.5% axial strain some discrete compaction bands (approximately 1-2 grain diameters wide) have formed within the central region of the sample and are associated with ~40-60% grain size reduction (Figure 4.9a). By 5% axial strain, several discrete compaction bands have developed across the centre of the sample, with individual bands increasing in thickness to around 2-3 grain diameters (Figure 4.8b). By 10% axial strain, the central region of most intensive grain size reduction and localisation has become wider and most of the bands have widened or merged to become diffuse. Due to most of the grains in this region undergoing intensive fracturing (Figure 4.9c) it is difficult to discern individual bands and the majority of the grains have undergone a ~60-80% size reduction. In contrast, the sample with the highest starting porosity and largest grain size exhibits very minimal grain crushing at 2.5% axial strain (Figure 4.9d) with no significant increase in grain fracturing by 5% axial strain (Figure 4.8g and f). However, by 10% axial strain, more significant grain fracturing is observed (Figure 4.9f), although this is distributed homogeneously through the sample, rather than being concentrated in a central region like the low porosity, small grain size samples (Figure 4.9a-c). Figure 4.9g shows micrographs and grain size reduction colourmaps for the 27% porosity, 987 μm grain size sample deformed to 2.5% axial strain. This sample shows less grain crushing (~40-60%) than its 5% axial strain counterpart (~70-90%), however both samples show similar homogeneously distributed deformation, with no evidence of compaction localisation.

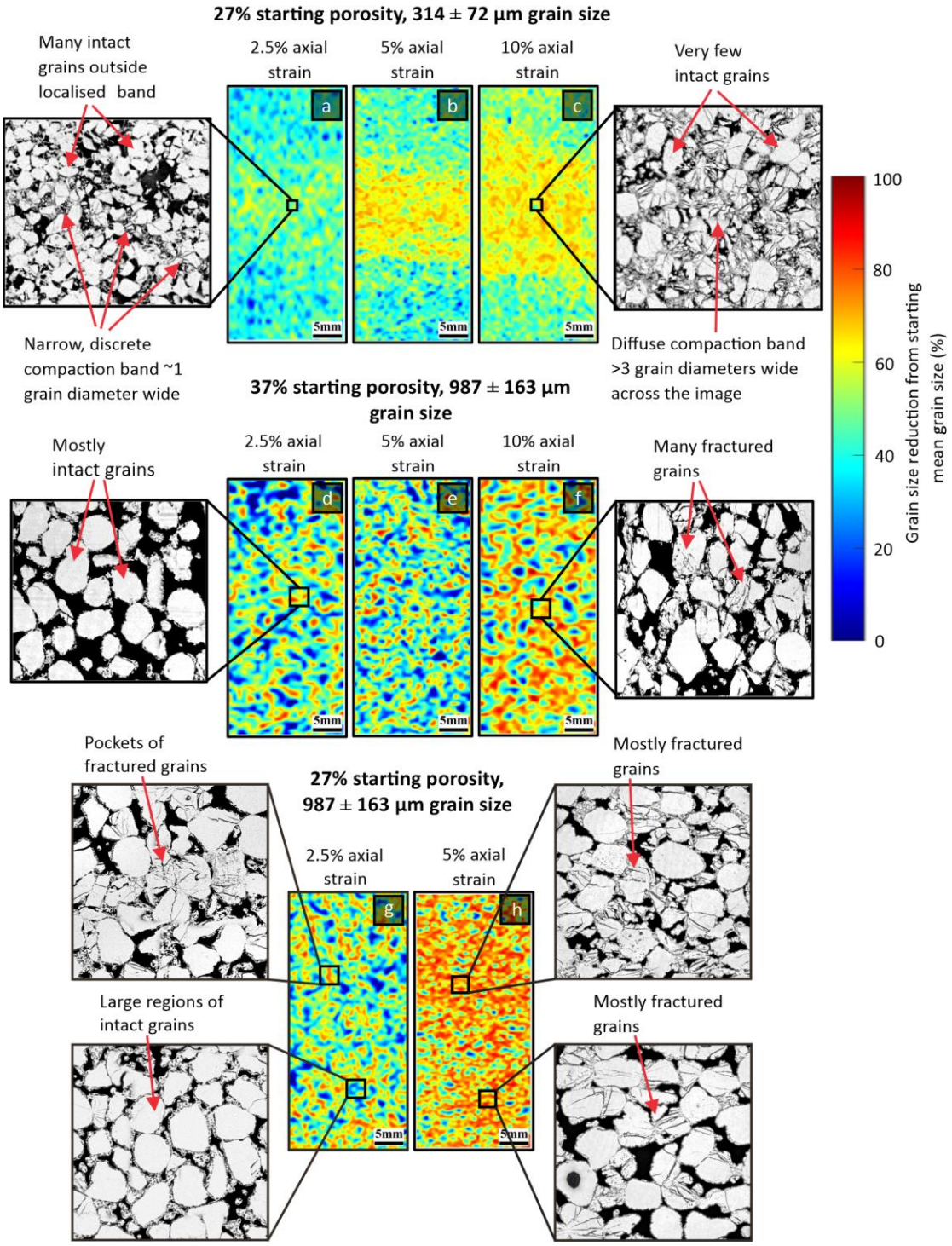

Figure 4.9. *a–f). High-contrast BSE micrographs and grain size reduction colourmaps for the endmember sandstones produced in this study, deformed to different amounts of axial strain (2.5%, 5% and 10%). Colourmaps for the 27% starting porosity, 987 µm sample taken to 2.5% and 10% axial strain are also presented in g) and h).*

4.3.2.3 Porosity change colourmaps of deformed samples

Figure 4.10 displays colourmaps that show the change in porosity of the 12 deformed sandstones. Unlike for grain size reduction, there is a less obvious pattern in porosity change across the range of different starting porosity and grain size sandstones tested in this study. This may, in part, be due to the REA analysis being performed on the whole sample scale, meaning some of the subtle porosity changes associated with individual compaction band formation are not fully captured. The largest porosity reductions (up to ~15%) generally occur in the highest starting porosity samples (Figure 4.10i-l). However, comparison with the grain size distribution colourmaps in Figure 4.7 shows that areas of intense grain size reduction are not necessarily associated with a significant reduction in porosity. This is particularly evident in the highest starting porosity samples. It does appear though that the regions where discrete and diffuse compaction bands formed in the 27% porosity samples, at grain sizes of 314 μm and 411 μm respectively (Figure 4.7a and b), correlate with regions of porosity reduction in the porosity change colourmaps (Figure 4.10a and b).

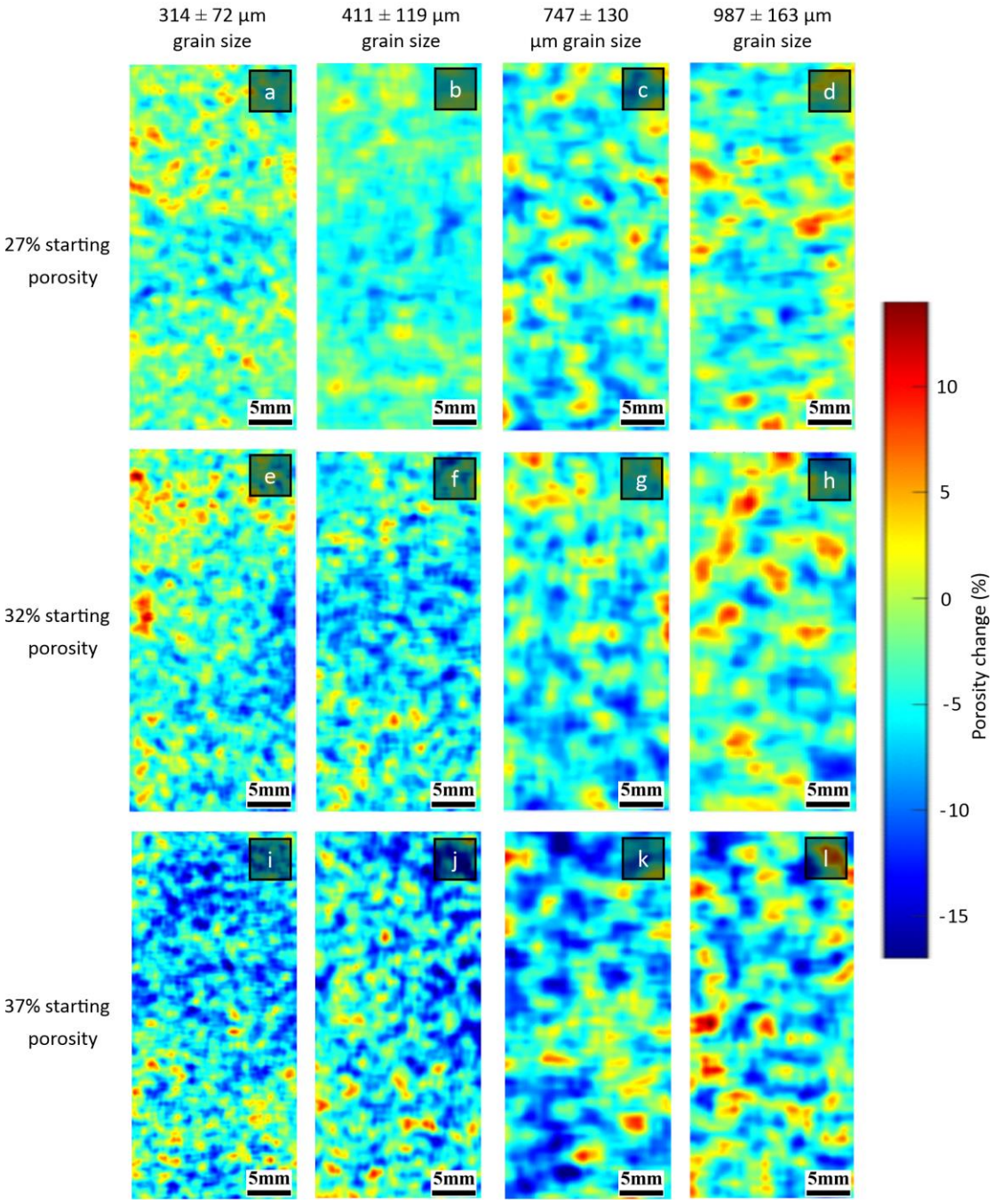

Figure 4.10. *Porosity change colourmaps produced from the micrographs in Figure 4.6, for the 12 deformed synthetic sandstones.*

4.4 Discussion

4.4.1 The role of grain size and porosity on localisation

Our results have demonstrated that compaction localisation is only evident in the samples with the two smallest starting grain sizes of 314 μm and 411 μm and lowest starting porosity of 27%. Unlike in some previous laboratory studies where deformed regions have been reported at the ends of the samples (Baud et al., 2004; Stanchits et al., 2009), in both of these specimens a more intensely deformed region formed in the sample centre and there was limited grain fracturing observed towards the sample ends (Figure 4.7a and b). However, the type of compaction bands within these central deformed zones varied. In the 314 μm sample, discrete, anastomosing bands were observed, separated by pockets of intact grains, whereas the 411 μm sample displayed diffuse bands with fewer intact grains within the central deformed zone (Figure 4.8). Discrete compaction bands similar to those identified in the 314 μm, 27% porosity sample have been observed in previous experimental studies on natural sandstones with similar porosities and grain sizes - e.g., Bentheim (Klein et al., 2001), Bleurswiller (Fortin et al., 2005) and Berea sandstones (Baud et al., 2004). Although previous studies have sometimes found that the formation of compaction bands is associated with stress drops in the mechanical data (Baud et al., 2004, 2006; Tembe et al., 2008), we observe no such response in the mechanical data for these samples, nor in the 27%, porosity 314 μm samples taken to 2.5% and 10% axial strain (Figure SM 4.7). With increasing grain size to 747 μm and 987 μm at 27% porosity, no compaction bands were observed, and grain fracturing occurred homogeneously across the samples (Figure 4.7c and d). This was also the case for the 27% porosity, 987 μm grain size sample deformed to 2.5% axial strain (Figure 4.9g). These observations indicate that grain size exerts an important control on the formation of compaction bands in high-porosity sandstones and also whether they are discrete or diffuse in nature. Our experiments have also demonstrated that transitions from discrete to diffuse compaction bands can occur with increasing amounts of axial strain, as observed for the 314 μm sample (Figure 4.9a-c), suggesting that sometimes

discrete bands form initially and then widen and coalesce as more strain is accumulated. This indicates that after a certain density of discrete bands have formed in the sample, it becomes more energetically favourable during continued deformation to widen these bands than to develop new bands. However, not all diffuse bands form via the widening of existing discrete bands, as was the case for the 411 μm sample where only diffuse bands were observed, highlighting further the importance of initial grain size on the nature of compaction localisation. Previous studies have suggested that other factors such as, porosity, mineralogy, and grain size distribution potentially influence the formation of diffuse or discrete compaction bands (Baud et al., 2004; Cheung et al., 2012; Klein et al., 2001); however, since these properties were controlled in our synthetic specimens, we conclude that the grain size exerts a dominant control.

Our results show that porosity also controls the development of compaction localisation since compaction bands were only formed in samples with the lowest starting porosities of 27%. The porosity change maps highlight differences between the compaction behaviour of the three starting porosities, with the largest porosity reductions observed in the 37% porosity samples (Figure 4.10). Since the 37% and 32% porosity samples displayed only minor grain fracturing when compared to the 27% porosity samples (Figure 4.8), the porosity reduction must be accommodated by a different mechanism in the higher porosity samples. This is most likely to be via grain rearrangement, whereby the cement bonds are broken allowing the grains to move more freely and slide past each other. Once the grains have formed a more efficient packing arrangement and can no longer move past one another, they will begin to fracture, as observed when the 987 μm 37% porosity sample was deformed to 10% axial strain (Figure 4.9f). In contrast, the 27% porosity samples already have a more efficient packing arrangement, meaning that when a differential stress is applied, the cement bonds are able to support the aggregate and prevent grain sliding, resulting in the deformation being accommodated by grain fracturing instead, which in turn can lead to localisation (depending on the starting grain size). These observations suggest that the packing arrangement and the strength of cement bonds could play a key role in the development of localisation, with cement potentially needed to

amplify stress heterogeneities that produce the cascading grain fracturing required to propagate compaction bands, an observation which is supported by the absence of compaction bands forming in experiments on loose sand where intergranular cohesion is low (Crawford et al., 2004; Hangx & Brantut, 2019). Indeed, BSE images comparing cement coatings on the grains of our synthetic sandstones with cement coatings in similar natural sandstones with different localisation behaviours, show marked differences in the type and distribution of cement (Figure SM 4.9), suggesting that the cement properties may be key parameters in controlling localisation behaviour. Recent experimental work, where compaction localisation was observed in aggregates of sintered glass beads with porosities of 35% (Carbillet et al., 2021), further indicate that interparticle bond strength may be important for controlling localisation, with compaction bands forming in these high porosity samples potentially as a result of the strength provided by the sintering procedure. Previous discrete element modelling (DEM) of deforming granular aggregates has also suggested that the nature of compaction localisation (i.e., diffuse or discrete) may be influenced by cement bond strength, with a switch from diffuse to discrete bands observed in the models when the bond-strength was increased (Marketos & Bolton, 2009). Further experiments are needed to constrain the role of cement and interparticle bond strength in controlling localisation and the mechanical behaviour of porous sandstones.

The type of localised features expected to form during experiments (i.e., compaction, shear or dilation bands) can be predicted theoretically using the bifurcation approach of Rudnicki & Rice (1975); see also Issen & Rudnicki (2000). We calculated the relevant plastic constitutive parameters required for the bifurcation analysis from our experimental data, following the procedure outlined by Wong et al. (1997) - see supplementary Text SM 4.1 and Table SM 4.1 for more information on the bifurcation analysis. We found that compaction localisation was only predicted for the sample with the lowest porosity and smallest grain size (Figure SM 4.10) which, incidentally, did develop discrete compaction bands during deformation (Figure 4.8b). The bifurcation analysis was unable to predict the development of the diffuse compaction bands observed in the 27% porosity 411 μm sample (Figure 4.8d). Discrepancies between the

predicted mode of localisation and the theoretical predictions may be due to the various damage mechanisms not being captured by the constitutive model (Baud et al., 2004).

4.4.2 Comparison with natural compaction bands

Compaction bands have been documented in numerous field studies of natural sandstones, particularly in the Navajo and Aztec sandstones in the USA and sandstones from the Provence region in France (Eichhubl et al., 2010; Fossen et al., 2011, 2015; Mollema & Antonellini, 1996; Schultz, 2009; Schultz et al., 2010; Soliva et al., 2013). Natural PCBs have generally been recorded in units with porosities between 20-30% and grain sizes ranging from 0.3–0.8 mm (Fossen et al., 2018). The laboratory results from this study support these field observations, since compaction bands were identified in the samples with starting porosities of 27% and grain sizes of 314 μm and 411 μm. However, qualitative field observations suggest that coarser sandstones tend to develop more compaction localisation. Consequently, questions arise as to why we did not observe compaction bands in the coarser grained 27% porosity samples, particularly the 747 μm specimen which lies within the field-observed bounds. One possibility is that the cylindrical samples used in our study were the same dimensions for all the grain sizes and porosities tested, however, there may be an element of scale-dependent behaviour, perhaps necessitating the use of larger samples if discrete compaction bands are to be observed in samples with larger grain sizes (747 μm and 987 μm). Our experimental results support the field observations of an absence of PCBs observed in units with porosities above ~30%. It is therefore possible that natural compaction bands cannot form above this value, potentially due to strain being accommodated primarily by grain rearrangement, rather than grain fracturing. However, caution should be taken when interpreting relationships between porosity and compaction bands in natural sandstones, as the current porosity of the unit may not be the porosity at the time of deformation and compaction band formation; the bands may have formed earlier in the diagenetic history when the porosity of the sandstone was higher.

Previous studies have observed that the density of compaction bands within the same sandstone unit is often higher in beds with coarser grain sizes and higher porosities compared

to those with lower porosities and grain sizes (Mollema & Antonellini, 1996; Schultz et al., 2010; Skurtveit et al., 2014). While this appears to contrast with our results, in nature, these different beds of sandstone would have been subjected to the same stress field, and because coarse-grained sandstones have much smaller yield strengths (Figure 4.3), they are more likely to inelastically deform and produce compaction bands than in low porosity, fine-grained sandstone beds which may not even reach yield under the same stress conditions. Many previous laboratory studies into compaction band formation have been performed on sandstones that require stresses that are much higher than would typically be found in sedimentary basins in nature (Fossen et al., 2011; Sternlof et al., 2005). For example, experiments performed on sandstones such as Berea and Bentheim have required confining pressures as high as 300 MPa, equivalent to an overburden of 12 km (assuming a conservative geobaric gradient of 25 MPa/km), in order to form compaction bands. The compaction bands which were identified in this study, however, were formed at much lower effective pressures of 93 and 75 MPa, equivalent to overburden depths on the order of 3.7 and 3 km respectively. These values are more reasonable for natural sandstone burial depths; for instance, the compaction bands in the Aztec Sandstone (Nevada) identified by Sternlof et al. (2005), were estimated to form at depths of 2.5 km, while those in the Navajo Sandstone in Utah were estimated to form at approximately 1 km depth (Fossen et al., 2011). The synthetic sandstones used in this study may therefore provide a more realistic analogue to natural field sandstones than some of the sandstones commonly used in laboratory studies. Sternlof et al. (2005) also suggested that the dimensions (length and thickness) and damage intensity observed in the field were substantially lower than in laboratory specimens, an observation which Baud et al. (2004) also made for the discrete compaction bands formed in samples of Bentheim and Diemeldstadt sandstone. We also observe a significant amount of damage in the experimental compaction bands formed in the synthetic sandstones, since the localisation is always associated with significant grain crushing in our samples and is the primary localisation identifier over porosity reduction. Diffuse compaction bands, like those observed in our 27% porosity 411 μm sample

(Figure 4.8c-d), have not yet been reported in natural settings, possibly because they are harder to identify than discrete compaction bands, as suggested by Baud et al. (2004). Therefore, future field and experimental studies are required in order to gain a better understanding of these structures.

4.5 Conclusions

In this study we used synthetic sandstones, with three different starting porosities and four different starting grain sizes, to systematically study the effect of these properties on compaction localisation. Our results show that grain size plays an important role in compaction localisation, with discrete compaction bands oriented normal to the axial loading direction only found in the sample with the lowest starting porosity (27%) and smallest grain size (314 μm), while diffuse bands were observed for the same porosity but with a larger grain size of 411 μm. At coarser grain sizes the 27% porosity samples exhibited homogeneously distributed grain crushing without any evidence of localisation. In the samples where compaction bands were observed to form, they were associated more with a localised region of intense grain size reduction rather than a significant reduction in porosity. At the intermediate starting porosity tested in this study (32%), grain fracturing was relatively intense across the samples for all grain sizes, however, there was no evident compaction localisation. The highest starting porosity of 37% displayed no localised grain size reduction at any of the starting grain sizes and grain crushing was much more limited, implying grain rearrangement and comminution were the most dominant deformation mechanisms. Our results demonstrate that compaction bands are most likely to form in response to inelastic deformation in fine-grained sandstones with porosities <30%, in agreement with field observations of natural compaction bands; however, fine-grained units will require higher stresses to initiate inelastic compaction than coarser grained units and these stresses may not always be achieved at the typical burial depths of sedimentary basins in nature.

Supplementary material

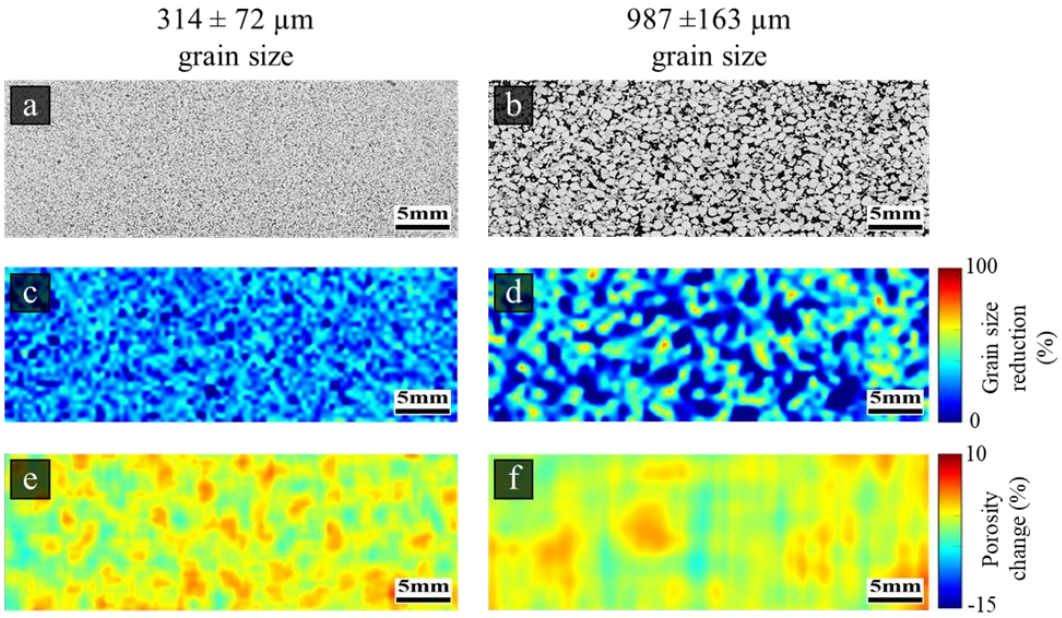

Supplementary Figure 4.1. *Whole core slice BSE micrographs for the 27% starting porosity, fine grain size (a) and coarse grain size (b) sandstone samples. Graphs of grain size reduction as a percentage decrease from the starting mean grain size (c and d) are also displayed for both samples, as are porosity change colourmaps (e and f).*

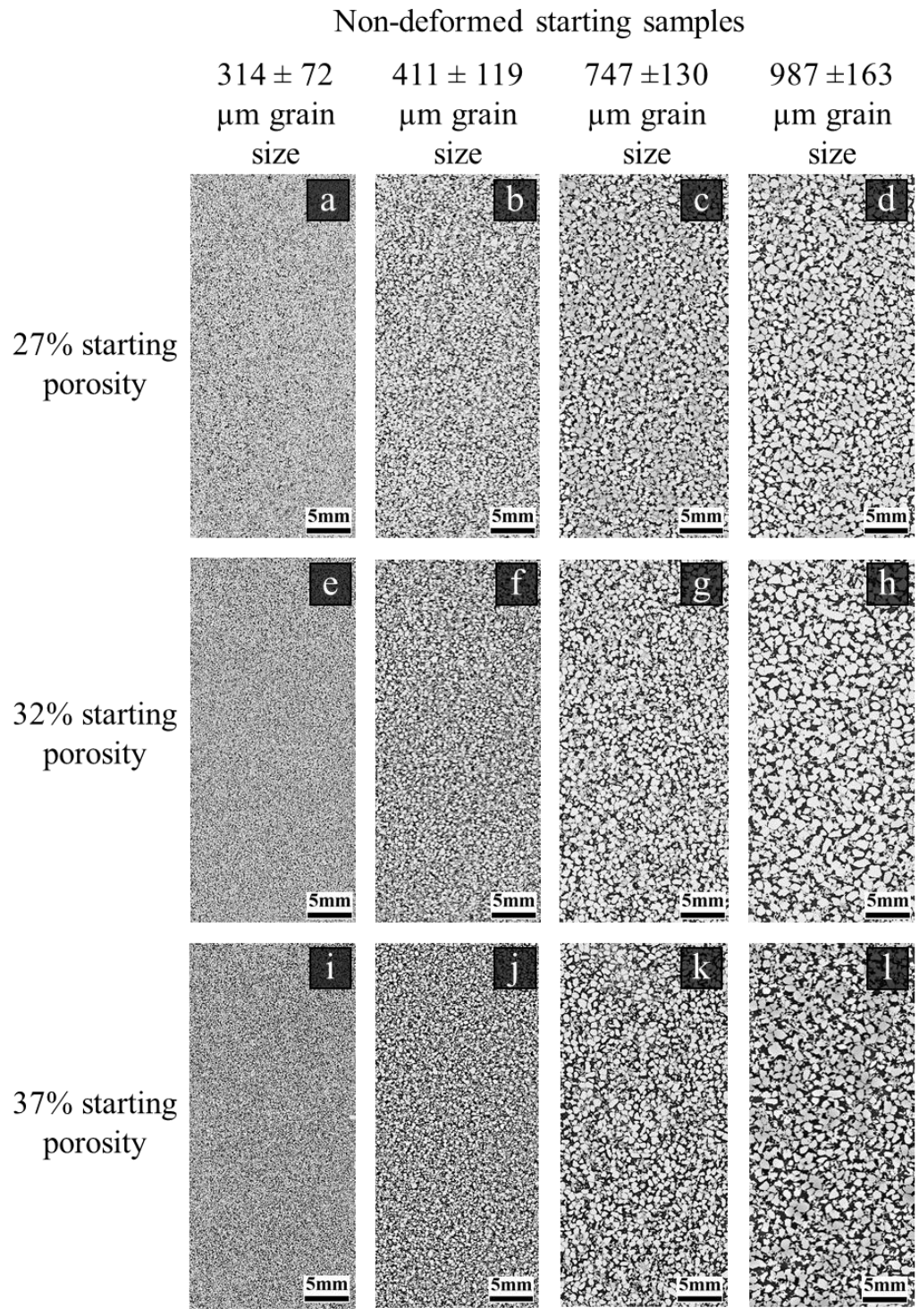

Supplementary Figure 4.2. *Whole core BSE images of the 12 undeformed synthetic sandstone samples.*

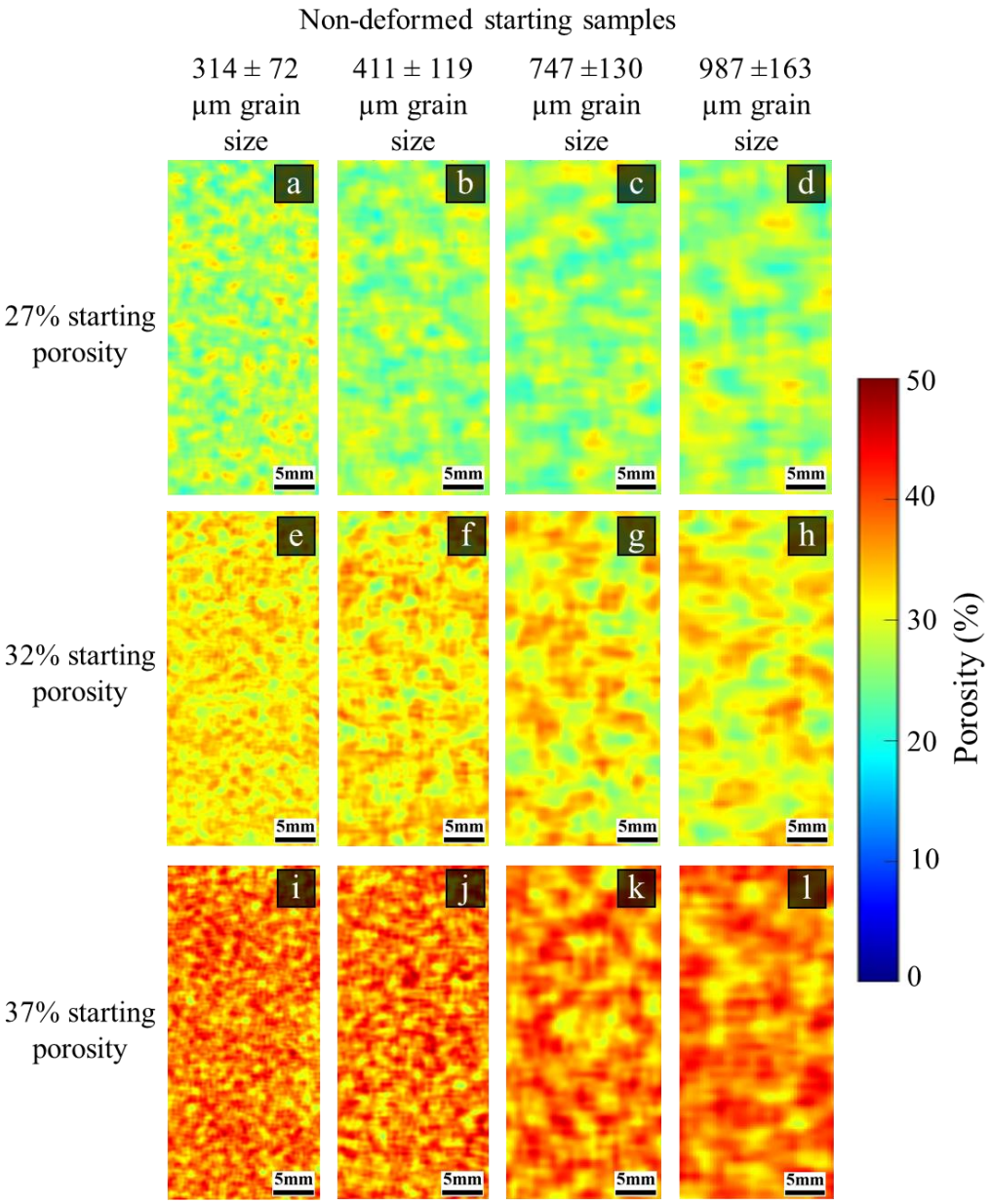

Supplementary Figure 4.3. *Porosity maps for the 12 undeformed synthetic sandstone samples. The maps highlight the homogenous distribution of porosity in the starting samples, indicating that the production process does not impart any significant inelastic damage to the samples.*

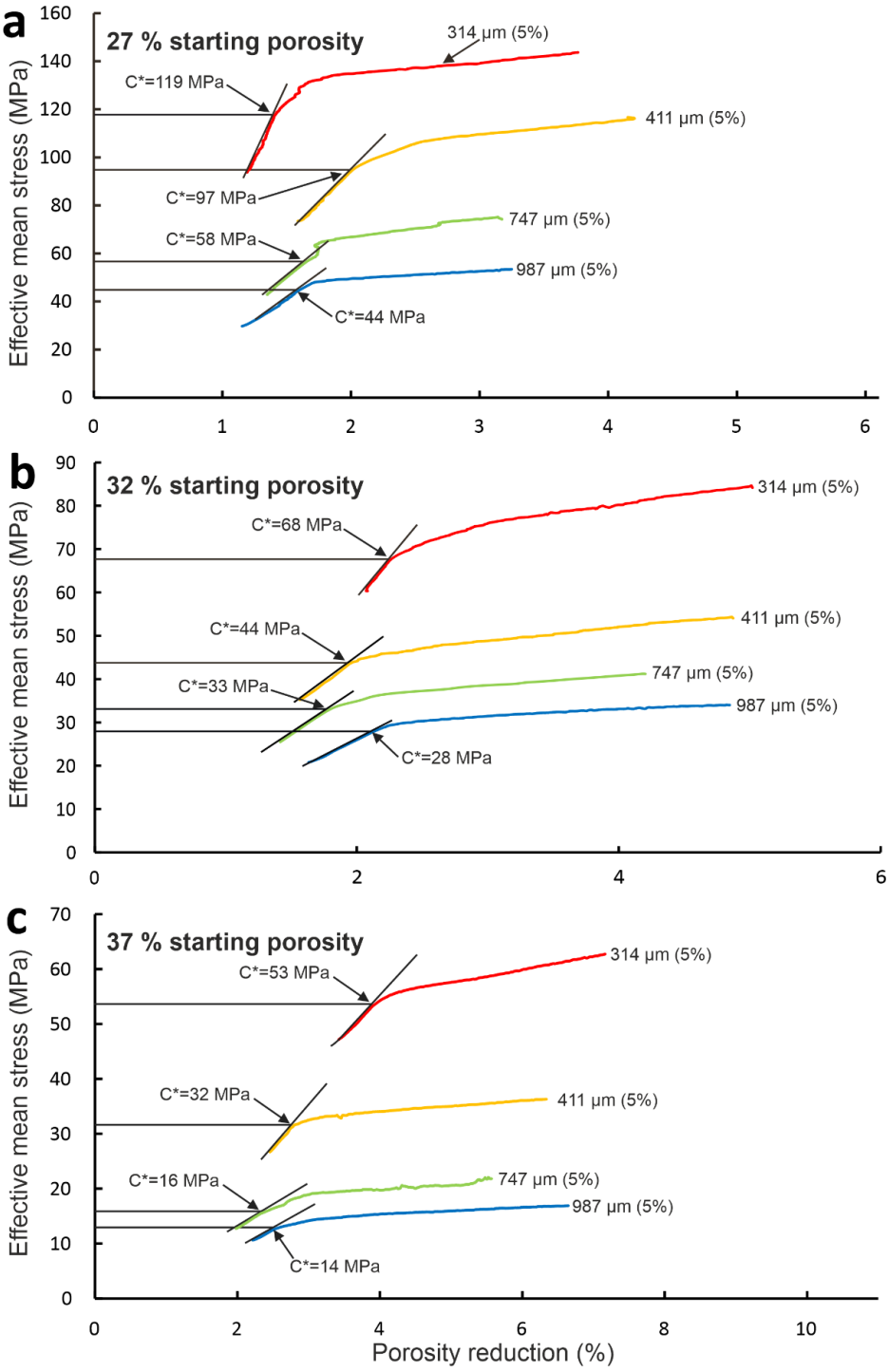

Supplementary Figure 4.4. *Graphs displaying the identification of C* through deviation from linear elastic pore volume (porosity) reduction for the 12 synthetic sandstones taken to 5% axial strain.*

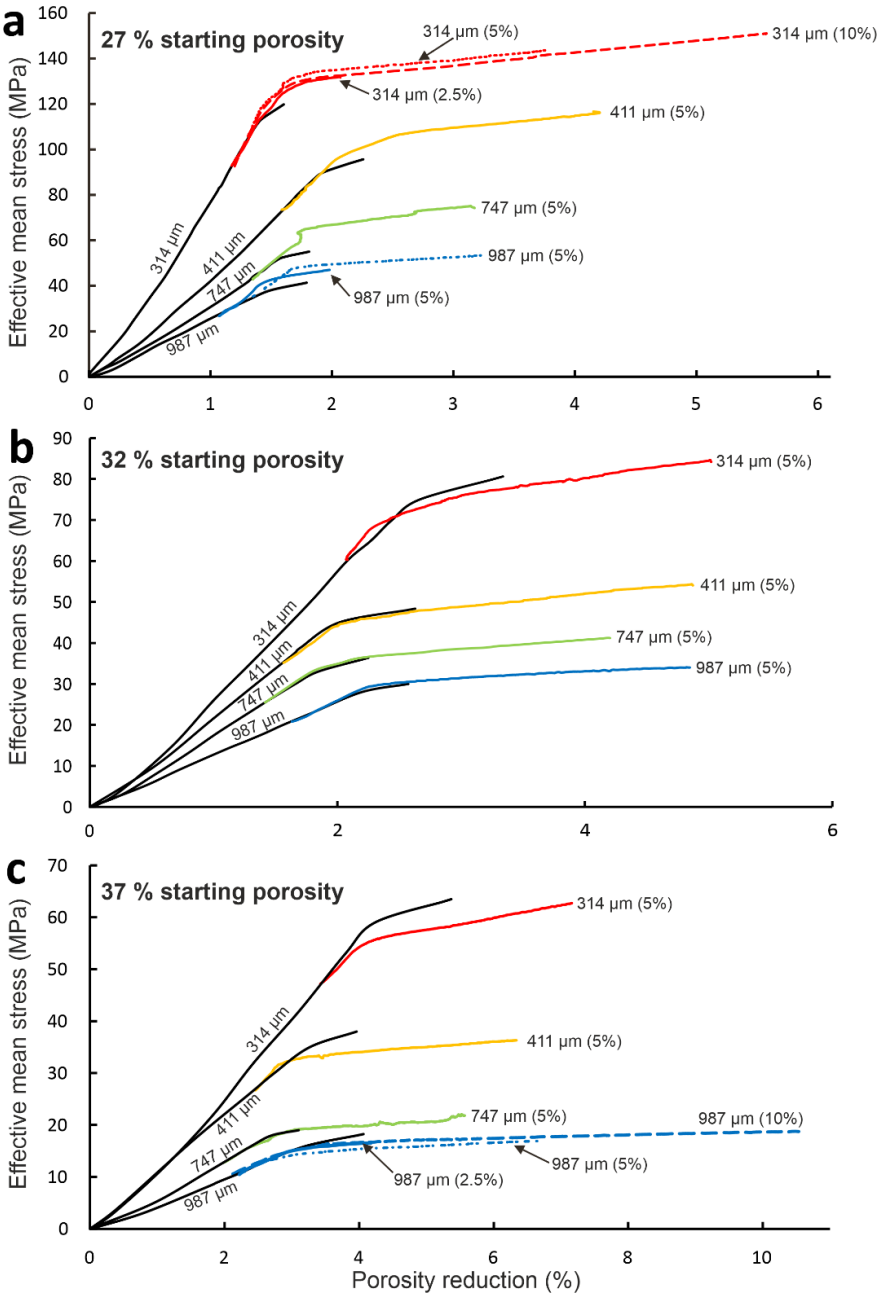

Supplementary Figure 4.5. *Graphs of porosity reduction versus effective mean stress for the 12 synthetic sandstones for a) 27%, b) 32% and c) 37% starting porosity. The 5 additional samples with 27% porosity, 314 µm and 37% porosity, 987 µm taken to 2.5% and 10% axial strain are also displayed, as is the 27% porosity, 987 µm sample taken to 2.5% axial strain. Unlike in Figure 4.2, these porosity reduction graphs have been plotted on different scales due to the very large porosity reductions on the x-axis, as a result of the inclusion of the 10% axial strain samples.*

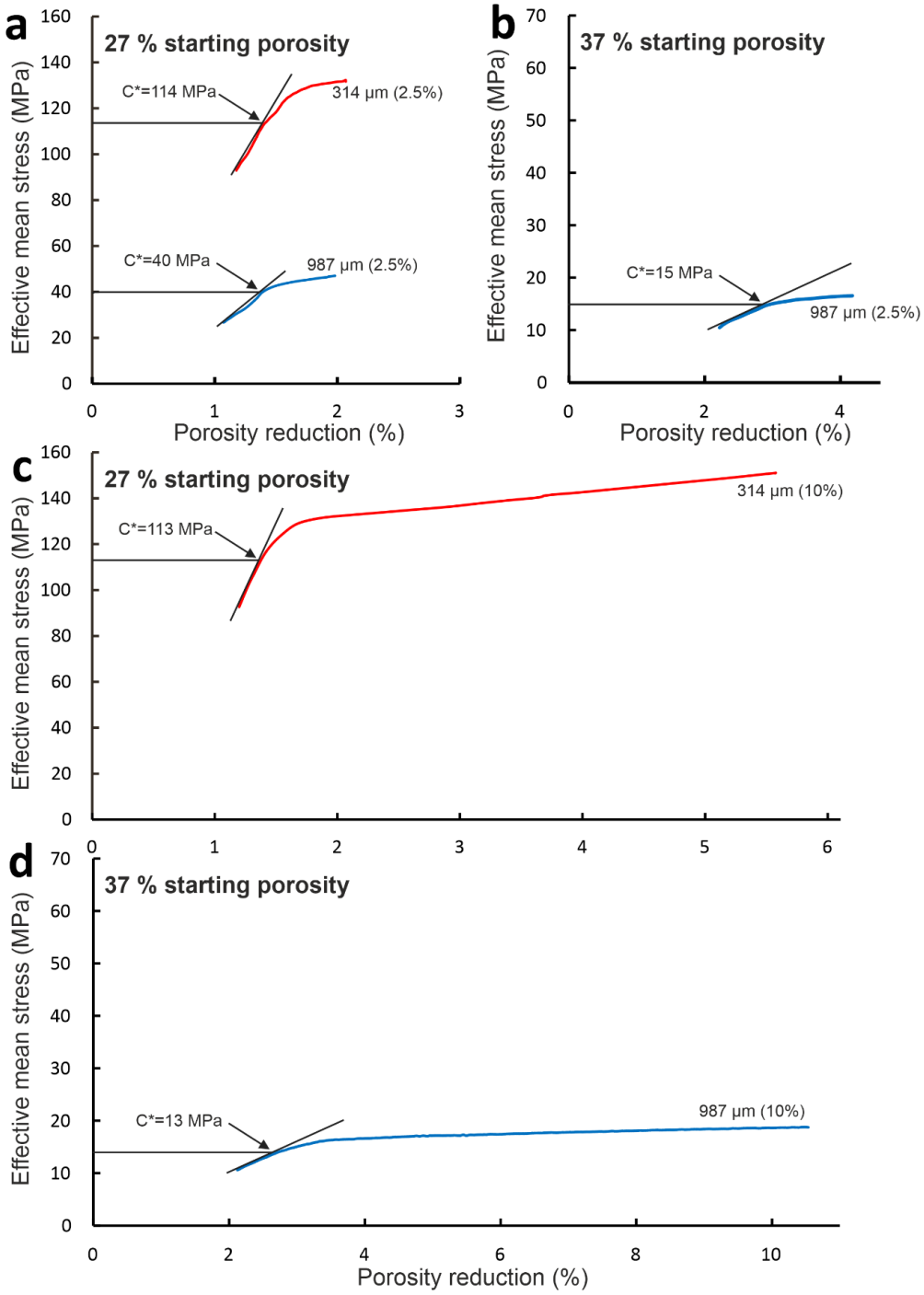

Supplementary Figure 4.6. *Graphs displaying the identification of C* through deviation from linear elastic pore volume (porosity) reduction for the additional 5 synthetic sandstones taken to 2.5% and 10% axial strain.*

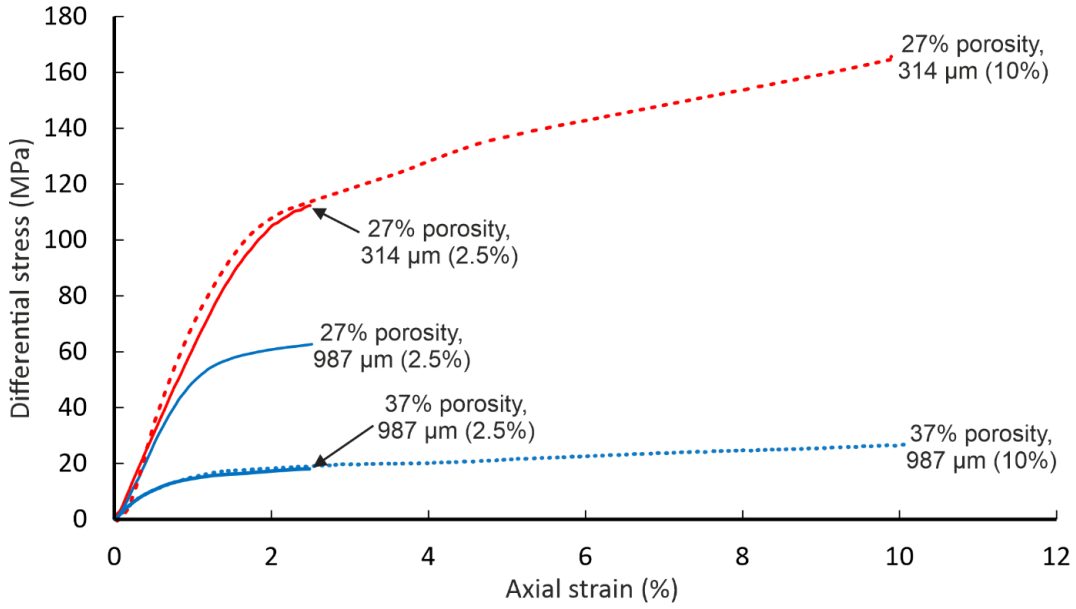

Supplementary Figure 4.7. *Axial loading curves for the additional 5 synthetic sandstones taken to 2.5% and 10% axial strain.*

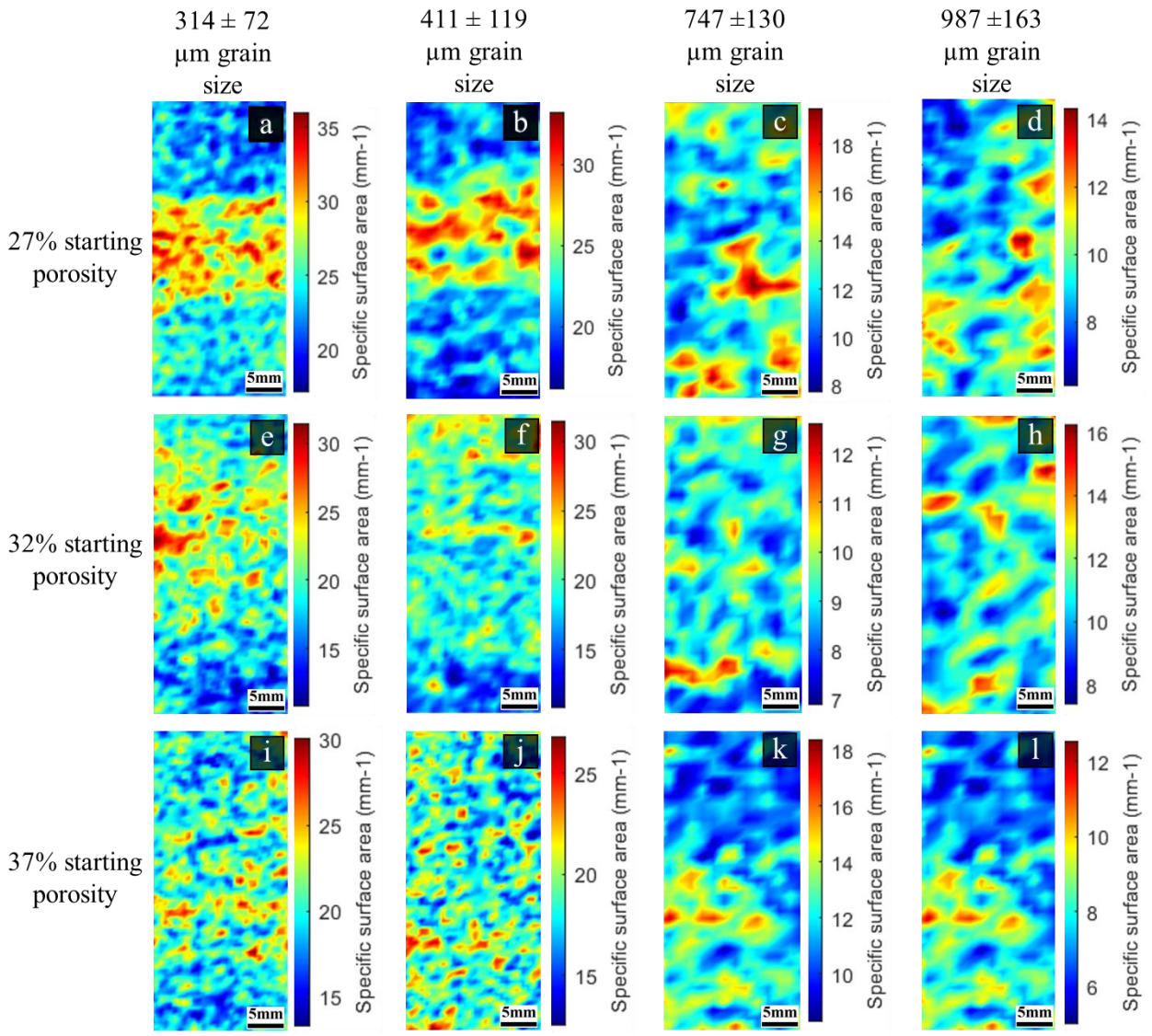

Supplementary Figure 4.8. *Specific surface area maps of the solid/grain space for the 12 deformed synthetic sandstones (a – l) constructed using the methodology of Rabbani et al. (2014b). Regions of intense localisation are associated with the discrete and diffuse compaction bands in the two samples with the smallest grain sizes and lowest starting porosities (a and b). However, there is less of a discernible pattern in the other samples, particularly at larger grain sizes.*

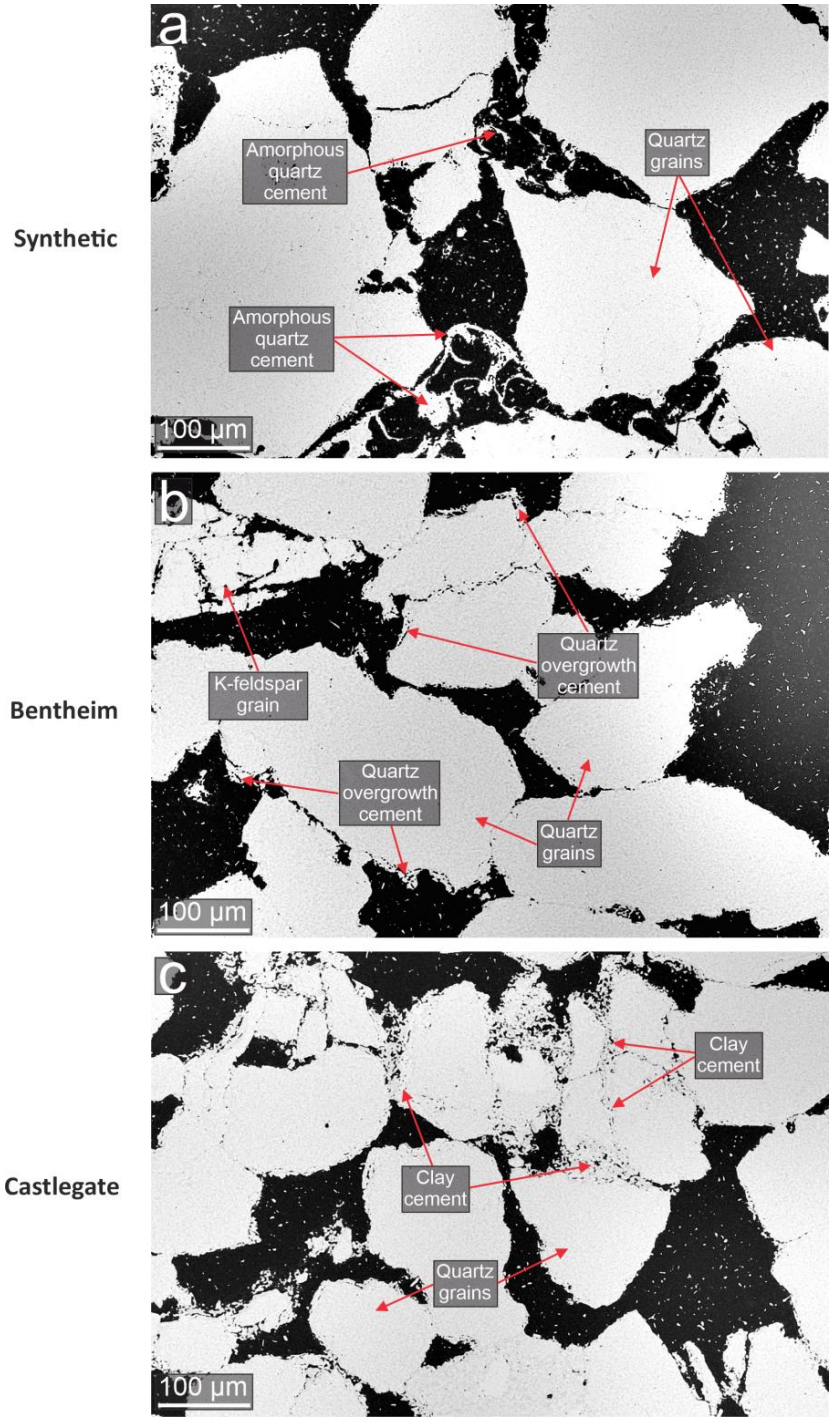

Supplementary Figure 4.9. *BSE images of 3 similar porosity (~27%) sandstones each with a different cement type. a) BSE image of the amorphous quartz cement within the 27%, 314 µm synthetic samples in this study, prior to deformation. b) Syntaxial quartz overgrowth cement in the Bentheim Sandstone. c) Clay cement in Castlegate Sandstone. The differing cement types may influence the micromechanics of deformation in different ways.*

Text S1

The onset of localised deformation in porous rocks can be predicted using non-associative flow laws. The type of localised structure that should occur during porous rock deformation can be predicted using the dilatancy factor (β) and internal friction (μ) parameters laid out by Rudnicki & Rice (1975). We have determined these parameters from our triaxial tests using the methodology outlined by Wong et al. (1997).

In *P*-*Q* space, Wong et al. (1997) states that the friction parameter (μ) can be evaluated as $\sqrt{3}/3$ times the slope of the failure envelope. We estimate (μ) from the slope of the yield curve in the region of 85% of *P**, while the elastic and inelastic triaxial loading data for 85% of *P** is used to determine (β). The results are displayed in Table SM 4.1. The dilatancy factor (β) is given by:

$$\beta = -\sqrt{3}\,\frac{\Delta\Phi^p/\Delta\varepsilon^p}{(3-\Delta\Phi^p/\Delta\varepsilon^p)}$$

where $\Delta\Phi^p/\Delta\varepsilon^p$ is an inelastic compaction factor where the superscript *p* denotes the plastic portion of the porosity and strain components and is given by:

$$\frac{\Delta\Phi^p}{\Delta\varepsilon^p} = \frac{(\Delta\Phi/\Delta\varepsilon) - \Phi\beta_\phi[\Delta(\sigma_1-\sigma_3)/\Delta\varepsilon]/3}{1-[\Delta(\sigma_1-\sigma_3)/\Delta\varepsilon]/E}$$

Where:

Φ = Porosity
ε = Axial strain
$\beta\phi$ = Pore compressibility
σ_1 = maximum principal stress
σ_3 = minimum principal stress
E = Young's modulus of the porous aggregate

The Young's modulus (E) can be determined from the slope of the initially linear part of a plot differential stress versus axial strain. The pore compressibility is defined to be (Wong et al., 1997):

$$\beta_\phi = \frac{1}{\Phi}\left(\frac{1}{V_{T^i}}\frac{\partial V_\phi}{\partial P}\right)$$

Where V_{T^i} is the initial bulk volume of the sample and V_ϕ is the pore volume (under the current effective stress conditions). The bracketed term corresponds to the slope of a plot of porosity change versus effective mean stress.

Supplementary Table 4.1. *Collation of elastic moduli and constitutive parameters for the yield curves of the 12 synthetic sandstones.*

Sample	Young's Modulus $\boldsymbol{E}$, GPa	Pore compressibility $\boldsymbol{\beta_\phi}$, 10^{-4} MPa^{-1}	Compaction factor $\Delta\boldsymbol{\Phi}\ /\Delta\boldsymbol{\varepsilon}$	Inelastic compaction factor $\Delta\boldsymbol{\Phi^p}/\Delta\boldsymbol{\varepsilon^p}$	Internal friction parameter, μ	Dilatancy factor, β
314 μm, 27% φ	7.13	3.55	0.306	0.306	-1.60	-0.184
314 μm, 32% φ	3.74	11.5	0.685	0.154	-0.427	-0.414
314 μm, 37% φ	3.14	26.4	0.758	0.696	-0.930	-0.541
411 μm, 27% φ	5.82	9.05	0.531	0.197	-1.048	-0.237
411 μm, 32% φ	3.72	16.1	0.471	0.509	-0.563	-0.309
411 μm, 37% φ	2.65	14.4	0.346	0.179	-0.424	-0.159
747 μm, 27% φ	4.72	12.5	0.357	0.431	-0.438	-0.236
747 μm, 32% φ	3.04	6.54	0.741	0.008	-0.569	-0.412
747 μm, 37% φ	2.42	17.6	0.672	0.302	-0.650	-0.408
987 μm, 27% φ	4.44	11.7	0.305	0.867	-0.426	-0.197
987 μm, 32% φ	2.91	23.3	0.500	1.11	-0.577	-0.348
987 μm, 37% φ	1.92	47.03	0.904	1.03	-0.426	-0.789

For our experiments, compaction localisation was only predicted in the sample with the lowest porosity and smallest grain size which, incidentally, developed discrete compaction bands, whereas shear localisation was predicted for the rest of the samples (Figure SM 4.6). The bifurcation analysis was unable to predict the development of the diffuse compaction band observed in the 27% porosity 411 µm sample (Figure 4.8c and d). This is likely because the microstructural properties of the rock, such as the nature of grain contacts, pore geometry and porosity will affect its localisation behaviour, and the interplay between these elements may not be fully captured by the theoretical prediction.

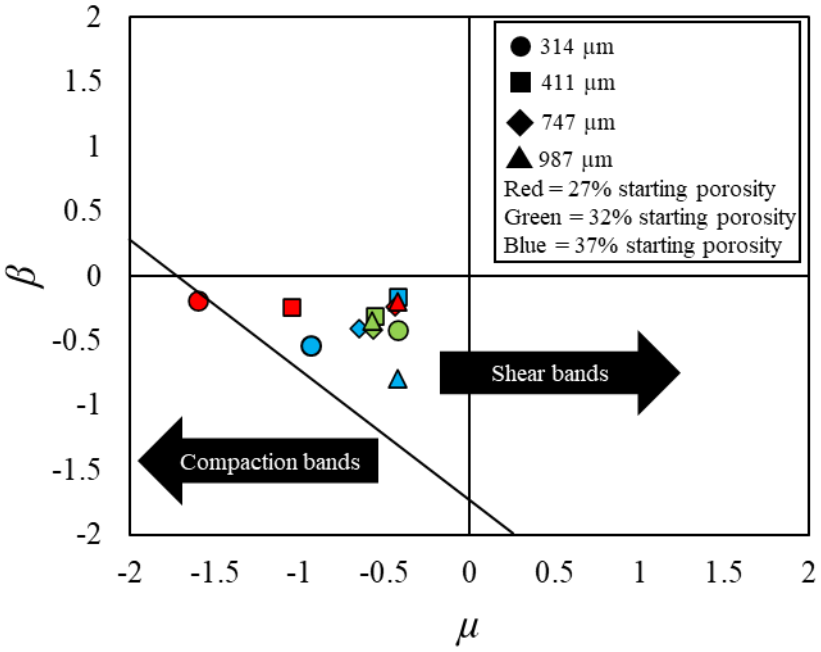

Supplementary Figure 4.10. *A plot of dilatancy factor (β) versus friction parameter (μ) for the 12 synthetic sandstone samples. The sample with the lowest starting porosity and smallest mean grain size plots in the region associated with compaction band formation, while the other 11 samples plot in the region associated with localised shear bands- see Issen & Rudnicki (2000) for more details on the theoretical analysis.*

5 The effect of cement type on the occurrence and nature of compaction localisation in three high-porosity sandstones

Abstract

Compaction bands are a type of strain localisation structure which form perpendicular to the maximum principal stress in the subsurface and can significantly disrupt fluid flow in porous sandstone reservoirs, potentially impacting on industrial fluid injection/extraction. The properties of sandstones that determine whether or not compaction bands form is still obscure. In this study we examine the role of cement on compaction band formation. We perform triaxial tests on three sandstones, Bentheim, Castlegate and a synthetic sandstone which possess very similar porosities (~26-29%) and grain sizes (~230-300 μm), but which are cemented differently, with syntaxial quartz overgrowths, clay, and amorphous quartz cement respectively. Each sample forms discrete compaction bands when taken to 5% axial strain at a starting effective stress equivalent to 85% of its hydrostatic yield (P^*) value. However, the location and distribution of the compaction bands differs within each sample. In Bentheim Sandstone, the compaction bands are only located at the sample ends. By contrast, in Castlegate Sandstone, compaction bands are distributed throughout the whole sample and in the synthetic specimen, the bands only form within the central region of the sample. Our results suggest that cement type plays a significant role in the micromechanics of deformation within each of the sandstones, which in turn, determines where the compaction bands nucleate and develop. Additionally, since all the compaction bands identified are discrete (≤3 grain diameters in width), rather than diffuse (>3 grain diameters in width) as typically seen in nature, we suggest that cement is not the primary control regarding the preference for the formation of diffuse or

discrete compaction bands. Our study highlights the potential importance of cement on compaction band formation in sandstones.

5.1 Introduction

When porous rocks such as sandstones are subjected to an applied differential stress, the deformation can be accommodated in the form of localised deformation structures, known as deformation bands (Aydin, 1978; Fossen et al., 2018). Depending on the effective stress at which these structures were formed, they can be categorised kinematically into 3 types. Dilation bands, which form at low effective stress relative to the hydrostatic yield value (P^*), shear bands at intermediate effective stress and compaction bands at high effective stress (Fossen et al., 2007, 2018). Each type of deformation band can influence fluid flow in reservoirs by altering the localised porosity and permeability and thus, creating or destroying permeability pathways (Ballas et al., 2015; Main et al., 2003; Ngwenya et al., 2003). This makes the attempt to understand their formation crucial for the extraction and injection of fluids in the oil and gas, water and CO_2 sequestration industries (Hangx et al., 2010, 2013; Sternlof et al., 2006). Perhaps the most important type of deformation band to form in porous reservoirs are compaction bands, since they are typically associated with very intense grain crushing and often a reduction in pore size, porosity, and permeability (Charalampidou et al., 2011; Fossen et al., 2018). Compaction bands can be subdivided into two types; pure compaction bands (PCBs) and shear-enhanced compaction bands (SECBs) (Eichhubl et al., 2010; Fossen et al., 2018). PCBs form normal to the maximum principal stress direction and are characterised as narrow, tabular zones of inelastic deformation, which have accommodated pure compaction (volume loss) with no evidence of shear strain. SECBs form oblique to the loading direction and accommodate a small element of shear strain (Charalampidou et al., 2014).

Since their identification by Mollema & Antonellini (1996), numerous laboratory studies have attempted to investigate the lithological properties of sandstones which promote the development of compaction bands (Baud et al., 2004, 2015; Klein et al., 2001; Olsson &

Holcomb, 2000; Stanchits et al., 2009). The role of porosity has been examined by several studies (DiGiovanni et al., 2000; Olsson et al., 2002; Olsson & Holcomb, 2000; Olsson, 2001; Wong et al., 2001), with the results indicating that compaction bands in natural sandstones can only form in porosities of ~13-30% (Carbillet et al., 2021), with some authors observing them to preferentially develop in high porosity sandstones (Baud et al., 2004). The nucleation of compaction bands has also been suggested to preferentially develop in sandstones with local heterogeneities, such as high-porosity regions (Baud et al., 2015; Fortin et al., 2005), large pores (Louis et al., 2007) or artificially cut notches (Fortin et al., 2009), due to the stress concentrations these features produce (Stanchits et al., 2009). However, compaction bands have also been produced in sandstones that appear to be initially homogeneous at the sample scale, suggesting that other factors also influence their formation (Fortin et al., 2006; Klein et al., 2001).

The role of grain size distribution was examined by Cheung et al. (2012), who found that discrete compaction bands formed over a wide range of pressures in the well-sorted Bleurswiller Sandstone, whilst no bands developed in the poorly-sorted Boise Sandstone, which deformed by distributed cataclastic flow. Recently, the role of grain size was also examined by Rice-Birchall et al. (2022) using synthetic sandstones with controlled properties. They found that compaction bands preferentially developed in sandstones with starting porosities of 27% (as opposed to 32% or 37%) and grain sizes of 314 μm and 411 μm (as opposed to 747 μm and 987 μm). Coarser grained samples at the same starting porosity (27%) deformed by distributed cataclastic flow.

Cement is a key defining property of sandstones, although to date, there have been no experimental studies examining how cement might play a role in compaction localisation. The most relevant studies in this regard have analysed the deformation characteristics of unconsolidated sand, for instance, Hangx & Brantut (2019) who performed triaxial deformation experiments on unconsolidated Ottawa sand with a porosity of 36%. However, they did not observe any localised deformation in the compactant deformation regime. The role of cement

has also been examined in some discrete element method (DEM) modelling studies. Liu et al. (2015) concluded cement strength to be one of the key properties affecting the pattern of sinuous compaction bands, whereas Marketos & Bolton (2009) found that the nature of compaction localisation (i.e., diffuse or discrete) may also be influenced by cement bond strength, with a switch from diffuse to discrete bands when the bond-strength was increased. The results of these studies, examining cement (or lack thereof) do seem to suggest that cement exerts some control, both on whether compaction localisation develops, and on the patterns (sinuous or straight) and morphology (diffuse or discrete) of the bands themselves.

The aim of this study therefore, is to perform the first set of experimental tests on sandstones where the control of cement on compaction localisation is systematically studied. To achieve this, we selected three sandstones, each with very similar microstructural properties (i.e., porosity, grain sorting, grain size, grain shape, mineralogy) but with differing cement types. Each sandstone was subjected to the same triaxial test conditions relative to their microstructurally determined yield strengths and so the results of this study provide insight into the role that cement type plays in localisation development.

5.2 Methods and materials

5.2.1 Microstructural properties of the starting samples

The three sandstones selected to use in this study were Bentheim Sandstone, a shallow marine sandstone from Germany; Castlegate Sandstone, a fluvial sandstone from Utah (USA); and an artificial synthetic sample. The synthetic sample was produced in the laboratory using the methodology of Rice-Birchall et al. (2021) whereby sand grains are cemented together using the chemical reaction between sodium silicate solution and hydrochloric acid, which precipitates amorphous quartz cement between the grains. The quantity of the cement and the porosity can both be controlled by varying the degree of compression of the mould during the reaction and by varying the quantity of reactants. In this study, the technique was used to lithify very well-sorted, subangular/subrounded quartz grains, to produce homogeneous sandstone

cores for testing, with similar properties to the 2 natural sandstones. Prior to mechanical testing, a range of analytical techniques were deployed to determine the microstructural properties of each sandstone, with these displayed in Table 5.1. Bentheim, Castlegate and the synthetic sample have average porosities of 26.1%, 29.5% and 27.4% respectively, determined via helium porosimetry. Laser diffraction particle size analysis with a Beckman Coulter LS 13 320, complimented with further analysis using the grain size quantification program GRADISTAT (Blott & Pye, 2001) found each of the samples to be well-sorted, with an average grain size of 254 ± 107 μm for Bentheim Sandstone, 228 ± 68 μm for Castlegate Sandstone and 314 ± 72 μm for the synthetic sample. The grain shapes were analysed using 2D quantitative image analysis of the starting material in the image analysis program Fiji, with each of the samples being composed primarily of subangular to subrounded grains. The bulk mineralogical compositions for each sandstone were determined using X-ray powder diffraction (XRD), with Bentheim Sandstone composed of 97% Quartz, 2% K-feldspar and 1% kaolinite; Castlegate Sandstone of 93% Quartz, 3% K-feldspar, 1% muscovite, 1% illite, and 2% kaolinite and the synthetic sample of 90% Quartz, 5% K-feldspar and 5% plagioclase. The composition, distribution and morphology of the cement was determined using energy-dispersive X-ray spectroscopy (EDS) with a JEOL JSM 6610 scanning electron microscope (SEM). Bentheim Sandstone is cemented with diagenetic syntaxial quartz overgrowths, whereas Castlegate Sandstone is predominantly clay cemented with small amounts of quartz overgrowth on some of the quartz grains. The grains in the synthetic sample are cemented with amorphous quartz, as described in Rice-Birchall et al. (2021).

For the triaxial tests, cylindrical cores approximately 20 mm in diameter and 50 mm in length were drilled from the Bentheim and Castlegate sandstone blocks, perpendicular to the bedding direction, while synthetic sandstones of a similar size were produced using the aforementioned methodology. Each core was then precision ground to produce parallelism of the two opposing faces to a tolerance of ± 0.01 mm using a surface grinder, ready for mechanical testing.

Table 5.1. *Compilation of the microstructural properties for the three sandstones in this study. Our mineralogical observations for the Bentheim and Castlegate sandstones are supported by those from other studies (DiGiovanni et al., 2007; Peksa et al., 2015).*

Sandstone	Average porosity (%)	Grain size (μm)	Grain sorting	Grain shape	Cement type	Mineralogy (%)
Bentheim	26.1	254 ± 107	Well-sorted	Subangular/ subrounded	Quartz cement (diagenetic syntaxial overgrowths) (Peksa et al., 2015)	Quartz (97), K-feldspar (2), kaolinite (1)
Castlegate	29.5	228 ± 68	Well-sorted	Subangular/ subrounded	Authigenic clays present as pore lining and cement and sometimes as pore filling material. Very small amounts of cementing silica overgrowth on quartz grains. Some detrital muscovite in pore space. Well-connected pore network (DiGiovanni et al., 2007)	Quartz (93), K-feldspar (3), muscovite (1), illite (1), kaolinite (2)
Synthetic	27.4	314 ± 72	Well-sorted	Subangular/ subrounded	Amorphous quartz cement	Quartz (90), plagioclase (5), K-feldspar (5)

5.2.2 Triaxial deformation experiments

5.2.2.1 Deformation apparatus

Triaxial tests were conducted to determine the mechanical properties of the three sandstones and to inelastically deform the samples to try to produce compaction bands. The experimental apparatus used was a high-pressure triaxial deformation rig designed and built at the University of Liverpool (Mitchell & Faulkner, 2008). It consists of servo-controlled confining and pore pressure systems which can monitor pressure to a resolution better than 0.01 MPa. Argon was used as the pore fluid in this study as it is chemically inert and so minimises the effects of any creep behaviour via sub-critical crack growth (Atkinson & Meredith, 1981; Heap et al., 2009). The pore-fluid pressure was maintained at 20 MPa during all experiments

in this study. Each sample was inserted into an annealed copper jacket (20.2 mm internal diameter and 0.3 mm wall thickness), prior to being inserted into the deformation apparatus, with two porous discs placed on either side of the sample. The sample and copper jacket were then inserted into a Viton™ jacket to prevent any leaks of the confining fluid into the sample, should the wall of the thin copper jacket perforate during pressurisation and deformation. This jacket arrangement was chosen as the copper jacket provides support of the sample after the test so that microstructures could be preserved.

The axial load was generated by a servo-controlled electromechanical piston and is measured by an internal force gauge to a resolution better than 0.03 kN. The axial displacement is measured by an LVDT attached to the base of the loading column. The axial strain that the sample experiences is calculated by subtracting the elastic deformation taken up by the loading column from the total axial displacement. The stiffness of the loading column is 119 kN/mm.

5.2.2.2 Experimental procedure

The hydrostatic yield strengths (P^*) for the Bentheim, Castlegate and the synthetic sandstones were determined by incrementally increasing the confining pressure to apply a hydrostatic load, while the pore volume changes were monitored as the pore-fluid pressure was kept constant at 20 MPa. P^* was identified by the deflection in the hydrostatic loading curve marking the onset of inelastic deformation (Zhang et al., 1990).

The high-resolution stress-probing methodology of Bedford et al. (2018) was used to map the yield curves for each sandstone from a single sample in P-Q space, where P is the effective mean stress ($P = \left(\frac{\sigma_1+\sigma_2+\sigma_3}{3}\right) - P_f$), P_f is the pore-fluid pressure and Q is the differential stress ($Q = \sigma_1 - \sigma_3$). This method has previously been shown to produce the same results as using multiple samples to map out the yield curve (Bedford et al., 2018, 2019; Rice-Birchall et al., 2021). To map the yield curve for each sample, the confining pressure was incrementally reduced from P^* and the yield curve was probed by axially loading the sample between each incremental reduction in pressure. For each probing increment the samples were

axially loaded at a rate of 1 μm/s (strain rate ≈ 2×10^{-5} s^{-1}) until yield was identified by the departure from quasi-linear loading, whereupon the axial load was immediately withdrawn (at a rate of 5 μm/s) to ensure minimal inelastic damage was imparted onto the sample. The confining pressure was then reduced further, and the stress-probing procedure repeated to map the rest of the yield curve. Once P^* was determined, new, non-deformed samples were inserted into the deformation apparatus and loaded at an effective pressure equivalent to ~85% of P^* to 5% axial strain at a displacement rate of 1 μm/s.

5.2.3 Microstructural analysis

After the three axial loading experiments, each core was vacuum impregnated with a low-viscosity epoxy resin in preparation for microstructural analysis of the whole core. Three cores of the intact Bentheim, Castlegate and synthetic sandstone starting material were prepared the same way, so as to perform microstructural analysis of the sandstones prior to deformation. Three smaller samples of the starting materials were also produced and impregnated in order to conduct EDS, since this analysis required smaller samples. Once the epoxy had set, the cores were cut in half down their long axes and this surface polished and carbon coated ready for imaging using a Hitachi TM3000 scanning electron microscope (SEM). Backscatter scanning electron (BSE) images were collected at 50× magnification, with these images stitched together using GigaPan Stitch software to produce a whole core image. The stitched images were then uploaded into the image analysis program Fiji (Schindelin et al., 2012) and binarised into porosity (white) and grains (black) in order to perform detailed image analysis. Maps of porosity distribution were constructed for each of the samples using the techniques outlined by Rice-Birchall et al. (2021), which involves dividing the image up into a series of overlapping grids, the size of which is determined using statistical representative elementary area (REA) analysis. Grain size variations in this study were presented as equivalent radius, which is the radius of a circle with the same area as a that of a measured binary grain (Heilbronner & Barrett, 2013). Colourmaps of percentage reduction in grain size from the starting mean grain size across each sample were produced, using the formula:

$$Grain\ size\ reduction\ (\%) = \frac{R_m - R}{R_m} \times 100 \qquad (5.1)$$

where R_m is the mean equivalent grain radius of the non-deformed sample and R is the equivalent grain radius calculated for each individual grain in the deformed sample.

5.3 Results

5.3.1 Microstructure of the starting material

Figure 5.1 displays whole core BSE images for the Bentheim, Castlegate and synthetic sandstones. The maps for the three samples show that they each have homogeneous porosity and grain size distributions, indicating that there are no obvious heterogeneities in the starting material, such as fractures or bedding contacts which may significantly influence the nature of the deformation. Since Castlegate Sandstone has smaller grains than the other two samples, a smaller REA grid size was specified, which is the reason for the smaller-scale porosity fluctuations observed in the porosity map.

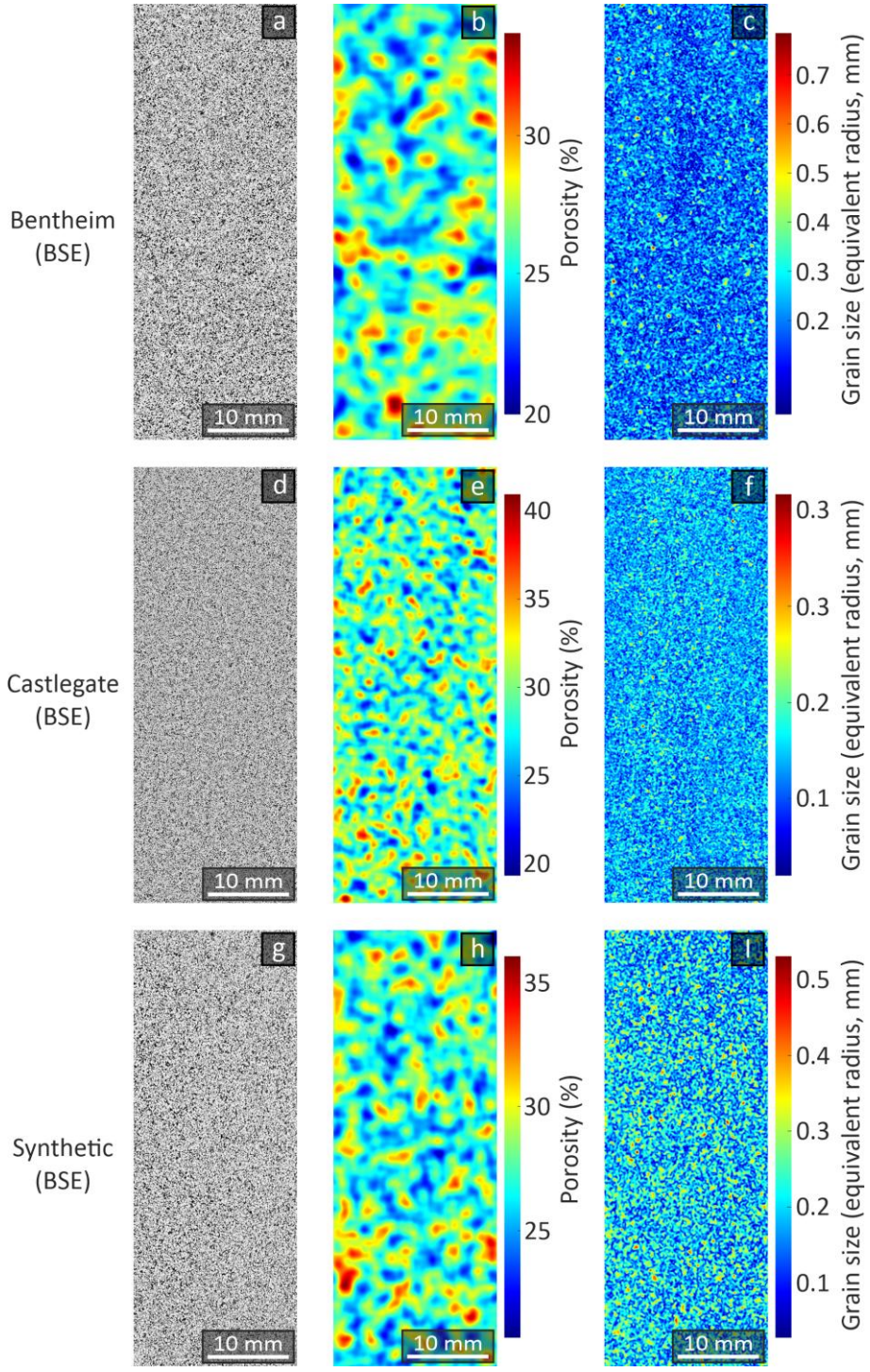

Figure 5.1. *BSE images (a, d, g), porosity distribution maps (b, e, h) and grain size distribution maps (c, f, i) of the non-deformed starting material for the Bentheim, Castlegate and synthetic sandstone.*

5.3.2 Cement characteristics and microstructure

In Figure 5.2 BSE images are displayed which highlight the different cements present within each of the 3 sandstones. EDS maps for each of the images are also displayed in supplementary material (Figures SM 5.1-5.3) which, along with XRD, were used to aid in the determination of the cement composition. The grains in Bentheim Sandstone are cemented by syntaxial quartz overgrowths, in agreement with other studies examining this sandstone (Klein et al., 2001; Peksa et al., 2015). The syntaxial quartz is most visible away from the grain contacts, indicating cementation at depth, following mechanical compaction (Dapples, 1962). By contrast, Castlegate Sandstone is cemented predominantly with kaolinite, muscovite and illite phyllosilicate clay minerals. Unlike in Bentheim Sandstone, the clays surround many of the grains, although few clay minerals can be seen filling the pore space, suggesting the clays are primarily grain-cementing, rather than pore filling, supported by the observations of DiGiovanni et al. (2007) (Table 5.1 and Figure 5.2b). As seen in Rice-Birchall et al. (2021), the synthetic sandstone samples display amorphous silica cement that forms sinuous, branching structures which are most-concentrated near the grain contacts (Figure 5.2c). However, in places the cement does accumulate within some of the smaller pore spaces.

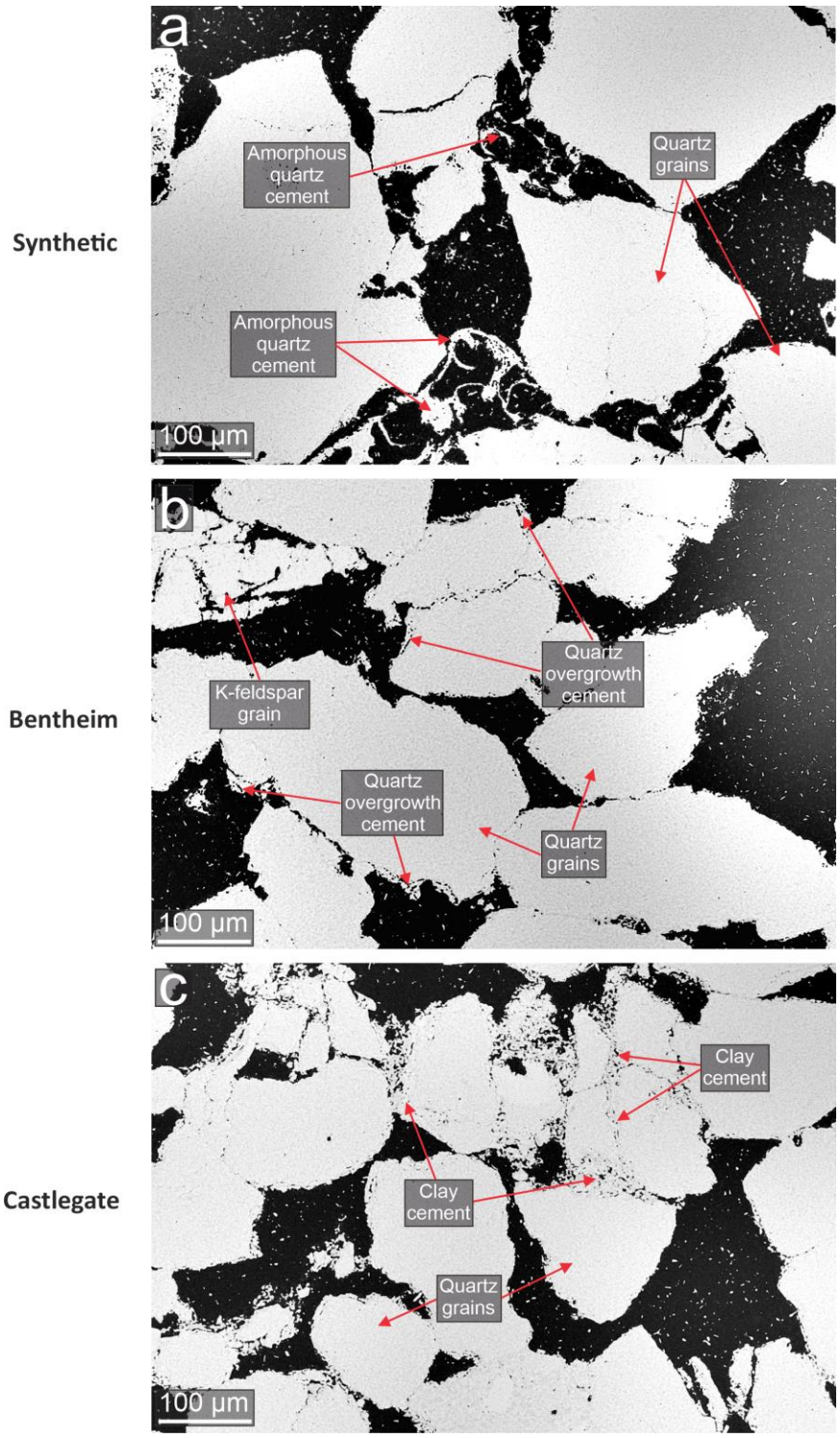

Figure 5.2. *BSE images of Bentheim (a), Castlegate (b) and synthetic (c) sandstones, produced in order to identify the different cement types in each. EDS maps for each of the images in this figure are presented in the supplementary material (Figures SM 5.1-5.3).*

5.3.3 Mechanical results

Figure 5.3 displays a compilation of mechanical data produced for each of the three sandstones. Figure 5.3a displays a plot of axial strain versus differential stress. Deviation from quasi-linear elastic axial loading marks the onset of yield (*C**). Each of the samples displays strain-hardening behaviour beyond their respective yield points, with Bentheim Sandstone also exhibiting numerous stress drops, which are often indicative of the formation of shear fractures and shear bands (Tembe et al., 2008). Young's modulus values extracted from the linear part of the axial loading curve are displayed in Table 5.2. Castlegate Sandstone exhibits the lowest value of 5.2 GPa, due to its shallower loading curve and lower *C**, compared to Bentheim Sandstone (9.28 GPa) and the synthetic sample (7.12 GPa).

Figure 5.3b displays porosity change versus effective mean stress during hydrostatic loading for each sample. This can be compared with the porosity evolution from axial loading, because in a conventional axisymmetric triaxial test, where the confining pressure is being held constant during axial loading, the effective mean stress will increase by $\Delta\sigma_1/3$ as the axial stress is increased. Each sample experienced inelastic compaction and porosity reduction, with Castlegate Sandstone undergoing the largest porosity reduction of around 8.5%, whilst Bentheim Sandstone displayed a porosity reduction of 5.5% and the synthetic sample showed a reduction of 4.4%. Table 5.2 also displays bulk modulus values extracted from the linear section of the hydrostatic loading curve. Again, Castlegate Sandstone exhibits the lowest value of 4.2 GPa, due to its greater compressibility compared to Bentheim Sandstone (6.9 GPa) and the synthetic sample (5.16 GPa).

The yield curves of the 3 sandstones plotted from the triaxial data are displayed in Figure 5.3c. The curves are all broadly elliptical, although they have a steep, overhanging compaction limb on the high-pressure side close to the region of *P**. Although Castlegate Sandstone exhibits a measured *P** value similar to that of Bentheim Sandstone, it exhibits significantly lower axial yield strengths, resulting in a yield curve with a much higher aspect ratio (2.14) compared to Bentheim (1.6) and the synthetic sandstone (1.16).

As well as the calculated values of *P**, Table 5.2 also displays the theoretical values calculated using the using the Hertzian contact model of Zhang et al. (1990).

$$P^* \propto (R\phi)^{-3/2} \qquad (5.2)$$

where R is grain radius (mm) and ϕ is fractional porosity. The model generates *P** values of 166, 162 and 95 MPa for Bentheim, Castlegate and the synthetic sandstone respectively, which are each significantly lower than those determined experimentally, of 235 MPa (Bentheim), 218 MPa (Castlegate) and 113 MPa (synthetic).

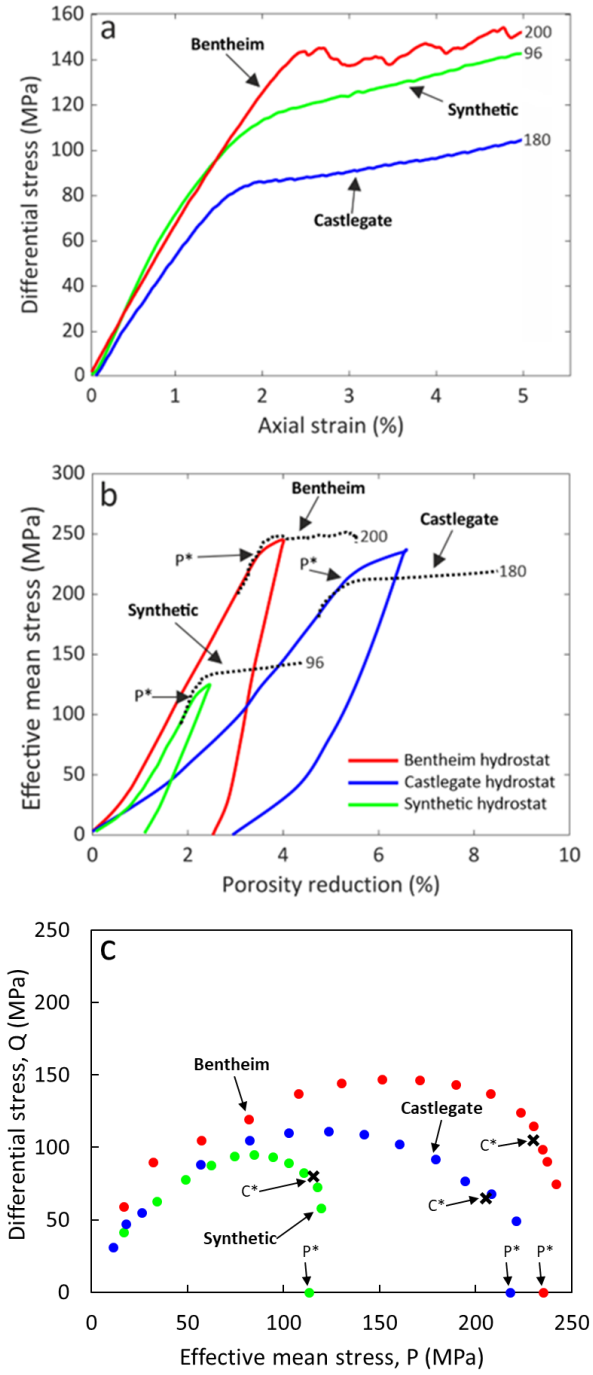

Figure 5.3. *Mechanical data from triaxial compression experiments on the Bentheim, Castlegate and synthetic sandstone samples, each taken to 5% axial strain. a) Differential stress versus axial strain. b) Effective mean stress versus porosity reduction. c) Yield curves for the 3 sandstones plotted in P-Q space. The values next to the curves in a) and b) correspond to the effective mean stress at the initiation of axial loading.*

Table 5.2. *Mechanical and elastic properties obtained from the mechanical tests on each of the 3 sandstones. Bulk modulus has been calculated from the quasi-linear section of the hydrostatic loading curves and Young's modulus from the quasi-linear elastic part of the axial loading curves, prior to yielding.*

Sandstone	**Average porosity (%)**	**Grain size (μm)**	***P**** **(measured, (MPa eff)**	***P**** **(theoretical, (MPa eff)**	***C**** **(MPa eff)**	**Bulk Modulus (GPa)**	**Young's Modulus (GPa)**
Bentheim	26.1	254 ± 107	235	166	237	6.9	9.28
Castlegate	29.5	228 ± 68	218	162	200	4.2	5.2
Synthetic	27.2	314 ± 72	113	95	118	5.16	7.12

5.3.4 Microstructure of the deformed samples

Figure 5.4 displays a compilation of microstructural data for the 3 deformed sandstones taken to 5% axial strain. Bentheim Sandstone exhibits discrete compaction bands, which are concentrated at the top and bottom of the sample, whilst the grains in the rest of the sample remain relatively intact (Figure 5.4a-d). These bands are the thickest of the three samples at predominantly 3 grain diameters width and also show the most intense grain fracturing and grain size reduction. By contrast, in Castlegate Sandstone, the deformation manifests as numerous discrete bands, primarily 2 grain diameters width which are pervasive across most of the sample from end to end (Figure 5.4e-h). Distribution is relatively homogeneous, and they do not appear more concentrated in a particular region, such as the sample ends. The discrete bands are characterised by intense grain fracturing and pore collapse. In the synthetic sandstone, the localisation is distributed across the central third of the sample and is characterised by many fractured grains, within which are discrete compaction bands with a width of around 2 grain diameters which exhibit the most intense grain crushing and compaction (Figure 5.4i-l). In terms of porosity reduction, Castlegate Sandstone exhibits the largest overall decrease, relative to its starting porosity, while Bentheim Sandstone exhibits the smallest. The individual discrete

bands do not appear to be fully resolved by the porosity maps, possibly because of their small size in relation to the calculated REA size of the sampling window.

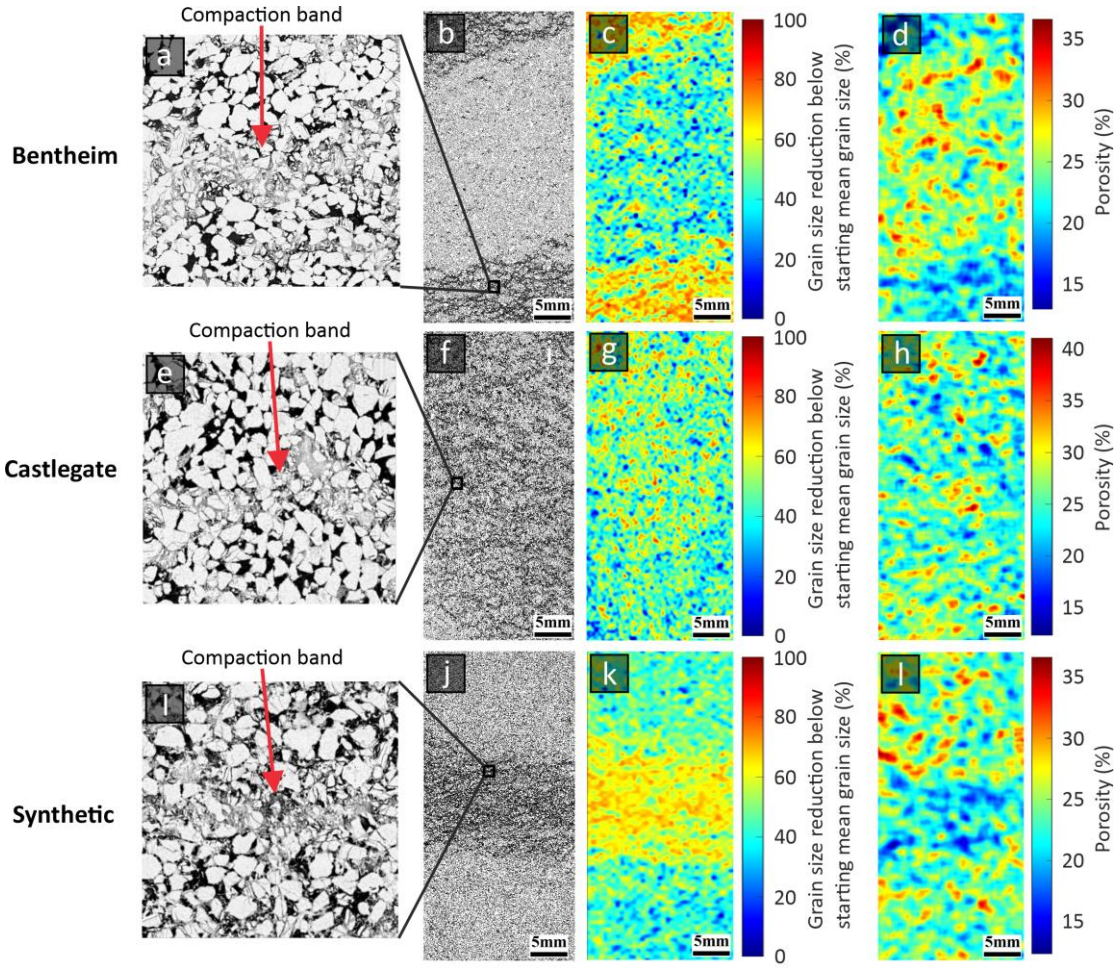

Figure 5.4. *Comparison of Bentheim, Castlegate and the synthetic sandstone which have similar microstructural characteristics but different cements (Table 5.1). Discrete bands (≤3 grain diameters width) are identified from the SEM images for each of the sandstones (a, e, i); however, the distribution of the bands varies significantly. The three sandstones are also analysed in terms of grain size reduction (c, g, k) and porosity (d, h l).*

5.4 Discussion

Our results highlight how the nature and distribution of compaction bands vary in three sandstones with similar microstructural properties but different cement types. In Bentheim Sandstone, the compaction bands all develop at the ends of the specimen and are associated with a localised reduction in porosity and permeability (Figure 5.4b, c, d). However, in Castlegate Sandstone, the bands are distributed throughout the whole sample (Figure 5.4f) and in the synthetic specimen, they develop only across the sample centre (Figure 5.4j). Similarly to Bentheim Sandstone, the synthetic sandstone displays localised porosity and grain size reductions associated with the compaction bands (Figure 5.4k, l). However, in Castlegate Sandstone, these reductions are less obvious, potentially due to the small size (1-2 grain diameters), close spacing and pervasive distribution of the bands, meaning that on the whole sample scale these property variations may be harder to differentiate from the intact regions (Figure 5.4g, h).

Our analysis has shown that the primary difference between the three sandstones is the type of cement, with Bentheim Sandstone cemented by syntaxial quartz overgrowths (Figure 5.2a), Castlegate Sandstone with clays (Figure 5.2b) and the synthetic sample with amorphous quartz (Figure 5.2c)- also see supplementary material Figures SM 5.1-5.3. The syntaxial quartz overgrowths in Bentheim Sandstone will be the strongest of the three sandstone cements, and the clays the weakest (Dyke & Dobereiner, 1991). The different cement types will likely affect the micromechanics involved during axial loading and compaction band formation, which may explain the different band distributions observed. Indeed, the mechanical and elastic data show some evidence for the possible effect of the different cement types and strengths, particularly regarding the clays present in Castlegate. Although this sample exhibits a P^* almost as high as Bentheim (Table 5.2), the elastic Young's modulus and bulk modulus are lower than that of the synthetic sample, which has a much lower P^* value due to its larger grains and higher porosity. Similarly, the Castlegate Sandstone yield curve has a much higher aspect ratio than the synthetic sample with lower peak yield values than Bentheim Sandstone (Figure 5.3c). These

discrepancies may be due to the more ductile nature of the clay cements, which are weaker than the syntaxial and amorphous quartz and thus, enable the movement of the grains at lower axial stresses (He et al., 2019; Pijnenburg et al., 2018, 2019a). The clays in Castlegate Sandstone may also explain the greater amount of permanent deformation observed at the end of hydrostatic loading (Figure 5.3b) compared to the other two samples, as the clays will deform in a more ductile manor, accommodating small grain movements as the pressure is increased.

Bands observed at the ends of laboratory-deformed sandstones have been seen previously in Bentheim Sandstone and other natural sandstones (Baud et al., 2004; Klein et al., 2001). This has been suggested to be due to end cap friction between the sample and the loading platen triggering local stress heterogeneities, resulting in the nucleation of compaction bands which migrate inwards (Fortin et al., 2006; Olsson & Holcomb, 2000). However, since the other two samples we examined do not show bands exclusively at the specimen ends (Figure 5.4f and j), it is possible that cement is having some control over this mechanism. The strong syntaxial quartz cement of Bentheim Sandstone may inhibit the breaking of cement bonds and the movement of grains during axial loading (Hangx & Brantut, 2019), reducing the buildup of local stress heterogeneities throughout the sample, which is supported by its high elastic moduli values and mechanical yield strengths (Figure 5.3 and Table 5.2). Consequently, due to its homogeneous nature (Figure 5.1a, b, c) the stress concentrations may first develop near the loading platens at the sample ends, where the stress heterogeneities are highest. By contrast, the weak clay-cement in Castlegate Sandstone will deform ductiley under compression (DiGiovanni et al., 2007; Pijnenburg et al., 2019b), as supported by the mechanical and elastic data (Figure 5.3 and Table 5.2), resulting in specimen-wide grain rearrangement. Grain movement during inelastic loading may also reduce the stress concentrations near the loading platens, whilst also developing new stress heterogeneities, which could potentially act as nucleation sites for compaction bands at other points within the sample. Similar to Castlegate, the bands in the synthetic sample were not confined to the specimen ends (Figure 5.4j), meaning that the stress concentrations at the loading platens were not responsible for their nucleation.

Instead, the bands developed in the sample centre, likely from a large pore or other stress heterogeneity. However, unlike Castlegate, the compaction bands appear to propagate out from the sample centre, rather than also nucleating pervasively throughout. This may indicate that rather than nucleating from a new stress concentration, each band developed from a pre-existing one, which is supported by the tortuous, closely spaced nature of the synthetic bands (Figure 5.4c). It may be that the more ductile nature of the clay cement in the Castlegate Sandstone acts to reduce the stress concentrations around compaction bands, suggesting why they are more widely distributed, as the bands may be more likely to develop from a new stress heterogeneity, rather than a pre-existing band (Figure 5.3), however, further experiments would be needed to examine this.

It is interesting to note that each of the bands observed in the three samples in this study are discrete and are clearly separated by intact grains, rather than developing as diffuse compaction fronts (Figure 5.4a, e, i). This suggests that cement is not the primary control on diffuse versus discrete compaction band formation in high porosity sandstones, as has been suggested in some modelling studies (Marketos & Bolton, 2009).

5.5 Conclusions

We have conducted triaxial tests on 3 high-porosity sandstones, with similar microstructural properties but different cement types. Each sample formed discrete compaction bands when taken to 5% axial strain at a starting stress equivalent to 85% of its P^* value. However, location and distribution of the compaction bands differed in each sample. In Bentheim Sandstone, which is cemented with strong syntaxial quartz overgrowths, the compaction bands were located at either end of the sample. By contrast, in Castlegate Sandstone, which is cemented weakly with clays, the compaction bands were distributed throughout the whole sample and in the amorphous quartz-cemented synthetic sample, the bands were only present across the sample centre. Our results suggest that the cement type and its varying strength, is playing a role in the micromechanics of deformation between the three

samples, which in turn, determines where the compaction bands nucleate and develop. However, since all the compaction bands identified were discrete, rather than diffuse in nature, we suggest that cement is not the primary control regarding the preference for either type. Our results have provided a brief overview of the potential importance of cement, regarding compaction localisation in sandstones. Further work should concentrate on how other cement-related factors, such as its quantity and distribution also affect compaction band formation.

Supplementary material

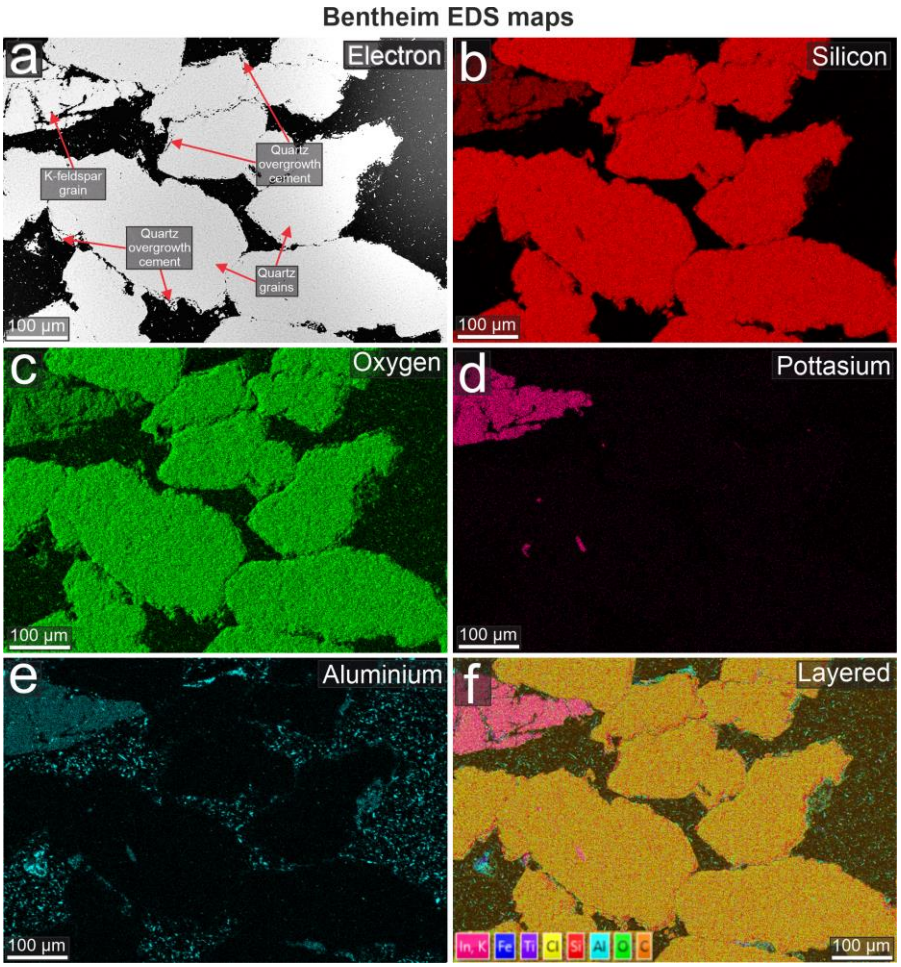

Supplementary Figure 5.1. *BSE image (a) and EDS maps (b-f) produced for Bentheim Sandstone to determine the mineralogical composition of the cement. Only the key element maps have been included in the figure, although small quantities of other trace elements appear in the layered map (f).*

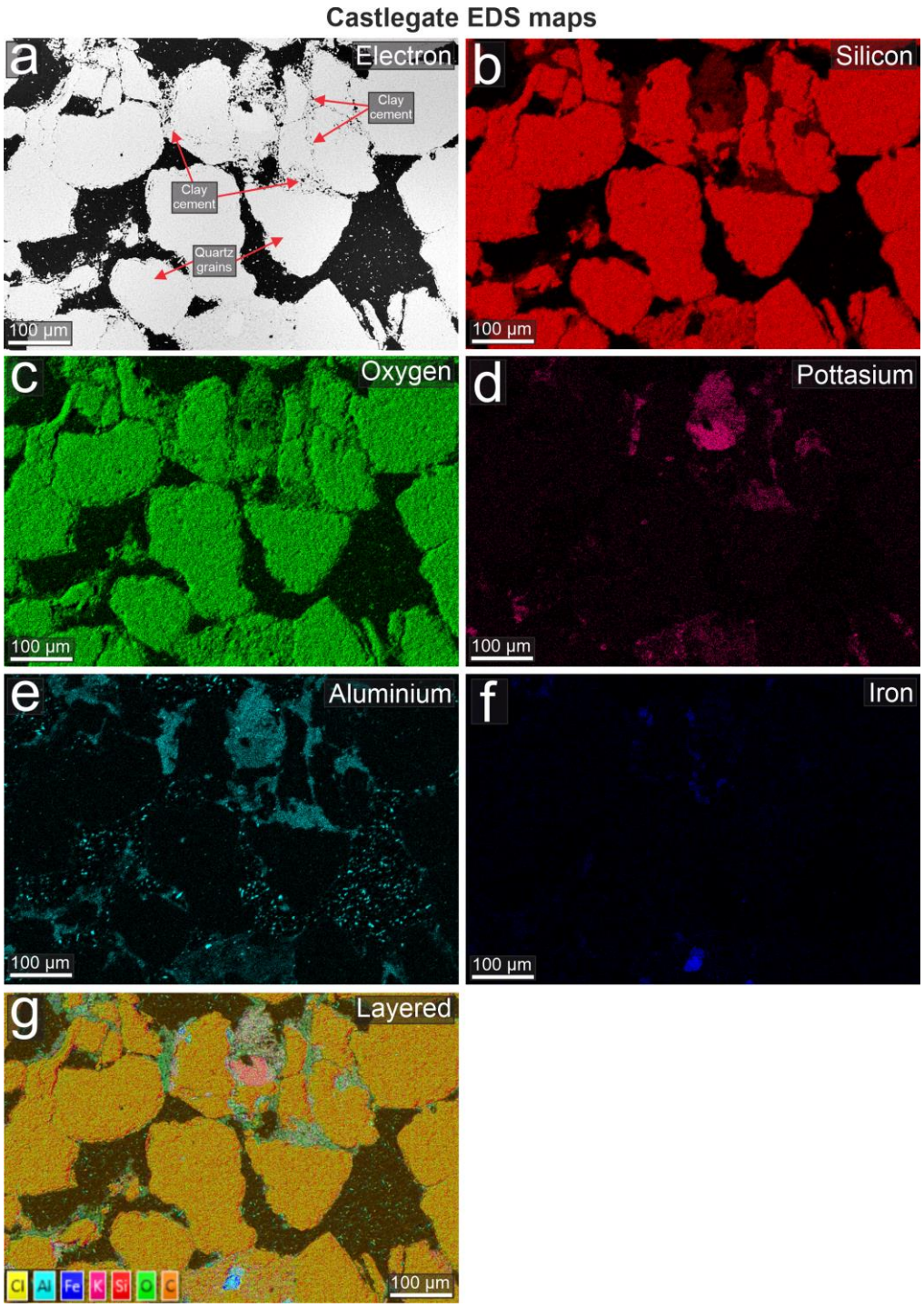

Supplementary Figure 5.2. *BSE image (a) and EDS maps (b-g) produced for Castlegate Sandstone to determine the mineralogical composition of the cement. Only the key element maps have been included in the figure, although small quantities of other trace elements appear in the layered map (g).*

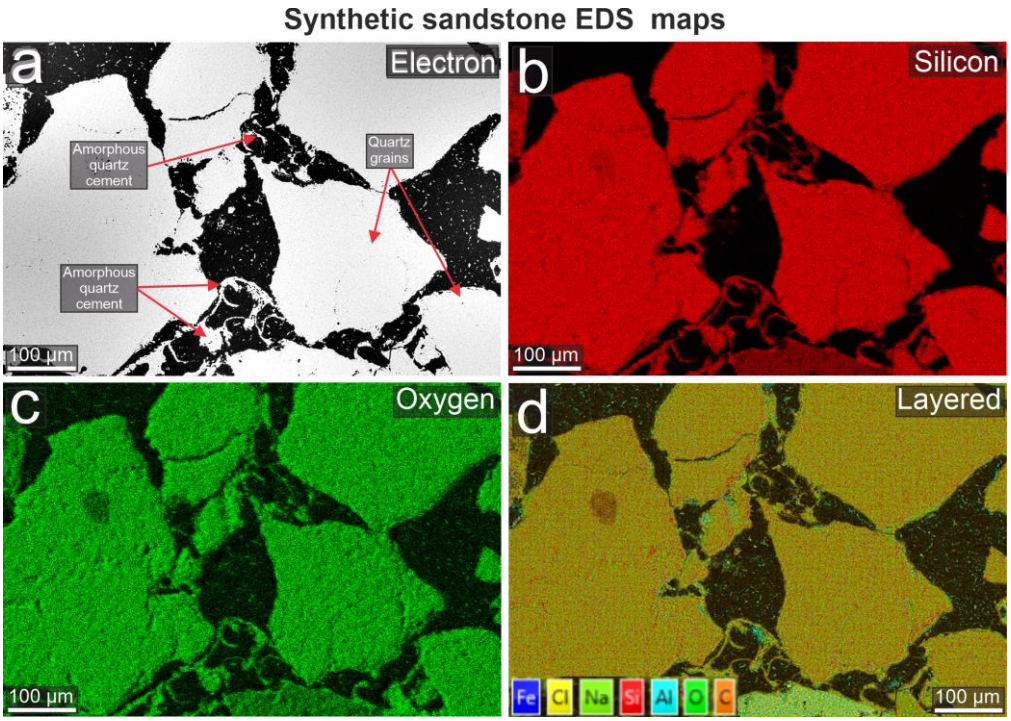

Supplementary Figure 5.3. *BSE image (a) and EDS maps (b-d) produced for the synthetic sandstone to determine the mineralogical composition of the cement. Only the key element maps have been included in the figure, although small quantities of other trace elements appear in the layered map (d).*

6 Strain localisation in Castlegate Sandstone under triaxial compression

Abstract

Strain localisation can significantly influence fluid flow in porous sandstone reservoirs, potentially impacting on industrial fluid injection/extraction. The nature of the localised features that form is dependent on the effective stress conditions at which deformation occurs. Here, we perform a serious of triaxial compression experiments on Castlegate Sandstone and document the evolution in orientation and nature of strain localisation with increasing effective confining pressure. At low confinement, deformation localises into sets of dilational conjugate shear bands orientated ~30° to the maximum compressive stress (σ_1). As confinement is increased, the localisation features transition into sets of conjugate compactional shear bands and compaction bands, and finally, into sets of sub-parallel compaction bands, orientated perpendicular to σ_1, as the effective mean stress approaches the hydrostatic yield pressure (P^*). The deformation bands are associated with intense cataclasis, and primarily, localised porosity decrease, and their densities and intensities increase with both increasing effective mean stress and increasing axial strain. Two additional samples taken only to 2.5% axial strain at 190 and 210 MPa exhibit density and intensity values approximately half that of those taken to 5% axial strain. All the compaction bands observed in this study are discrete and develop pervasively throughout the samples even at 2.5% axial strain, indicating that some lithological, as opposed to stress control, is influencing their shape and distribution. These results may aid in the prediction of the type of strain localisation structures present in reservoirs, and their densities and intensities, where the burial and stress histories are known.

6.1 Introduction

Deformation bands are sub-seismic strain localisation structures which can form in porous sandstone reservoirs, and are commonly associated with changes in porosity, permeability and grain size (Aydin & Johnson, 1978; Ballas et al., 2015). Consequently, industrial processes such as fluid extraction during groundwater or petroleum production, or fluid injection during geothermal or CO_2 sequestration projects, may be significantly inhibited by these structures (Allen et al., 2020; Ballas et al., 2013). Deformation bands can form in every tectonic regime (strike-slip, extensional and compressional) (Soliva et al., 2016), provided that the porosity is high enough within the host sandstone (>13%), and kinematically they can be categorised into three main types: dilation bands, shear bands and compaction bands (Fossen et al., 2018). The evolution of porosity and grain size within a deformation band varies depending on the type of band that forms (e.g., porosity increases in dilational bands but decreases in compaction bands), which will have implications for fluid-flow at the reservoir-scale. It is therefore important to understand the stress conditions that lead to the formation of the different types of deformation band and the subsequent evolution of porosity and grain size within the host sandstone.

In sandstones which experience strain localisation, the nature of the deformation bands that form are dependent upon the effective mean stress at the onset of inelastic deformation in response to a differential stress being applied (Baud et al., 2004). In general, previous laboratory experiments have shown that at low effective mean stress, strain localisation manifests as brittle faulting or by the formation of dilational shear bands (DSBs), which transition, as the effective mean stress is increased, into high-angle shear bands with a component of compaction- referred to as compactional shear bands (CSBs). As the effective mean stress is increased further, approaching the hydrostatic yield strength (P^*), the localised bands transition into pure compaction bands (PCBs), which form subperpendicular to the maximum compressive stress (σ_1) (Baud et al., 2004; Bésuelle et al., 2000; Olsson & Holcomb, 2000). For porous rocks, the transition from dilational behaviour at low confinement to compactional behaviour at high

confinement is also represented when the onset of inelastic deformation is mapped out as a yield curve in *P*-*Q* space, where *P* is the effective mean stress ($P = \left(\frac{\sigma_1+\sigma_2+\sigma_3}{3}\right) - P_f$), P_f is the pore-fluid pressure and *Q* is the differential stress ($Q = \sigma 1 - \sigma 3$) (Wong et al.,1997). Typically, most sandstones have elliptical yield curves when plotted in *P*-*Q* space (Bedford et al., 2019), with the low pressure side of the yield curve associated with dilatational structures (e.g., DSBs) and the high pressure side associated with compactional deformation. It should be noted that in the compactional regime, although deformation may sometimes localise into compactional deformation bands (e.g., CSBs or PCBs), many sandstones experience distributed compaction via cataclastic flow at these conditions, with no obvious localisation features forming (Bedford et al., 2019; Menéndez et al., 1996; Wong et al., 1997). The lithological properties that determine whether a sandstone experiences localised or distributed deformation during inelastic compaction are still debated; however, previous works have shown that the nature of compactional deformation is sensitive to variations in the initial porosity, grain size, intergranular cement and grain size distribution (e.g., Cheung et al., 2012; Rice-Birchall et al., 2022).

In this study, we perform a series of triaxial compression experiments on Castlegate Sandstone, which has been shown previously to undergo strain localisation during inelastic compaction (DiGiovanni et al., 2007; Ingraham et al., 2013; Olsson & Holcomb, 2000). We investigate how the localisation behaviour varies in *P*-*Q* space by axially loading cylindrical core samples of Castlegate Sandstone over a range of effective mean stresses which cover both the dilational and compactional deformation regimes. We also perform detailed quantitative microstructural analyses on the deformed samples, to document how the lithological properties (e.g., porosity, grain size, damage intensity) of the sandstone evolves, in response to different deformation conditions.

6.2 Methods and materials

6.2.1 Sample preparation

Castlegate Sandstone is a fluvial sandstone from Utah (USA). It is primarily composed of quartz (93%) and some K-feldspar grains (3%), which are loosely cemented with small quantities of muscovite/illite (2%) and kaolinite (2%), determined using X-ray powder diffraction (XRD) and energy dispersive spectroscopy (EDS). The block used in this study was purchased from Kocurek Industries and has an average grain size of 228 ± 68 μm, quantified using laser diffraction particle size analysis with a Beckman Coulter LS 13 320, and a porosity of 28-30%, measured using a helium porosimeter. Cylindrical cores, approximately 20 mm in diameter and 50 mm in length (Figure 6.1a), were drilled from the Castlegate Sandstone block, perpendicular to the bedding direction, and precision ground to a tolerance of ± 0.01 mm using a surface grinder.

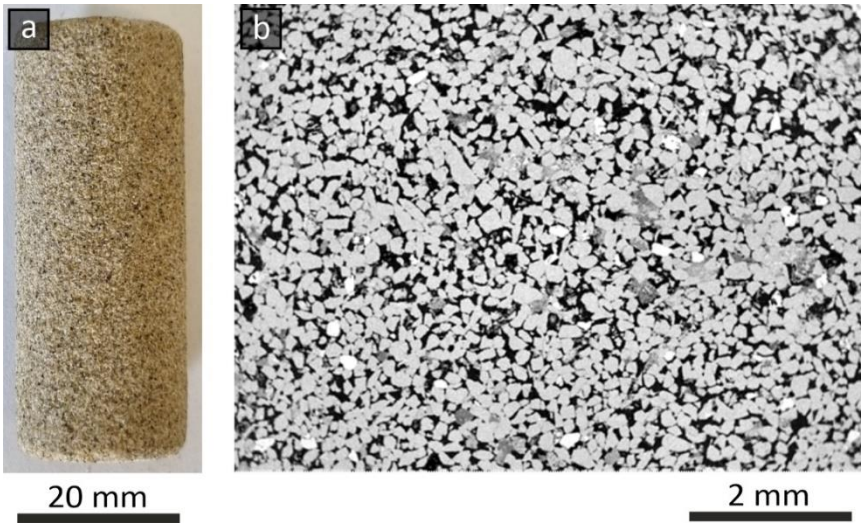

Figure 6.1. *Core of Castlegate Sandstone (a) and backscatter SEM image (b) displaying the microstructure of a sample of non-deformed Castlegate Sandstone. The sandstone is well-sorted with an average grain size of 228 ± 68 μm. The grains are mostly subangular.*

6.2.2 Triaxial deformation experiments

6.2.2.1 Deformation apparatus

Triaxial tests were conducted to determine the mechanical properties of Castlegate Sandstone and to inelastically deform the samples to investigate their localisation behaviour over a range of effective mean stresses. The experimental apparatus used was a high-pressure triaxial deformation rig (Figure 6.2), designed and built at the University of Liverpool (Mitchell & Faulkner, 2008). It is comprised of servo-controlled confining and pore pressure systems which are capable of monitoring pressure to a resolution better than 0.01 MPa. The maximum working confining pressure of the rig is 250 MPa, with silicon oil used as the confining medium. Pore-fluid pressures of 200 MPa can be obtained, with the servo-controlled pore-pressure pump also acting as a volumometer to monitor pore volume changes to a resolution better than 0.1 mm^3. De-ionised water was used as the pore fluid in this study and the pore-fluid pressure was maintained at 20 MPa during each experiment. Prior to insertion into the deformation apparatus, each sample was inserted into an annealed copper jacket (0.3 mm wall thickness) with two porous discs placed on either side of the sample. The sample and copper jacket were then inserted into a Viton™ jacket to prevent any leaks of the confining fluid into the sample, should the wall of the thin copper jacket perforate during deformation.

The axial load was generated by a servo-controlled electromechanical piston and measured by an internal force gauge to a resolution better than 0.03 kN. The axial displacement was measured by an LVDT attached to the base of the loading column. The axial strain that the sample experienced was calculated by subtracting the elastic deformation taken up by the loading column from the total axial displacement. The stiffness of the loading column is 119 kN/mm.

6.2.2.2 Experimental procedure

The hydrostatic yield strength (P^*) of Castlegate Sandstone was first determined, in order to constrain the upper bounds of the yield curve in P-Q space. This was done by incrementally increasing the confining pressure to apply a hydrostatic load, while the pore

volume change was monitored as the pore-fluid pressure was held constant at 20 MPa. P^* was identified by the deflection in the hydrostatic loading curve, marking the onset of inelastic deformation (Zhang et al., 1990). Once P^* was determined, the rest of the Castlegate Sandstone cores were axially deformed over a range of different starting effective mean stresses below P^* (2-210 MPa). Each sample was loaded to 5% axial strain at a displacement rate of 1 μm/s (strain rate $\approx 2 \times 10^{-5}$ s^{-1}) and the deformed samples were then recovered after the experiments and prepared for microstructural analyses.

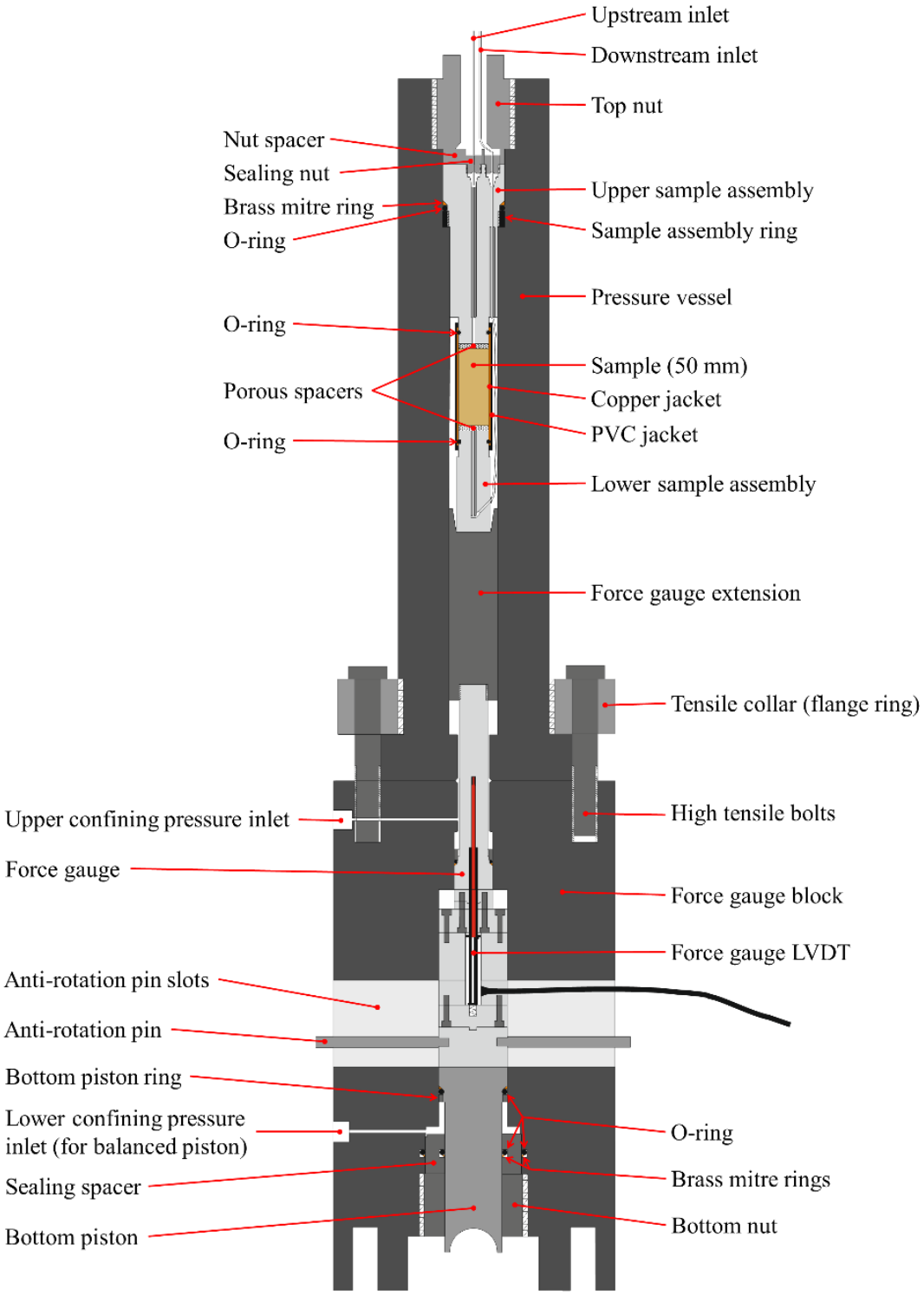

Figure 6.2. *Schematic drawing of the triaxial deformation apparatus used in this study. Modified after Mitchell & Faulkner (2008).*

6.2.3 Microstructural analysis

6.2.3.1 Sample preparation and construction of specific surface area and porosity colourmaps

Upon removal from the deformation apparatus, the cores were oven dried for 24 hours before being vacuum impregnated with a low-viscosity epoxy resin so that they could be prepared for microstructural analysis. A core of the intact starting material (i.e., undeformed) was also prepared in the same way. Once epoxied, the cores were cut in half down their long axes and this surface was then polished and carbon coated ready for imaging using a Hitachi TM3000 scanning electron microscope (SEM). At low effective stresses (2–70 MPa), shear offset in the copper jacket was used to establish the optimum angle at which to cut the samples (Figure SM 6.1), whereas at higher effective stresses (150–210 MPa) the localisation formed approximately normal to the maximum principal stress so the samples could be cut at any orientation along their long axes. However, at intermediate pressures of 70-130 MPa the jackets showed no shear offset (Figure SM 6.1), and so any localisation was unlikely to be subperpendicular to σ_1. Therefore, to establish the optimum orientation to cut these specimens, whole sample X-ray micro-CT scans were performed using a Zeiss Xradia Versa 620 X-ray CT (Figure SM 6.2). Given the relatively large size of the deformed cores (~50 × 20 mm) these scans were performed at low resolution, although this provided enough detail to resolve the localisation orientations (see supplementary material Figure SM 6.2).

Once the samples were cut and polished, backscatter electron (BSE) images were collected at 50× magnification; these images were then stitched together using GigaPan Stitch software to produce a whole core image. The stitched images were uploaded into the image analysis program Fiji (Schindelin et al., 2012) and binarised into porosity (white) and grains (black) so detailed image analysis could be performed. For the localised structures to be observed, further processing stages were required. The easiest method for identifying localisation from backscatter electron (BSE) images is by studying grain size reduction, since this is a diagnostic marker of strain localisation (Rice-Birchall et al., 2022). The grain

boundaries were therefore identified in Fiji, which turned these white, while the grains and pores themselves remained black. The white grain boundary regions were then enhanced by applying a median filter to remove smaller speckles, and finally, a Gaussian filter was applied to further heighten the contrast of the localised features.

Maps of porosity distribution were constructed for each of the deformed Castlegate Sandstone samples to examine how the spatial evolution of porosity varied during loading at different effective mean stresses. To create these maps, the original binary image was divided into grid squares with a 90% overlap between each neighbouring square, using the MATLAB-based distinct block processing function Blockproc (Hugo et al., 2015). For each overlapping square a porosity value was obtained, using the percentage of black (grain) and white (porosity) pixels in each square The data were then smoothed to remove any overlap artifacts and displayed as a porosity colourmap (Rice-Birchall et al., 2021). The asymptotic approach of statistical representative elementary area (REA) analysis was used to determine the sampling window size inputted into Blockproc (Brown et al., 2000; Bruns et al., 2017; Dyskin & Pasternak, 2015; Koestel et al., 2020; Mu et al., 2016; Zhang et al., 2000) and was calibrated using an undeformed specimen of Castlegate Sandstone (Figure 6.1b). Since the REA is defined as the minimum visual area over which microscale characteristics (i.e., porosity) remain constant (Kong et al., 2018; Saraji & Piri, 2015), the calibration using a non-deformed image ensured that any heterogeneities in the starting material of the synthetic sandstone were recorded.

The methodology of Rabbani et al. (2014b) was implemented to calculate 2D specific surface area distribution of the solid/grain space for each of the samples, which is defined as:

$$2D\ Specific\ surface\ area = \frac{grain\ perimeter}{grain\ area} \tag{6.1}$$

The original binary image was processed to show the grain outlines and a non-overlapping grid was applied across the image of the same size as determined from the REA porosity analysis. For each square, the perimeter and area of the grains within the square were

determined, with these being used to calculate a value of specific surface area (SSA) for each. These values were then used to construct a colourmap of SSA distribution for each sample.

Small-scale maps of porosity distribution 'overlain' over BSE images were also produced to examine how the porosity changed within the localised bands. Here the image calculator in Fiji was used, which performs arithmetic and logical operations between two images (Ferreira & Rasband, 2012). In this case, the source image (*img1*) was the rgb porosity colourmap for the desired area and the destination image (*img2*) was the 8-bit greyscale BSE image of the same area. Both images were scaled to the same size (1100 × 1100 pixels), and the 'minimum' operator was performed on both images. This executes the function:

$$img1 = \min(img1, img2) \tag{6.2}$$

which replaces each pixel for the same given coordinates in each image with the lowest value pixel out of the two images. This operation gives the impression that the porosity map has been overlain over the BSE image, since the dark porosity regions in *image 2* are always the lowest pixel values (i.e., around 0) from the two images and so the contrast between the grains and the pore space is preserved. However, the light colour of the white grains produces much higher pixel values (around 255) and so the white colour of the grains is replaced by the darker rgb colours of the porosity map.

6.2.3.2 Calculating localisation trace orientations using FracPaQ

The localisation trace orientations, relative to σ_1, are key for determining how the deformation characteristics of the sandstone change with increasing effective stress. To quantitatively analyse the trace orientations of our deformed samples, the MATLAB toolbox FracPaQ was used. FracPaQ was initially developed for the purpose of fracture pattern analysis (Healy et al., 2017), however, it can also be used for examining sample-scale localisation structures such as shear and compaction bands. Firstly, the input images must be correctly processed. Node files are the most robust and preferred input file type for FracPaQ because they provide XY coordinate pairs of each node along every fracture/localisation trace (Healy et

al., 2017). In order to prepare the enhanced SEM images for FracPaQ, Fiji was used to apply a Gaussian filter to better constrain the localisation features and the 'skeletonise' function was then run which repeatably removes pixels from the edges of objects in a binary image until they are reduced to single pixel-wide structures. In our case, each object was a localisation trace. Excess skeletons or noise below 3 pixels in length were removed at this stage using the skeleton pruning function in Fiji. The binary image skeleton was then uploaded into CorelDRAW as a bitmap, where it was converted into an SVG file using the technical illustration option which automatically traces the inputted bitmap as curves. These curves were then converted into multiple straight lines, bounded by node pairs. However, since the nature of the FracPaQ analysis means that each separate line is analysed, it was important to remove excess nodes, using the automated node removal function in CorelDRAW, so as to reduce the number of data points for each trace. The SVG file was finally imported into FracPaQ and processed using an SVG to TXT conversion script. Once this was completed, the file was ready for analysis. The localisation trace orientations can be assessed using several different plots in FracPaQ. Trace angles are defined as the angle of the trace segment measured clockwise from the Y-axis, for the default assumption that the Y-axis (long-axis) is the loading direction (σ_1). Length-weighted rose diagrams were then plotted for each sample.

6.2.3.3 Determination of localisation intensity and density using FracPaQ

Maps of localisation density and intensity were also constructed using FracPaQ to quantitatively establish the spatial distribution and characteristics of the localisation traces. These were constructed using the circular scan window method of Mauldon et al. (2001) (Figure SM 6.3), applied to the coordinate geometry of the fracture trace network of the 2D trace images. Fracture density is defined as the number of fractures per unit area and is calculated as $m/2\pi r^2$, where m is the number of fractures terminating within a circle of radius r and fracture intensity is defined as the total length of cracks in a given area and calculated as $n/4r$, where n is the number of fractures intersecting the perimeter of the circle (Figure SM 6.3). A 2D grid of commensurate, evenly spaced circular scan windows which fits within the trace image area was

generated by FracPaQ and the intersections (*n*) and terminations (*m*) of the fracture segments within these circles were calculated (Figure SM 6.3a). The centre of each circle was then assigned a computed value of intensity/density and this grid of values was contoured using the standard MATLAB triangulation function to produce the maps of estimated fracture density and estimated fracture intensity.

6.3 Results

6.3.1 Mechanical results

6.3.1.1 Hydrostatic loading data

The hydrostatic loading curve for Castlegate Sandstone is displayed in Figure 6.3. After an initial stiffening of the sandstone at effective mean stresses <~80 MPa, quasi-linear elastic loading is then observed until a deflection in the loading curve occurs at an effective mean stress of ~212 MPa. This deflection marks the hydrostatic yield point (P^*) and the onset of inelastic deformation (red cross in Figure 6.3). The porosity evolution during unloading of the sample confirms that the deformation was inelastic, since the porosity does not return to its initial value (approximately 4% porosity reduction).

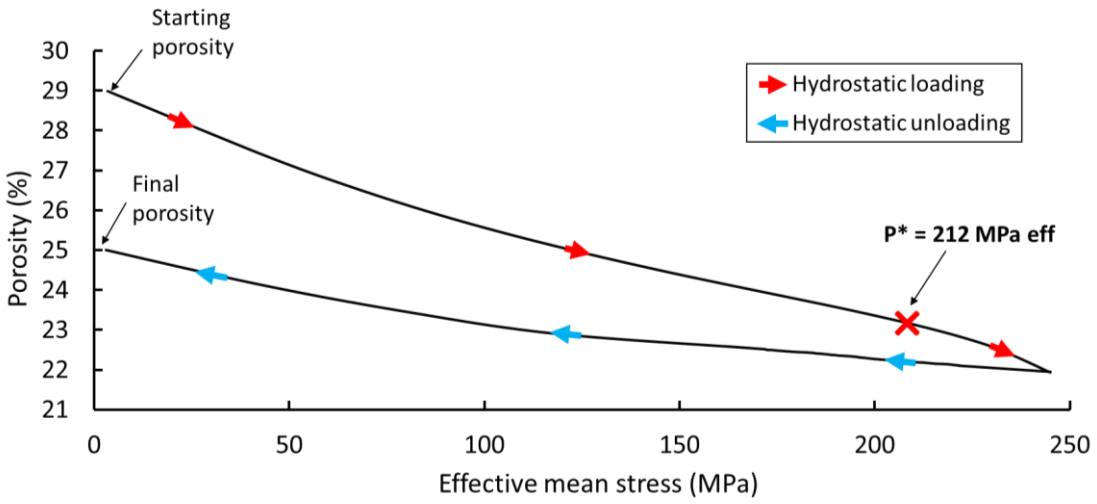

Figure 6.3. *Hydrostatic loading data for Castlegate Sandstone. A deflection in the loading curve at an effective mean stress of 212 MPa marks P* (denoted by a red cross). The pore volume change was also monitored during unloading, revealing an inelastic porosity reduction of approximately 4%.*

6.3.1.2 Triaxial loading data

Figure 6.4 displays a compilation of mechanical data from the triaxial deformation experiments on Castlegate Sandstone. Axial strain versus differential stress curves for samples loaded at effective mean stresses between 2–210 MPa are shown in Figure 6.4a. Deviation from quasi-linear elastic loading marks the onset of yield. Beyond yield, samples loaded at the lowest effective mean stresses (2-50 MPa) exhibit stress drops, inidicative of shear failure. After the post-yield stress drop, these samples then deform at relatively constant differential stress. Samples deformed at intermediate effective mean stresses (70-110 MPa) do not experience a significant stress drop, but instead, deform at relatively constant differential stress immediately following yield. The samples deformed at the highest effective mean stresses (≥130 MPa) experience post-yield strain hardening, with the magnitude of the hardening increasing at higher effective mean stress. Porosity reduction versus effective mean stress during axial loading is

plotted in Figure 6.4b. During a conventional axisymmetric triaxial test, the effective confining pressure (which provides σ_2 and σ_3) is held constant during axial loading. Therefore, as the axial stress is increased by an increment $\Delta\sigma_1$, the effective mean stress increases by an increment of $\Delta\sigma_1/3$. In our experiments the samples loaded at effective mean stresses ≥30 MPa all experienced bulk compaction, whereas the samples loaded below this value (2, 5 and 10 MPa) experienced dilation (Figure 6.4b). The total amount of porosity reduction after 5% axial strain increases with increasing effective mean stress.

The yield points determined from the mechanical data are plotted in *P*-*Q* space (Figure 6.4c), revealing the complete yield curve for Castlegate Sandstone. The yield curve has an elliptical geometry, as typically observed for porous sandstones (Wong et al., 1997), although we find it has a steep, overhanging limb on the compaction side (high-pressure side), close to the region of *P**, as reported in some previous studies (Bedford et al., 2018; Klein et al., 2001). We also note that the yield points from the samples axially loaded at starting effective mean stresses of 30-70 MPa plot on the low-pressure side of the yield curve, which is typically associated with dilational deformation. However, these samples experienced bulk compaction (Figure 6.4b). Similar observations of some compactional yield points plotting on the low-pressure side of the yield curve were also made by Bedford et al. (2019) for Boise and Idaho Gray sandstones. Comparison of this yield curve which was produced using water-saturated samples, with its counterpart produced using Argon-saturated ones in Chapter 5 (Figure 5.3c), reveals that the former has lower yield values and a smaller P*, likely due to the effect of water weakening.

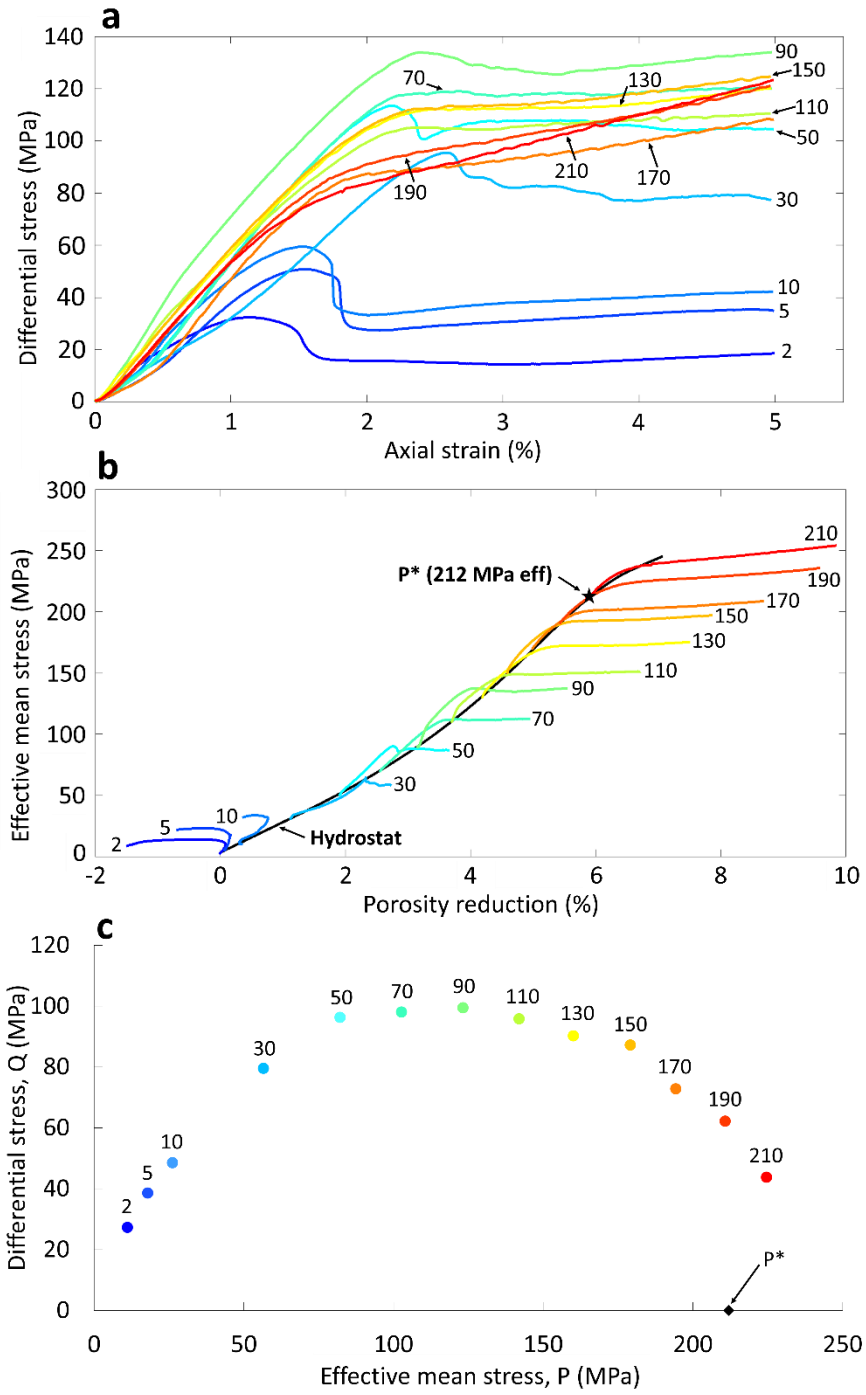

Figure 6.4. *Mechanical data from triaxial compression experiments on Castlegate Sandstone samples taken to 5% axial strain. a) Differential stress versus axial strain. b) Effective mean stress versus porosity reduction. The values next to the curves correspond to the effective mean stress at the initiation of axial loading. c) Yield points for Castlegate Sandstone plotted in P-Q space.*

6.3.2 Microstructural results

6.3.2.1 Specific surface area and porosity

Figure 6.5 displays processed binary BSE images (see section 6.2.3.1), porosity distribution maps and specific surface area maps for each of the deformed Castlegate Sandstone samples, shown in relation to their inelastic yield points plotted in *P*-*Q* space. The darker areas in Figure 6.5a correspond to regions of intense grain crushing, highlighting localised shear and compaction features (Fossen et al., 2018). At the lowest effective mean stress of 2 MPa, a single DSB is present, associated with significant cataclasis, although several large grains are preserved within it (Figure 6.6a). Along the band decreases and increases in porosity are observed, with the former related to the regions of most intense grain crushing (Figure 6.7a) and the latter to areas of the least intense grain fracturing (Figure 6.7b). In the samples loaded at 5 and 10 MPa, the DSBs form as single, well-defined conjugate sets (Figure 6.5) with one of the conjugate bands associated with very intense grain crushing (Figure 6.6b) and porosity reduction (Figure 6.7c and e) and the other with limited grain crushing and porosity increase (Figure 6.7d). As the effective mean stress increases to 30-130 MPa, the shear bands all become associated with localised porosity reductions (Figure 6.5b and Figure 6.7f-k), and none with the porosity increases seen at lower confinement (≤10 MPa). The shear bands are also associated with more intense cataclasis at these conditions, with fewer large intact grains being preserved inside the bands (Figure 6.6c-e). The number of shear bands increases in the samples as the effective mean stress is increased, as does the angle of the bands with respect to the maximum compressive stress (σ_1) (Figure 6.5a). At effective mean stresses ≥150 MPa the conjugate sets are no longer present (Figure 6.5a), and the localisation features transition into tortuous, discrete (<3 grain diameters width) compaction bands (Figure 6.6f and g) which are narrower than the shear bands observed at lower pressures but which again show localised porosity reductions (Figure 6.7l-o). On the whole sample scale (Figure 6.5a), the compaction band intensity is so high that the deformation appears to be homogeneously distributed (i.e., cataclastic flow). However, when observed at higher magnifications it can be seen that each individual band is

separated by regions of intact grains (Figure 6.6f and g and Figure 6.7l-o). These discrete compaction bands form subperpendicular to σ_1, however, due to their high density, tortuous nature and close spacing, especially when compared to the shear bands, they are harder to identify on the large-scale porosity maps (Figure 6.5b).

The SSA distribution maps show an overall trend of increasing overall damage intensity with increasing effective mean stress. However, similarly to the porosity maps, they most clearly capture the localisation in the samples loaded at effective stresses of 2, 5 and 10 MPa but also capture some of the localised structures present in samples loaded at 30 and 50 MPa. Beyond these samples, there is a gradual increase in damage intensity; however, similarly as for porosity, the individual localised features cannot be identified. The average SSA for each of the samples is plotted in Figure SM 6.4b and increases with increasing effective mean stress.

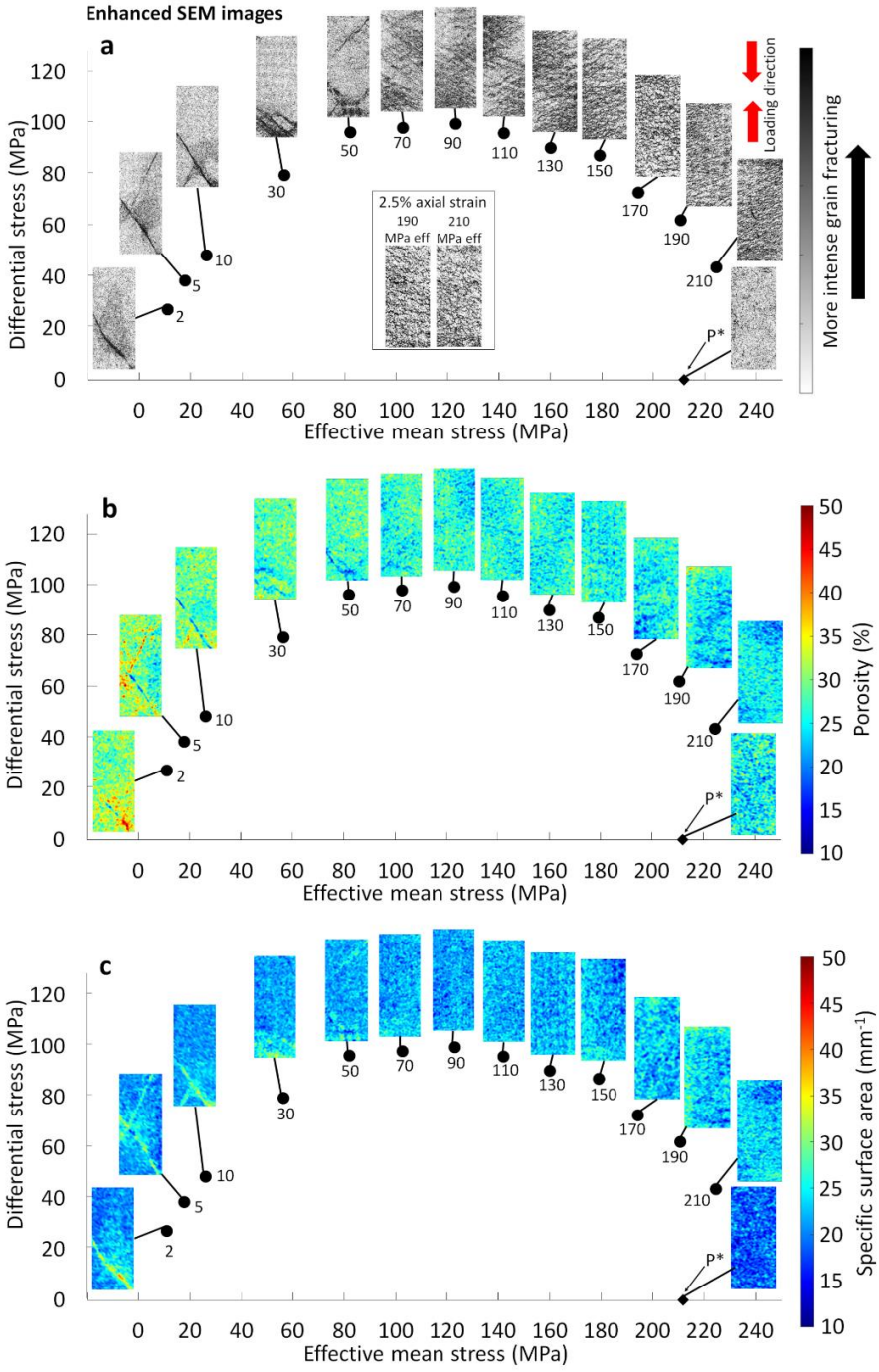

Figure 6.5. *Whole-sample microstructural images for each of the deformed Castlegate Sandstone samples, shown in relation to their inelastic yield points plotted in P-Q space. a) Processed, binary BSE micrographs, b) porosity colourmaps, and c) specific surface area colourmaps. The panel in a) shows microstructural images for the two samples loaded at effective stresses of 190 and 210 MPa to only 2.5% axial strain.*

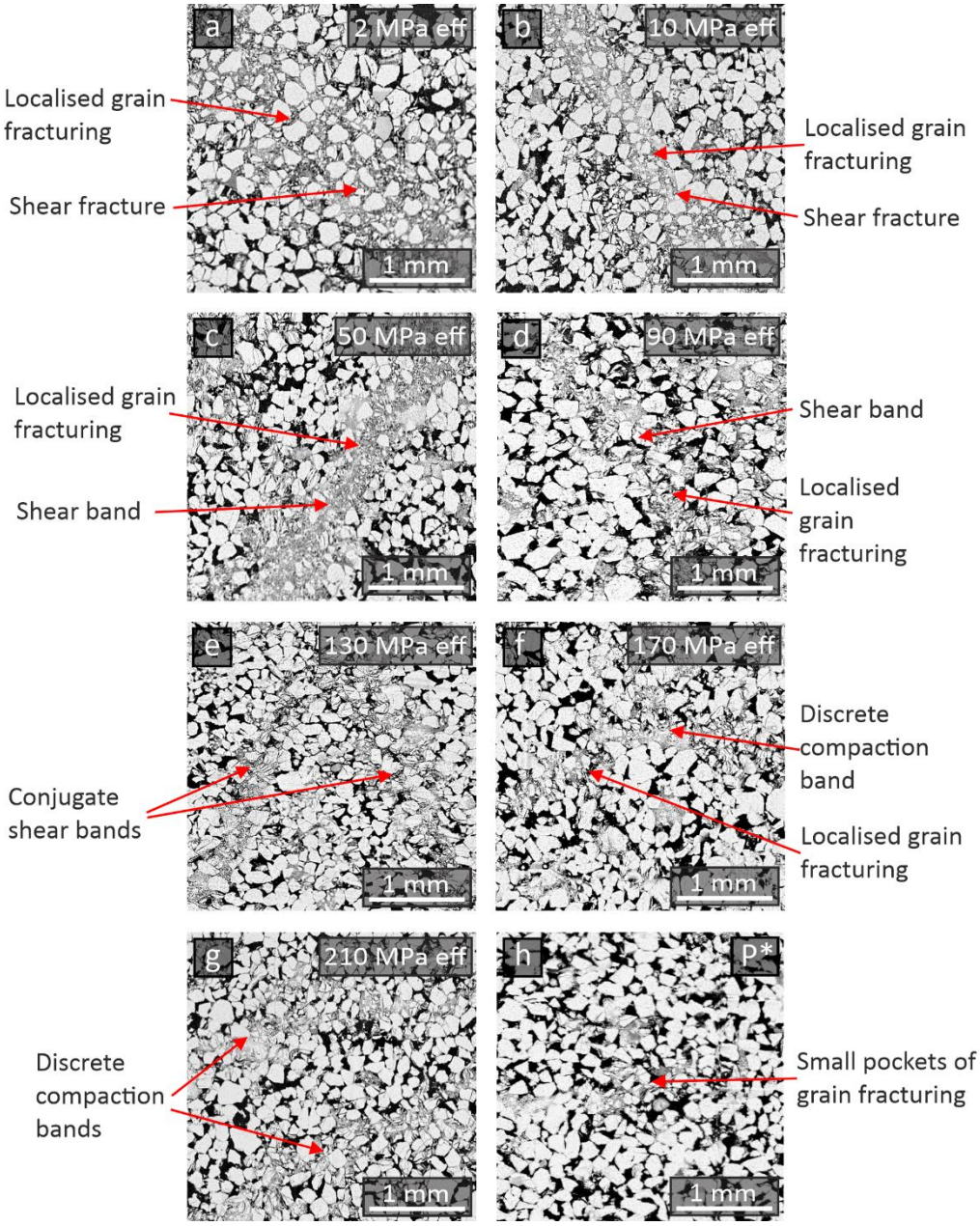

Figure 6.6. *Zoomed, high-contrast BSE images of seven Castlegate Sandstone samples post-axial loading (a-g) highlighting the change in localised deformation with increasing starting effective stress. h) shows the deformed microstructure of the sample loaded hydrostatically in order to identify P* (Figure 6.3).*

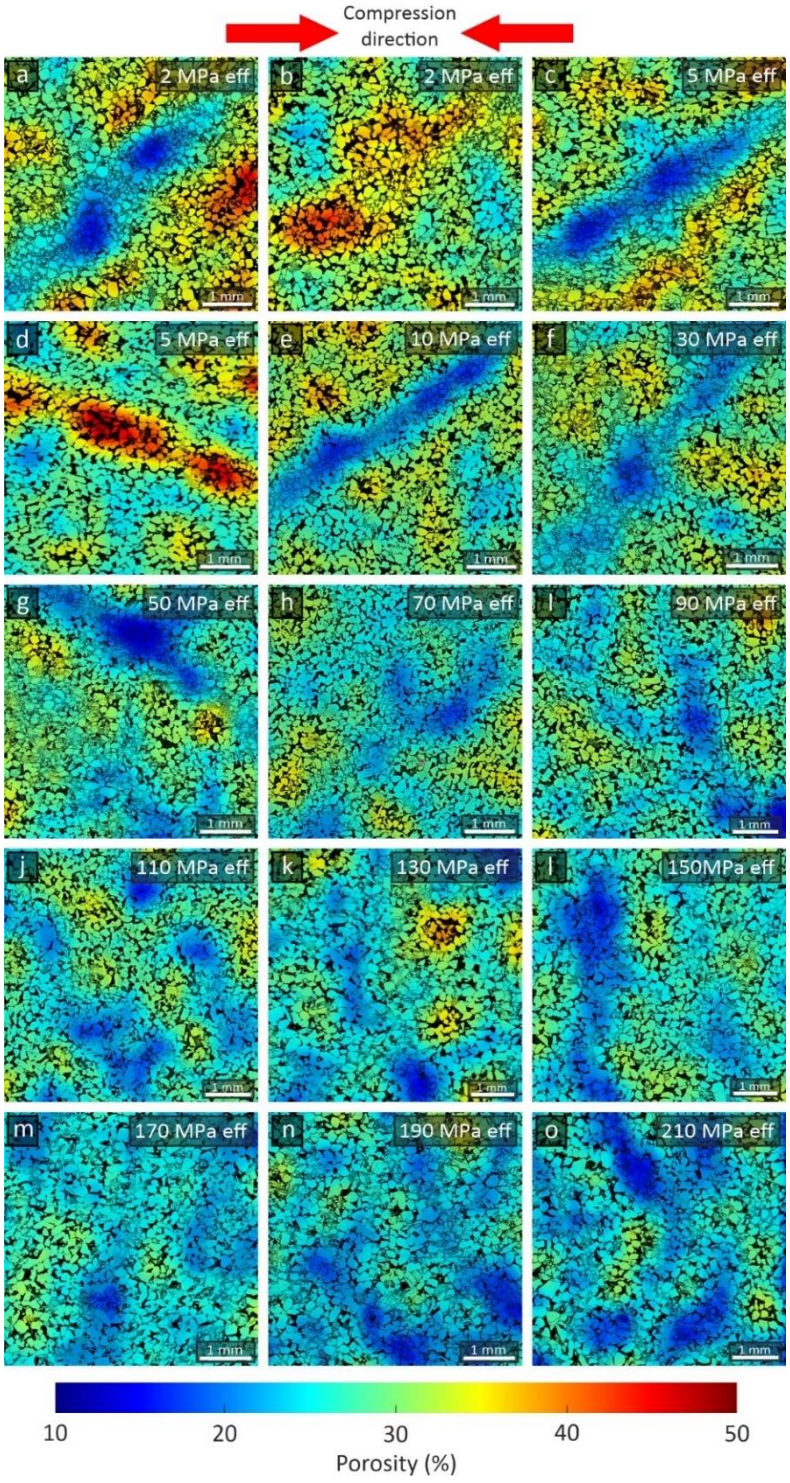

Figure 6.7. *Porosity distribution maps combined with BSE images for each of the Castlegate Sandstone samples. In each sample, grain size reduction is generally associated with a porosity decrease. However, some significant reductions are also produced by closely spaced grains which have significantly reduced the pore space without being fractured.*

6.3.2.2 Localisation trace orientation

In Figure 6.8 rose diagrams for each of the localisation trace images around the yield curve are displayed. An evolution in trace orientation is observed from shear fractures at around 20-40° relative to σ_1 at low effective mean stress, to compaction bands subperpendicular to σ_1 at high effective mean stress. In the central region of the yield curve there is a transitional zone (between yield points 70-130 MPa) where both conjugate shear bands and compaction bands are present, indicated by the high frequency of bands at approximately ±45° as well as those at around 90° to σ_1.

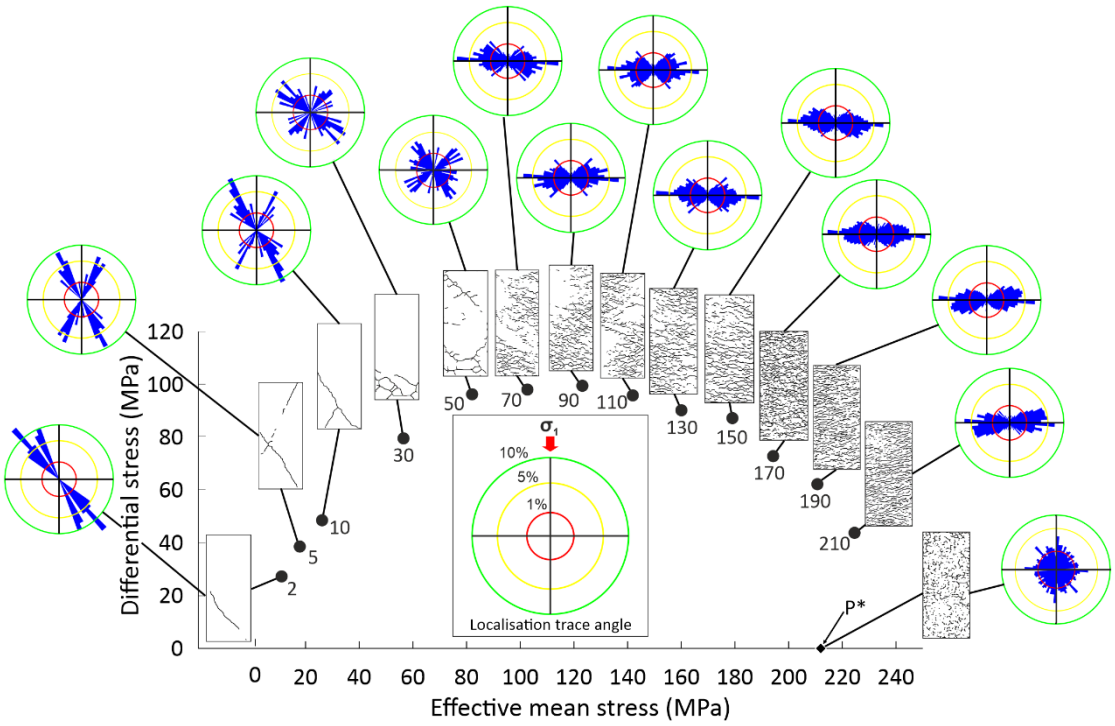

Figure 6.8. *Yield curve produced for Castlegate Sandstone showing the corresponding localisation trace images for each sample. Rose diagrams have been produced for each trace image showing the localisation orientations. The red, yellow and green circles within the rose diagrams represent percentage frequencies of 1%, 5% and 10% respectively, as shown in the legend.*

6.3.2.3 Density and intensity of localisation traces

Figure 6.9 displays colourmaps of density (6.9a) and intensity (6.9d) of the localisation traces for each sample. The colourmaps display a visual trend of increasing density and intensity with increasing effective mean stress. Similarly to the porosity and SSA maps (Figure 6.5b and c), the intensity colourmaps effectively pick out the shear localisation at low effective mean stresses; however, as the traces become more numerous and closely spaced at high effective mean stress, individual traces become merged together making it appear that the deformation was distributed homogeneously (the photo micrographs in Figure 6.6f-g show this was not the case).

To investigate further the controls on localisation density and intensity, we performed two additional experiments on samples loaded at 190 and 210 MPa effective stress and taken to a total of 2.5% axial strain, instead of 5% axial strain, as was done in the rest of the experiments. The density and intensity colourmaps for the samples taken to 2.5% axial strain are shown in Figure 6.9b and e. Visually, the colourmaps for these two samples display lower values of localisation trace density and intensity than their counterparts that were deformed to 5% axial strain. Panels showing overall values of intensity and density for each sample plotted against effective mean stress are shown in Figure 6.10 and quantitatively support the colourmap data by exhibiting linear trends of increasing density and intensity with increasing effective mean stress. When the bulk values of density and intensity for the samples taken to 2.5% axial strain are plotted, the amount of localisation damage accumulated is approximately half of that accumulated by the equivalent 5% axial strain samples.

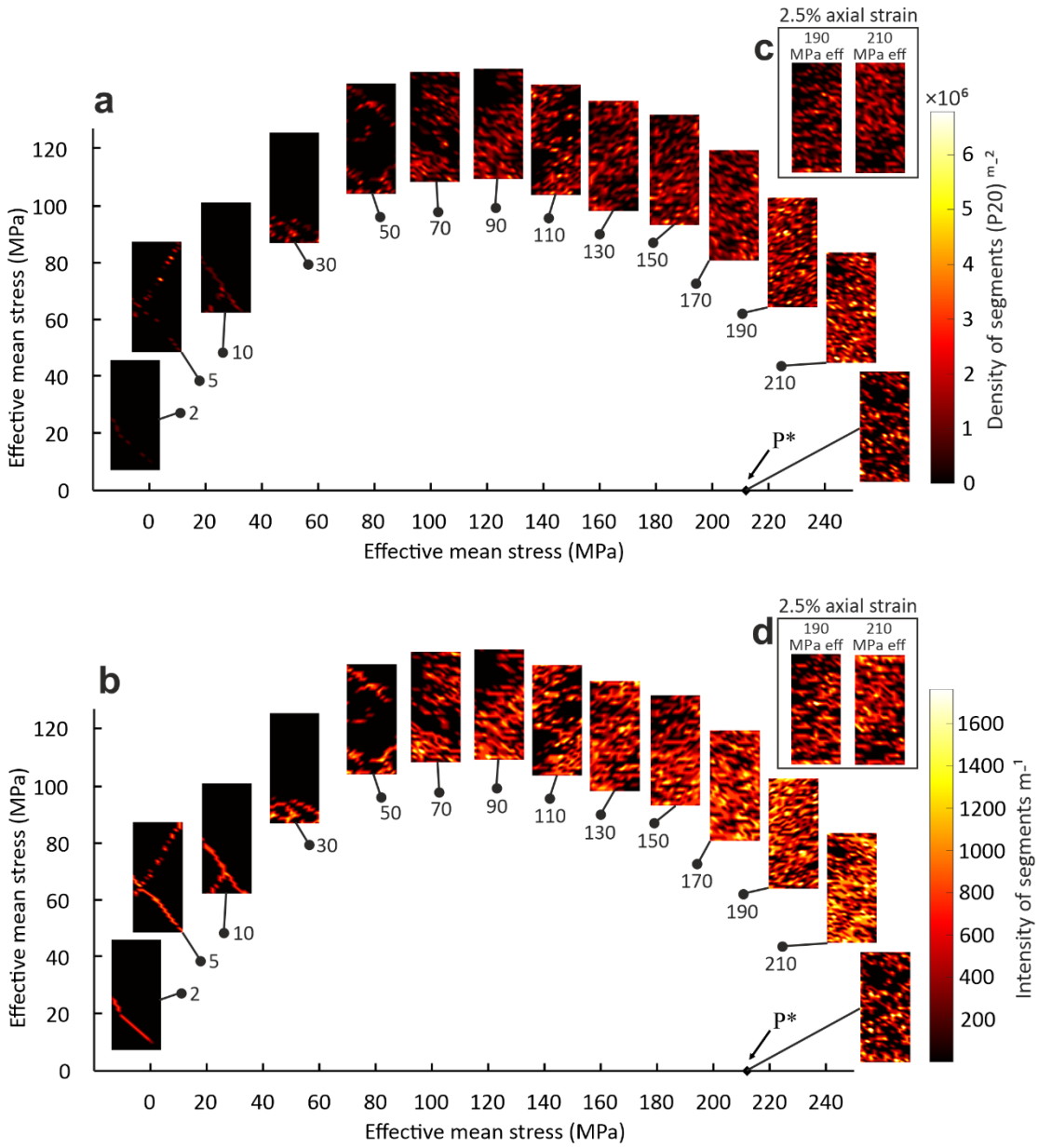

Figure 6.9. *Colourmaps of a) localisation trace density and b) localisation trace intensity for the deformed Castlegate Sandstone samples, shown in relation to their inelastic yield points plotted in P-Q space. Colourmaps of density and intensity for two samples (190 MPa and 210 MPa), taken to 2.5% axial strain, are shown in panels c and d respectively.*

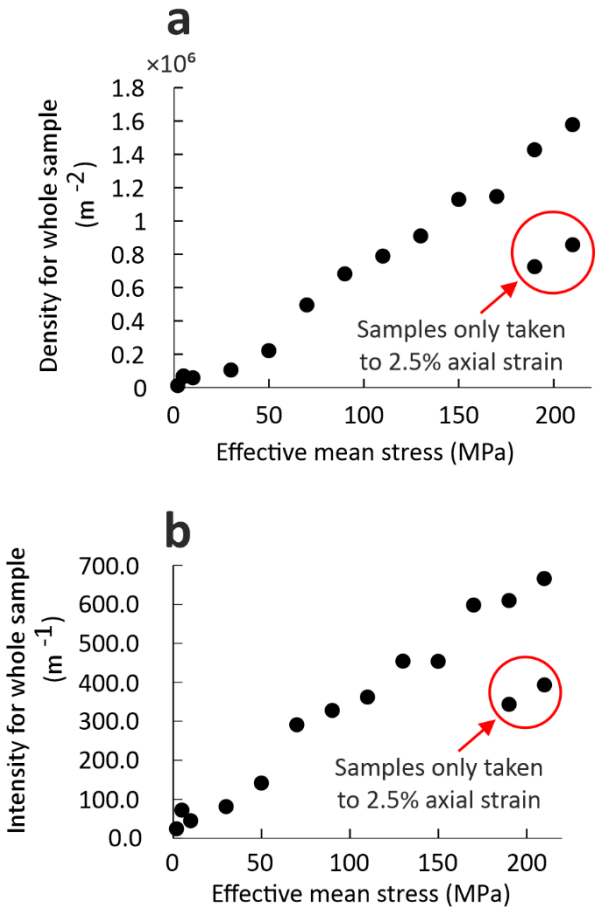

Figure 6.10. *Graphs displaying overall values of density (a) and intensity (b) versus effective mean stress for each density and intensity porosity map shown in Figure 6.9. The 190 MPa and 210 MPa samples taken to only 2.5% axial strain are circled in red.*

6.4 Discussion

6.4.1 Mode of deformation in Castlegate Sandstone

Our results for Castlegate Sandstone have corroborated the findings of previous studies on laboratory-deformed sandstones (Baud et al., 2004; Wong et al., 2001) by documenting a transition from DSBs to compaction bands with increasing effective stress (Figure 6.5a). At 2 MPa effective stress, failure is accommodated by the development of a single DSB at ~30° to σ_1 (Figure 6.5a), characterised by regions of intense cataclasis (Figure 6.6a) and porosity decrease (Figure 6.7a). At slightly higher effective stresses of 5 and 10 MPa, each sample develops one set of conjugate shear bands (Figure 6.5a), with one of the bands containing significant cataclasis and associated porosity decrease, while the other shows lesser grain crushing and a porosity increase (Figure 6.7c-e). At 30 and 50 MPa, the failure mode transitions into sets of multiple, smaller shear bands (Figure 6.5a) with each band now associated with porosity reduction (Figure 6.7f-g) due to their localised cataclasis (Figure 6.6c). The enhanced SEM images (Figure 6.5a) and rose diagrams (Figure 6.8) indicate a transitional region at ~70-130 MPa, whereby the samples contain sets of conjugate shear bands and also compaction bands (Figure 6.5 and 6.8). From an effective stress of 150 MPa to 210 MPa there are no evident conjugate shear bands and the band type switches to the formation of discrete compaction bands in a subparallel array (Figure 6.5a and Figure 6.8).

The results of our study have also shown a correlation between increasing effective stress and both the density and intensity of deformation bands, thus building upon initial observations by Mair et al. (2000) and Bésuelle et al. (2000) for the Locharbriggs and Vosges sandstones. It is likely that at higher effective stresses the increase in the grain-grain contact force enables fractures to nucleate more readily, while the greater frictional cohesion during axial loading prevents grains sliding past one another, resulting in inelastic deformation being accommodated primarily via grain fracturing, rather than by grain rearrangement (Hertz, 1881; Zhang et al., 1990). We have also shown that the density and intensity of compaction bands

increases with increasing axial strain, in line with previous studies (Baud et al., 2004; Klein et al., 2001; Ngwenya et al., 2003; Vajdova et al., 2004), highlighted by the increase in compaction band density in the 190 MPa and 210 MPa samples when the axial strain was increased from 2.5 to 5%. (Figure 6.10).

6.4.2 Lithological versus stress control on localisation

Our results have established that for Castlegate Sandstone, the mode and angle of the localisation is controlled by the effective pressure at the onset of axial shortening (Figure 6.5 and Figure 6.8). However, the variation in the type of localisation that is exhibited by sandstones across similar confining pressure ranges is testament to the control that lithology also has. Many sandstones have been shown to deform by homogeneous cataclastic flow at high pressure, rather than through the development of localised compaction bands (Baud et al., 2004; Bedford et al., 2019; Cheung et al., 2012; Menéndez et al., 1996) which raises the question as to why certain sandstones such as Castlegate fail by localised compaction, whereas others do not. Some studies have established that factors such as porosity and grain size distribution play a role, since bands have not been observed in sandstone with porosities outside the range of around 13-30% (Carbillet et al., 2021; Fossen et al., 2018; Rice-Birchall et al., 2022; Wong et al., 2001) or with poorly-sorted grain size distributions (Cheung et al., 2012). Recent laboratory studies have also examined the role of grain size and found that sandstones with larger mean grain sizes preferentially fail by localised cataclastic flow rather than compaction localisation (Rice-Birchall et al., 2022). The compaction bands we observe in Castlegate Sandstone support these observations (Figure 6.6f and g) since it can be described as a well-sorted, fine-grained sandstone with a porosity in the region of 28-30% and so fits the criteria of being able to form localised compaction bands.

Our results demonstrate that the Castlegate Sandstone we tested forms discrete, rather than diffuse compaction bands (Figure 6.6f and g), although the reasons for some sandstones preferentially developing a certain type is still not fully understood (Liu et al., 2015). The formation of the discrete bands in Castlegate Sandstone must be a result of its lithology and not

due to the starting effective stress or increasing effective mean stress during axial loading (Figure 6.4b), since discrete bands were the only type of compaction band to form (Figure 6.5a and Figure 6.6f and g). There is also no evidence of the discrete bands becoming wider as the axial strain is increased from 2.5 to 5% in the 190 and 210 MPa samples (Figure 6.5a), thus indicating that in Castlegate, accumulated inelastic strain is accommodated through the development of new discrete bands, rather than by the widening of pre-existing ones. The compaction bands are also pervasive throughout the whole sample (Figure 6.5a), whereas compaction bands in other studies have been shown to migrate from the sample ends with increasing axial shortening or with increasing starting effective pressure (Baud et al., 2004; Vajdova et al., 2004). Since the compaction bands in Castlegate Sandstone are always distributed relatively evenly throughout the whole specimen, even in the 2.5% axial strain samples (Figure 6.5a), it is likely that their distribution is also due to some inherent lithological property which affects the distribution of the stress concentrations, and consequently, controls where the compaction bands nucleate. The results of this study may provide insight regarding the ability to predict the type of deformation that will develop and its relative density and intensity in natural reservoir settings, so long as the burial and stress history of the reservoir unit is known.

6.5 Conclusions

We have conducted a comprehensive investigation examining how changing effective stress from 2-210 MPa affects the nature of localisation in Castlegate Sandstone. Our microstructural results show that the orientation and type of localisation changes systematically with increasing effective stress. At low effective stress, DSBs form, orientated ~30° to the maximum compressive stress (σ_1). At higher pressures, multiple sets of conjugate shear bands develop and as the effective stress is further increased, a transitional region is entered whereby compaction bands and shear bands are both present. As the effective mean stress approaches the hydrostatic yield pressure (P^*), the localisation transitions into sets of sub-parallel, discrete compaction bands orientated perpendicular to σ_1. The deformation bands themselves are

associated with a porosity reduction due to intense cataclasis, and we observe their density and intensity to increase with both increasing effective mean stress and increasing axial strain. The results from two additional samples axially loaded to only to 2.5% axial strain at effective mean stresses of 190 and 210 MPa showed these samples to exhibit approximately half the density and intensity values of compaction band traces taken to 5% axial strain. Each of the compaction bands we identified in Castlegate Sandstone was discrete and there was no evidence for bands becoming wider or more diffuse when the axial strain was increased from 2.5 to 5% in the 190 and 210 MPa samples, thus suggesting that strain in Castlegate Sandstone is accommodated through the development of new bands rather than the widening of pre-existing ones. The compaction bands also developed pervasively throughout the whole sample, even at low axial strains, with these observations suggesting that the preference for pervasive, discrete bands in Castlegate Sandstone is a lithologically controlled one and is not a result of either starting effective stress or increasing effective mean stress. These results have implications in predicting the type of localised deformation and its density and intensity within sandstone reservoirs if the burial and stress history of the reservoir is known.

Supplementary material

Supplementary Figure 6.1. *Castlegate Sandstone samples in their copper jackets, post-deformation. For samples 2–50 MPa, the strain was recorded sufficiently in the jacket to establish the angle at which to cut along their long axes for SEM analysis. For samples 150–210 MPa, the subperpendicular nature of the compaction bands that formed meant that these could be cut lengthways at any position. However, samples 70-130 MPa were analysed using an X-ray micro-CT to identify the orientation of the localised structures in 3D, since these samples showed no significant evidence of strain localisation in the jackets and much of the deformation was assumed to not have formed subperpendicular to* σ_1.

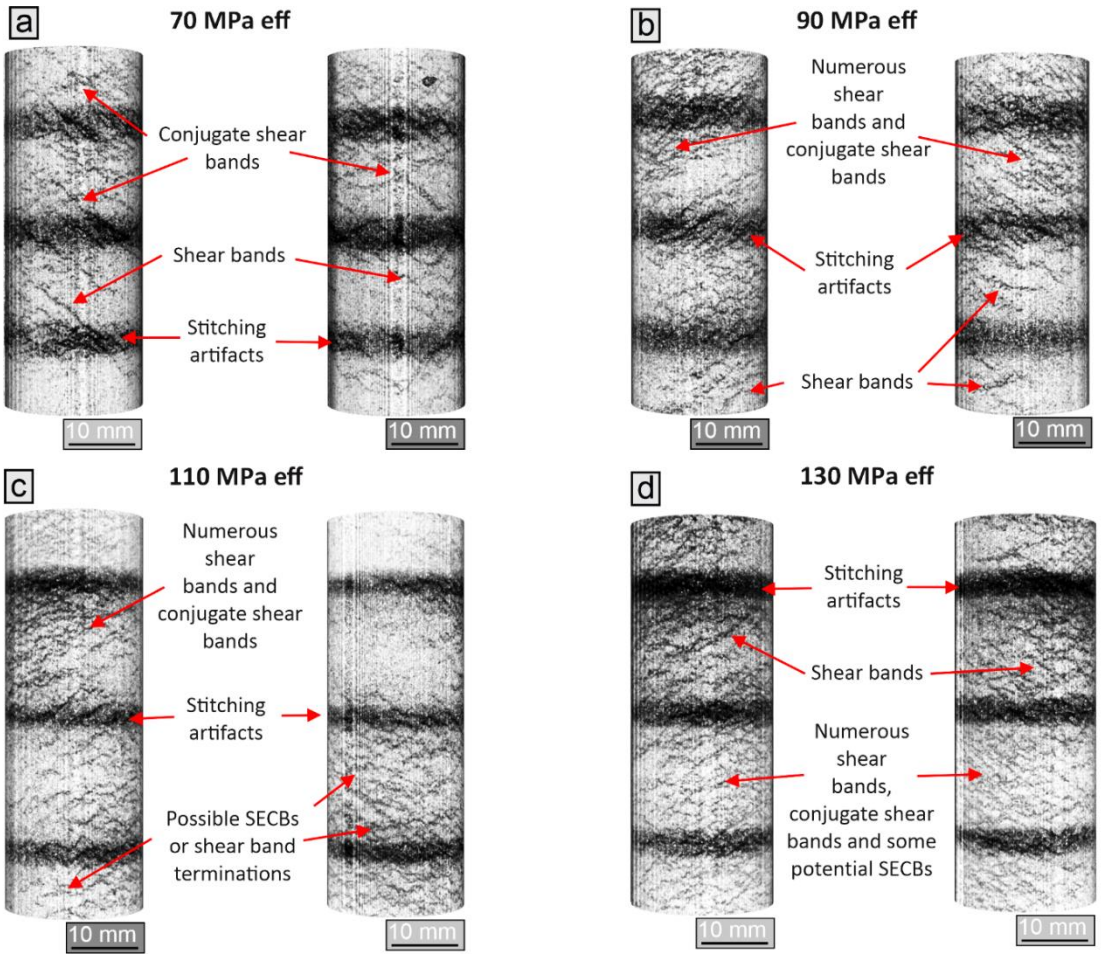

Supplementary Figure 6.2. *Processed micro-CT images of samples axially loaded at effective stresses of 70 MPa (a), 90 MPa, (b), 110 MPa (c) and 130 MPa (d). The samples were analysed to obtain the general orientations of the localisations and thus, establish the appropriate position at which to cut the samples for SEM analysis so that the true orientations of the localisations were imaged. The thick, dark, horizontal bands are a product of the automatic image stitching by the micro-CT software. Note that these images are not shown in the same orientation as the high-contrast SEM images in Figure 6.5a.*

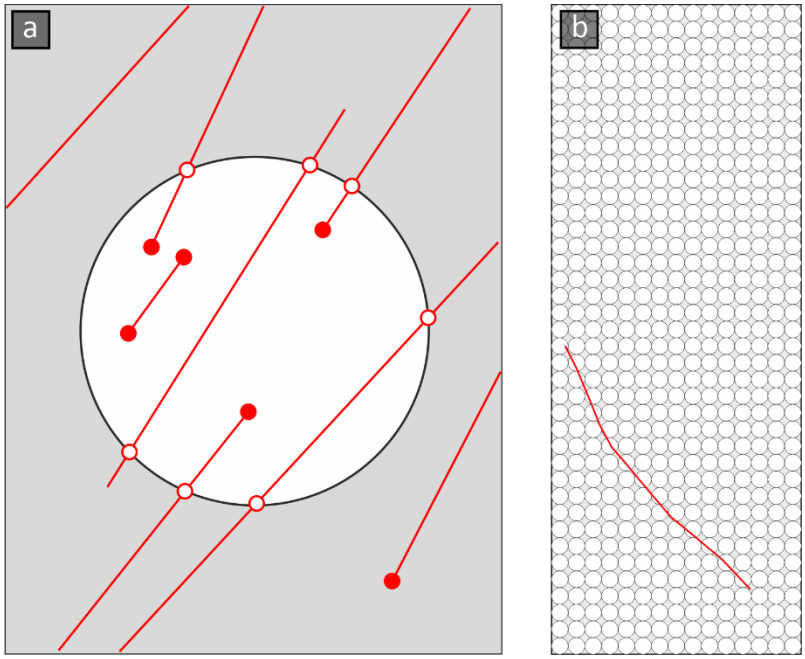

Supplementary Figure 6.3. *a) Circular scanline with n trace intersections (white dots, n=7) and circular window (white) with m trace endpoints (red dots, m=5), adapted from Mauldon et al. (2001). Fracture intensity is calculated as n/4r, where n is the number of fractures intersecting the perimeter of the circle of radius r. Fracture density is calculated as m/2π2, where m is the number of fractures terminating within the circle. b) Visualisation of the circles used to fit within the fracture trace map for the 2 MPa effective stress sample.*

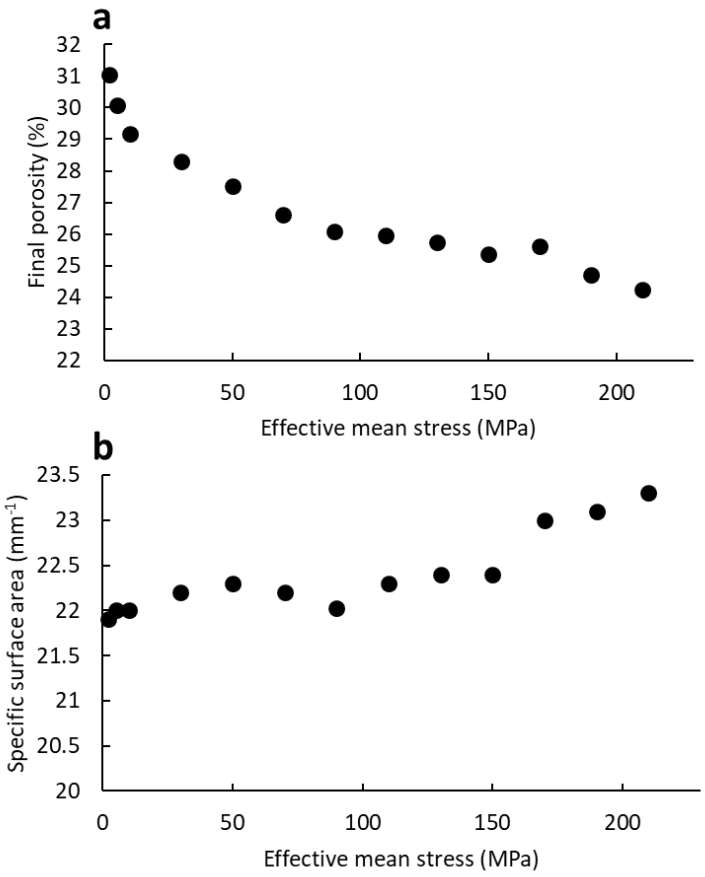

Supplementary Figure 6.4. *Graphs displaying the average porosity and specific surface area (SSA) respectively with changing effective mean stress for each Castlegate Sandstone sample shown in Figure 6.5b and Figure 6.5c.*

7 Summary and suggestions for future work

This aim of this study was to develop a better understanding of compaction bands in high-porosity sandstones, with particular focus on the microstructural properties which promote and control their formation. Specifically, the two key questions to be addressed were: 1). What microstructural properties of sandstones promote or inhibit the growth of compaction bands and 2). How do variations in microstructural properties and other external physical factors affect the nature and distribution of compaction localisation in sandstone? The following chapter summarises the main conclusions presented in *Chapters 3*, *4*, *5* and *6* and the extent to which they have addressed these research aims. The implications of these results with regard to the geomechanical processes associated with fluid injection/extraction in sandstone reservoirs, is also examined, as well as suggestions for future work, which should build upon the results from this study and address the gaps in the research that still remain.

7.1 Summary of results

In *Chapter 2*, new workflows for the processing and analysis of stitched, SEM images of deformed sandstone cores were described. A significant proportion of the chapter was focused on the construction of 2D porosity colourmaps, since the scale-dependent nature of porosity meant that determining the appropriate porosity scale to use which was both large enough to be representative of the total sample porosity but also small enough to allow small-scale porosity variations to be observed, was particularly complex. Both the size and overlap of the grid squares was found to control the quality and resolution of the colourmaps produced. Increasing grid overlap from 0 to 90% produced a better-resolved image, with overlap less than 10% failing to accurately reflect the true porosity variations. The grid size (0.1 or 0.2 CV) also controlled the porosity map produced. The larger grid size of 0.1 CV resolved most of the localised structures, though, with less precision than the 0.2 CV image and the low porosity regions were usually wider in the colourmap compared to the original image. However, the smaller grid size did encounter problems when the pore space was heterogeneous, and it

produced very high or low porosity values due to larger pores falling outside the bounds of the REA. Consequently, the 0.1 CV porosity maps reflect a more accurate representation of porosity distribution, with fewer extreme peaks, although it does mean that if the size of the localised structures such as compaction bands are very small, then their porosity may not be resolved, because the REA of the band may be much lower than the REA of the whole sample.

In *Chapter 3* a new methodology for the production of high-porosity synthetic sandstones was outlined. The production method involves consolidating loose sand with an amorphous quartz cement, precipitated via the neutralisation reaction between sodium silicate solution and hydrochloric acid. Detailed image analysis, including the construction of porosity and grain size distribution maps and pore coordination analysis performed on the samples, found them to be homogeneous with no significant stratification or heterogeneity in the grain or pore network caused by the production process. This suggests that relatively homogenous samples are produced, making them suitable for mechanical testing. The amorphous cement shows some surface cracking which is likely associated with desiccation as the samples are dried in the oven; however, the strong linearity of the elastic part of hydrostatic loading curves suggests that these cracks are mostly superficial.

The 36-38% porosity synthetic sandstones produced have realistic and reproducible uniaxial compressive and tensile strengths of 5.18 (± 0.76) MPa and 0.167 (± 0.117) MPa respectively, as well as hydrostatic yield strengths (P^*) of 67–69 MPa. They also exhibit yield curves with a comparable geometry to natural sandstones of similar porosity and grain size and display elastic moduli within the expected range for natural sandstones.

In *Chapter 4*, the technique for producing synthetic sandstones outlined in *Chapter 3* was used, to examine the effect of grain size and porosity on the nature of compaction localisation in high porosity sandstones. Twelve synthetic sandstones were produced with starting porosities of 27, 32 and 37% and mean grain sizes of 314, 411, 747 and 987 μm. Each sample was axially loaded at 85% of its P^* value to 5% axial strain. Only the sample with the

lowest initial porosity (27%) and smallest grain size (314 m) exhibits discrete compaction bands (≤3 grain diameters width), normal to the axial loading direction, whereas diffuse bands (>3 grain diameters width) are seen for the same porosity but at a greater grain size of 411 μm. These findings suggest that grain size plays a significant role in determining whether compaction bands in high-porosity sandstones are discrete or diffuse. The results also show that transitions from discrete to diffuse compaction bands can occur with increasing axial strain, as seen for the 314 μm sample which exhibits a transition from discrete to diffuse compaction bands from 5-10% axial strain, indicating that discrete bands may emerge initially before widening and coalescing as more strain is accumulated.

The findings further demonstrate that porosity controls the growth of compaction localisation, since compaction bands only develop in the samples with the lowest starting porosities of 27%. In contrast to the 27% porosity samples, those with the highest starting porosity (37%) show the largest porosity reductions and the least amounts of grain fracturing. These observations suggest that the higher porosity samples require a different mechanism for porosity reduction, which is likely to be predominantly grain rearrangement, in which the cement connections are broken to allow the grains to move more freely and slide past one another. Once the grains have formed a more efficient packing arrangement and are locked in place, they will begin to fracture, as seen in the 987 μm 37% porosity sample when taken to 10% axial strain. When the 27% porosity samples are subjected to an applied deviatoric stress, because they already have a more effective packing arrangement, the cement bonds are able to support the aggregate and prevent grain sliding. As a result, the deformation is accommodated by grain fracturing, which can subsequently result in localisation (depending on the starting grain size). These findings suggest that the packing arrangement and the strength of cement bonds may play an important role in the development of compaction localisation, with cement potentially being required to amplify stress heterogeneities that produce the cascading grain fracturing required to propagate compaction bands- an observation supported by the absence of compaction bands in experiments on loose sand with low intergranular cohesion.

The findings of field studies of PCBs, which have recorded them in units with porosities between 20-30% and grain sizes ranging from 0.3–0.8 mm, are supported by the laboratory results from this study, as compaction bands are seen in samples with starting porosities of 27% and grain sizes of 314 μm and 411 μm. However, discrepancies remain between field and laboratory observations, including the damage intensities of laboratory compaction being much greater, and requiring stresses which are much higher than would typically be found in sedimentary basins in nature.

Overall, the results of our laboratory study investigating the role of porosity and grain size show that compaction bands are most likely to form in response to inelastic deformation in finer-grained sandstones with porosities below 30%, which is consistent with observations of natural compaction bands in the field. However, fine-grained units will need higher stresses to initiate inelastic compaction than coarser-grained units, and these stresses may not always be achieved at the stress levels most sedimentary basins experience.

Chapter 5 presents the results of triaxial tests performed on 3 different high-porosity sandstones, Bentheim, Castlegate and a synthetic sandstone (produced using the methodology in Chapter 3) that each possess very similar microstructural properties, such as porosity (~26-29%) and grain size (~230-300 μm), but with 3 different cement types. Bentheim Sandstone is cemented with syntaxial quartz overgrowths, Castlegate Sandstone with predominantly clay cement and the synthetic sandstone, with amorphous quartz. When loaded to 5% axial strain at a starting stress equivalent to 85% of its P^* value, each sample forms discrete compaction bands. However, the location and distribution of the compaction bands varies between samples. The compaction bands in Bentheim Sandstone are located at the samples ends. In contrast, the compaction bands in Castlegate Sandstone are distributed throughout the entire specimen, whereas the bands in the amorphous quartz-cemented synthetic sample are only present across the sample centre. These findings indicate that the cement type, as well as its varying strength, plays a role in the micromechanics of deformation between the three samples, determining where the compaction bands nucleate and develop. Initial evidence for this is seen in the

mechanical and elastic data. Castlegate Sandstone exhibits lower Young's modulus and bulk modulus than the synthetic sample, which has a much lower P^* value due to its larger grains and higher porosity. However, although Castlegate Sandstone has a higher P^* than the synthetic sample, it has similar peak axial yield values to the synthetic sandstone and much lower values than Bentheim Sandstone. The greater ductility of the clay cements, which makes them weaker than syntaxial and amorphous quartz and allows the grains to migrate at lower axial stresses, may be the cause of these disparities.

The strength of the cement in each sample may control the differing distributions of the discrete compaction bands. The strong syntaxial quartz cement of Bentheim Sandstone may prevent the breaking of cement bonds and the movement of grains during axial loading, thereby preventing the accumulation of local stress heterogeneities throughout the sample. Consequently, since the sample is homogeneous, the stress concentrations might first appear around the loading platens at the sample ends, where the stress heterogeneities are greatest. The weak clay cement in Castlegate Sandstone however, will deform ductiley under compression, causing specimen-wide grain rearrangement and creating additional stress heterogeneities. These heterogeneities may serve as nucleation sites for compaction bands at other locations within the sample, while grain movement during inelastic loading may also diminish the stress concentrations close to the loading platens. Since the bands in the synthetic sample are not restricted to the ends of the specimens the stress concentrations at the loading platens were not responsible for their formation. Instead, the bands formed in the middle of the sample, probably as a result of a large pore or other type of stress heterogeneity.

Rather than forming as diffuse compaction fronts, the bands found in the three sandstones are distinct and clearly separated by undamaged grains. This shows that, contrary to what some modelling studies have suggested, cement is not a major factor regulating the formation of discrete compaction bands versus diffuse ones in high porosity sandstones. Our findings imply that within the 3 samples, the micromechanics of deformation, which in turn

dictates where the compaction bands occur, are affected by the type of cement and its varied strength, although cement type does not seem to influence the type of band that forms.

In *Chapter 6* a comprehensive investigation examining how changing effective stress from 2-210 MPa affects the nature of localisation in Castlegate Sandstone was presented. The microstructural results show that the orientation and type of localisation changes systematically with increasing effective stress. DSBs form at low pressures, orientated ~30° to the maximum compressive stress (σ_1). Multiple sets of conjugate shear bands form at higher pressures, and as the effective stress increases further, a transitional region is entered in which compaction bands and shear bands coexist. The localisation then changes into sets of sub-parallel, discrete compaction bands oriented perpendicular to σ_1, as the effective mean stress approaches the hydrostatic yield pressure (P^*).

The findings also reveal a positive linear relationship between increasing effective stress and the density and intensity of deformation bands. Given that greater frictional cohesion during axial loading prevents grains from sliding past one another, it is likely that at higher effective stresses, an increase in grain-grain contact force makes it easier for fractures to form. As a result, inelastic deformation is likely accommodated primarily through grain fracturing rather than grain rearrangement.

The results show that the Castlegate Sandstone samples tested preferentially develop discrete compaction bands rather than diffuse ones. Since discrete bands are the only type of compaction band to emerge, the formation of the discrete bands in Castlegate Sandstone must be a result of some lithological property and caused by the initial effective stress or rising effective mean stress during axial loading. Furthermore, the in 190 and 210 MPa samples, there is no evidence of the discrete bands widening as the axial strain is increased from 2.5 to 5%, suggesting that accumulated inelastic strain is accommodated through the creation of new discrete bands rather than via the widening of pre-existing ones. The compaction bands in Castlegate Sandstone are also distributed relatively evenly throughout the entire specimen, even

in the samples taken to only 2.5% axial strain. Consequently, the distribution of these bands may be influenced by some inherent lithological characteristic of Castlegate Sandstone which affects the distribution of stress concentrations and, as a result, regulates where the compaction bands nucleate. Provided the burial and stress history of the reservoir unit are known, the findings of this study may shed light on the ability to anticipate the type of deformation that might emerge, together with its relative density and intensity, in natural reservoir settings.

The key findings and conclusions outlined in the previous chapters can be integrated into a greater understanding of the microstructural and physical properties that control compaction band formation. By utilising the synthetic sandstone methodology, systematic laboratory-produced sandstones with controlled properties were able to be directly compared to the results of experiments on natural sandstones. The results of these studies have shown that grain size and porosity are key microstructural properties which control whether or not compaction bands form in sandstones, with cement-type also likely playing a key role. The results from these studies also indicate further complexity in compaction band formation. The type of bands (diffuse or discrete) has been shown to vary as a function of grain size, while cement type appears to playa key role in the distribution of compaction bands within sandstones. These observations of the control of microstructural sandstone properties must also be examined alongside the effects of physical external influences, such as pressure, which often makes decoupling what is having the primary control on compaction band formation extremely challenging. While the results from *Chapter 6* have provided a detailed analysis of the direct effect of pressure on compaction band formation, extrapolating results such as these to field observations, or to other laboratory tests is difficult, due to the great complexity and number of possible interplaying factors which control compaction band formation.

7.2 Implications for sandstone reservoirs

Due to the implications for reservoir and geotechnical engineering, there has been much interest regarding the processes surrounding sandstone compaction. SECBs and PCBs

can both decrease porosity and permeability within reservoirs, reducing overall reservoir quality and resulting in significant economic and temporal costs. *Chapters 4* and *5* showed how key microstructural properties, such as porosity, grain size and cement type influence the type of deformation within sandstones at the same relative pressure conditions (85% of P*). Higher-porosity, larger grain size sandstones are more likely to deform via distributed cataclastic flow and grain rearrangement, while the type of cement to plays a significant role in the distribution of strain localisation in sandstones which were able to form compaction bands. In *Chapter 6*, the effect of external factors, specifically effective pressure and axial strain was shown to control the nature of localisation, with localised compaction bands forming at high effective pressures. Quantitative analysis of the localisation traces found their densities and intensities to increase linearly with increasing effective pressure, while the number of localisation traces also increased with increasing axial strain.

Since compaction bands are sub-seismic structures, they are often excluded from reservoir geology, engineering, and fluid flow models. The ability to combine microstructural data, such as porosity, grain size and cement with information relating to the stress history and current stress conditions of the reservoir may significantly aid predictions regarding the formation of compaction localisation structures, as well as contributing towards details about their abundance and distribution within the reservoir unit. Consequently, these data will better inform fluid injection and extraction projects on where to drill to reduce the likelihood of forming these structures within the reservoir unit, as well as potentially avoiding units which have a high chance of containing pre-existing compaction bands.

7.3 Future work

While this project has shed light on some of the microstructural and physical properties that control compaction band formation, it has also highlighted the numerous complexities associated with strain localisation in porous sandstones. Porosity, grain size, grain sorting and cement each exert some influence on compaction band formation, however, the control of other

microstructural properties, such as mineralogy and grain shape have not been studied systematically. Furthermore, while we have shown that the role of cement is important, further studies are required to establish how its mineralogy, strength, quantity, and distribution affects the mechanics of compaction band formation. Future systematic laboratory studies are therefore required to uncover what other rock properties are important for localisation. The interplay between these microstructural properties during deformation is also an interesting area of future research and would be a suitable avenue for modelling studies to explore.

Both diffuse and discrete compaction bands have been identified in this research. However, the microstructural or physical factors which result in a preference for either type are still poorly understood. Resolving this issue requires more systematic laboratory studies, as well as field studies, since questions arise as to why diffuse bands have still not been identified in nature. Future studies should also seek to reconcile some of the disparities between laboratory and field-based observations. Previous investigations have remarked at the fact that the stresses required to form laboratory compaction bands are much higher than those experienced in the formation of natural bands, as well as the amount of cataclasis being higher in laboratory-deformed compaction bands.

8 References

Abdallah, Y., Sulem, J., Bornert, M., Ghabezloo, S., & Stefanou, I. (2021). Compaction Banding in High-Porosity Carbonate Rocks: 1. Experimental Observations. Journal of Geophysical Research: Solid Earth, 126(1), e2020JB020538.

Acar, Y. B., & El-Tahir, E. A. (1986). Low strain dynamic properties of artificially cemented sand. *Journal of Geotechnical Engineering*, *112*(11), 1001–1015.

Aldrich Jr, M. J. (1969). Pore pressure effects on Berea sandstone subjected to experimental deformation. *Geological Society of America Bulletin*, *80*(8), 1577–1586.

Allen, M. J., Faulkner, D. R., Worden, R. H., Rice-Birchall, E., Katirtsidis, N., & Utley, J. E. P. (2020). Geomechanical and petrographic assessment of a CO2 storage site: Application to the Acorn CO2 Storage Site, offshore United Kingdom. *International Journal of Greenhouse Gas Control*, *94*, 102923. https://doi.org/10.1016/j.ijggc.2019.102923

Armitage, P. J., Faulkner, D. R., Worden, R. H., Aplin, A. C., Butcher, A. R., & Iliffe, J. (2011). Experimental measurement of, and controls on, permeability and permeability anisotropy of caprocks from the CO2 storage project at the Krechba Field, Algeria. *Journal of Geophysical Research: Solid Earth*, *116*(B12).

Arizzi, A., Martinez-Huerga, G., Sebastián Pardo, E. M., & Cultrone, G. V. (2015). Mineralogical, textural and physical-mechanical study of hydraulic lime mortars cured under different moisture conditions. *Materiales de Construcción, 65* (318).

Asahina, D., Pan, P.-Z., Sato, M., Takeda, M., & Takahashi, M. (2019). Hydraulic and mechanical responses of porous sandstone during pore pressure-induced reactivation of fracture planes: an experimental study. *Rock Mechanics and Rock Engineering*, *52*(6), 1645–1656.

Ass' ad, J. M., Tatham, R. H., & McDonald, J. A. (1992). A physical model study of microcrack-induced anisotropy. *Geophysics, 57*(12), 1562–1570.

ASTM, C. (2016). Standard test method for compressive strength of hydraulic cement mortars (using 2-in. or [50-mm] cube specimens). *Annual Book of ASTM Standards, 4*.

Atkinson, B. K., & Meredith, P. G. (1981). Stress corrosion cracking of quartz: a note on the influence of chemical environment. *Tectonophysics, 77*(1–2), T1–T11.

Atkinson, B. K. (1984). Subcritical crack growth in geological materials. *Journal of Geophysical Research: Solid Earth*, *89*(B6), 4077–4114.

Aydin, A. (1978). Small faults formed as deformation bands in sandstone. In *Rock Friction and Earthquake Prediction* (pp. 913–930). Springer.

Aydin, A., & Ahmadov, R. (2009). Bed-parallel compaction bands in aeolian sandstone: their identification, characterization and implications. *Tectonophysics*, *479*(3–4), 277–284.

Aydin, A., & Johnson, A. M. (1978). Development of faults as zones of deformation bands and as slip surfaces in sandstone. *Pure and Applied Geophysics*, *116*(4), 931–942.

Aydin, A., Borja, R. I., & Eichhubl, P. (2006). Geological and mathematical framework for failure modes in granular rock. *Journal of Structural Geology*, *28*(1), 83–98.

Bachu, S. (2008). CO2 storage in geological media: Role, means, status and barriers to deployment. *Progress in Energy and Combustion Science*, *34*(2), 254–273.

Ballas, G., Soliva, R., Sizun, J.-P., Fossen, H., Benedicto, A., & Skurtveit, E. (2013). Shear-enhanced compaction bands formed at shallow burial conditions; implications for fluid flow (Provence, France). *Journal of Structural Geology*, *47*, 3–15.

Ballas, G., Fossen, H., & Soliva, R. (2015). Factors controlling permeability of cataclastic deformation bands and faults in porous sandstone reservoirs. *Journal of Structural Geology*, *76*, 1–21.

Balsamo, F., & Storti, F. (2011). Size-dependent comminution, tectonic mixing, and sealing behavior of a "structurally oversimplified" fault zone in poorly lithified sands: Evidence for a coseismic rupture? Bulletin, 123(3–4), 601–619.

Bandyopadhyay, A., & Abdullah, H. (2013). A Laboratory Study of Strong and Weak Sandstones.

Baud, P., & Meredith, P. G. (1997). Damage accumulation during triaxial creep of Darley Dale sandstone from pore volumometry and acoustic emission. *International Journal of Rock Mechanics and Mining Sciences*, *34*(3–4), 24-e1.

Baud, P., Zhu, W., & Wong, T.-F. (2000). Failure mode and weakening effect of water on sandstone. *Journal of Geophysical Research: Solid Earth*, *105*(B7), 16371–16389.

Baud, P., Klein, E., & Wong, T.-F. (2004). Compaction localization in porous sandstones: spatial evolution of damage and acoustic emission activity. *Journal of Structural Geology*, *26*(4), 603–624.

Baud, P., Louis, L., David, C., Rawling, G. C., & Wong, T.-F. (2005). Effects of bedding and foliation on mechanical anisotropy, damage evolution and failure mode. *Geological Society, London, Special Publications*, *245*(1), 223–249.

Baud, P., Vajdova, V., & Wong, T.-F. (2006). Shear-enhanced compaction and strain localization: Inelastic deformation and constitutive modeling of four porous sandstones. *Journal of Geophysical Research: Solid Earth*, *111*(B12).

Baud, P., Meredith, P., & Townend, E. (2012). Permeability evolution during triaxial compaction of an anisotropic porous sandstone. *Journal of Geophysical Research: Solid Earth*, *117*(B5).

Baud, P., Wong, T.-F., & Zhu, W. (2014). Effects of porosity and crack density on the compressive strength of rocks. *International Journal of Rock Mechanics and Mining Sciences*, *67*, 202–211.

Baud, P., Reuschlé, T., Ji, Y., Cheung, C. S., & Wong, T. (2015). Mechanical compaction and strain localization in Bleurswiller sandstone. *Journal of Geophysical Research: Solid Earth*, *120*(9), 6501–6522.

Baud, P., Hall, S., Heap, M. J., Ji, Y., & Wong, T-F. (2021). The Brittle-Ductile Transition in Porous Limestone: Failure Mode, Constitutive Modeling of Inelastic Deformation and Strain Localization. Journal of Geophysical Research: Solid Earth, 126(5), e2020JB021602.

Bear, J. (1972). *Dynamics of fluids in porous media*. Courier Corporation.

Bedford, J. D., Faulkner, D. R., Leclère, H., & Wheeler, J. (2018). High-resolution mapping of yield curve shape and evolution for porous rock: The effect of inelastic compaction on porous bassanite. *Journal of Geophysical Research: Solid Earth*, *123*(2), 1217–1234.

Bedford, J. D., Faulkner, D. R., Wheeler, J., & Leclère, H. (2019). High-resolution mapping of yield curve shape and evolution for high porosity sandstone. *Journal of Geophysical Research: Solid Earth*.

Bell, F. G., Culshaw, M. G., Forster, A., & Nathanail, C. P. (2009). The engineering geology of the Nottingham area, UK. *Geological Society, London, Engineering Geology Special Publications*, *22*(1), 1–24.

Bergaya, F., Dion, P., Alcover, J. F., Clinard, C., & Tchoubar, D. (1996). TEM study of kaolinite thermal decomposition by controlled-rate thermal analysis. *Journal of Materials Science*, *31*(19), 5069–5075.

Bésuelle, P. (2001). Compacting and dilating shear bands in porous rock: Theoretical and experimental conditions. *Journal of Geophysical Research: Solid Earth*, *106*(B7), 13435–13442.

Bésuelle, P., Desrues, J., & Raynaud, S. (2000). Experimental characterisation of the localisation phenomenon inside a Vosges sandstone in a triaxial cell. *International Journal of Rock Mechanics and Mining Sciences*, *37*(8), 1223–1237.

Bésuelle, P., Baud, P., & Wong, T.-F. (2003). Failure mode and spatial distribution of damage in Rothbach sandstone in the brittle-ductile transition. In *Thermo-Hydro-Mechanical Coupling in Fractured Rock* (pp. 851–868). Springer.

Bisschop, J., & Wittel, F. K. (2011). Contraction gradient induced microcracking in hardened cement paste. *Cement and Concrete Composites*, *33*(4), 466–473.

Bjørlykke, K. (1999). An overview of factors controlling rates of compaction, fluid generation and flow in sedimentary basins. *Growth, Dissolution and Pattern Formation in Geosystems*, 381–404.

Blott, S. J., & Pye, K. (2001). GRADISTAT: a grain size distribution and statistics package for the analysis of unconsolidated sediments. *Earth Surface Processes and Landforms*, *26*(11), 1237–1248.

Brace, W., Walsh, J. B., & Frangos, W. T. (1968). Permeability of granite under high pressure. *Journal of Geophysical Research*, *73*(6), 2225–2236.

Brace, W. F. (1978). Volume changes during fracture and frictional sliding: A review. *Pure and Applied Geophysics*, *116*(4), 603–614.

Brahme, A., Staraselski, Y., Inal, K., & Mishra, R. K. (2012). Determination of the minimum scan size to obtain representative textures by electron backscatter diffraction. *Metallurgical and Materials Transactions A*, *43*(13), 5298–5307.

Brown, G. O., Hsieh, H. T., & Lucero, D. A. (2000). Evaluation of laboratory dolomite core sample size using representative elementary volume concepts. *Water Resources Research*, *36*(5), 1199–1207.

Bruns, S., Stipp, S. L. S., & Sørensen, H. O. (2017). Statistical representative elementary volumes of porous media determined using greyscale analysis of 3D tomograms. *Advances in Water Resources*, *107*, 32–42.

Cuesta-Cano, A. C., Van Stappen, J. F., Wolterbeek, T. K., & Hangx, S. J. (2021). Uniaxial compaction of sand using 4D X-ray tomography: The effect of mineralogy on grain-scale compaction mechanisms. *Materials Today Communications*, *26*, 101881.

Carbillet, L., Heap, M. J., Baud, P., Wadsworth, F. B., & Reuschle, T. (2021). Mechanical compaction of crustal analogs made of sintered glass beads: the influence of porosity and grain size. *Journal of Geophysical Research: Solid Earth*, *126*(4), e2020JB021321.

Carles, P., & Lapointe, P. (2004). Water-weakening of under stress carbonates: New insights on pore volume compressibility measurements. In *SCA Annual International Symposium* (Vol. 27, pp. 1–12).

Carmichael, R. S. (2017). *Practical Handbook of Physical Properties of Rocks and Minerals (1988)*. CRC press.

Carroll, M. M. (1991). A critical state plasticity theory for porous reservoir rock. *Recent Advances in Mechanics of Structured Continua*, *117*, 1–8.

Castleman, K. R. (1996). *Digital image processing*. Prentice Hall Press.

Charalampidou, E.-M., Hall, S. A., Stanchits, S., Lewis, H., & Viggiani, G. (2011). Characterization of shear and compaction bands in a porous sandstone deformed under triaxial compression. *Tectonophysics*, *503*(1–2), 8–17. https://doi.org/10.1016/j.tecto.2010.09.032

Charalampidou, E.-M., Hall, S. A., Stanchits, S., Viggiani, G., & Lewis, H. (2014). Shear-enhanced compaction band identification at the laboratory scale using acoustic and full-field methods. *International Journal of Rock Mechanics and Mining Sciences*, *67*, 240–252.

Charalampidou, E.-M., Stanchits, S., & Dresen, G. (2017). Compaction bands in a porous sandstone sample with pre-induced shear bands. In *International Workshop on Bifurcation and Degradation in Geomaterials* (pp. 391–398). Springer.

Charalampidou, E.-M., Combe, G., Viggiani, G., & Lanier, J. (2009). Mechanical behavior of mixtures of circular and rectangular 2D particles. In *AIP Conference Proceedings* (Vol. 1145, pp. 821–824). American Institute of Physics.

Chen, Y., Joffre, D., & Avitabile, P. (2018). Underwater dynamic response at limited points expanded to full-field strain response. *Journal of Vibration and Acoustics, 140*(5), 051016.

Chen, X., Roshan, H., Lv, A., Hu, M., & Regenauer-Lieb, K. (2020). The dynamic evolution of compaction bands in highly porous carbonates: the role of local heterogeneity for nucleation and propagation. Progress in Earth and Planetary Science, 7(1), 1–19.

Cheng, C. H., & Toksöz, M. N. (1979). Inversion of seismic velocities for the pore aspect ratio spectrum of a rock. *Journal of Geophysical Research: Solid Earth*, *84*(B13), 7533–7543.

Cheung, C. S., Baud, P., & Wong, T.-F. (2012). Effect of grain size distribution on the development of compaction localization in porous sandstone. *Geophysical Research Letters*, *39*(21).

Cilona, A., Faulkner, D. R., Tondi, E., Agosta, F., Mancini, L., Rustichelli, A., et al. (2014). The effects of rock heterogeneity on compaction localization in porous carbonates. *Journal of Structural Geology*, *67*, 75–93.

Conde-Vázquez, C., de Miguel-San Martín, O., & García-Herbosa, G. (2019). Artificial arenite from wastes of natural sandstone industry. *Materiales de Construcción*, *69*(333), 178.

Costa, S. E. D., Neto, E. B., Oliveira, M. C. A., & Santos, J. S. C. (2017). Mechanical and petrophysical analysis of synthetic sandstone for enhanced oil recovery applications. *Brazilian Journal of Petroleum and Gas, 11*(3).

Crawford, B. R., Gooch, M. J., & Webb, D. W. (2004). Textural controls on constitutive behavior in unconsolidated sands: Micromechanics and cap plasticity. In *Gulf Rocks 2004, the 6th North America Rock Mechanics Symposium (NARMS)*. American Rock Mechanics Association.

Cuss, R. J., Rutter, E. H., & Holloway, R. F. (2003). The application of critical state soil mechanics to the mechanical behavior of porous sandstones. *International Journal of Rock Mechanics and Mining Sciences, 40*(6), 847–862.

Dapples, E. C. (1962). Stages of diagenesis in the development of sandstones. *Geological Society of America Bulletin*, *73*(8), 913–934.

David, C., Menendez, B., & Bernabe, Y. (1998). The mechanical behavior of synthetic sandstone with varying brittle cement content. *International Journal of Rock Mechanics and Mining Sciences*, *35*(6), 759–770.

David, C., Wong, T.-F., Zhu, W., & Zhang, J. (1994). Laboratory measurement of compaction-induced permeability change in porous rocks: Implications for the generation and maintenance of pore pressure excess in the crust. *Pure and Applied Geophysics*, *143*(1–3), 425–456.

David, C., Dautriat, J., Sarout, J., Delle Piane, C., Menéndez, B., Macault, R., & Bertauld, D. (2015). Mechanical instability induced by water weakening in laboratory fluid injection tests. *Journal of Geophysical Research: Solid Earth*, *120*(6), 4171–4188.

Deng, S., Zuo, L., Aydin, A., Dvorkin, J., & Mukerji, T. (2015). Permeability characterization of natural compaction bands using core flooding experiments and three-dimensional image-based analysis: Comparing and contrasting the results from two different methods. *AAPG Bulletin*, *99*(1), 27–49.

DiGiovanni, A. A., Fredrich, J. T., Holcomb, D. J., & Olsson, W. A. (2007). Microscale damage evolution in compacting sandstone. *Geological Society, London, Special Publications*, *289*(1), 89–103.

DiGiovanni, A. A., Fredrich, J. T., Holcomb, D. J., & Olsson, W. A. (2000). Micromechanics of compaction in an analogue reservoir sandstone. In *4th North American Rock Mechanics Symposium*. American Rock Mechanics Association.

DiMaggio, F. L., & Sandler, I. S. (1971). Material model for granular soils. *Journal of the Engineering Mechanics Division*, *97*(3), 935–950.

Dobereiner, L. (1984). Engineering geology of weak sandstones.

Dost, B., Ruigrok, E., & Spetzler, J. (2017). Development of seismicity and probabilistic hazard assessment for the Groningen gas field. *Netherlands Journal of Geosciences*, *96*(5), s235–s245.

Dropek, R. K., Johnson, J. N., & Walsh, J. B. (1978). The influence of pore pressure on the mechanical properties of Kayenta sandstone. *Journal of Geophysical Research: Solid Earth*, *83*(B6), 2817–2824.

Dyke, C. G., & Dobereiner, L. (1991). Evaluating the strength and deformability of sandstones. Geological Society of London.

Dyskin, A. V., & Pasternak, E. (2015). Asymptotic analysis of fracture propagation in materials with rotating particles. *Engineering Fracture Mechanics*, *150*, 1–18.

Eichhubl, P., Hooker, J. N., & Laubach, S. E. (2010). Pure and shear-enhanced compaction bands in Aztec Sandstone. *Journal of Structural Geology*, *32*(12), 1873–1886.

El Bied, A., Sulem, J., & Martineau, F. (2002). Microstructure of shear zones in Fontainebleau sandstone.

Eneng, M., & Rifki, S. (2018). Effects of the Precipitation pH of Sodium Silicate on the Amorphous Silica Characteristics and its capability in the Pb and Cd Adsorption. *Research Journal of Chemistry and Environment*, 7.

Falcon-Suarez, I., Marín-Moreno, H., Browning, F., Lichtschlag, A., Robert, K., North, L. J., & Best, A. I. (2017). Experimental assessment of pore fluid distribution and geomechanical changes in saline sandstone reservoirs during and after CO2 injection. *International Journal of Greenhouse Gas Control*, *63*, 356–369.

Ferreira, T., & Rasband, W. (2012). ImageJ user guide. *ImageJ/Fiji*, *1*, 155–161.

Fischer, G. J. (1992). The determination of permeability and storage capacity: Pore pressure oscillation method. In *International Geophysics* (Vol. 51, pp. 187–211). Elsevier.

Fjar, E., Holt, R. M., Raaen, A. M., Risnes, R., & Horsrud, P. (2008). *Petroleum related rock mechanics* (Vol. 53). Elsevier.

Folk, R. L. (1954). The distinction between grain size and mineral composition in sedimentary-rock nomenclature. *The Journal of Geology*, *62*(4), 344–359.

Fortin, J., Schubnel, A., & Guéguen, Y. (2005). Elastic wave velocities and permeability evolution during compaction of Bleurswiller sandstone. *International Journal of Rock Mechanics and Mining Sciences*, *42*(7–8), 873–889.

Fortin, J., Stanchits, S., Dresen, G., & Gueguen, Y. (2009). Acoustic emissions monitoring during inelastic deformation of porous sandstone: comparison of three modes of deformation. *Pure and Applied Geophysics*, *166*(5–7), 823–841.

Fortin, J., Stanchits, S., Dresen, G., & Guéguen, Y. (2006). Acoustic emission and velocities associated with the formation of compaction bands in sandstone. *Journal of Geophysical Research: Solid Earth*, *111*(B10).

Fossen, H., Schultz, R. A., Shipton, Z. K., & Mair, K. (2007). Deformation bands in sandstone: a review. *Journal of the Geological Society*, *164*(4), 755–769.

Fossen, H., Schultz, R. A., & Torabi, A. (2011). Conditions and implications for compaction band formation in the Navajo Sandstone, Utah. *Journal of Structural Geology*, *33*(10), 1477–1490. https://doi.org/10.1016/j.jsg.2011.08.001

Fossen, H., Zuluaga, L. F., Ballas, G., Soliva, R., & Rotevatn, A. (2015). Contractional deformation of porous sandstone: Insights from the Aztec Sandstone, SE Nevada, USA. *Journal of Structural Geology*, *74*, 172–184.

Fossen, H., Soliva, R., Ballas, G., Trzaskos, B., Cavalcante, C., & Schultz, R. A. (2018). A review of deformation bands in reservoir sandstones: geometries, mechanisms and distribution. *Geological Society, London, Special Publications*, *459*(1), 9–33.

Fredrick, J. T., Deitrick, G. L., Arguello, J. G., & DeRouffignac, E. P. (1998). Reservoir compaction, surface subsidence, and casing damage: a geomechanics approach to mitigation and reservoir management. In *SPE/ISRM rock mechanics in petroleum engineering*. OnePetro.

Gal, D., Dvorkin, J., & Nur, A. (1998). A physical model for porosity reduction in sandstones. *Geophysics*, *63*(2), 454–459.

Glover, P. W. J., Baud, P., Darot, M., Meredith, P. G., Boon, S. A., LeRavalec, M., et al. (1995). α/β phase transition in quartz monitored using acoustic emissions. *Geophysical Journal International*, *120*(3), 775–782.

Gomez, J. S., Chalaturnyk, R. J., & Zambrano-Narvaez, G. (2019). Experimental Investigation of the Mechanical Behavior and Permeability of 3D Printed Sandstone Analogues Under Triaxial Conditions. *Transport in Porous Media*, *129*(2), 541–557.

Gong, L., Nie, L., & Xu, Y. (2020). Geometrical and Topological Analysis of Pore Space in Sandstones Based on X-ray Computed Tomography. *Energies*, *13*(15), 3774.

Griffith, A. A. (1921). VI. The phenomena of rupture and flow in solids. Phil. Trans. R. Soc. Lond. A, 221(582–593), 163–198.

Groisman, A., & Kaplan, E. (1994). An experimental study of cracking induced by desiccation. *EPL (Europhysics Letters)*, *25*(6), 415.

Haimson, B. C. (2001). Fracture-like borehole breakouts in high-porosity sandstone: are they caused by compaction bands? *Physics and Chemistry of the Earth, Part A: Solid Earth and Geodesy*, *26*(1–2), 15–20.

Haimson, B., & Lee, H. (2004). Borehole breakouts and compaction bands in two high-porosity sandstones. *International Journal of Rock Mechanics and Mining Sciences*, *41*(2), 287–301.

Han, G., & Dusseault, M. B. (2003). Description of fluid flow around a wellbore with stress-dependent porosity and permeability. *Journal of Petroleum Science and Engineering*, *40*(1–2), 1–16.

Hangx, S. J. T., Spiers, C. J., & Peach, C. J. (2010). Creep of simulated reservoir sands and coupled chemical-mechanical effects of CO2 injection. *Journal of Geophysical Research: Solid Earth*, *115*(B9).

Hangx, S. J. T., van der Linden, A., Marcelis, F., & Bauer, A. (2013). The effect of CO2 on the mechanical properties of the Captain Sandstone: Geological storage of CO2 at the Goldeneye field (UK). *International Journal of Greenhouse Gas Control*, *19*, 609–619. https://doi.org/10.1016/j.ijggc.2012.12.016

Hangx, S. J. T., & Brantut, N. (2019). Micromechanics of High-Pressure Compaction in Granular Quartz Aggregates. *Journal of Geophysical Research: Solid Earth*, *124*(7), 6560–6580.

He, W., Chen, K., Hayatdavoudi, A., Sawant, K., & Lomas, M. (2019). Effects of clay content, cement and mineral composition characteristics on sandstone rock strength and deformability behaviors. *Journal of Petroleum Science and Engineering*, *176*, 962–969.

Healy, D., Rizzo, R. E., Cornwell, D. G., Farrell, N. J., Watkins, H., Timms, N. E., et al. (2017). FracPaQ: A MATLAB™ toolbox for the quantification of fracture patterns. *Journal of Structural Geology*, *95*, 1–16.

Heap, M. J., Baud, P., & Meredith, P. G. (2009). Influence of temperature on brittle creep in sandstones. *Geophysical Research Letters*, *36*(19).

Heap, M. J., Faulkner, D. R., Meredith, P. G., & Vinciguerra, S. (2010). Elastic moduli evolution and accompanying stress changes with increasing crack damage: implications for stress changes around fault zones and volcanoes during deformation. *Geophysical Journal International*, *183*(1), 225–236.

Heap, M. J., Brantut, N., Baud, P., & Meredith, P. G. (2015). Time-dependent compaction band formation in sandstone. *Journal of Geophysical Research: Solid Earth*, *120*(7), 4808–4830.

Hecht, C. A., Bönsch, C., & Bauch, E. (2005). Relations of Rock Structure and Composition to Petrophysical and Geomechanical Rock Properties: Examples from Permocarboniferous Red-Beds. *Rock Mechanics and Rock Engineering*, *38*(3), 197–216. https://doi.org/10.1007/s00603-005-0047-6

Heggheim, T., Madland, M. V., Risnes, R., & Austad, T. (2005). A chemical induced enhanced weakening of chalk by seawater. *Journal of Petroleum Science and Engineering*, *46*(3), 171–184.

Heilbronner, R., & Barrett, S. (2013). *Image analysis in Earth Sciences: microstructures and textures of earth materials* (Vol. 129). Springer Science & Business Media.

Herring, A. L., Harper, E. J., Andersson, L., Sheppard, A., Bay, B. K., & Wildenschild, D. (2013). Effect of fluid topology on residual nonwetting phase trapping: Implications for geologic CO2 sequestration. *Advances in Water Resources*, *62*, 47–58.

Hertz, H. (1881). On the contact of elastic solids. *Z. Reine Angew. Mathematik*, *92*, 156–171.

Holcomb, D. J., & Olsson, W. A. (2003). Compaction localization and fluid flow. *Journal of Geophysical Research: Solid Earth*, *108*(B6).

Hu, D. W., Zhou, H., Zhang, F., & Shao, J.-F. (2010). Evolution of poroelastic properties and permeability in damaged sandstone. *International Journal of Rock Mechanics and Mining Sciences*, *47*(6), 962–973.

Huang, J. T., & Airey, D. W. (1998). Properties of artificially cemented carbonate sand. *Journal of Geotechnical and Geoenvironmental Engineering*, *124*(6), 492–499.

Huang, L., Baud, P., Cordonnier, B., Renard, F., Liu, L., & Wong, T.-F. (2019). Synchrotron X-ray imaging in 4D: Multiscale failure and compaction localization in triaxially compressed porous limestone. *Earth and Planetary Science Letters*, *528*, 115831.

Hugo, R. C., Bernsen, S., Breen, K., & Ruzicka, A. (2015). Phase analysis of large EDS datasets with Matlab. *Microscopy and Microanalysis*, *21*(S3), 2023–2024.

Ingraham, M. D., Issen, K. A., & Holcomb, D. J. (2013). Response of Castlegate sandstone to true triaxial states of stress. *Journal of Geophysical Research: Solid Earth*, *118*(2), 536–552.

Ishutov, S., Hasiuk, F. J., Harding, C., & Grey, J. N. (2015). 3D printing sandstone porosity models. *Interpretation*, *3*(3), SX49–SX61.

Issen, K. A., & Rudnicki, J. W. (2000). Conditions for compaction bands in porous rock. *Journal of Geophysical Research: Solid Earth*, *105*(B9), 21529–21536.

Jaeger, J. C., Cook, N. G., & Zimmerman, R. (2009). *Fundamentals of rock mechanics*. John Wiley & Sons.

Jones, S. M., McCann, C., Astin, T. R., & Sothcott, J. (1998). The effects of pore-fluid salinity on ultrasonic wave propagation in sandstones. *Geophysics*, *63*(3), 928–934.

Katsman, R., Aharonov, E., & Haimson, B. C. (2009). Compaction bands induced by borehole drilling. *Acta Geotechnica*, *4*(3), 151–162.

Klein, E., Baud, P., Reuschlé, T., & Wong, T.-F. (2001). Mechanical behaviour and failure mode of Bentheim sandstone under triaxial compression. *Physics and Chemistry of the Earth, Part A: Solid Earth and Geodesy*, *26*(1–2), 21–25.

Koestel, J., Larsbo, M., & Jarvis, N. (2020). Scale and REV analyses for porosity and pore connectivity measures in undisturbed soil. *Geoderma*, *366*, 114206.

Kong, L., Ostadhassan, M., Li, C., & Tamimi, N. (2018). Can 3-D printed gypsum samples replicate natural rocks? An experimental study. *Rock Mechanics and Rock Engineering*, *51*(10), 3061–3074.

Kong, L., Ostadhassan, M., Hou, X., Mann, M., & Li, C. (2019). Microstructure characteristics and fractal analysis of 3D-printed sandstone using micro-CT and SEM-EDS. *Journal of Petroleum Science and Engineering*, *175*, 1039–1048.

Lesmes, D. P., & Frye, K. M. (2001). Influence of pore fluid chemistry on the complex conductivity and induced polarization responses of Berea sandstone. *Journal of Geophysical Research: Solid Earth*, *106*(B3), 4079–4090.

Li, H., Tang, X., Wang, R., Lin, F., Liu, Z., & Cheng, K. (2016). Comparative study on theoretical and machine learning methods for acquiring compressed liquid densities of 1, 1, 1, 2, 3, 3, 3-heptafluoropropane (r227ea) via song and mason equation, support vector machine, and artificial neural networks. *Applied Sciences*, *6*(1), 25.

Lin, C.-H., Lee, V. W., & Trifunac, M. D. (2005). The reflection of plane waves in a poroelastic half-space saturated with inviscid fluid. *Soil Dynamics and Earthquake Engineering*, *25*(3), 205–223.

Lintao, Y., Marshall, A. M., Wanatowski, D., Stace, R., & Ekneligoda, T. (2017). Effect of high temperatures on sandstone–a computed tomography scan study. *International Journal of Physical Modelling in Geotechnics*, 1–16.

Liu, C., Pollard, D. D., Gu, K., & Shi, B. (2015). Mechanism of formation of wiggly compaction bands in porous sandstone: 2. Numerical simulation using discrete element method. *Journal of Geophysical Research: Solid Earth*, *120*(12), 8153–8168.

Liu, Z., Wang, H., Blackbourn, G., Ma, F., He, Z., Wen, Z., et al. (2019). Heavy oils and oil sands: global distribution and resource assessment. *Acta Geologica Sinica-English Edition*, *93*(1), 199–212.

Lock, P. (2001). Estimating the permeability of reservoir sandstones using image analysis of pore structure.

Loebl, J. (1985). *Image analysis: principles and practice*. Joyce Loebl.

Louis, L., Wong, T.-F., Baud, P., & Tembe, S. (2006). Imaging strain localization by X-ray computed tomography: discrete compaction bands in Diemelstadt sandstone. *Journal of Structural Geology*, *28*(5), 762–775.

Louis, L., Wong, T.-F., & Baud, P. (2007). Imaging strain localization by X-ray radiography and digital image correlation: Deformation bands in Rothbach sandstone. *Journal of Structural Geology*, *29*(1), 129–140.

Lu, J., Healy Jr, D. M., & Weaver, J. B. (1994). Contrast enhancement of medical images using multiscale edge representation. *Optical Engineering*, *33*(7), 2151–2161.

Madland, M. V., Finsnes, A., Alkafadgi, A., Risnes, R., & Austad, T. (2006). The influence of CO2 gas and carbonate water on the mechanical stability of chalk. *Journal of Petroleum Science and Engineering*, *51*(3–4), 149–168.

Main, I. G., Kwon, O., Ngwenya, B. T., & Elphick, S. C. (2000). Fault sealing during deformation-band growth in porous sandstone. *Geology*, *28*(12), 1131–1134.

Main, I. G., Kwon, O., Mair, K., Ngwenya, B., Elphick, S., Grueshow, E., & Rudnicki, J. (2003). Effect of compaction and dilatancy on the evolution of permeability in porous sandstones. In *EGS-AGU-EUG Joint Assembly* (p. 1162).

Mair, K., Main, I., & Elphick, S. (2000). Sequential growth of deformation bands in the laboratory. *Journal of Structural Geology*, *22*(1), 25–42.

Mair, K., Elphick, S., & Main, I. (2002). Influence of confining pressure on the mechanical and structural evolution of laboratory deformation bands. *Geophysical Research Letters*, *29*(10), 49–1.

Mann, R. L., & Fatt, I. (1960). Effect of pore fluids on the elastic properties of sandstone. *Geophysics*, *25*(2), 433–444.

Marketos, G., & Bolton, M. D. (2009). Compaction bands simulated in discrete element models. *Journal of Structural Geology*, *31*(5), 479–490.

Mauldon, M., Dunne, W. M., & Rohrbaugh Jr, M. B. (2001). Circular scanlines and circular windows: new tools for characterizing the geometry of fracture traces. *Journal of Structural Geology*, *23*(2–3), 247–258.

Menéndez, B., Zhu, W., & Wong, T.-F. (1996). Micromechanics of brittle faulting and cataclastic flow in Berea sandstone. *Journal of Structural Geology*, *18*(1), 1–16.

Mitchell, T. M., & Faulkner, D. R. (2008). Experimental measurements of permeability evolution during triaxial compression of initially intact crystalline rocks and implications for fluid flow in fault zones. *Journal of Geophysical Research: Solid Earth*, *113*(B11).

Mollema, P. N., & Antonellini, M. A. (1996). Compaction bands: a structural analog for anti-mode I cracks in aeolian sandstone. *Tectonophysics*, *267*(1–4), 209–228.

Mu, Y., Sungkorn, R., & Toelke, J. (2016). Identifying the representative flow unit for capillary dominated two-phase flow in porous media using morphology-based pore-scale modeling. *Advances in Water Resources*, *95*, 16–28.

Ngwenya, B. T., Elphick, S. C., Main, I. G., & Shimmield, G. B. (2000). Experimental constraints on the diagenetic self-sealing capacity of faults in high porosity rocks. *Earth and Planetary Science Letters*, *183*(1–2), 187–199.

Ngwenya, B. T., Kwon, O., Elphick, S. C., & Main, I. G. (2003). Permeability evolution during progressive development of deformation bands in porous sandstones. *Journal of Geophysical Research: Solid Earth*, *108*(B7).

Nicholson, E. D., Goldsmith, G., & Cook, J. M. (1998). Direct observation and modeling of sand production processes in weak sandstone. In *SPE/ISRM Rock Mechanics in Petroleum Engineering*. Society of Petroleum Engineers.

Olsson, W. A., & Holcomb, D. J. (2000). Compaction localization in porous rock. *Geophysical Research Letters*, *27*(21), 3537–3540.

Olsson, W. A., Holcomb, D. J., & Rudnicki, J. W. (2002). Compaction localization in porous sandstone: Implications for reservoir mechanics. *Oil & Gas Science and Technology*, *57*(5), 591–599.

Olsson, W. A. (2001). Quasistatic propagation of compaction fronts in porous rock. *Mechanics of Materials*, *33*(11), 659–668.

Orlic, B. (2016). Geomechanical effects of CO2 storage in depleted gas reservoirs in the Netherlands: Inferences from feasibility studies and comparison with aquifer storage. *Journal of Rock Mechanics and Geotechnical Engineering*, *8*(6), 846–859.

Osinga, S., Zambrano-Narvaez, G., & Chalaturnyk, R. J. (2015). Study of geomechanical properties of 3D printed sandstone analogue. In *49th US Rock Mechanics/Geomechanics Symposium*. American Rock Mechanics Association.

Palchik, V. (1999). Influence of Porosity and Elastic Modulus on Uniaxial Compressive Strength in Soft Brittle Porous Sandstones. *Rock Mechanics and Rock Engineering*, *32*(4), 303–309. https://doi.org/10.1007/s006030050050

Pan, R., Zhang, G., Li, S., An, F., Xing, Y., Xu, D., & Xie, R. (2016). Influence of mineral compositions of rocks on mechanical properties. In *50th US Rock Mechanics/Geomechanics Symposium*. OnePetro.

Paterson, M. S., & Wong, T.-F. (2005). *Experimental Rock Deformation - The Brittle Field*. Springer Science & Business Media.

Peksa, A. E., Wolf, K.-H. A., & Zitha, P. L. (2015). Bentheimer sandstone revisited for experimental purposes. *Marine and Petroleum Geology*, *67*, 701–719.

Perras, M. A., & Vogler, D. (2019). Compressive and tensile behavior of 3D-Printed and natural sandstones. *Transport in Porous Media*, *129*(2), 559–581.

Philit, S., Soliva, R., Labaume, P., Gout, C., & Wibberley, C. (2015). Relations between shallow cataclastic faulting and cementation in porous sandstones: first insight from a groundwater environmental context. *Journal of Structural Geology*, *81*, 89–105.

Pijnenburg, R. P. J., Verberne, B. A., Hangx, S. J. T., & Spiers, C. J. (2018). Deformation behavior of sandstones from the seismogenic Groningen gas field: role of inelastic versus elastic mechanisms. *Journal of Geophysical Research: Solid Earth*, *123*(7), 5532–5558.

Pijnenburg, R. P. J., Verberne, B. A., Hangx, S. J. T., & Spiers, C. J. (2019a). Inelastic deformation of the Slochteren sandstone: Stress-strain relations and implications for induced seismicity in the Groningen gas field. *Journal of Geophysical Research: Solid Earth*, *124*(5), 5254–5282.

Pijnenburg, R. P. J., Verberne, B. A., Hangx, S. J. T., and Spiers, C. J. (2019b). Intergranular clay films control inelastic deformation in the Groningen gas reservoir: Evidence from split-cylinder deformation tests. *Journal of Geophysical Research: Solid Earth*, *124*(12), 12679-12702.

Pittman, E. D. (1979). Porosity diagenesis and productive capability of sandstone reservoirs.

Pons, A., David, C., Fortin, J., Stanchits, S., Menéndez, B., & Mengus, J. M. (2011). X-ray imaging of water motion during capillary imbibition: A study on how compaction bands impact fluid flow in Bentheim sandstone. *Journal of Geophysical Research: Solid Earth*, *116*(B3).

Prager, W. (1956). A new method of analyzing stresses and strains in work-hardening plastic solids.

Primkulov, B., Chalaturnyk, J., Chalaturnyk, R., & Zambrano Narvaez, G. (2017). 3D printed sandstone strength: curing of furfuryl alcohol resin-based sandstones. *3D Printing and Additive Manufacturing*, *4*(3), 149–156.

Prosser, D. J., Daws, J. A., Fallick, A. E., & Williams, B. P. J. (1993). Geochemistry and diagenesis of stratabound calcite cement layers within the Rannoch Formation of the

Brent Group, Murchison Field, North Viking Graben (northern North Sea). *Sedimentary Geology*, *87*(3–4), 139–164.

Rabbani, A., Jamshidi, S., & Salehi, S. (2014a). An automated simple algorithm for realistic pore network extraction from micro-tomography images. *Journal of Petroleum Science and Engineering*, *123*, 164–171.

Rabbani, A., Jamshidi, S., & Salehi, S. (2014b). Determination of specific surface of rock grains by 2D imaging. *Journal of Geological Research*, *2014*.

Rabbani, A., Ayatollahi, S., Kharrat, R., & Dashti, N. (2016). Estimation of 3-D pore network coordination number of rocks from watershed segmentation of a single 2-D image. *Advances in Water Resources*, *94*, 264–277.

Rathore, J. S., Fjaer, E., Holt, R. M., & Renlie, L. (1995). P-and S-wave anisotropy of a synthetic sandstone with controlled crack geometryl 1. *Geophysical Prospecting*, *43*(6), 711–728.

Rice-Birchall, E., Faulkner, D. R., & Bedford, J. D. (2021). The manufacture, mechanical properties, and microstructural analysis of synthetic quartz-cemented sandstones. *International Journal of Rock Mechanics and Mining Sciences*, *146*, 104869.

Rice-Birchall, E., Faulkner, D. R., & Bedford, J. D. (2022). The effect of grain size and porosity on the nature of compaction localisation in high-porosity sandstone. *Journal of Structural Geology*, *164*, 104740.

Risnes, R., Madland, M. V., Hole, M., & Kwabiah, N. K. (2005). Water weakening of chalk—Mechanical effects of water–glycol mixtures. *Journal of Petroleum Science and Engineering*, *48*(1–2), 21–36.

Rizzo, R. E., Healy, D., Heap, M. J., & Farrell, N. J. (2018). Detecting the Onset of Strain Localization Using Two-Dimensional Wavelet Analysis on Sandstone Deformed at Different Effective Pressures. *Journal of Geophysical Research: Solid Earth*, *123*(12), 10–460.

Robert, R., Robion, P., Souloumiac, P., David, C., & Saillet, E. (2018). Deformation bands, early markers of tectonic activity in front of a fold-and-thrust belt: Example from the Tremp-Graus basin, southern Pyrenees, Spain. *Journal of Structural Geology*, *110*, 65–85.

Roscoe, K. H., & Burland, J. B. (1968). On the generalized stress-strain behaviour of wet clay.

Roscoe, K. H., Schofield, A. N., & Wroth, C P. (1958). On the yielding of soils. Geotechnique, 8(1), 22–53.

Rudnicki, J. W., & Rice, J. R. (1975). Conditions for the localization of deformation in pressure-sensitive dilatant materials. *Journal of the Mechanics and Physics of Solids*, *23*(6), 371–394.

Rutter, E. H. (1976). A discussion on natural strain and geological structure-the kinetics of rock deformation by pressure solution. *Philosophical Transactions of the Royal Society of London. Series A, Mathematical and Physical Sciences*, *283*(1312), 203–219.

Rutter, E. H., & Glover, C. T. (2012). The deformation of porous sandstones; are Byerlee friction and the critical state line equivalent? *Journal of Structural Geology*, *44*, 129–140. https://doi.org/10.1016/j.jsg.2012.08.014

Sahimi, M. (2011). *Flow and transport in porous media and fractured rock: from classical methods to modern approaches*. John Wiley & Sons.

Salami, Y., Dano, C., & Hicher, P.-Y. (2019). An experimental study on the influence of the coordination number on grain crushing. *European Journal of Environmental and Civil Engineering*, *23*(3), 432–448.

Sammis, C., King, G., & Biegel, R. (1987). The kinematics of gouge deformation. *Pure and Applied Geophysics*, *125*(5), 777–812.

Saraji, S., & Piri, M. (2015). The representative sample size in shale oil rocks and nano-scale characterization of transport properties. *International Journal of Coal Geology*, *146*, 42–54.

Sari, M., Sarout, J., Poulet, T., Dautriat, J., & Veveakis, M. (2022). The Brittle–Ductile Transition and the Formation of Compaction Bands in the Savonnières Limestone: Impact of the Stress and Pore Fluid. *Rock Mechanics and Rock Engineering*, 1–13.

Sattler, T., & Paraskevopoulou, C. (2019). Implications on characterizing the extremely weak Sherwood sandstone: case of slope stability analysis using SRF at two oak quarry in the UK. *Geotechnical and Geological Engineering*, *37*(3), 1897–1918.

Sayers, C. M., & Han, D.-H. (2002). The effect of pore fluid on the stress-dependent elastic wave velocities in sandstones. In *SEG technical program expanded abstracts 2002* (pp. 1842–1845). Society of Exploration Geophysicists.

Schimmel, M. T. W., Hangx, S. J. T., & Spiers, C. J. (2022). Effect of pore fluid chemistry on uniaxial compaction creep of Bentheim sandstone and implications for reservoir injection operations. *Geomechanics for Energy and the Environment*, *29*, 100272.

Schindelin, J., Arganda-Carreras, I., Frise, E., Kaynig, V., Longair, M., Pietzsch, T., et al. (2012). Fiji: an open-source platform for biological-image analysis. *Nature Methods*, *9*(7), 676–682.

Schofield, A. N., & Wroth, P. (1968). *Critical state soil mechanics* (Vol. 310). McGraw-hill London.

Schultz, R. A. (2009). Scaling and paleodepth of compaction bands, Nevada and Utah. *Journal of Geophysical Research: Solid Earth*, *114*(B3).

Schultz, R. A., Okubo, C. H., & Fossen, H. (2010). Porosity and grain size controls on compaction band formation in Jurassic Navajo Sandstone. *Geophysical Research Letters*, *37*(22).

Shahin, G., Viggiani, G., & Buscarnera, G. (2020). Simulating spatial heterogeneity through a CT-FE mapping scheme discloses boundary effects on emerging compaction bands. *International Journal of Solids and Structures*, *206*, 247–261.

Shen, Y.-J., Zhang, Y.-L., Gao, F., Yang, G.-S., & Lai, X.-P. (2018). Influence of temperature on the microstructure deterioration of sandstone. *Energies*, *11*(7), 1753.

Shi, X., Cai, W., Meng, Y., Li, G., Wen, K., & Zhang, Y. (2016). Weakening laws of rock uniaxial compressive strength with consideration of water content and rock porosity. *Arabian Journal of Geosciences*, *9*(5), 369.

Skurtveit, E., Ballas, G., Fossen, H., Torabi, A., Soliva, R., & Peyret, M. (2014). Sand textural control on shear-enhanced compaction bands in poorly-lithified sandstone.

Soliva, R., Schultz, R. A., Ballas, G., Taboada, A., Wibberley, C., Saillet, E., & Benedicto, A. (2013). A model of strain localization in porous sandstone as a function of tectonic setting, burial and material properties; new insight from Provence (southern France). *Journal of Structural Geology*, *49*, 50–63.

Soliva, R., Ballas, G., Fossen, H., & Philit, S. (2016). Tectonic regime controls clustering of deformation bands in porous sandstone. *Geology*, *44*(6), 423–426.

Stanchits, S., Fortin, J., Gueguen, Y., & Dresen, G. (2009). Initiation and Propagation of Compaction Bands in Dry and Wet Bentheim Sandstone. *Pure and Applied Geophysics*, *166*(5–7), 843–868. https://doi.org/10.1007/s00024-009-0478-1

Sternberg, S. R. (1983). Biomedical image processing. *Computer*, *16*(01), 22–34.

Sternlof, K. R., Chapin, J. R., Pollard, D. D., & Durlofsky, L. J. (2004). Permeability effects of deformation band arrays in sandstone. *AAPG Bulletin*, *88*(9), 1315–1329.

Sternlof, K. R., Rudnicki, J. W., & Pollard, D. D. (2005). Anticrack inclusion model for compaction bands in sandstone. *Journal of Geophysical Research: Solid Earth*, *110*(B11).

Sternlof, K. R., Karimi-Fard, M., Pollard, D. D., & Durlofsky, L. J. (2006). Flow and transport effects of compaction bands in sandstone at scales relevant to aquifer and reservoir management. *Water Resources Research*, *42*(7).

Tembe, S., Vajdova, V., Wong, T.-F., & Zhu, W. (2006). Initiation and propagation of strain localization in circumferentially notched samples of two porous sandstones. *Journal of Geophysical Research: Solid Earth*, *111*(B2).

Tembe, S., Baud, P., & Wong, T.-F. (2008). Stress conditions for the propagation of discrete compaction bands in porous sandstone. *Journal of Geophysical Research*, *113*(B9). https://doi.org/10.1029/2007JB005439

Tiab, D., & Donaldson, E. C. (2015). *Petrophysics: theory and practice of measuring reservoir rock and fluid transport properties*. Gulf professional publishing.

Tillotson, P., Sothcott, J., Best, A. I., Chapman, M., & Li, X.-Y. (2012). Experimental verification of the fracture density and shear-wave splitting relationship using synthetic silica cemented sandstones with a controlled fracture geometry. *Geophysical Prospecting*, *60*(3), 516–525.

Toksoz, M. N., Cheng, C. H., & Timur, A. (1976). Velocities of seismic waves in porous rocks. *Geophysics*, *41*(4), 621–645.

Tsang, C.-F., Neretnieks, I., & Tsang, Y. (2015). Hydrologic issues associated with nuclear waste repositories. *Water Resources Research*, *51*(9), 6923–6972.

Vajdova, V., Wong, T.-F, Farrell, D. E., Challa, V., & Issen, K. A. (2003). Experimental observation and numerical simulation of initiation and propagation of compaction

bands in a sandstone, paper presented at 16th ASCE Engineering Mechanics Conference. *Seattle, Wash*.

Vajdova, V., & Wong, T.-F. (2003). Incremental propagation of discrete compaction bands: Acoustic emission and microstructural observations on circumferentially notched samples of Bentheim. *Geophysical Research Letters*, *30*(14), SDE8-1.

Vajdova, V., Baud, P., & Wong, T.-F. (2004). Permeability evolution during localized deformation in Bentheim sandstone. *Journal of Geophysical Research: Solid Earth*, *109*(B10).

Wadsworth, F. B., Vasseur, J., Scheu, B., Kendrick, J. E., Lavallée, Y., & Dingwell, D. B. (2016). Universal scaling of fluid permeability during volcanic welding and sediment diagenesis. *Geology*, *44*(3), 219–222.

Walsh, J. B. (1965). The effect of cracks on the uniaxial elastic compression of rocks. *Journal of Geophysical Research*, *70*(2), 399–411.

Wang, J., Cao, Y., Liu, K., Liu, J., Xue, X., & Xu, Q. (2016). Pore fluid evolution, distribution and water-rock interactions of carbonate cements in red-bed sandstone reservoirs in the Dongying Depression, China. *Marine and Petroleum Geology*, *72*, 279–294.

Warren, J. K. (2006). *Evaporites: sediments, resources and hydrocarbons*. Springer Science & Business Media.

Wasantha, P. L. P., Ranjith, P. G., Zhao, J., Shao, S. S., & Permata, G. (2015). Strain rate effect on the mechanical behaviour of sandstones with different grain sizes. *Rock Mechanics and Rock Engineering*, *48*(5), 1883–1895.

Weldes, H. H., & Lange, K. R. (1969). Properties of soluble silicates. *Industrial & Engineering Chemistry*, *61*(4), 29–44.

Weszka, J. S., & Rosenfeld, A. (1978). Threshold evaluation techniques. *IEEE Transactions on Systems, Man, and Cybernetics*, *8*(8), 622–629.

Wilhelm, S., & Kind, M. (2015). Influence of pH, temperature and sample size on natural and enforced syneresis of precipitated silica. *Polymers*, *7*(12), 2504–2521.

Wolcott, J. M., Monger, T. G., Sassen, R., & Chinn, E. W. (1989). The effects of CO2 flooding on reservoir mineral properties. In *SPE International Symposium on Oilfield Chemistry*. Society of Petroleum Engineers.

Wong, T.-F., & Wu, L.-C. (1995). Tensile stress concentration and compressive failure in cemented granular material. *Geophysical Research Letters*, *22*(13), 1649–1652.

Wong, T.-F., David, C., & Zhu, W. (1997). The transition from brittle faulting to cataclastic flow in porous sandstones: Mechanical deformation. *Journal of Geophysical Research: Solid Earth*, *102*(B2), 3009–3025.

Wong, T.-F., Baud, P., & Klein, E. (2001). Localized failure modes in a compactant porous rock. *Geophysical Research Letters*, *28*(13), 2521–2524.

Wong, T.-F., & Baud, P. (1999). Mechanical Compaction of Porous Sandstone. *Oil & Gas Science and Technology*, *54*(6), 715–727. https://doi.org/10.2516/ogst:1999061

Wood, D. M. (1990). *Soil behaviour and critical state soil mechanics*. Cambridge university press.

Wu, X. Y., Baud, P., & Wong, T.-F. (2000). Micromechanics of compressive failure and spatial evolution of anisotropic damage in Darley Dale sandstone. *International Journal of Rock Mechanics and Mining Sciences*, *37*(1–2), 143–160.

Wu, J., Feng, M., Yu, B., Zhang, W., Ni, X., & Han, G. (2018). Experimental investigation on dilatancy behavior of water-saturated sandstone. *International Journal of Mining Science and Technology*, *28*(2), 323–329.

Wu, H., Papazoglou, A., Viggiani, G., Dano, C., & Zhao, J. (2020). Compaction bands in Tuffeau de Maastricht: insights from X-ray tomography and multiscale modeling. Acta Geotechnica, 15(1), 39–55.

Yang, S.-Q., Jing, H.-W., & Cheng, L. (2014). Influences of pore pressure on short-term and creep mechanical behavior of red sandstone. *Engineering Geology*, *179*, 10–23.

Yang, P., Clapworthy, G., Dong, F., Codreanu, V., Williams, D., Liu, B., et al. (2016). GSWO: A programming model for GPU-enabled parallelization of sliding window operations in image processing. *Signal Processing: Image Communication*, *47*, 332–345.

Yang, S.-Q., Jing, H.-W., & Wang, S.-Y. (2012). Experimental investigation on the strength, deformability, failure behavior and acoustic emission locations of red sandstone under triaxial compression. *Rock Mechanics and Rock Engineering*, *45*(4), 583–606.

Yates, P. G. J. (1992). *The material strength of sandstones of the Sherwood Sandstone Group of north Staffordshire with reference to microfabric*. Geological Society of London.

Yu, C., Ji, S., & Li, Q. (2016). Effects of porosity on seismic velocities, elastic moduli and Poisson's ratios of solid materials and rocks. *Journal of Rock Mechanics and Geotechnical Engineering*, *8*(1), 35–49.

Yu, J., Xu, W., Jia, C., Wang, R., & Wang, H. (2019). Experimental measurement of permeability evolution in sandstone during hydrostatic compaction and triaxial deformation. *Bulletin of Engineering Geology and the Environment*, *78*(7), 5269–5280.

Zhang, D., Zhang, R., Chen, S., & Soll, W. E. (2000). Pore scale study of flow in porous media: Scale dependency, REV, and statistical REV. *Geophysical Research Letters*, *27*(8), 1195–1198.

Zhang, J., Wong, T.-F., & Davis, D. M. (1990). Micromechanics of pressure-induced grain crushing in porous rocks. *Journal of Geophysical Research: Solid Earth*, *95*(B1), 341–352.

Zhang, J. J., & Bentley, L. R. (1999). Change of bulk and shear moduli of dry sandstone with effective pressure and temperature. *CREWES Res Rep*, *11*, 01–16.

Zhu, W., & Wong, T.-F. (1997). Shear-enhanced compaction in sandstone under nominally dry and water-saturated conditions. *International Journal of Rock Mechanics and Mining Sciences*, *34*(3–4), 364-e1.

Zoback, M. D. (2010). *Reservoir geomechanics*. Cambridge University Press.